DEVELOPMENT OF NOVEL FAR-RED/NEAR-INFRARED DYE-HCRBPII BASED IMAGING TAGS FOR BACKGROUND-FREE LIVE CELL IMAGING

By

Wei Sheng

A DISSERTATION

Submitted to
Michigan State University
in partial fulfillment of the requirements
for the degree of

Chemistry — Doctor of Philosophy

2019

ABSTRACT

DEVELOPMENT OF NOVEL FAR-RED/NEAR-INFRARED DYE-HCRBPII BASED IMAGING TAGS FOR BACKGROUND-FREE LIVE CELL IMAGING

By

Wei Sheng

Modern fluorescence imaging technologies, including deep-tissue imaging and super-resolution microscopies, require novel fluorescent labeling tags possessing non-conventional optical features, among which most desired ones are high brightness in the far-red/near-infrared (NIR) region and turn-on/off control in a spatiotemporal manner. Previously, we demonstrated the ability of fine tuning the absorption spectra of a protein-bound natural chromophore over an unprecedented range (474 ~ 664 nm). The goal of this PhD research is to exploit protein-ligand interactions for the development of protein-based pigments as NIR fluorescent tags for background-free live cell imaging.

In the past half century, tremendous efforts have been invested in the optimization and derivatization of GFP-like fluorescent proteins (FPs). More recently, growing attention on phytochrome-based FPs has even upsized the repertoire of available FPs with many enhanced optical features. Giving this advancement, certain pitfalls are still limiting their uses in modern fluorescence imaging. In this context, synthetic dyes provide a broader chemical space for tailoring desired optic features including spectral wavelengths, brightness, stability, and many more photophysical and/or photochemical functionalities.

To achieve high contrast imaging with minimal background interference, three different strategies have been applied here. 1) NIR emission is approached by utilizing a

dye capable of specific complexation with a target protein via imine bond formation. Upon protonation of the imine, the complex experiences a large bathochromic shift as a result of a strong intramolecular charge transfer (ICT) process. A light-triggered imine isomerization is further incorporated to furnish a photoswitchable tag and negate the routine wash steps in live cell experiments. Rational protein engineering affords a faster variant that allows unprecedented spatiotemporal control of this no-wash bright NIR imaging. (2) A rare organic super photobase is identified, exhibiting a 14-unit change in pK_a upon light excitation. Steady-state and ultrafast spectroscopic measurements ascribe this event to an excited-state proton transfer (ESPT) process. This ESPT feature is recapitulated in a protein-ligand micro-environment, yielding protein-dye complexes with extremely high fluorescence quantum yields (up to 92%) and large pseudo-Stokes shifts (> 200 nm). Our optimal mutant bound to the dye boasts millisecond binding rate and enables live cell imaging with negligible background. (3) A general approach to fluorogenicity, i.e., the ability to turn on fluorescence, is designed by coupling a quenching moiety capable of photoinduced electron transfer (PeT) to our dyes. The fluorescence is negligible before the Michael addition of engineered cysteine residue (the trigger) with the quencher moiety. A 30-fold fluorescence enhancement is achieved *in vitro* with an electronically tuned quencher group. Currently, further modifications are in progress to optimize the quenched system for *in vivo* applications.

Dedicated to Anna, my parents, my grandma, and my dear friends,
for your everlasting encouragement and enlightenment

ACKNOWLEDGEMENTS

The first and most important person in my PhD research period is my advisor Professor Dr. Babak Borhan. I am exceedingly grateful to him for his inculcation of me with an independent and resilient research attitude, which I deem as the most critical character he incarnated into my mind that is beneficial for not only my research, but also my reflections towards life. Babak is a very knowledgeable and insightful scholar with endless energy and enthusiasm for chemistry research. As spotlighted by his three distinct research areas that span widely from total synthesis and synthetic methodologies to bioorganic chemistry and CD spectroscopies, his well-rounded figure as a "**chemist**" (rather than a pure organic chemist) always inspires me to grow into the same type of multifaceted researcher that solves scientific problem by exploiting every means of technologies from all scientific disciplines. This influence is pivotal in developing my own research interest throughout my PhD program. Babak's continuous support and encouragement helped me pursuing the research subjects *vide infra* that may not be regarded as traditional organic chemistry topics by many others. Nourished by his open-mindedness, I was able to explore and experiment into different chemistry disciplines for the fulfillment of my PhD central theme, and comfortably claim myself as a problem-solving scientist without putting any boundary to my research.

There are many other group members I need to express gratitude to. Dr. Chrysoula Vasileiou is not just a senior in the succession of PhD researchers of the bio-oriented projects in the group, more importantly to me she is a listener, a helper, and a life-long

friend that supports my life as a foreign student in the United States. Dr. Ipek Yapici is the senior member who guided me into the subject of research and also a good friend who paid heartful attention to my well-being inside the group. Her rhapsodic joyfulness and emotion always make the days in Rm.600 extremely vivid. I always enjoyed talking and discussing with Dr. Hadi Gholami for broad synthetic topics and graduate life. Shared more common feelings than other lab folks, the small Chinese community of Dr. Xinliang Ding, Dr. Jun Zhang, and Dr. Yi Yi has made my graduate life in US much smoother and connected, as our shared joyfulness comes from the leisure time and is beyond the research laboratory. I am also grateful to my many dear friends for their mutual supports: Hadi Nayebi, Nastaran Salehi Marzijarani, Xiaopeng Yin, Yubai Zhou, Chenchen Yang, Peng Wang, Ruipeng Mu, Tayeb Kakeshpour. The list should also include other current and past lab members and can go miles long.

Support and collaborations are also vital to my research. I am very thankful to my committee members Dr. Xuefei Huang, Dr. James Geiger, and Dr. William Wulff, for their help in the graduate courses and useful guidance and comments on my research projects. Especially I am grateful to Dr. Geiger for the intense collaboration with his research group on my research projects. Being more specifically, I am thankful to Dr. Zahra Assar, Dr. Alireza Ganbarpour, and Nona Ehyaei for their constructive suggestions and the protein crystallography work. I obtained many instructions from different people on operations of essential instrumentation that facilitated my research work. Thanks to Dr. Melinda Frame for the help with fluorescence microscopes, Dr. Tony Schilmiller and Dr. Lijun Chen for the training of high-resolution mass spectrometer, and Dr. Dan Holmes for NMR. For

collaborations inside group, I am grateful to Dr. Elizabeth Santos for her indefatigable effort in protein engineering which attributes to the better understanding of hCRBPII and Dr. Setare Tahmasebi Nick for her crucial input in the photoswitch project. I greatly enjoyed the collaboration with laser spectroscopists Dr. Muath Nairat, Dr. Marcus Dantos and Dr. Ehud Pines for their invaluable and incredible work on the photobase project. The collaboration with Chenchen Yang, Dr. Margaret Young, Dr. Sofia Lunt and Dr. Richard Lunt on the material engineering project widely expanded my research scope and capability.

Research is not the sole part of the graduate life. Chasing a dream of research and becoming a graduate student on the other side of earth can be extremely challenging. The endless love, understanding, and support from my parents will never be paid back. Even possessing the enthusiasm to chemistry, my faith in pursuing the degree would have worn out if without the dedicated backup and care from my beloved wife Anna. My final sincere acknowledgement is devoted to Mr. Thomas Almer, Mrs. Andree Almer, and Mrs. Rita Hsieh. Fate has brought them to me and bonded us as family while I am thousands of miles away from home.

TABLE OF CONTENTS

LIST OF TABLES ..... **x**

LIST OF FIGURES ..... **xi**

LIST OF SCHEMES ..... **xxiv**

KEY TO SYMBOLS AND ABBREVIATIONS ..... **xxvi**

CHAPTER I. A BRIEF OVERVIEW: THE EMERGING FIELD OF MODERN FLUORESCENCE IMAGING TAGS AND NEAR-INFRARED EMITTERS. **1**

I.1 Constitutively fluorescent proteins 1
I.1.1 The origin of FPs, and the innate chromophores 3
I.1.2 Classification of FPs 5
I.2 General applications of fluorescence imaging 10
I.2.1 Modern imaging applications of FPs 11
I.2.2 Other trending applications of fluorescence bioimaging 17
I.2.2.1 Biosensing 17
I.2.2.2 Emerging new imaging agents and their applications 22
I.2.2.3 Multimodality fluorescence imaging and intraoperative imaging guided cancer surgery 28
I.3 Site-specific labeling methods for *in vivo* fluorescence imaging 30
I.3.1 Covalent enzymatic labeling 30
I.3.2 Noncovalent affinity labeling 33
I.3.3 Bioorthogonal chemical labeling 37
I.3.4 Labeling approaches with short oligomer tags 42
I.4 Ongoing pursuit of far-red/near-infrared fluorochromes 45
I.4.1 Far-red and NIR FPs 46
I.4.2 NIR organic dyes 48
I.4.2.1 Polymethine dyes 48
I.4.2.2 Donor-Acceptor NIR dyes 54
I.4.2.3 Other NIR dyes 60
REFERENCES 64

CHAPTER II. DEVELOPING DYE-HCRBPII COMPLEXES INTO NO-WASH BACKGROUND-FREE NEAR-INFRARED TAGS VIA PHOTOSWITCHING. **97**

II.1 Preliminary work towards the hCRBPII-based fluorescent tag 98
II.2 The requirements of a successful fluorescence imaging tag 101
II.3 Early attempts in finding fluorescent ligands for hCRBPII 103
II.4 Approach to NIR emission with large Stokes shift 110
II.5 Discovery of photochromic dye-hCRBPII complexes 117

II.6 Developing CF-1 into a NIR tag for no-wash *in vivo* imaging 125
II.7 Engineering ps4 into a truly fluorogenic tag for spatiotemporal imaging 139
II.8 Conclusion and future research directions 146
II.8.1 Future structural modification of FR-1V 147
II.8.2 FR-1V/hCRBPII as a dual-emission ratiometric pH probe 148
II.9 Experimental section 151
REFERENCES 183

CHAPTER III. EXCITED STATE PROTON TRANSFER OF FR PHOTOBASES AND DEVELOPING DYE-HCRBPII COMPLEXES INTO BRIGHT, LONG STOKES SHIFT, FAST-FORMING TAGS VIA EXCITED-STATE HYDROGEN BONDING 188
III.1 Discovery of intermolecular ESPT in the solution study of FR0 189
III.2 Time-resolved study of FR0-SB ESiPT 197
III.3 Recapitulate ESHB in hCRBPII complexes to develop bright, long Stokes Shift, and fast-forming imaging tag 212
III.3.1 ESHB of photoacids and the applications 212
III.3.2 ESHB in dye/hCRBPII complexes 214
III.3.3 A bright ESHB tag with large Stokes shift and fast-forming kinetics 218
III.4 Dual-color live cell imaging enabled by a single dye 222
III.5 Conclusion and significance 227
III.6 Experimental section 228
REFERENCES 233

CHAPTER IV. MINIMIZING IMAGING BACKGROUND OF DYE-HCRBPII TAGS VIA PHOTOINDUCED ELECTRON TRANSFER QUENCHING. 238
IV.1 Current strategies to enable no-wash live cell imaging 238
IV.1.1 Fluorogenicity based on physical interaction with environments 239
IV.1.2 Fluorogenicity based on chemical modification of fluorophores 241
IV.2 Designing a PeT-quencher tethered FR0 as a dark stain 249
IV.3 Modification of the maleimide quencher and *in vitro, in vivo* studies 258
IV.4 Conclusion and future directions 272
IV.5 Experimental section 274
REFERENCES 285

LIST OF TABLES

Table II-1 Spectral features of selected **DiAI-2V**/hCRBPII complexes. 106

Table II-2 Spectral features of **FR** dyes in different organic solvents. 113

Table II-3 Spectral features of **FR-1V** and its SB in different solvents. 115

Table II-4 Wavelength comparison of **FR-1V** and its SB, PSB. 116

Table II-5 Selected **FR-1V**/hCRBPII mutants showing fluorescent photochromism. ...122

Table II-6 Feature comparison between **ps4** and **ps5**. 141

Table II-7 Comparison of **CF-1** and **CF-2** with other far-red/NIR FPs.[a] 146

Table III-1 Spectral comparison of **FR0**-SB and **FR-1V**-SB in organic solvents. 190

Table IV-1 Oligomeric nature of **psES235** cysteine mutations. 265

Table IV-2 QY and fluorescence recovery kinetics of **psES325** and **psWS51-54**. 268

Table IV-3 HRMS of **Q2mFR0**/hCRBPII adducts. 269

LIST OF FIGURES

Figure I-1 Structure of Aequorea victoria GFP. Showing the side (left) and top (right) views of the protein, the intrinsically generated fluorophore, and several key residues for chromophore maturation (PDB ID: 1w7s). 1

Figure I-2 A representative set of chromophores responsible for fluorescence in constitutively fluorescent metazoan proteins. 2

Figure I-3 Reported fluorescence brightness (extinction coefficient times fluorescence quantum yield) of a number of popular or unique fluorescent proteins as a function of emission wavelength. The dashed line serves as a guide to highlight the general trend. The coloring of the tags approximates the appearance of the corresponding emission wavelength to the naked eye. The brightness of some fluorophores has been altered by a small amount for clearer visual presentation. Copied from ref [7]. 3

Figure I-4 Phylogenetic tree of representative FPs, copied from ref [17]. The branches with a posterior probability of 0.95 are collapsed. Individual sequences are represented by boxes corresponding to their color type (see legend). Representative FPs are shown with their commercial names and/or mutant derivatives in brackets. 6

Figure I-5 Application of fluorescent proteins. Dark gray and light gray petals show structural and functional applications, respectively. This artwork is copied from ref [17]. 10

Figure I-6 Three image sequences show the FLAP image in pseudocolour (left panel) and phase-contrast image (right panel) at the following times after bleaching: 0 s (a, d and g), 50 s (b and e), 100 s (c, f and h) and 200 s (i). In these sequences the individual channels were acquired in multi-tracking mode. Bleach region shown as a circle in each image. Threshold level set to 8% of maximum signal. Bleach times 8.6 s (a) and 13.5 s (d and g). Scale bars 10 μm. Image copied from ref [84]. 12

Figure I-7 Three modes of FRET sensing for biomolecular interactions. Artwork copied from ref [85]. 13

Figure I-8 Schematic representation of the FLINC-AKAR design principle, the domain structure of FLINC–AKAR1 and the acquisition of super-resolution activity images with pcSOFI. Artwork copied from ref [95]. 15

Figure I-9 In vivo dynamic GSH imaging. (a) Chemical structure of QG3.0 probe. (b) Real-time GSH imaging with QG3.0 (1 μM) in A549 cells under glucose-deprivation with a perfusion system. Overlay and time-lapse ratio imaging of GSH under high-glucose (25 mM: 25G) or glucose-free (0 mM: 0G) conditions. 1: 0–3 min, 25 mM glucose; 3–12 min, 0 mM glucose; 12–30 min, 25 mM glucose. 2: 0–3 min, 25 mM glucose; 3–30 min, 0 mM

glucose. scale bars, 20 μm. (c) Time-course of GSH concentration under glucose deprivation (red, condition 1; blue, condition 2). Images and plot copied from ref [121]. 19

Figure I-10 Methods of voltage sensing with small molecules. (a) Voltage-dependent traverse of solvatochromic dyes in lipid membranes. (b) Electrochromic voltage-sensing. (c) Voltage-dependent FRET acceptor redistribution. (d) Voltage-sensing based on PeT perturbation. Artwork copied from ref [128]. 20

Figure I-11 Spontaneous voltage and epifluorescence imaging with BeRST 1 in GFP-labeled cells of rat hippocampal neurons. (a) GFP and (b) stained with BeRST 1. Scale bar is 20 μm. (c) Optical traces of spontaneous activity in neurons from panels (a) and (b). Numbers next to traces correspond to indicated cells in panel (b). Optical sampling rate is 500 Hz. Images and plot copied from ref [131]. 21

Figure I-12 Cell surface tension imaging. (a) Schematic of the FRET-quenching mechanism of tension sensor function, copied from ref [132]. (b) Reflection interference contrast microscopy (RICM) and fluorescence overlay, and quantified heat map of tension for cells cultured on the cRGDfK (TAMRA-QSY9) and SHAVSS (Alexa 488-TAMRA) peptide tension probe surfaces. Scale bar: 20 μm. Images copied from ref [134]. 22

Figure I-13 Schematic representation of dye-loading NP design for multicolor imaging via sequential FRET cascade. 23

Figure I-14 Tracking RGB barcoded cancer cells in zebrafish embryo. A) Six batches of D2A1 cells were labeled with fluorescent NPs generating RGB barcodes. Labeled cells were then mixed and injected intravascularly in 2 d postfertilization zebrafish embryos. B–D) Tumor cells that arrested in the vasculature are imaged, at 3 h post-injection, in the caudal plexus region of the zebrafish embryo. Clusters and individual cells can be found and distinguished based on their color. Images copied from ref [142]. 24

Figure I-15 $^1O_2$-sensitizer-amplified NIR afterglow. (a) Schematic illustration of the proposed mechanism. (b) Schematic illustration of SPN-NCBS pre-irradiated by an 808-nm laser for afterglow enhancement versus a 514-nm laser. (c) Afterglow luminescence images of SPN-NCBS pre-irradiated at 514 (left) or 808 nm (right). The NP solutions were pre-irradiated by 808- or 514-nm laser for 1 min, and then the afterglow images were acquired under bioluminescence mode with an acquisition time of 30 s after removal of the laser source. Images copied from ref [144]. 25

Figure I-16 Schematic representations of nucleic acids-based imaging probes. (a) Spinach sensor, comprising Spinach (black), a transducer (orange), and a target-binding aptamer (blue). Target (purple) binding to the aptamer promotes stabilization of the transducer stem, enabling Spinach to fold and activate DFHBI (green) fluorescence. (b) General structure of molecular beacons. 27

Figure I-17 Schematic labeling reactions of SNAP/CLIP-tags. 31

Figure I-18 Fluorogenic TMP-tag. (a) Cartoon of the trimeric TMP-quencher-fluorophore to be cleaved in a proximity-induced S_N2 reaction. (b) Structure of TMP-BHQ1-Atto520. 33

Figure I-19 Design of the PYP-tag mutant PYP3R and its fluorogenic probe, with a focus on electrostatic interactions and the pK_a value of the leaving group. Copied from ref [236]. 35

Figure I-20 Y-FAST-tag. (a) Schematic showing the spectral changes during Y-FAST binding: spectral shift and QY increase. (b) Confocal time lapse showing two cycles of labeling/unlabeling (Ex/Em 488/493-575 nm) of HeLa cells expressing Y-FAST. Cells were repeatedly incubated with HMBR-containing culture medium for 20 s and HMBR-free culture medium for 40 s. HMBR concentration was 5 μM. (c) Temporal evolution of the cell fluorescence upon addition (+) and removal (-) of HMBR. Images and plots copied from ref [238]. 36

Figure I-21 Fluorogenic ligands of FAP: thiazole orange (TO) and malachite green (MG). 37

Figure I-22 Two-step labeling scheme of site-specific protein labeling via PRIME and chelation-assisted CuAAC. In the first step, W37VLplA covalently attaches a copper-chelating picolyl azide (pAz) onto genetically fused LAP. In step two, CuAAC selectively derivatizes pAz with a probe-conjugated terminal alkyne. 42

Figure I-23 The ideal NIR window for in vivo imaging, showing minimal light absorption by haemoglobin (Hb, green), oxyhaemoglobin (HbO_2, red) (<650 nm) and water (>900 nm). Copied from ref [306]. 45

Figure I-24 Phytochrome-derived BV-binding FP. (a) Scheme showing Z/E isomerization between Pr and Pfr states of BV adduct. (b) Absorption spectra of Pr and Pfr states. Q band is the major absorption. Soret band is the pyrrole absorption. (c) A truncated PAS-GAF NIR FP (PDB ID: 4XTQ).....46

Figure I-25 Indocyanine green (ICG). 47

Figure I-26 Representative non-convergent polymethine cyanines. (a) Cyanines with various rigidified heptamethine backbones and terminal groups. (b) Conformation-restrained pentamethine cyanines. (c) Large Stokes shift heptamethine cyanines. 49

Figure I-27 Chemical structures of PPCy dyes. (a) Standard PPCys. (b) Further-extended PPCys. (c) PPCy aza-BODIPY analogues. 50

Figure I-28 NIR BODIPYs. (a) BODIPY framework. (b) aza-BODIPYs. (c) "coupled" BODIPYs. (d) "restricted" BODIPYs. 52

Figure I-29 NIR ring-fused BODIPYs. (a) [a/h]-fused BODIPYs. (b) [b/g]-fused BODIPYs. 53

Figure I-30 (a) NIR fluorescent squaraines. (b) NIR-II absorptive croconates. Scheme shows mesoionic oxidation. 55

Figure I-31 Restricted and C10-replaced rhodamines. 56

Figure I-32 Representative NIR D-A-D type of dyes. 57

Figure I-33 Selected ICT dyes and D-A hybrids. 58

Figure I-34 Selected NIR rylenes. 59

Figure I-35 Selected NIR porphyrinoids. 60

Figure I-36 Examples of NIR AIEgen. (a) Red-shifted TPE emission by extended conjugation. (b) Aggregation-induced bathochromic shift in emission. 61

Figure II-1 Crystal structure of hCRBPII KL mutant complexed with all-*trans*-retinal. Retinal is shown in red. The active lysine residue Q108K is shown in light green. Other key residues engineered to regulate the absorption wavelength of the bound retinylidene are shown in teal, with oxygen atoms colored red and nitrogen atoms colored blue (PDB ID: 4EXZ). The scheme shows the iminium (PSB) formation between lysine 108 and retinal aldehyde. 99

Figure II-2 Structure of **MCRA** and its schematic PSB formation with active lysine 132 of CRABPII. The absorption (red) and emission (blue) spectra are of the R132K:R111L (KL) mutant complex with **MCRA**. 100

Figure II-3 Crystal structure of hCRBPII-KL (Q108K:K40L) mutant, highlighting the cavity for ligand binding (meshed cages). PDB ID: 4EXZ. The bound all-*trans*-retinal is deleted for clarity. 104

Figure II-4 Live cell imaging with DiAI-2V and MCRA for performance testing. a) Clone map of hCRBPII mutant KLVSWW:L117E in ECFG-GalT vector. b) Comparison of images of DiAI-2V and MCRA complexed with KLVSWW:L117E in HeLa cells. Cells were stained with 250 nM of each dye and incubated for 10 min at 37 °C. Cells were washed with DPBS twice before imaging. ECFP channel: λex = 458 nm, BP 475-525. MCRA channel: λex = 594 nm, LP 615. DiAI-2V channel: λex = 514 nm, LP 560. BR: bright-field. 108

Figure II-5 Different resonance forms proposed for push-pull chromophores and related shape of the absorption spectra. The charge distribution along the push-pull systems of merocyanines and cyanines are depicted by three states: M^1 (neutral for merocyanine, zwitterionic for cyanine), M^2 (least bond length alteration), and M^3 (bipolar for

merocyanine, inverted zwitterionic for cyanine). Merocyanines are featured by one electron rich amine group (D, donor) and one more electronegative terminal group (A, acceptor) on either ends of the push-pull chain. Typical cyanines bear one neutral amine (D) and one charged iminium (A) on either ends of the push-pull chain. 109

Figure II-6 Schematic cross section of the ground state and the lowest excited singlet state potential hypersurfaces along the reaction coordinate corresponding to the ICT state model. 111

Figure II-7 Normalized spectra of **FR-1V** in various solvents: (a) absorbance, (b) emission. Normalized spectra of **FR-1V**-SB (*n*-butylamine) in various solvents: (c) absorbance, (d) emission. Tol: toluene; THF: tetrahydrofuran; EA: ethyl acetate; DCM: dichloromethane; DMF: *N,N*-dimethyl formamide; DMSO: dimethyl sulfone; MeCN: acetonitrile; EtOH: ethanol; MeOH: methanol. Scheme shows the SB formation between **FR-1V** and *n*-butylamine. 114

Figure II-8 Comparison of (a) absorbance and (b) emission spectra of **FR-1V**-SB and **FR-1V**-PSB in DMSO and ethanol. 116

Figure II-9 Flexible docking of **FR-1V** with all-*trans*-retinal bound hCRBPII KL mutant (PDB ID: 4EXZ). Green stick is the crystal structure of retinal. Orange stick is the pose of **FR-1V**. Docking was performed by AutoDock Vina. Residues within 5.5 Å distance to **FR-1V** are highlighted in line form. 120

Figure II-10 *Cis-trans* imine photoisomerization of all-*trans*-retinal bound CRABPII complexes. a) The iterative color switching of all-*trans* retinal/CRABPII complex under UV and green light irradiations. (PDB ID: 4YFP) b) Scheme illustrating the photocycle of retinylidene imine isomerization and the acid-base equilibrium of the thermodynamic SB and kinetic PSB. Figure and scheme are reproduced from ref [43]. 121

Figure II-11 Normalized absorption and emission spectra of the two photoswitching states of **CF-1** (**FR-1V**/**ps4** complex). “OFF” state: the colorless thermal equilibrated state after binding. “ON” state: the blue-colored state after UV irradiation. The equilibrium illustrates the reversible switching under different conditions. 123

Figure II-12 Binding of **ps4** (20 μM) and **FR-1V** in PBS buffer (pH 7.3) over time, incubated at 25 °C. (a) Stacked traces of absorbance spectra, **FR-1V** (7 μM); (b) Time-course absorbance spectrum monitored at 378 nm, **FR-1V** (6 μM). Data points were fitted to an exponential rise function. 125

Figure II-13 Switching fatigue resistance of **CF-1**. Stacked traces of (a) absorbance spectra, (b) emission spectra, over cycles of alternate UV and yellow light irradiations. For each cycle, excitation at 378 nm lasts 20 s with U-360 UV Bandpass filter (Blue); excitation at 600 nm lasts 15 min with Y-50 (500nm) Longpass filter (Yellow). (c) **CF-1** absorbance monitored at 600 nm, and (d) **CF-1** emission intensities monitored at the

maxima of “OFF” and “ON” states in non-degassed solutions. 0.6% absorption and 1% emission intensities decreased per cycle. All measurements were in PBS (pH 7.3). ..126

Figure II-14 CF-1’s emission switching time of the "OFF" and "ON" states. Monitored at the emission maxima under continuous excitation. 127

Figure II-15 Temperature-dependent **CF-1** ON-to-OFF thermal switching, absorbance monitored at 600 nm. 128

Figure II-16 Thermal ON-to-OFF switching of **CF-1**. Rate constants plotted against temperature. (a) Arrhenius plot. (b) Eyring plot. 130

Figure II-17 Thermal versus yellow light-assisted (LP 500 filter) ON-to-OFF switching of **CF-1**, monitored at absorption maximum. Data points collected at 3-min interval. 130

Figure II-18 Working pH range of **CF-1**. Stacked traces of emission spectra of “OFF” (Ex. = 378 nm) and “ON” (Ex. = 600 nm) states: (a) pH 7 to 9; (b) pH 7 to 6. (c) pH-dependent fluorescence intensities of “OFF” and “ON” states, showing 80% intensities within pH 6.6 ~ 7.6 range. 131

Figure II-19 MTT assay of **FR-1V** in (a) HeLa and (b) U2OS cell lines. The absorbance was measured 550 nm, and corrected at 655 nm. Cells were treated with **FR-1V** for 24 h before MTT staining. Error bars represent the standard deviation of the readouts from (*n* = 6) cells. 132

Figure II-20 Size exclusion chromatography of hCRBPII mutant **ps4** expressed and purified from BL21(DE3)pLysS (buffer: 10 mM Tris·HCl, 2 M NaCl, pH 8.1) using a BioLogic DuoFlow QuadTec 10 system (Bio-Rad) equipped with a Superdex 120 16/600 GL size-exclusion column (GE Healthcare). 133

Figure II-21 Schematic maps of the (a) hCRBPII-ECFP and (b) EGFP-hCRBPII-SP fusion constructs. SP: signaling peptides. SP = 3×NLS (nuclear localization sequence), NES (nuclear export sequence), and CAAX (prenylation tag). 134

Figure II-22 Time serial confocal fluorescence images of U2OS cells expressing construct pFlagCMV2-EGFP-**ps4**-3×NLS, stained with 1 μM **FR-1V** and incubated at (a) 20 °C, and (b) 37 °C. Channels: EGFP (Green), λ_{ex} = 488 nm, BP 505-530; **CF-1_ON** (Red), λ_{switch} = 405 nm, λ_{ex} = 594 nm, LP 650. Scale bar, 20 μm.....135

Figure II-23 CF-1 labeling in U2OS and HEK293 cell lines. Left and middle column: cells expressing C-terminal ECFP, showing whole cell fluorescence. Right column: cells expressing N-terminal EGFP, showing nuclei-localized fluorescence. NLS = nuclear localization sequence. BR: bright-field. Channels: ECFP, λ_{ex} = 458 nm, BP 465-510IR; EGFP, λ_{ex} = 488 nm, BP 505-530; **CF-1**_ON, λ_{switch} = 405 nm, λ_{ex} = 594 nm, LP 650; Bright field, λ_{ex} = 488 nm. Cells were stained with 1 μM **FR-1V** and incubated at 37 °C for 5 min before imaging. No washing steps required. Scale bar, 20 μm. 136

Figure II-24 Compartmentalized **CF-1**_ON labeling in HeLa cells. (a) Labeling of different **CF-1** fusion proteins. NLS = nuclear localization sequence. NES = nuclear export sequence. CAAX = prenylation tag. DIC = differential interference contrast. Cells were stained with 2 μM **FR-1V** and incubated at 37 °C for 5 min before imaging. No washing steps required. Scale bar, 10 μm.....137

Figure II-25 Labeling specificity of nuclei-localized **CF-1** in HeLa cells. Top left: EGFP channel; top right: **CF-1**_ON channel; bottom left: merged channels + brightfield; bottom right: line profiles of fluorescence intensities in two channels along the blue arrow in the merged image. Scale bars, 20 μm. 138

Figure II-26 Normalized absorption and emission spectra of the two photoswitching states of **CF-2** (**FR-1V**/**ps5** complex).....139

Figure II-27 Switching fatigue resistance of **CF-2** monitored at 605 nm absorbance in PBS (pH 7.3). For each cycle, excitation at 378 nm lasts 20 s with U-360 UV Bandpass filter; excitation at 600 nm lasts 15 min with Y-50 (500 nm) Longpass filter. 140

Figure II-28 (a) Time-course absorbance spectrum monitored at 382 nm of **ps5** and **FR-1V** binding. Data points were fitted to an exponential rise function. (b) Time-course spectrum of **CF-2** ON-to-OFF thermal switching at 23 °C. Absorbance monitored at 605 nm. Data points were fitted to an exponential decay function. 141

Figure II-29 Compartmentalized **CF-2**_ON labeling in HeLa cells. Labeling of different **CF-2** fusion proteins. NLS = nuclear localization sequence. NES = nuclear export sequence. CAAX = prenylation tag. DIC = differential interference contrast. Cells were stained with 2 μM **FR-1V** and incubated at 37 °C for 5 min before imaging. No washing steps required. Scale bar, 10 μm.....142

Figure II-30 Labeling specificity of nuclei-localized **CF-2** in HeLa cells. Top left: EGFP channel; top right: **CF-2**_ON channel; bottom left: merged channels + DIC; bottom right: line profiles of fluorescence intensities in two channels along the blue arrow in the merged image. Scale bars, 20 μm. Circles and number indicating mean SBR *(n* = 440). 143

Figure II-31 ON-to-OFF thermal switching kinetics of (a) **CF-1** and (b) **CF-2** in HeLa cells. Region of interest was excited continuously with 594 nm laser (1.63 μW). Mean ROI intensity was recorded every 6 sec. 144

Figure II-32 *In cellulo* NIR fluorescence (LP650) "ON/OFF" cycling of HeLa cells expressing EGFP-**ps5**-CAAX, showing 10 switching cycles. Arrows: OFF-to-ON, 405 nm laser 4 sec; ON-to-OFF, r.t. 3 min. Scale bar: 10 μm. 144

Figure II-33 Spatiotemporal confocal imaging of HeLa cells, expressing nuclei-localized EGFP-fused **ps5**. Cells were stained with 2 μM **FR-1V** for 5 min at 37 °C and imaged without washing. Red channel: **CF-2**_ON. Following the arrows: before switch-on; 1st cell

switch-on; 2nd cell switch-on; 3rd cell switch-on; whole field switch-on. Compare with green channel: colocalized reference EGFP. Scale bars, 10 μm. 145

Figure II-34 The prototype of a dual-emission ratiometric pH probe. a) Stacked traces of the absorption spectra of **FR-1V/ph1** (Q108K:K40L:T51V:T53S:V62E) complex upon iterative light irradiation. UV = U-360 UV Bandpass filter. VIS = Y-50 (500 nm) Longpass filter. Stacked traces of b) SB and c) PSB emission under different pH. d) The correlation of the logarithmic fluorescence ratio and pH. A linear function is presented. 150

Figure III-1 Normalized spectra of **FR0** in various solvents: (a) absorbance, (b) emission. Normalized spectra of **FR0**-SB *(n*-butylamine) in various solvents: (c) absorbance, (d) emission. Tol: toluene; THF: tetrahydrofuran; EA: ethyl acetate; DCM: dichloromethane; DMF: *N,N*-dimethyl formamide; DMSO: dimethyl sulfone; ACN: acetonitrile; EtOH: ethanol; MeOH: methanol. Scheme shows the SB formation between **FR0** and *n*-butylamine. 189

Figure III-2 Solvatochromism of **FR0**, **FR-1V**, and their SBs as evident by their emission wavelengths in different solvents. Plots illustrate the correlation between wavenumbers and solvent polarities. The short wavelength emission maxima of **FR0**-SB in ethanol and methanol were selected for the plot. Reichardt's $E_T(30)$ scale is applied. 191

Figure III-3 QY as a function of solvent polarity of **FR0**-SB and **FR-1V**-SB. 192

Figure III-4 (a) Absorption and emission of **FR0**-SB in ethanol. (b) Excitation spectra of **FR0**-SB in ethanol at 460 nm and 630 nm, corrected against Rhodamine-B. 193

Figure III-5 (a) Stacked absorption traces of **FR0**-SB acidification with hydrochloric acid. (b) Absorption and emission spectra of acidified **FR0**-SB. 194

Figure III-6 Absorption and emission spectra of **FR0**-SB in different alcoholic solvents. (a) methanol, (b) ethanol, (c) 1-propanol, (d) 2-propanol, (e) *n*-amyl alcohol, (f) ethylene glycol. Traces labeled with *Peak-i* (1 ~ 4) are fluorescence spectra simulated by second derivative fitting with a Voigtian amplitude distribution using PeakFit™. The *Envelope* traces are the convolution of multiple *Peak-i*, showing a perfect overlap with the experimental spectra. 195

Figure III-7 Absorption and emission spectra of **FR0**-SB dissolved in acetic acid. (a) Absorption spectrum, showing ammonium peaks at 342 nm and iminium peaks at 472 nm. (b) Emission spectra excited at 472 nm. (c) Emission spectra excited at 342 nm. In (b) and (c), emission traces labeled with *Peak-i* are simulated by second derivative fitting with a Voigtian amplitude distribution using PeakFit™. The *Envelope* traces are the convolution of multiple *Peak-i*. 196

Figure III-8 Steady-state absorption (solid) and emission (shaded) spectra of **FR0**-SB in (a) acetonitrile (ACN) and (b) ethanol (EtOH). The spectra of **FR0**-PSB (acidified by perchloric acid in ethanol) are also overlaid. 199

Figure III-9 TCSPC traces with single exponential fits for **FR0**-SB near the emission maxima when dissolved in ACN and EtOH. Inset shows that the red emission trace at 650 nm of **FR0**-SB is identical to the **FR0**-PSB emission. 200

Figure III-10 Isotopic effect of **FR0**-SB in EtOH and ethanol-d_6 (EtOD). (a) Steady-state absorption and emission spectra of **FR0**-SB in EtOH and EtOD. (b) TCSPC decay curves of **FR0**-SB LW emission along with single exponential decay fits in EtOH and EtOD. An isotope effect of 1.6 is observed in EtOD. 201

Figure III-11 TCSPC decay curves of **FR0**-SB LW emission with single exponential decay fits in MeOH and methanol-d_4 (MeOD). An isotope effect of 2.0 is observed in MeOD. 202

Figure III-12 (a) Transient absorption spectra of **FR0**-SB at various time intervals after excitation in EtOH. Labeled arrows show the steps during the ESPT process. (b) Energy progression during the proton transfer process. 203

Figure III-13 (a) Transient absorption of **FR0**-SB in ACN, showing the long-lived excited state absorption and stimulated emission signals from the non-protonated form with biexponential fits at the frequencies of (b) excited state absorption and (c) stimulated emission signals. 205

Figure III-14 Stimulated emission signal from the transient absorption of **FR0**-PSB in acidic EtOH. Two decay components are observed, with a fast one corresponding to an intramolecular response from **FR0**-SB, and a slow one corresponding to the excited state lifetime. 206

Figure III-15 (a) Evolution associated spectra (EAS) of the four levels used in the sequential global analysis model to describe the proton transfer dynamics of **FR0**-SB in EtOH. (b) Population kinetics of the four levels used in the global analysis model. 207

Figure III-16 Transient absorption trace showing the energy progression during the excited state **FR0**-SB proton transfer process in MeOH. 208

Figure III-17 Transient absorption traces at (a) 570 nm where stimulated emission from the intermediate formation is observed, and (b) 650 nm where stimulated emission from **FR0**-PSB can be seen while dissolved in EtOH (black) and EtOD (red). Biexponential decay constants are given in the inset along with the pre-exponential factors in parentheses. An isotope effect of 1.5 is observed during the formation of the partially proton transferred intermediate, while an isotope effect of 2.0 is observed during the formation of final protonated **FR0**-PSB. 209

Figure III-18 Transient absorption traces at (a) 580 nm where stimulated emission from the intermediate formation is observed, and (b) 660 nm where stimulated emission from **FR0**-PSB can be seen while dissolved in MeOH (black) and MeOD (red). Biexponential decay constants are given in the inset along with the pre-exponential factors in

parentheses. An isotope effect of 2 is observed during the formation of the intermediate as well as in the final protonated form formation. 210

Figure III-19 The observed intermolecular ESPT dynamics in EtOH along with the associated time constants for the steps as obtained from global analysis (black) and the TCSPC data (colored). 211

Figure III-20 Normalized fluorescence spectra of **FR0**-SB in the acetonitrile solution of imidazole. The arrow shows the LW emission band (630-660 nm) emerging with the addition of imidazole (from blue to red), indicating the proton transfer from imidazole to **FR0**-SB. 212

Figure III-21 Potential residues facilitating excited state hydrogen bonding on **FR-1V** imine nitrogen atom. Residues within 5 Å to the nitrogen atom are shown in green. Residues within 6 Å distance are shown in red and magenta. The pose of **FR-1V** is simulated with a flexible docking method by using AutoDock Vina. The protein matrics is extracted from hCRBPII mutant **KL** (PDB ID: 4EXZ). **FR-1V**:carbon (cyan), nitrogen (blue), hydrogen (grey). Magenta residues are simulated with PyMOL. 216

Figure III-22 Representative **FR**/hCRBPII complexes showing excited state hydrogen bonding long wavelength emissions. Mutant Q108K:K40D:T53A:R58L:Q38F:Q4F:V62E is in the dimeric form. 217

Figure III-23 Excitation spectrum of **FR-1V**/**psES235** 600 nm emission. The red trace is the excitation spectrum corrected against Rhodamine-B. The green trace is the absorption spectrum. The blue trace is the normalized brightness curve, plotting the product of ε and ϕ with each square as a data point. 218

Figure III-24 Binding kinetics of **FR-1V** with **psES235**. a) Pseudo-first order binding of **FR-1V** (10 μM) with **psES235** (20 μM). The binding was monitored at the 595 nm ESHB emission maximum. An exponential fit gives the binding half-time as 0.18 s. b) Second-order rate constant measurement. Variable concentrations of **FR-1V** were used to bind 100 nM of **psES235**. Observable rate constants were derived from single exponential fits. The second-order rate constant was then derived from the linear regression of observable pseudo first order rate constants as a function of concentration. All measurements were taken in PBS buffer (pH = 7.3). 219

Figure III-25 Compartmentalized **FR-1V/psES235** imaging in live HeLa cells. NLS = nuclear localization sequence. NES = nuclear export sequence. CAAX = prenylation tag. Cells were stained with 500 nM **FR-1V** and incubated at 37 °C for 1 min. Cells were washed 3 times with DPBS before imaging. Scale bar, 10 μm. 220

Figure III-26 ESHB fluorescence specificity of **FR-1V**/**psES235**. Top row shows the merged EGFP and LP615 channels in cell nuclei, cytosol, and plasma membrane-localized HeLa cells. Bottom row shows the line profile of colocalized EGFP and ESHB signal along the white arrows in the top images. Scale bar, 10 μm. 221

Figure III-27 Absorption and emission spectra of **FR-1V**/**psST61**. 223

Figure III-28 Binding kinetics of **FR-1V**/**psST61**. a) Binding of **FR-1V** (10 μM) and **psST61** (10 μM) monitored at the 630 nm fluorescence maximum. The intensity curve is fit with a single exponential function. b) Second-order rate constant measurement. Variable concentrations of **FR-1V** were used to bind 100 nM of **psST61**. Observable rate constants were derived from single exponential fits. The second-order rate constant was then derived from the linear regression of observable pseudo first order rate constants as a function of concentration. All measurements were taken in PBS buffer (pH = 7.3).....224

Figure III-29 Dual-color live cell imaging with **FR-1V** in HeLa cells co-transfected with pFlag-CMV2 vectors encoding EGFP-**psES235**-NES and EGFP-**psST61**-3xNLS. a) ESHB channel: λ_{ex} = 405 nm, LP615. b) PSB channel: λ_{ex} = 514 nm, LP650. c) Reference EGFP channel: λ_{ex} = 488 nm, BP505-530. d) Merged image of a) and b), showing well-defined edges of cell nuclei and surrounding cytosol. Cells were stained with 500 nM of **FR-1V** and incubated at 37 °C for 1 min, then washed with DPBS for 3 times before imaging. Scale bars, 20 μm. 225

Figure III-30 Crystal structure of **FR-1V**/**psST61** complex, showing two trajectories of the 40H residue in a 50:50 population ratio. The closer conformer has a 2.9 Å distance between the histidine and the imine nitrogen atom. Protein crystallized by Dr. Alireza Ghanbarpour. 226

Figure III-31 Proposed key residues for mutagenesis to suppress K40H ESHB. Distances are measured from the **FR-1V**/**psST61** crystal structure. 226

Figure IV-1 Jabloński diagrams of various energy/electron donor-acceptor (D-A) systems. a) Förster Resonance Energy Transfer (FRET). θ: angle between donor emission and acceptor absorption. b) Dexter Energy Transfer (DET). Artwork copied from ref [10]. 244

Figure IV-2 PeT mechanisms. a) Participation of fluorophore HOMO-LUMO and an empty quencher orbital. b) Participation of fluorophore HOMO-LUMO and a filled quencher orbital. 247

Figure IV-3 Structure of model PeT-quenched **FR** fluorophore. 249

Figure IV-4 Orbital diagram of **Q1FR-1V** and the corresponding *n*-butylimine (**Q1FR-1V_SB**), *n*-butyliminium (**Q1FR-1V_PSB**), calculated with DFT/B3LYP/6-31+G in vacuum. The orbital views on the left side are of **Q1FR-1V**. The color code of the right-side energy diagram is: blue (HOMO of **FR-1V/SB/PSB**), green (LUMO of maleimide), and red (LUMO of **FR-1V/SB/PSB**). 250

Figure IV-5 Orbital diagram of the *n*-butylimine of **FR-1V** tethered with maleimides bearing different substituents. Left-side orbital views are shown with non-substituted maleimide. The color code on the right-side diagram is: blue (HOMO of **FR-1V_SB**), green (LUMO of maleimides), and red (LUMO of **FR-1V_SB**). 251

Figure IV-6 Orbital diagram of the *n*-butyliminium of **FR-1V** tethered with maleimides bearing different substituents. Left-side orbital views are shown with non-substituted maleimide. The color code on the right-side diagram is: blue (HOMO of **FR-1V_PSB**), green (LUMO of maleimides), and red (LUMO of **FR-1V_PSB**). 252

Figure IV-7 Extinction coefficient, absorption and emission spectra of **Q1FR0** in ethanol. 254

Figure IV-8 Fluorescence recovery of **Q1FR0** after addition of *n*-propane thiol (PSH). 255

Figure IV-9 Fluorescence recovery of **Q1FR0** tested by sequential addition of *n*-butylamine (nBA) and *n*-propane thiol (PSH) in different order. a) Reaction scheme of two sequential addition orders. b) Stacked traces of time-dependent absorption of **Q1FR0** after addition of excess nBA. c) Stacked traces of time-dependent absorption of **Q1FR0_PSH** adduct after addition of excess nBA. b) and c) showed the same timescale of imine condensation of nBA with **Q1FR0** and **Q1FR0_PSH**. d) Emission spectrum of **Q1FR0** after the sequential addition of PSH then nBA. e) Emission spectrum of **Q1FR0** after the sequential addition of nBA then PSH. d) and e) were recorded with the same concentrations of **Q1FR0**, PSH, and nBA. 256

Figure IV-10 Low stability of **Q1FR0**. a) Picture shows the fluorescence of **Q1FR0** samples stored in ethanol at 4 °C overnight (O/N), freshly prepared in ethanol and DMSO. Samples are excited with UV handset. b) Possible degradation pathway. 257

Figure IV-11 a) Absorption and emission spectra of **Q2mFR0** in ethanol. b) Stacked absorption traces of **Q2mFR0** added with *n*-propane thiol (PSH) over time. c) Emission spectra of **Q2mFR0** before and after addition of *n*-propane thiol. d) Fluorescence recovery measured peak intensity. e) Fluorescence recovery measured by whole spectra integration. 261

Figure IV-12 Chemoselectivity and fluorescence recovery of **Q2mFR0** with sequential addition of *n*-butylamine (nBA) and *n*-propane thiol (PSH). a) Stacked absorption traces of **Q2mFR0** with excess nBA over time. b) Stacked absorption traces of **Q2mFR0_PSH** adduct with excess nBA over time. a) and b) were recorded in ethanol with same amount of **Q2mFR0**, nBA, and PSH. c) Absorption and emission spectra of **Q2mFR0_nBA**. d) Absorption and emission spectra of the final solution of **Q2mFR0_PSH** added with nBA. c) and d) were recorded in ethanol with same starting concentration of **Q2mFR0**. e) Emission spectra of **Q2mFR0** in ethanol with sequential addition of nBA then PSH. ..263

Figure IV-13 Flexible docking results of **Q2mFR0** in hCRBPII KL mutant (PDB ID: 4EXZ). Residues within 5 Å distance to the maleimide double bond carbon atoms are highlighted in cyan and stick form. **Q2mFR0** is covalently attached to the Q108K residue. The top 9 poses are stacked in and displayed line form. 264

Figure IV-14 Absorption and emission spectra of **Q2mFR0** and **psES235** cysteine mutants. a) Stacked absorption traces of **Q2mFR0** and **psWS54** over time. b) Emission spectrum of **Q2mFR0**/**psWS54** with 374 nm excitation. Emission spectra with excitation at corresponding absorption maxima at different time points after **Q2mFR0** addition to c) **psWS51** monomer, d) **psWS52** monomer, e) **psWS53** monomer. 266

Figure IV-15 Fluorescence recovery of **Q2mFR0**/**psWS51-54**. a) Fluorescence recovery kinetics monitored at 540 nm. b) Fluorescence recovery ratio of different cysteine mutants over **psES235** monitored at 540 nm at different time points. 267

Figure IV-16 Confocal imaging of HeLa cells expressing pFlag-CMV2 construct: EGFP-**psWS54**-3xNLS. Kalman averaging 4 was applied. The reference EGFP channel was excited with a 488 nm laser and collected with a BP505-530 bandpass filter. The **psWS54** channel was excited with a 405 nm laser and collected with a BP505-575IR bandpass filter. Same excitation power, gain and offset levels were applied. Cells were stained with 2 μM **Q2mFR0** and incubated at 37 °C for indicated time. No washing steps were applied before imaging. Scale bar: 20 μm.....270

Figure IV-17 Confocal imaging of HeLa cells expressing pFlag-CMV2 construct: EGFP-**psWS54**-3xNLS. The reference EGFP channel was excited with a 488 nm laser and collected with a BP505-530 bandpass filter. The **psWS54** channel was excited with a 405 nm laser and collected with a BP530-600 instead of a BP505-575IR bandpass filter. Cells were stained with 2 μM **Q2mFR0** at room temperature for 35 min. No washing steps were applied before imaging. Scale bar: 20 μm. 271

Figure IV-18 Non-specific fluorescence background of **Q2mFR0** at different time points. **Q2mFR0** (2 μM) was used to stain HeLa cells at room temperature. The field of view was excited with a 405 nm laser and images were acquired with a BP505-575IR bandpass filter. No washing steps were applied. Scale bar: 20 μm. 272

LIST OF SCHEMES

Scheme I-1 Proposed mechanism for the biogenesis of the GFP chromophore (Inset: atom numbering used in the text). 4

Scheme I-2 Proposed maturation mechanisms of representative chromophores from GFP-, DsRed- and Kaede-like naturally occurring fluorescent proteins. 7

Scheme I-3 Mechanistic representation of HaloTag, showing H272F mutation to trap fluorophore-labeled intermediate as a stable covalent adduct. R represents the labeling fluorophore. 32

Scheme I-4 Pictet–Spengler ligation of an aldehyde with a tryptamine nucleophile.....38

Scheme I-5 Traceless Staudinger ligation. 39

Scheme I-6 [3+2] cycloadditions. (a) SPAAC and representative cyclooctyenes. (b) SPANC. R is a labeling fluorophore. 40

Scheme I-7 (a) Tetrazole-alkene photoclick cycloaddition. (b) IEDDA tetrazine-alkene cycloaddition. 41

Scheme I-8 Labeling approaches based on short peptides. (a) FlAsH and ReAsH with tetracysteine motif. (b) Bis-boronic acid RhoBo with tetraserine motif. (c) Dimaleimide coumarin YC20 with vicinal dicysteine motif. 43

Scheme II-1 Structures of thiacarbocyanines (**ThCC**s) and diazaindenes (**DiAI**s), with different number of vinylene insertions between the head group and the aldehyde. ...105

Scheme II-2 FR series of ICT dyes, derivatized from **FR0** with different lengths and types of π-spacers. 112

Scheme II-3 Proposed mechanism for the *cis–trans* isomerization of the chromophore in Dronpa and Padron. Bright and dark states correspond to the *cis* and *trans* forms of the chromophore, respectively. The two forms are determined by the pK_a difference in the acid-base equilibrium. In Dronpa, the *cis* form is anionic and bright. 119

Scheme II-4 Postulated photoswitching cycle of **CF-1**. 124

Scheme II-5 Potential derivatives of **FR-1V** for improving optical properties. 147

Scheme II-6 Synthesis of **ThCC-1V**. 160

Scheme II-7 Unsuccessful attempts for the nucleophilic elongation of **ThCC-1V.** 162

Scheme II-8 Unsuccessful attempts for the electrophilic elongation of **57**. 162

Scheme II-9 Attempted synthesis of **ThCC-2V** and its phenylimine. 163

Scheme II-10 Synthesis of **DiAI**s. 165

Scheme II-11 Synthesis of **FR**s. 173

Scheme III-1 Schematic transformation of (a) single and (b) double ESiPT of **FR0**-SB in protic solvents. 197

Scheme IV-1 Synthesis of **Q1FR0**. 253

Scheme IV-2 Synthesis of 3-methoxy maleimide. 258

Scheme IV-3 First attempt to synthesize **Q2mFR0**. 259

Scheme IV-4 Attempts to synthesize **Q2mFR0** with different functionalized *N*-ethyl maleimides. 259

Scheme IV-5 Testing S_N2 reactions of maleimide **83**. 260

Scheme IV-6 Final synthesis of **Q2mFR0**. 260

Scheme IV-7 Chemoselectivity and fluorescence recovery of **Q2mFR0** with sequential addition of *n*-butylamine (nBA) and *n*-propane thiol (PSH). a) PSH then nBA. b) nBA then PSH. 262

Scheme IV-8 Detectable adducts of **Q2mFR0**/hCRBPII in HRMS. A sequential step of reductive amination after both imine formation and Michael addition was used to derivatize the complex into a more stable form for mass detection. 268

KEY TO SYMBOLS AND ABBREVIATIONS

A	alanine, Ala
C	cysteine, Cys
D	aspartic acid, Asp
E	glutamic acid, Glu
F	phenylalanine, Phe
G	glycine, Gly
H	histidine, His
I	isoleucine, Ile
K	lysine, Lys
L	leucine, Leu
M	methionine, Met
N	asparagine, Asn
P	proline, Pro
Q	glutamine, Gln
R	arginine, Arg
S	serine, Ser
T	threonine, Thr
V	valine, Val
W	tryptophan, Trp
Y	tyrosine, Tyr

Å	angstrom, 10^{-10} meter
cm	centimeter
***μ*m**	micrometer
nm	nanometer
Da	dalton
g	gram
mg	milligram
***μ*g**	microgram
M	molar
***μ*M**	micromolar
nM	nanomolar
mol	mole
mmol	millimole
xs	excess
h	hour
min	minute
sec	second
t	time
$\mathbf{t_{1/2}}$	half-life, maturation half-time
O/N	overnight
k	kinetic rate constant
ε	molar extinction coefficient

Φ	quantum yield
T	temperature
°C	degree Celsius
K	kelvin
mW	milliwatt
h	Planck's constant
R	gas constant
ν	frequency
Hz	hertz
cm^{-1}	wavenumber,
aq.	Aqueous
K_a	ionization constant
FL	fluorescence
UV	ultraviolet
Vis	visible
IR	infrared
NIR	near-infrared
Abs, λ_{abs}	absorbance, absorption wavelength maximum
Em, λ_{em}	emission wavelength maximum
Ex, λ_{ex}	excitation wavelength
SS	Stokes shift
LSS	long/large Stokes shift

SW	short-wavelength
LW	long-wavelength
QY	quantum yield
EQE	external quantum efficiency
BP	bandpass (filter)
LP	longpass (filter)
ESA	excited state absorption
LE	local excitation
SE	stimulated emission
TAS	transient absorption spectra
EAS	evolution associated spectra
FP	fluorescent protein
CP	chromoprotein
GFP	green fluorescent protein
EGFP	enhanced green fluorescent protein
BFP	blue fluorescent protein
YFP	yellow fluorescent protein
RFP	red fluorescent protein
PA-FP	photoactivatable fluorescent protein
PS-FP	photoswitchable fluorescent protein
RSFP	reversibly photoswitchable fluorescent protein
PS-RSFP	positively photoswitchable RSFP

NS-RSFP	negatively photoswitchable RSFP
FAP	fluorogen-activating protein
PYP	photoactive yellow protein
Y-FAST	Yellow Fluorescence-Activating and absorption-Shifting Tag
AIE	aggregation-induced emission
AIEgen	aggregation-induced emission luminogen/fluorogen
ACQ	aggregation-caused quenching
ESPT	excited state proton transfer
ESIPT	excited state intramolecular proton transfer
ESiPT	excited state intermolecular proton transfer
ESHB	excited state hydrogen bonding
GSPT	ground state proton transfer
FRET	Förster resonance energy transfer
ICT	intramolecular charge transfer
PLICT	planarized intramolecular charge transfer
TICT	twisted intramolecular charge transfer
MLCT	metal-ligand charge transfer
ESCT	excited state charge transfer
PeT	photoinduced electron transfer
TBET	through-bond energy transfer
TADF	thermally activated delayed fluorescence
IC	internal conversion

ISC	intersystem crossing
RIR	restriction of internal conversion
qABP	quenched activity-based probe
BiFC	bimolecular fluorescence complementation
FCCS	fluorescence cross-correlation spectroscopy
FLIP	fluorescence loss in photobleaching
FLINC	fluorescence fluctuation increase by contact
FLAP	fluorescence localization after photobleaching
FRAP	fluorescence recovery after photobleaching
FLIM	fluorescence lifetime imaging microscopy
FISH	fluorescence *in situ* hybridization
RESOLFT	reversible saturable optical fluorescence transition
PALM	photo-activated localization microscopy
STORM	stochastic optical reconstruction microscopy
pcSOFI	photochromic stochastic optical fluctuation imaging
FMI	fluorescence molecular imaging
hFMT	hybrid fluorescence molecular tomography
FGS	fluorescence-guided surgery
CALI	chromophore-assisted light inactivation
FALI	fluorophore-assisted light inactivation
PDT	photodynamic therapy
PTT	photothermal therapy

PAM	photoacoustic microscopy
PAT	photoacoustic tomography
FACS	fluorescence-activated cell sorting
TCSPC	time-correlated single-photon counting
N.D.	not determined
N.O.	not observed
SB	Schiff base
PSB	protonated Schiff base
HBA	H-bonding acceptor
HBD	H-bonding donor
EDG	electron donating group
EWG	electron withdrawing group
HOMO	highest occupied molecular orbital
LUMO	lowest unoccupied molecular orbital
MS	molecular sieve
nBA	*n*-butylamine
PSH	*n*-propane thiol
IPTG	isopropyl β-D-1-thiogalactopyranoside
LB	lysogeny broth
PBS	phosphate-buffered saline
FBS	fetal bovine serum
DMEM	Dulbecco's Modified Eagle's Medium

***p*-HBI**	4-(*p*-Hydroxy-benzylidene)-5-imidazolinone
hAGT	human O^6-alkylguanine-DNA alkyl transferase
TMP	trimethoprim
eDHFR	*E. coli* dihydrofolate reductase
ICG	indocyanine green
MB	methylene blue, molecular beacon
TO	thiazole orange
MG	malachite green
PPCy	pyrrolopyrrole
BODIPY	boron dipyrromethene
TPE	tetraphenylene
NCL	native chemical ligation
CuAAC	copper-catalyzed alkyne-azide cycloaddition
SPAAC	strain-promoted alkyne-azide cycloaddition
SPANC	strain-promoted alkyne-nitrone cycloaddition
IEDDA	Inverse-Electron-Demand Diels-Alder cycloaddition
DIBAL	diisobutylaluminium hydride
TBAB	tetrabutylammonium bromide
TsOH	*p*-toluenesulfonic acid
scFv	single-chain variable fragment
NP	nanoparticle
SNP	semiconductor nanoparticle

QD	quantum dot
NES	nuclear export sequence
NLS	nuclear localization sequence
CAAX	prenylation tag
VDP	vicinal dithiol peptide
DIC	differential interference contrast
SBR	signal-to-background ratio
POI	protein of interest
ROI	region of interest
PPI	protein-protein interaction

A BRIEF OVERVIEW: THE EMERGING FIELD OF MODERN FLUORESCENCE IMAGING TAGS AND NEAR-INFRARED EMITTERS.

The great advancement of modern biology started with the publication of the *Micrographia* by Hooke in 1665.[1] The microscope has provided an ideal and fundamental tool for biologists to study single- and multi-cellular organisms with the use of light. Even in the current era of modern biology, it still remains as the first requirement of many researchers to visually investigate the morphologies and structures of under study objects, or to follow dynamic biological processes.

I.1 Constitutively fluorescent proteins

In the field of microscopy, event was the discovery of the green fluorescent protein (GFP) cloned from the jellyfish *Aequorea victoria* in 1992,[2] and its subsequent demonstration as an *in vivo* tag for fluorescent imaging.[3] In the two decades that followed,

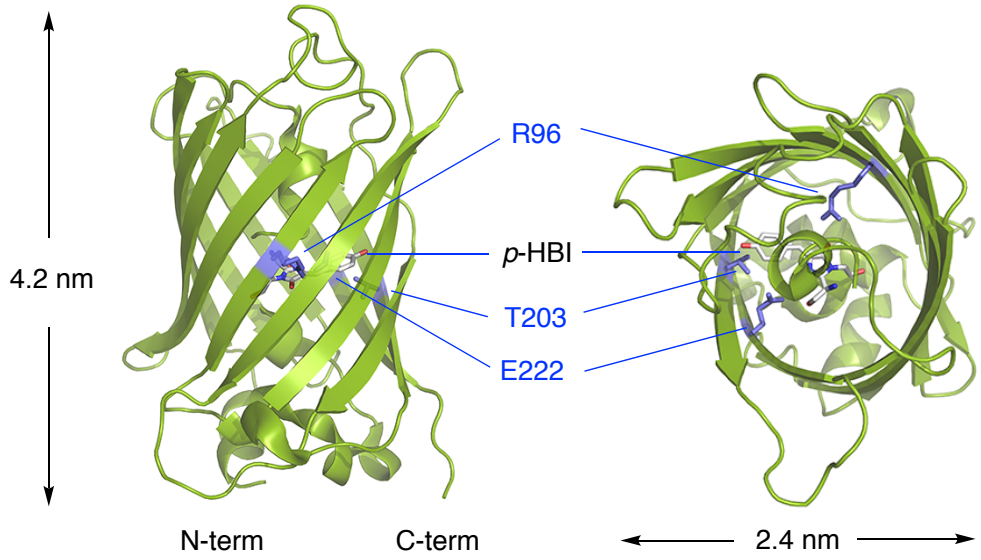


Figure 0-1 Structure of Aequorea victoria GFP. Showing the side (left) and top (right) views of the protein, the intrinsically generated fluorophore, and several key residues for chromophore maturation (PDB ID: 1w7s).

the biological research community witnessed the huge success of GFP and the large

family of its enhanced homologues, with the recognition of 2008 Nobel Prize in Chemistry jointly awarded to Osamu Shimomura, Martin Chalfie, and Roger Y. Tsien, “for the discovery and development of the green fluorescent protein, GFP”. Sharing the similar β-barrel structure surrounding the embedded chromophores, which forms 11 β-sheets that host an internal distorted helix (**Figure I-1**), fluorescent proteins (FP) and non-fluorescent chromoproteins (CP) other than *A. victoria* from Hydrozoa species were also found in the bioluminescent Anthozoa species with quite conservative scaffolds[4] (**Figure I-2**). Largely due to the commercial availability and certain advantages, GFP-like FPs have had an enormous impact on biological research activities.

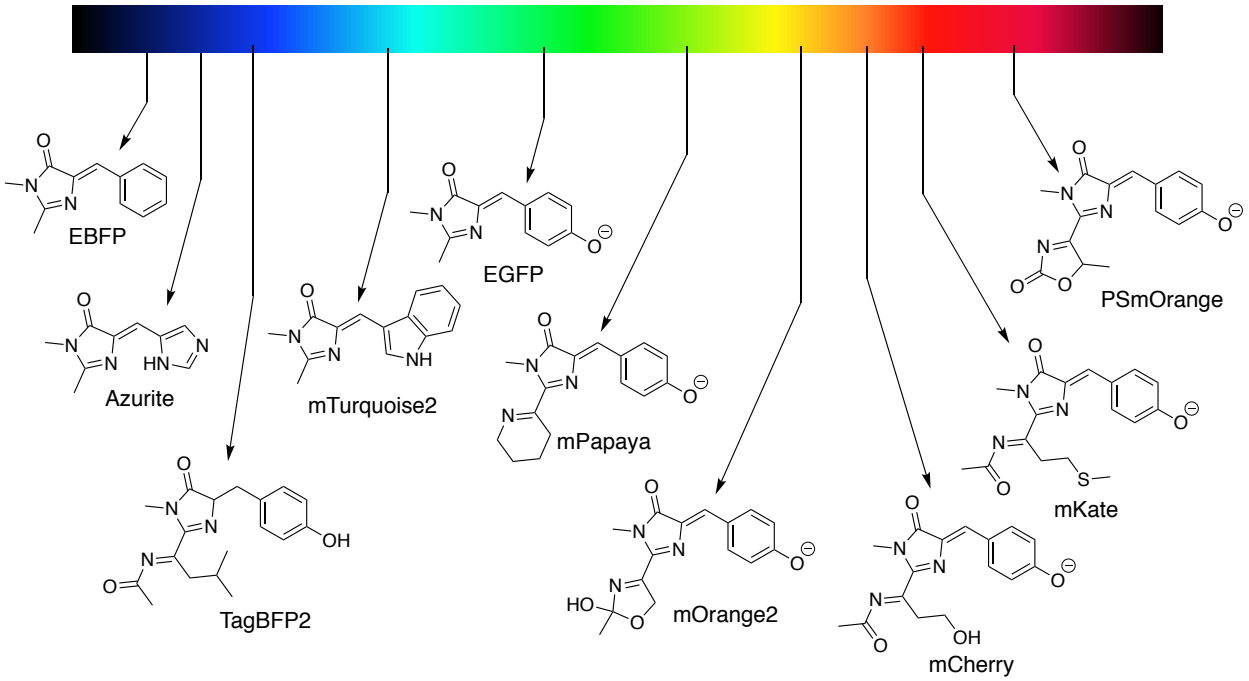


Figure 0-2 A representative set of chromophores responsible for fluorescence in constitutively fluorescent metazoan proteins.

I.1.1 The origin of FPs, and the innate chromophores

Current FPs span almost the entire palette of the visible spectrum, with an emission wavelength ranging from 442 nm to 645 nm (**Figure I-3**).[5-7] Unlike the bioluminescence found in bacteria, unicellular algae, coelenterates, beetles, fish, and others,[8] FPs do not require accessory cofactors or external enzyme and substrate to form intrinsic chromophores. The maturation of their embedded chromophore, 4-(*p*-hydroxy-benzylidene)-5-imidazolinone (*p*-HBI), is accomplished through an autocatalytic process. Based on a number of crystallographic observations,[9] the most widely accepted

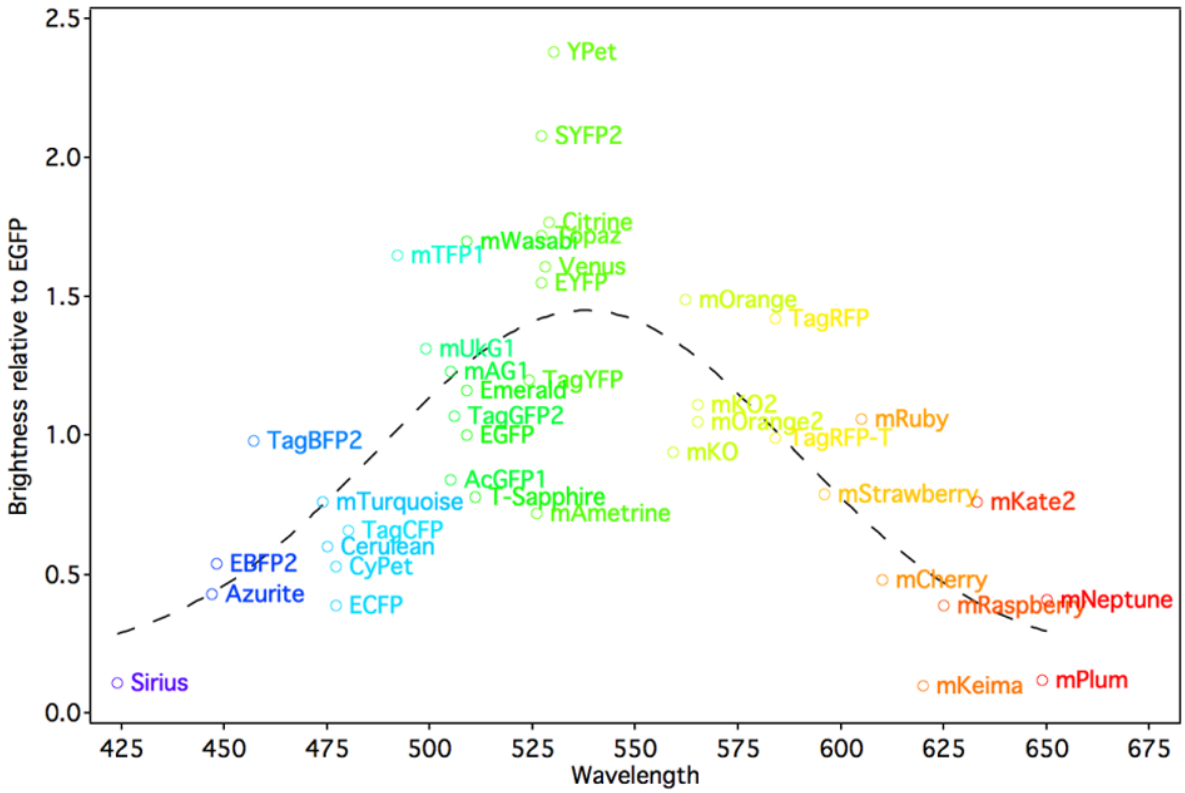
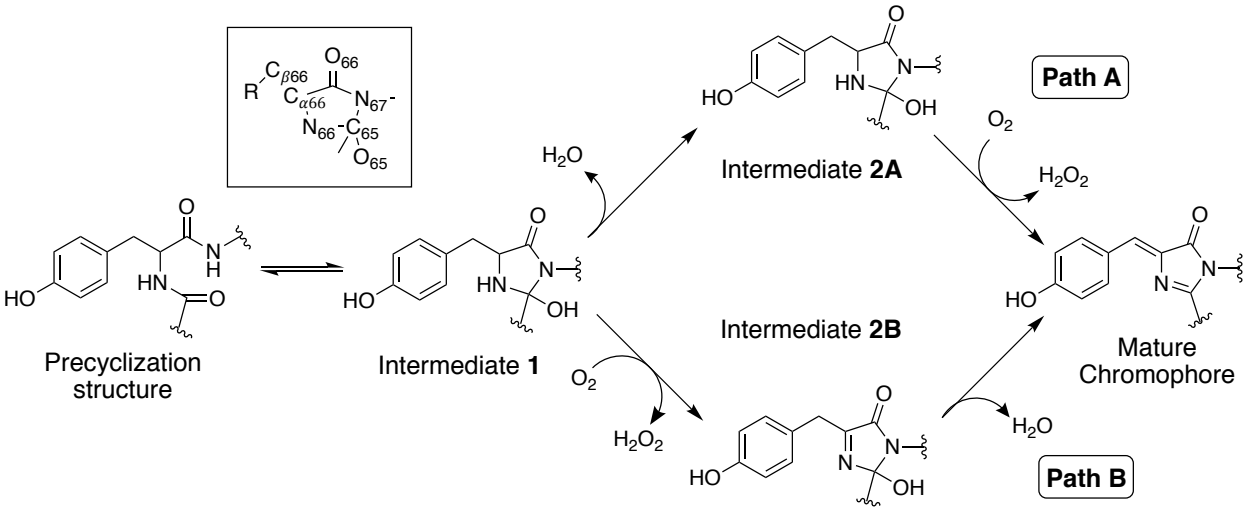


Figure 0-3 Reported fluorescence brightness (extinction coefficient times fluorescence quantum yield) of a number of popular or unique fluorescent proteins as a function of emission wavelength. The dashed line serves as a guide to highlight the general trend. The coloring of the tags approximates the appearance of the corresponding emission wavelength to the naked eye. The brightness of some fluorophores has been altered by a small amount for clearer visual presentation. Copied from ref [7].

mechanism for the formation of *p*-HBI is depicted as three sequential steps from the tripeptide Ser65-Tyr66-Gly67 (**Scheme I-1**, Path A): (1) internal nucleophilic attack of Gly67 amide nitrogen on the carbonyl carbon of Ser65, (2) dehydration of the hemi-aminal to form an imidazolin-5-one intermediate, (3) oxidation by molecular oxygen along the Cα-Cβ bond of Tyr66 to conjugate the imidazolone. The exact order of the three steps, however, is still unclear. The original mechanism proposed by Tsien orders the three steps as cyclization-dehydration-oxidation.[10] This mechanistic proposal is based on the observation of accumulated GFP intermediate in *E. coli* in anaerobic atmosphere. This



Scheme 0-1 Proposed mechanism for the biogenesis of the GFP chromophore (Inset: atom numbering used in the text).

pre-oxidation intermediate is supported by the 1 (±4) Da mass loss of Tyr66 β-carbon in their kinetic isotope study. In contrast, the Wachter group suggests a reversed order of oxidation and dehydration based on X-ray crystallographic and spectroscopic data of a Y66L GFP variant, which suggested the condensation product being trapped by ring oxidation (**Scheme I-1**, Path B).[11] In this pathway, the last step involves the elimination of the hydroxyl group in the form of a water molecule. This final transformation is coupled

to a proton-transfer reaction which may proceed through hydrogen-bonded solvent molecular network with Arg96 and Glu222, whereby the proton abstraction of the Gly67 amide nitrogen or the Tyr66 α-carbon is facilitated by the carboxylate of Glu222, and the formed α-enolate is stabilized by Arg96 through lowering of the respective pK_a values as an electrophile.[12-14] Despite the ambiguity in the exact order of the chromophore-forming process, Tyr66 and Gly67 remain strictly evolutionarily conserved among all naturally occurring FPs. In contrast, the residue at position 65 can be mutated to various amino acids. This mutation gives rise to numerous color variants throughout the FP families as shown in **Figure I-2**.

I.1.2 Classification of FPs

As mentioned earlier, many natural FPs have been found in various marine species other than *Aequorea victoria* over the decades. In the view of phylogeny, FP is an ancient Metazoan gene.[15] It has currently been identified in four different phyla of multicellular animals, namely, Cnidaria, Ctenophora, Arthropoda, and Chordata.[16] Interestingly, these four phyla cover most of the basic partitions of the metazoan tree of life (**Figure I-4**). The original GFP and its numerous engineered derivatives only constitute a very specific small branch in this tree of life, albeit sharing the similar β-barrel enclosing the chromophore. The most divergent FP sequences are found in the class Hydrozoa, nevertheless the colors are mostly green.[17] On the contrary, the class Anthozoa provides the greatest diversity of FP colors. Recent research efforts were focused on the Anthozoa class to identify internal chromophore with substantial red-shifted emission beyond 540 nm.[18-20] The most common two are the DsRed- and Kaede-like chromophores.

As shown in **Scheme I-2**, all of the intrinsic fluorescent proteins have chromophores consisting the same *p*-HBI scaffold with different side chains to extend the

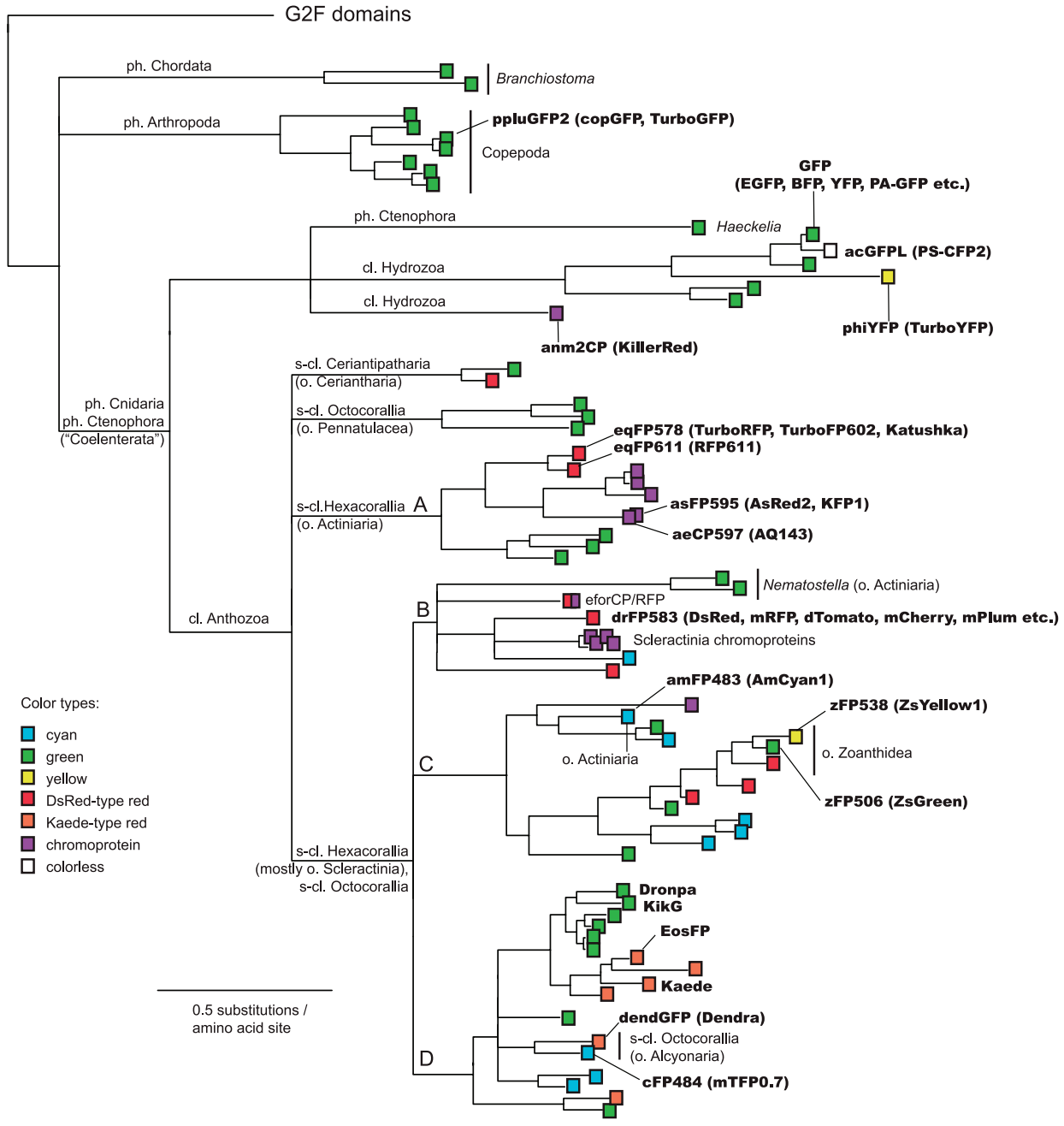
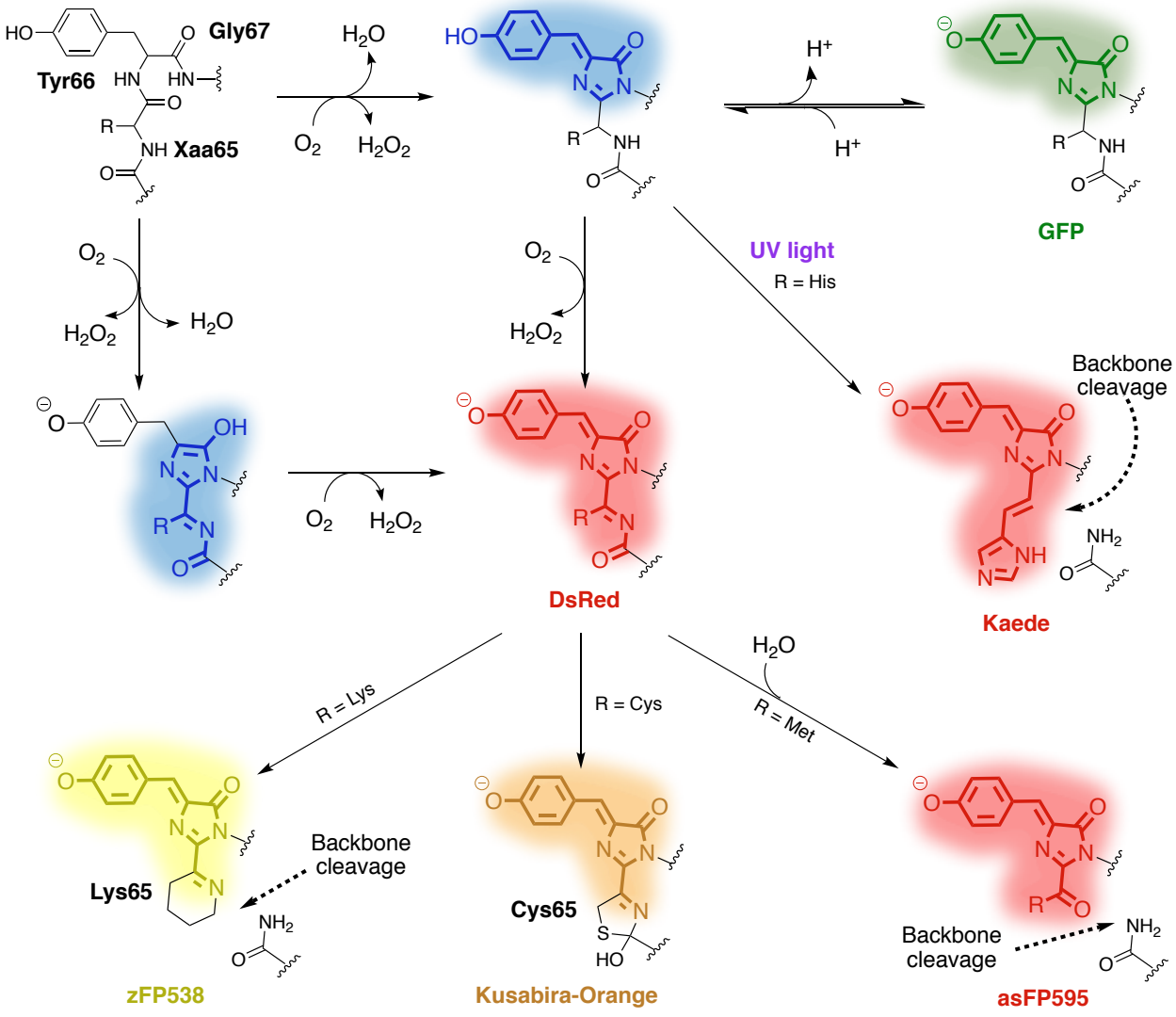


Figure 0-4 Phylogenetic tree of representative FPs, copied from ref [17]. The branches with a posterior probability of 0.95 are collapsed. Individual sequences are represented by boxes corresponding to their color type (see legend). Representative FPs are shown with their commercial names and/or mutant derivatives in brackets.

conjugation. Starting with the tripeptide, the GFP-like chromophore is formed through the sequential cyclization, dehydration and oxidation of the conservative Tyr66 and Gly67, and exists in an equilibrium between deprotonated and protonated forms, of which the latter one emits the green fluorescence. DsRed-like chromophore formation takes an extra oxidation step. A neutral blue-emitting intermediate from cyclization and dehydration of the tripeptide can be oxidized by molecular oxygen at the Cα-N bond of residue 65



Scheme 0-2 Proposed maturation mechanisms of representative chromophores from GFP-, DsRed- and Kaede-like naturally occurring fluorescent proteins.

(Xaa65 in **Scheme I-2**), thus extending the conjugation of the five-membered imidazolinone ring to an acylimine group instead of the phenolic Tyr66.[21, 22] While in some other FPs, DsRed-like chromophore can be oxidized from the neutral form of *p*-HBI equilibrium.[23] Further structural conversion can happen to DsRed-like chromophores on acylimine group through hydrolysis,[24] transimination,[25-27] or nucleophilic cyclization.[28, 29]

In contrast to GFP- and DsRed-like FPs, Kaede-like FPs show a remarkably different chromophore formation process. Once formed the equilibrated *p*-HBI precursor, the maturation process skips the additional oxidation observed in DsRed and stops at the GFP-type chromophore. Ultraviolet (UV)-violet light irradiation then initiates a peptide backbone cleavage between Tyr 66 and residue 65. In all of the Kaede-type FPs, His65 appears to be indispensable. Its imidazole ring results in extended conjugation with *p*-HBI scaffold from the photolysis and is responsible for the mature red form.[30] This photoactivation of Kaede-like FPs became popular and triggered the wide investigation and application of photoactivatable, photoconvertible, and photoswitchable FPs.

Rooted in the naturally occurring FPs, innumerable artificial FPs have also been engineered via mutagenesis. It is notable that the chromophore structure only determines part of the spectral properties, the surrounding amino acids and the highly ordered water molecules together form a wide range of interactions and build a network that encircles the whole β-barrel, significantly influencing the spectroscopic behavior, absorption and emission maxima, photostability, blinking, pH stability, etc. For example, a Thr203Tyr mutation induced a direct π-π stacking with the chromophore Tyr66, and resulted in significantly red-shifted excitation and emission maxima.[31]

Generally, based on excitation and emission wavelengths, FPs can be categorized into the following color regimes: UV FPs ($\lambda_{ex} < 380$ nm, $\lambda_{em} < 450$ nm, e.g., Sirius);[32] Blue FPs (λ_{ex} ranges 380 ~ 400 nm, $\lambda_{em} \sim 450$ nm, e.g., Azurite, EBFP2, TagBFP, etc.);[33-35] Cyan FPs ($\lambda_{ex} \sim 430$ nm, λ_{em} ranges 470 ~ 490 nm, e.g., ECFP, mTurquoise, Cerulean, etc.);[10, 36-38] Green FPs (λ_{ex} ranges 480 ~ 510 nm, λ_{em} ranges 500 ~ 520 nm, e.g., EGFP, Emerald, TagGFP2, TurboGFP, etc.);[35, 39-42] Yellow FPs (λ_{ex} ranges 510 ~ 530 nm, $\lambda_{em} \sim$ 540 nm, e.g., EYFP, Venus, mPapaya1, etc.);[31, 43-45] Orange FPs ($\lambda_{ex} \sim 550$ nm, $\lambda_{em} \sim 560$ nm, e.g., mOrange, mKO, etc.);[28, 46] Red FPs (λ_{ex} ranges 550 ~ 580 nm, λ_{em} ranges 580 ~ 610 nm, e.g., TagRFP, mRuby, mCherry, mScarlet, etc.);[46-49] Far-red FPs (λ_{ex} ranges 590 ~ 610 nm, λ_{em} ranges 630 ~ 670 nm, e.g., mKate2, mRaspberry, mNeptune, NirFP, etc.);[49-53] and Near-infrared (NIR) FPs (λ_{ex} ranges 680 ~ 700 nm, $\lambda_{em} > 680$ nm, e.g., iFP2.0, iRFP720, GAF-FP, etc.).[54-56]

Alternatively, FPs can be categorized based on their functions and utilities, such as large Stokes shift (LSS) FPs (SS > 100 nm, e.g., Sapphire, mKeima, LSS-mKate2, LSSmOrange, CyOFP1, Sandercyanin, etc.),[57-64] photoactivatable FPs (PAFP, of which the fluorescence can be turned on by an activation beam, e.g., PA-GFP, PamKate, etc.),[65, 66] photoconvertible FPs (of which the fluorescence wavelength can be irreversibly converted to another by a conversion beam, e.g., mMaple, mEos2, Dendra2, etc.),[67-69] and photoswitchable FPs (PSFP, of which the fluorescence wavelengths can be reversibly switched between two distinct states, e.g., Padron, Dronpa, Dreiklang, Kohinoor, etc.).[70-73] Studies are also trending towards further modulations of maturation,

pH stability, kindling, blinking, fluorescence lifetime, and oligomeric form, to name a few, resulting in a variety of FP variants for numerous fluorescence imaging applications.[74]

I.2 General applications of fluorescence imaging

Because of the integrity of their expression in aerobic environments, and their ability to be genetically fused to various proteins of interest (POI), FPs have found tremendous applications in molecular and cell biology in the past decades. Traditionally, FPs are used as passive reporters.[75] They can be labelled to proteins, nucleic acids (i.e., DNAs and RNAs), organelles, cells, and even organisms (for example, whole body imaging), for structural investigations. More detailed sub-categorizations of applications within each branch is depicted in **Figure I-5**. Impressively, with a wise choice of FPs,

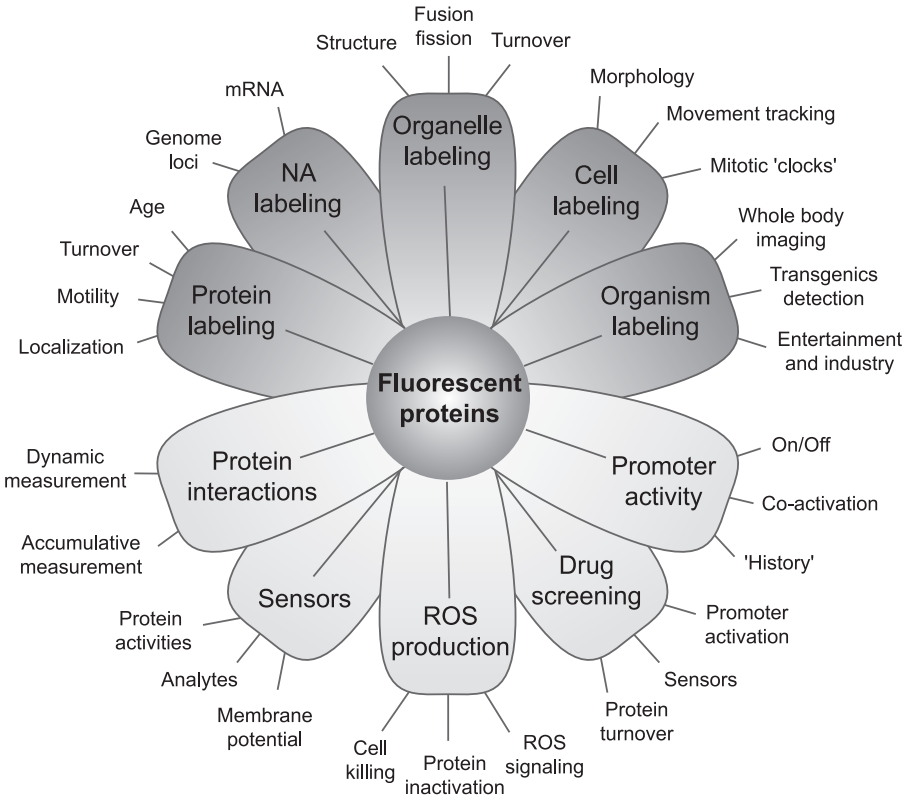


Figure 0-5 Application of fluorescent proteins. Dark gray and light gray petals show structural and functional applications, respectively. This artwork is copied from ref [17].

multicolor labeling can be achieved with up to six different colors on a routine basis performed with standard equipment, negating the requirement of spectral unmixing.[58] Potentially, the number of imaging channels can be further expanded by the combinatorial use of LSS FPs and PSFPs with spectrally resolved excitation and/or emission wavelengths.

I.2.1 Modern imaging applications of FPs

Although the selection of optimal FPs for a particular study can be complicated by multiple factors, such as maturation time, turnover rate, environmental sensitivity, blinking, and bleaching,[76] it is actually possible to exploit these photophysical and photochemical complexities to transform FPs from passive reporters into smart labels. Compared to classical labeling experiments,[77] new application fields are emerging, i.e., protein-protein interaction (PPI), sensor, ROS production, DNA sequencing, and drug screening, to name a few (**Figure I-5**).[78-80]

Normally, photobleaching is not a desired property for FP labeling. Nonetheless, this phenomenon can be utilized to study the mobility of POI when fused with FP. Two widely-used techniques are fluorescence recovery after photobleaching (FRAP) and fluorescence loss in photobleaching (FLIP). The basic principle of FRAP is to photobleach a small region of interest (ROI) inside the sample cell, then monitor the fluorescence recovery rate, which is determined by the mobility of unbleached FP fusions migrating from an adjacent non-photobleaching region.[81, 82] In contrast, FLIP monitors the rate of fluorescence decay in an ROI by constantly photobleaching its adjacent region, the principle of which follows the same idea of FP migration.[83] Another slightly complicated

yet fundamentally simple technique to study POI trafficking is fluorescence localization after photobleaching (FLAP). Different from FRAP and FLIP, FLAP requires two FPs fused together. During the study, one FP is photobleached, while the other FP remains intact and serves as an internal fluorescence reference. The intensity ratio profile of the two emission wavelengths is mapped pre- and post- photobleach. POI can then be tracked based on the change of the intensity ratio.[84, 85] A good example is shown in **Figure I-6**. The 2D heat maps in the left panels show the movement of labeled POIs in different region of the sample cells at various time stamps post photobleaching.

One interesting application of FPs based on their turnover rate is the Timer FPs. Timer FPs initially fluoresce at one wavelength. Over time, their emissions convert to a different wavelength by various maturation rates which may span from minutes to hours even days. This feature, similar to those of radical clocks, is suitable for the use to study progressive processes over a number of time scales. The first known Timer FP is DsRed-

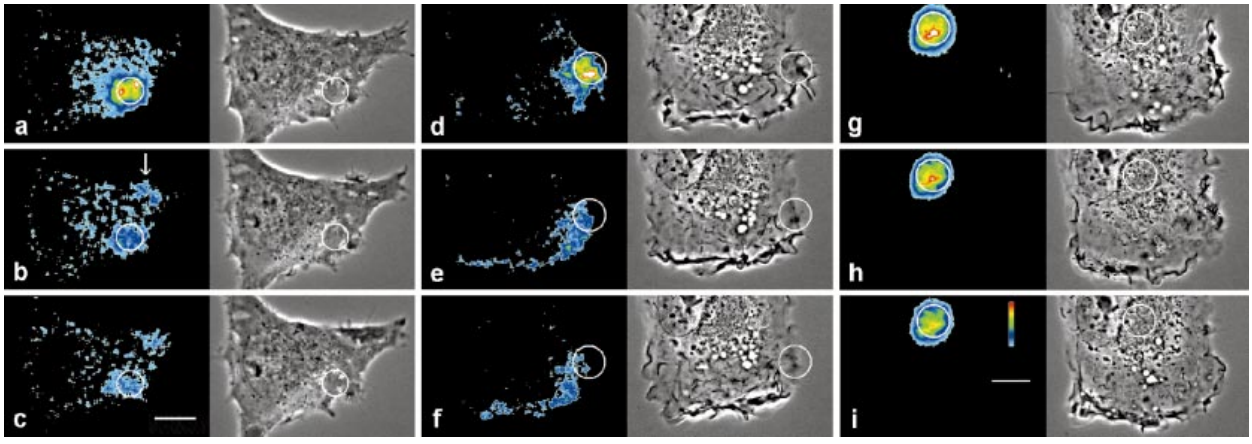


Figure 0-6 Three image sequences show the FLAP image in pseudocolour (left panel) and phase-contrast image (right panel) at the following times after bleaching: 0 s (a, d and g), 50 s (b and e), 100 s (c, f and h) and 200 s (i). In these sequences the individual channels were acquired in multi-tracking mode. Bleach region shown as a circle in each image. Threshold level set to 8% of maximum signal. Bleach times 8.6 s (a) and 13.5 s (d and g). Scale bars 10 μm. Image copied from ref [84].

E5 reported in 2000, which forms green GFP-like chromophore at the beginning and converts to a tetrameric form over time to become red.[86] Monomeric and faster Timer FPs have also been developed to meet the requirement of wider *in vivo* applications.[87]

Perhaps the most well-known technique to study protein-protein interaction is the Förster resonance energy transfer (FRET). In principle, if two fluorochromes are close in distance less than 10 Å, then the excited donor fluorochrome can transfer part of the energy to the acceptor fluorochrome via a non-radiative long-range dipole-dipole coupling, which requires the spectral overlap of the acceptor absorption spectrum and the donor emission spectrum, and the relative orientation of the acceptor absorption dipole moment and the donor emission dipole moment.[88] Although common FRET couples are not limited to FPs (for example, Cy3 and Cy5, FITC and TRITC, Alexa488 and Alexa610, etc.), FPs

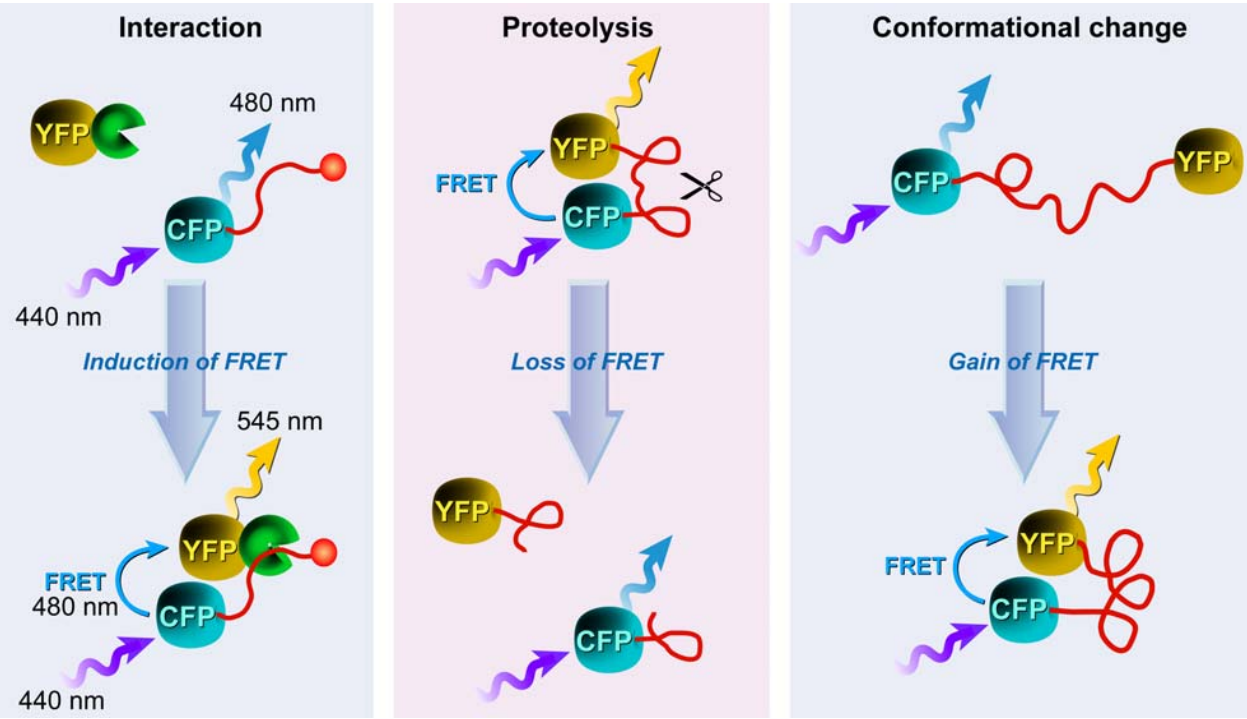


Figure 0-7 Three modes of FRET sensing for biomolecular interactions. Artwork copied from ref [85].

are the most widely used FRET pairs due to their genetic coding ability, among which the first truly effective pair is CFP and YFP.[89] There are three ways to utilize FRET in an imaging study (**Figure I-7**): 1) the interaction of two separately labeled POIs bring the FRET pair into close proximity and induce the FRET signal; 2) the FRET pair is initially labeled on the two termini of POI and the loss of FRET signal is traced when segmentation of POI happens; 3) the FRET pair is intramolecularly labeled on POI and the FRET signal is monitored when the POI undergoes conformational change upon protein interaction and/or ligand binding.

The application of FRET has been exploded in the past decades. However, the limitation of the experimental conditions, and possible artifacts such as signal cross-contamination, labeling efficiency, and variation in instrumental setup all increase the complexity in interpreting the intensity-based FRET measurement.[90] In this context, fluorescence lifetime imaging microscopy (FLIM) is developed to overcome these limitations, by taking advantage of the fact that the lifetime of FPs is not affected by these factors. Fluorescence lifetime (τ) is the unique photophysical character of fluorochromes including FPs. It does not depend on the fluorescence intensity, the concentration of the FPs, the intensity of excitation light source, the dichroic, or the detection responsiveness of photomultipliers. Moreover, it is generally less sensitive to moderate photobleaching.[91] FLIM has been successfully used with FRET to achieve FLIM-FRET imaging, which allows the investigation of protein micro-environment with resolution higher than that of conventional FRET. It should be noted that FLIM requires more sophisticated instrument setup and is sensitive to environment changes affecting FP nature.

Extending from the exploitation of FP photophysical characteristics such as photobleaching, energy transfer, turnover rate, and lifetime, an alternative technique to detect protein-protein interaction is based on fluorescence intensity fluctuation, or blinking. When two different FPs are in a limited spatial volume and are excited, the two emission intensities will fluctuate together and give a degree of cross-correlation. Fluorescence cross-correlation spectroscopy (FCCS) records the time-correlated fluctuation and provides a means to estimate the interdependence of diffusion rates of the two FPs, therefore to deduce the interaction between two POIs fused with the FPs.[92, 93] Importantly, FCCS differs from FRET in the way that FCCS is less demanding in the distance and the orientation between two FPs mandated by FRET, thus giving more freedom for study design. Besides, the correlation signal is usually more sensitive than the FRET signal, allowing fluorochromes with lower brightness to be used.[94] Recently, Zhang's group has further expanded the utilization of fluorescence correlation spectroscopy to combine with a super-resolution microscopic technique, photochromic stochastic optical fluctuation

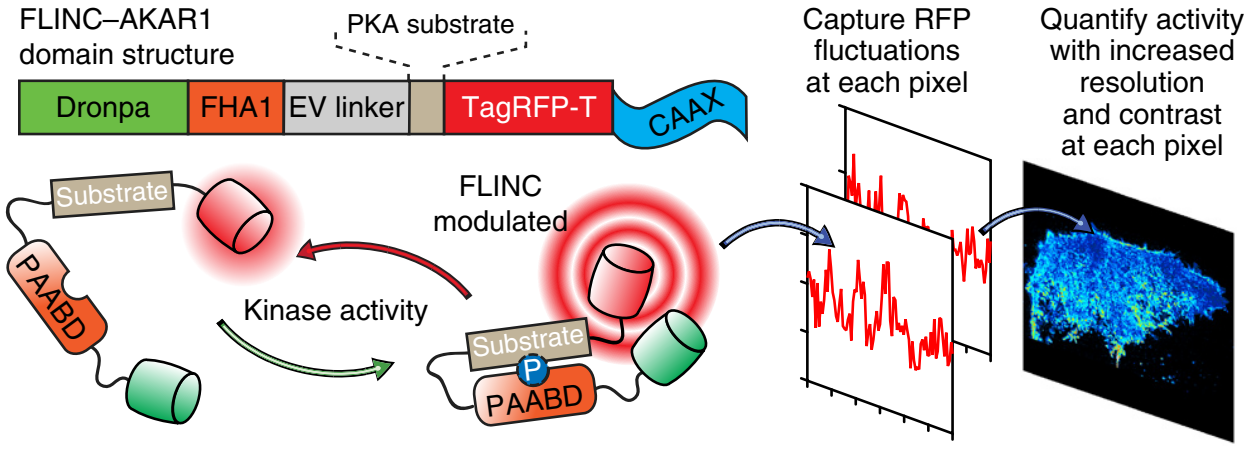


Figure 0-8 Schematic representation of the FLINC-AKAR design principle, the domain structure of FLINC–AKAR1 and the acquisition of super-resolution activity images with pcSOFI. Artwork copied from ref [95].

imaging (pcSOFI), and discovered the phenomenon which they termed fluorescence fluctuation increase by contact (FLINC).[95] Tagged with FLINC-based biosensors, they successfully visualized the activity of protein kinase A (PKA) with clustered A kinase-activity reporter (AKAR) proteins in microdomains on the plasma membranes of a living migrating α4CHO cell at super-resolution (**Figure I-8**).

In contrast to the use of tandem- or biomolecular- based FRET/FLIM/FCCS, FPs can be split into two complementary segments to image protein-protein interaction. A single FP gene is split into two halves and fused to two POIs, respectively. When the two POIs interact, the two split FP fragments are brought to close proximity and self-assembled into a whole FP which fluoresce as normal.[96, 97] Alternatively, this type of bimolecular fluorescence complementation (BiFC) can be used to investigate the topology transformation of a single POI. Besides the conventional applications in protein-protein interaction studies, BiFC has also found use in drug discovery and flow cytometry.[98, 99] However, care is necessary to avoid artifacts such as diffusion-limited signal loss, or complementation-induced POI interaction to affect the interpretation of the data.

While advanced applications of FPs are emerging from exploiting photophysical features of FPs, it should be noted that other FP can always be extensively engineered to meet various imaging demands, such as, pH-stable FPs for ratiometric pH-sensing,[100-103] PAFPs and reversibly photoswitchable FPs (RSFP) for super-resolution imaging/single-molecular nanoscopy (i.e., PALM, STORM, RESOLFT),[73, 104] and allosteric redox sensor.[105]

I.2.2 Other trending applications of fluorescence bioimaging

The discussion has hitherto been focused on FPs. Although there are innumerable FP variants possessing widely different features and showing successful applications in different areas, synthetic fluorochromes normally provide a higher degree of scaffold variety and have more freedom to modulate their photophysical characteristics. In this context, fluorescence bioimaging is tremendously advanced by invention of modern dyes and subsequent applications.

I.2.2.1 Biosensing

An ongoing hot field is fluorescence-based sensing of important molecular species involved in interesting biological and/or pathological processes.[106] The interactions between host and guest molecules were used to develop analyte-specific sensors at the time the 1987 Nobel Prize was awarded for supramolecular chemistry.[107-109] This approach, however, is often limited by the non-quantitative nature of noncovalent interactions. Inheriting the concepts of substrate-indicator recognition, fluorochromes have been chemically modulated to reaction-based analyte-specific molecular indicators that respond to various cationic, anionic, redox, metal, and biomacromolecular species, including biologically relevant H^+, F^-, CN^-, H_2O_2, RSH, NO, superoxides, nucleic acids, and enzymes.[110-112] Over the years, a vast number of reaction-based indicator systems have emerged from a variety of reactions (e.g., boron-oxygen displacement, spirocyclization, aza-cope rearrangement, etc.), and have been heavily reviewed.[113-115] These approaches are transplanted to chemoselective *in vivo* imaging to map the analyte

activities whereof either site-specific,[116, 117] or pan-cellular.[118-121] Efforts have also been made to fabricate polymer-based systems to increase signal intensity.[122-125]

More recently, design principles based on different photophysical and/or photochemical mechanisms have been applied to achieve ratiometric reaction-triggered sensing systems.[126] These principles include 1) intramolecular charge transfer (ICT): these probes have electron donor and acceptor parts which can interact with analyte and result in internal charge redistribution, leading to either absorption or emission wavelength shifts; 2) excited-state intramolecular proton transfer (ESIPT): these probes have signature large Stokes shift emission bands generated from fast intramolecular proton transfer between their proton donor and acceptor moieties, which can be used as ratiometric fluorescence readout as they are sensitive towards analyte binding; 3) FRET and TBET (denoting through-bond energy transfer): probes of these two types of energy transfer (through space or wave function, respectively) are composed of covalently linked donor emitter and acceptor emitter moieties, the latter of which is activated upon reaction with analytes and emits fluorescence signals; 4) monomer-excimer interchange: these probes form excimers at the dormant state and dissociate upon binding of analytes, resulting in wavelength shifting.

A noteworthy example is the real-time intracellular glutathione (GSH) dynamic quantification probe (QuicGSH) recently achieved by Urano's group.[121] This is the first reported reversible reaction-based GSH sensing system that demonstrates high sensitiveness and temporal resolution ($t_{1/2}$ = 620 ms at [GSH] = 1 mM). This work showed

the optimal combination of a tetramethyl rhodamine (TMR) and silicon rhodamine (SiR) FRET pair and a fast reversible thiol nucleophilic addition on SiR 9-position (**Figure I-9**).

A renewed research field is the direct noninvasive optical measurement of cell membrane voltage, or voltage-sensing, although for years patch clamp methods served as the gold standard for measuring ion currents and voltages related to neuron physiology.[127] Voltage sensing with fluorescent indicator has a long history. Early probes were only available for Ca^{2+} sensing, commonly based on genetically encodable voltage-sensitive phosphatases or rhodopsins. New small molecular design strategies have

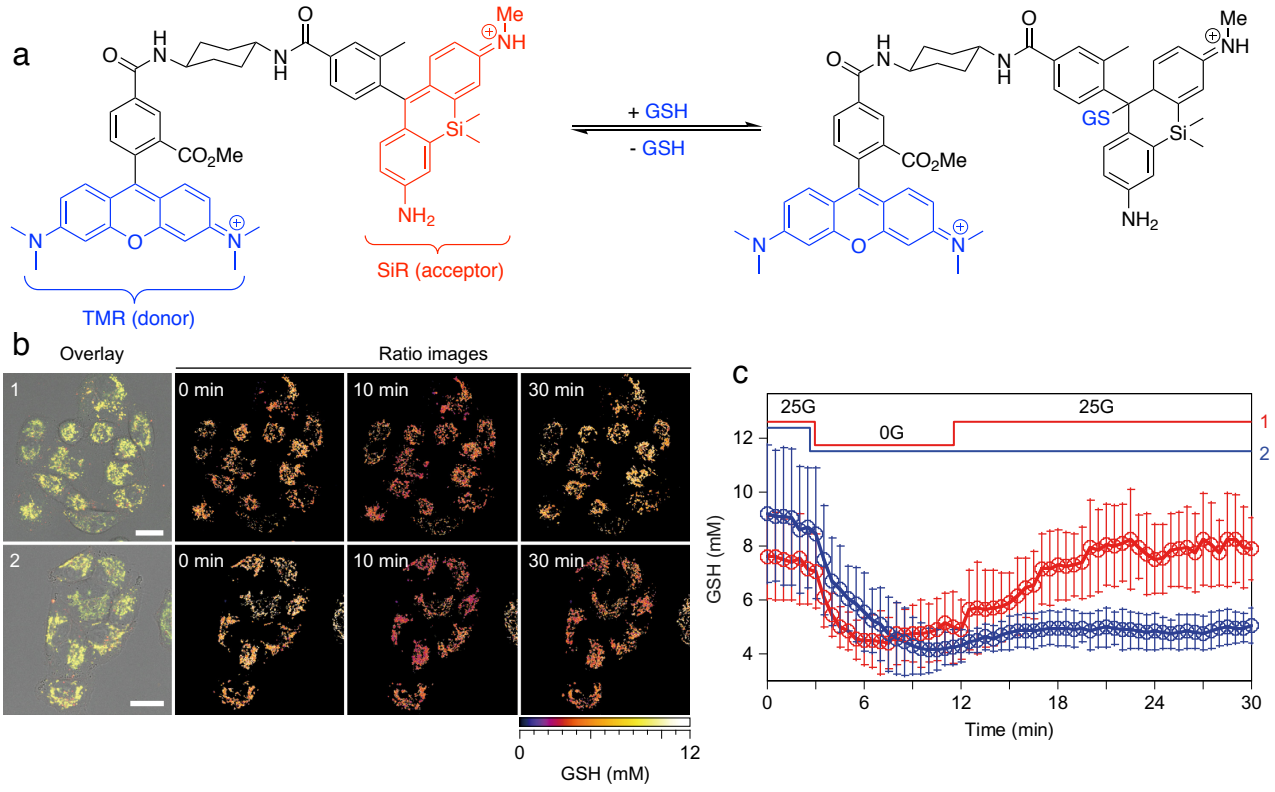


Figure 0-9 In vivo dynamic GSH imaging. (a) Chemical structure of QG3.0 probe. (b) Real-time GSH imaging with QG3.0 (1 μM) in A549 cells under glucose-deprivation with a perfusion system. Overlay and time-lapse ratio imaging of GSH under high-glucose (25 mM: 25G) or glucose-free (0 mM: 0G) conditions. 1: 0–3 min, 25 mM glucose; 3–12 min, 0 mM glucose; 12–30 min, 25 mM glucose. 2: 0–3 min, 25 mM glucose; 3–30 min, 0 mM glucose. scale bars, 20 μm. (c) Time-course of GSH concentration under glucose deprivation (red, condition 1; blue, condition 2). Images and plot copied from ref [121].

drawn interest in recent years. Briefly, amphipathic synthetic probes can span across the plasma membrane. The sensing output generally relies on the following mechanisms (**Figure I-10**): 1) solvatochromism, whereby the membrane voltage change perturbs the dipole moment of solvatochromic dyes and induces emission wavelength shifts; 2) electrochromism, whereby a molecular Stark effect counts for the fast shifts (fs to ps) in both absorption and emission wavelengths; 3) voltage-dependent redistribution of FRET pairs, of which the lipophilic acceptor emitter will redistribute upon polarizations and fractionally affect FRET signal; 4) photoinduced electron transfer (PeT) quenching of fluorescent molecular wires, the quenching sensitivity of which is affected by the external electric field and results in fluorescence readout turn-on/off.[128] An example is given below

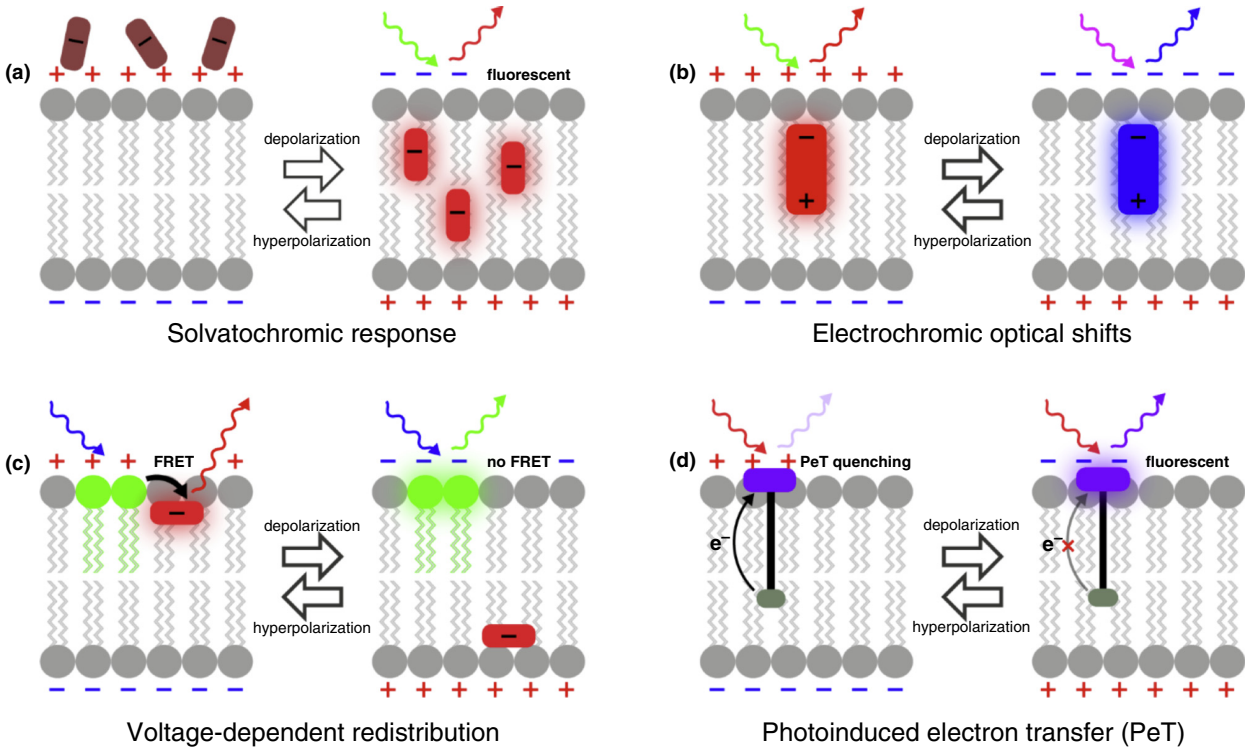


Figure 0-10 Methods of voltage sensing with small molecules. (a) Voltage-dependent traverse of solvatochromic dyes in lipid membranes. (b) Electrochromic voltage-sensing. (c) Voltage-dependent FRET acceptor redistribution. (d) Voltage-sensing based on PeT perturbation. Artwork copied from ref [128].

showing the VoltageFluor dyes developed in Tsien's lab which adopts the PeT approach.[129, 130] Recently, by substituting the fluorescein with silicon rhodamine in the molecular wire, Miller's group successfully developed BeRST 1 as the NIR version of VoltageFluor, and achieved spontaneous optical voltage-sensing with epifluorescence imaging in rat hippocampal neurons (**Figure I-11**).[131]

An interesting optical sensing area is the mechanical tension across cell surface. Transmembrane adhesion receptors are important in cell biology. They mediate cell-cell and cell-extracellular matrix adhesions, and transmit the mechanical forces to the chemo-mechanical coupling cycles controlling cell fate. Salaita's group designed a FRET-based emitter-quencher pair to study the interaction between membrane-anchored EGFR and silica chip immobilized EGF (**Figure I-12a**).[132] Later on, this strategy was expanded to

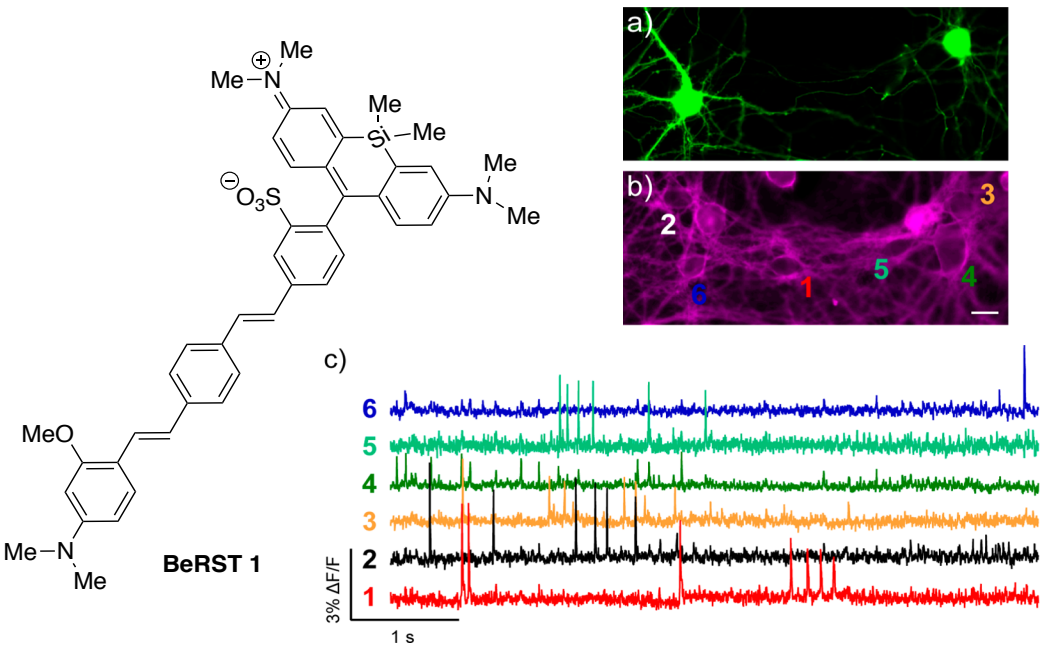


Figure 0-11 Spontaneous voltage and epifluorescence imaging with BeRST 1 in GFP-labeled cells of rat hippocampal neurons. (a) GFP and (b) stained with BeRST 1. Scale bar is 20 µm. (c) Optical traces of spontaneous activity in neurons from panels (a) and (b). Numbers next to traces correspond to indicated cells in panel (b). Optical sampling rate is 500 Hz. Images and plot copied from ref [131].

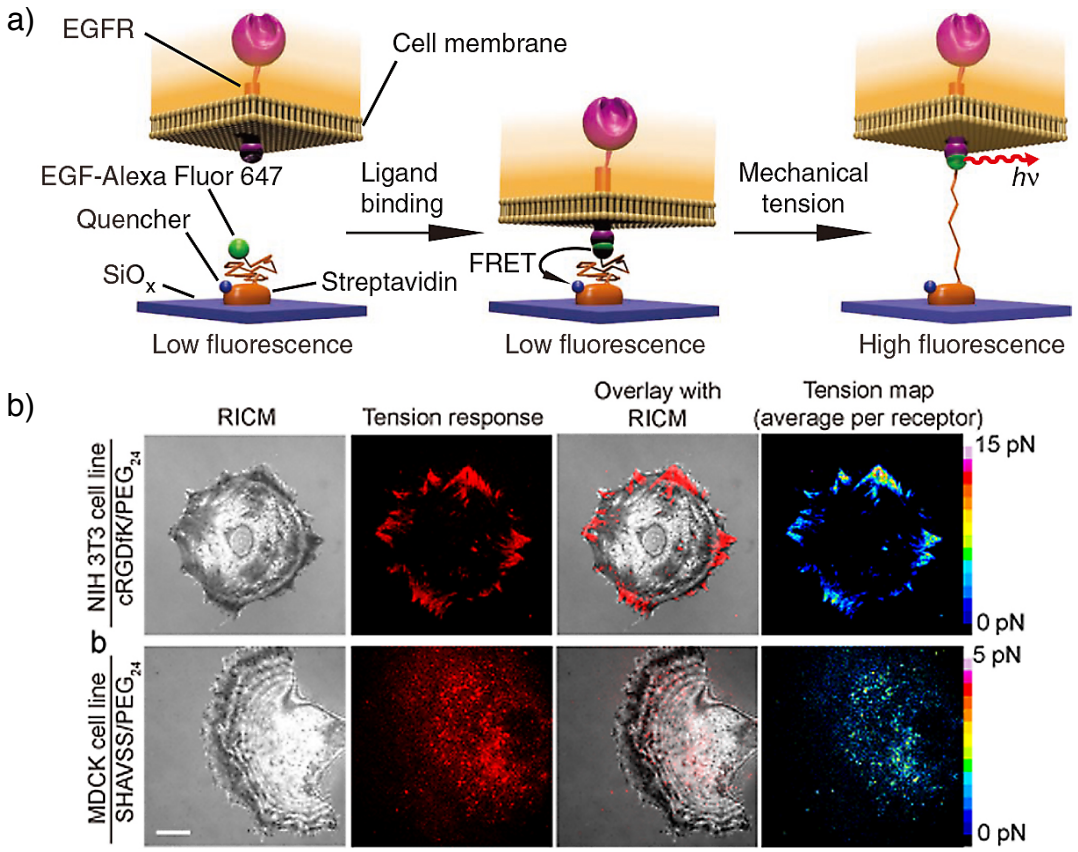


Figure 0-12 Cell surface tension imaging. (a) Schematic of the FRET-quenching mechanism of tension sensor function, copied from ref [132]. (b) Reflection interference contrast microscopy (RICM) and fluorescence overlay, and quantified heat map of tension for cells cultured on the cRGDfK (TAMRA-QSY9) and SHAVSS (Alexa 488-TAMRA) peptide tension probe surfaces. Scale bar: 20 μm. Images copied from ref [134].

nucleic acids by Chen's group.[133] The scope of this method was further extended by the combination of native chemical ligation (NCL) and solid-phase peptide synthesis (SPPS), which enabled wider choices of bio-orthogonal immobilized tension probes and extended imaging timescale (~ 3 days) to give quantified optical tension measurement (**Figure I-12b**).[134]

I.2.2.2 Emerging new imaging agents and their applications

Brightness is the soul of fluorescence imaging agents. The widely-used FPs and small molecular imaging probes, albeit with high fluorescence quantum yields (QY, Φ_{fl})

are normally limited by their extinction coefficients (ε), which determine the brightness as the product with QY (brightness = $\Phi_{fl} \times \varepsilon$). In view of this, fluorescent polymer nanoparticles (NPs) have recently emerged to meet the demand of superior brightness.[135]

Fluorescent polymer NPs can encapsulate large quantities of dyes. The brightness of the NPs is then enlarged by the dye-loading number, N (brightness = $\Phi_{fl} \times \varepsilon \times$ N). They usually can be > 100-fold brighter than their single molecular parents, and are also brighter than conjugate polymer NPs and inorganic quantum dots (QDs).[136] Because of their NP forms, they present a number of critically different properties. The sizes of dye-loading NPs are big, which is not ideal in some intracellular site-specific labeling applications, but is more suitable for tissue and whole animal labeling,[137] coating, and sensing.[138] The photostability of encapsulated dyes is arguably believed to be increased due to a more rigid polymer matrix that excludes oxygen and other chemicals relevant to photo-degradations. Nevertheless, high loading of dye molecules may cause aggregations in ground and/or excited states, leading to undesired spectral changes and photochemistry.[139] Compared to single dyes, of which the blinking is normally caused by intersystem-crossing to triplet states and electron transfer, dye-loading NPs can average

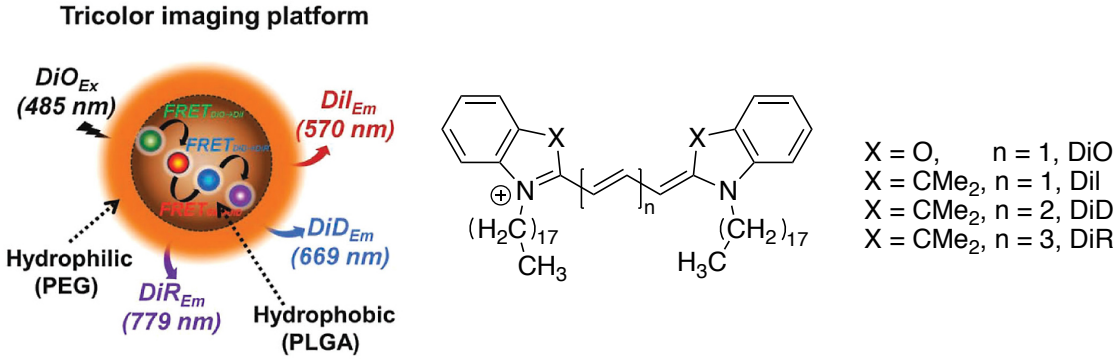


Figure 0-13 Schematic representation of dye-loading NP design for multicolor imaging via sequential FRET cascade.

out these effects and show continuous emission. In fact, aggregation-induced emission (AIE) based polymer NPs have been developed and shown no blinking. These AIE fluorogen (AIEgen) are also used to overcome the aggregation-caused quenching (ACQ), which becomes a major drawback when dye-loading is high.[140]

Another advantage of dye-loading NPs is the broad choices of dyes. This renders the flexibility to tune the colors and absorption/emission bandwidths. Wagh *et al.* prepared a dye-loading NP enclosing four different cyanine dyes that can deploy a sequential FRET

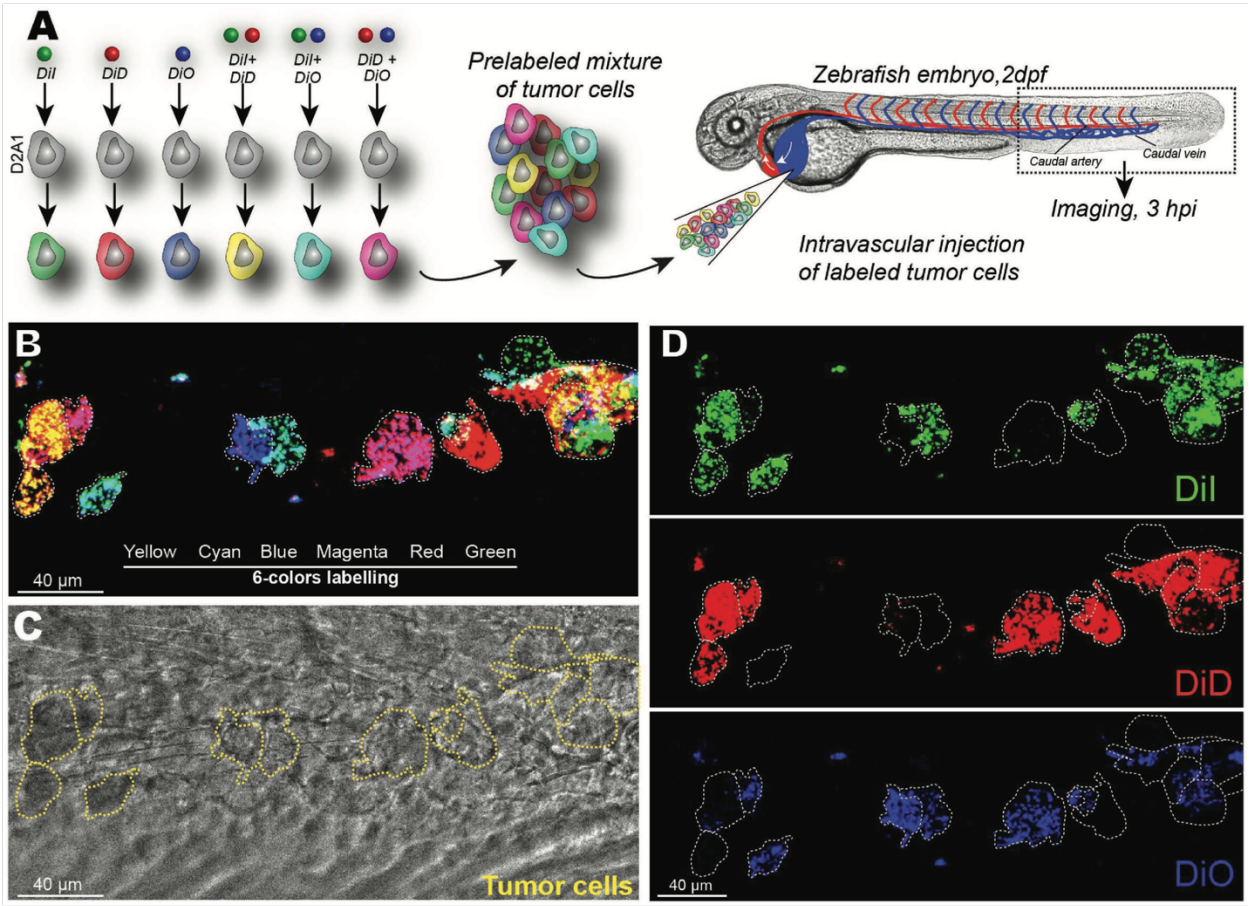


Figure 0-14 Tracking RGB barcoded cancer cells in zebrafish embryo. A) Six batches of D2A1 cells were labeled with fluorescent NPs generating RGB barcodes. Labeled cells were then mixed and injected intravascularly in 2 d postfertilization zebrafish embryos. B–D) Tumor cells that arrested in the vasculature are imaged, at 3 h post-injection, in the caudal plexus region of the zebrafish embryo. Clusters and individual cells can be found and distinguished based on their color. Images copied from ref [142].

cascade. This design enabled tricolor imaging with excitation of a single light source (**Figure I-13**).[141] Klymchenko's group took a different approach to establish a more sophisticated *in vivo* cell barcoding system for long-term multicellular developmental imaging tracking.[142] In their study, DiO, DiI, and DiD were also selected for dye loading. Other than FRET cascade, three types of NPs were prepared, and each contained only one cyanine dye. Very bulky perfluorinated tetraarylborates were used as counterions to prevent ACQ and achieve high dye loading. These NPs were then injected to D2A1 cancer cell line and 6 cell populations were generated from permutation of FRET-pairing for RGB cell barcoding. The prelabeled mixture of tumor cells were intravascularly

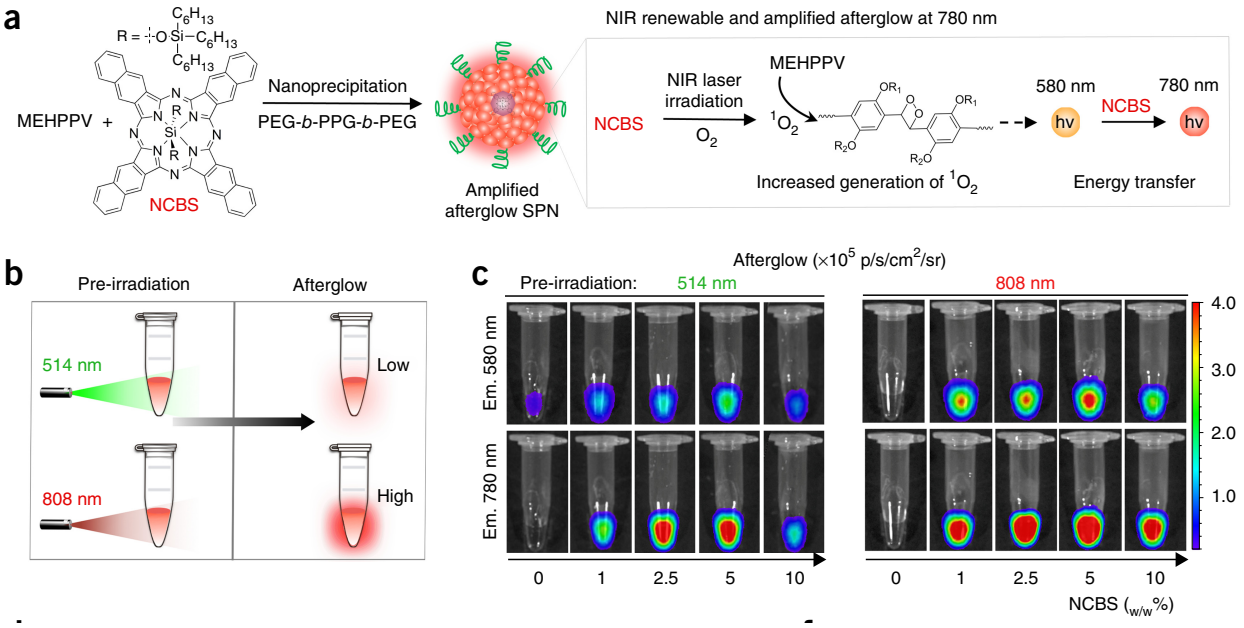


Figure 0-15 $^1O_2$-sensitizer-amplified NIR afterglow. (a) Schematic illustration of the proposed mechanism. (b) Schematic illustration of SPN-NCBS pre-irradiated by an 808-nm laser for afterglow enhancement versus a 514-nm laser. (c) Afterglow luminescence images of SPN-NCBS pre-irradiated at 514 (left) or 808 nm (right). The NP solutions were pre-irradiated by 808- or 514-nm laser for 1 min, and then the afterglow images were acquired under bioluminescence mode with an acquisition time of 30 s after removal of the laser source. Images copied from ref [144].

injected into zebrafish embryos, demonstrating a powerful tool for tracking cell migration (**Figure I-14**). This system was further used for tracking embryogenesis.

An interesting application of NP-based fluorescence is afterglow imaging. Different from conventional fluorescence imaging, thermal stimulation of the energy storage units in afterglow NPs causes slow release of photons, and results in luminescence after the end of light excitation.[143] As shown in **Figure I-15**, Pu's group used a substituted phenylenevinylene (MEHPPV)-based semiconductor NP (SNP) doped with a $^1O_2$ sensitizer, silicon 2,3-naphthalocyanine bis(trihexylsilyloxide) (NCBS), to demonstrate prolonged NIR-afterglow. An 808-nm laser irradiation sensitizes NCBS to release singlet oxygen, followed by vinyl trapping to form a PPV-dioxetane intermediate. Thermal stimulation breaks the dioxetane and releases 580-nm photons, of which the energy is transferred back to NCBS and emits 780-nm NIR light. This technique has been applied to *in vivo* afterglow imaging of lymph nodes and tumor in mice.[144]

In consideration of different forms of imaging agents, the essential core is mostly an organic fluorophore (while inorganic QDs, NPs, and Lanthanides are beyond the scope of this discussion), no matter what form of the carrier is (i.e., pure small molecules, proteins, polymers). In the past decade, considerable effort has expanded the scope to include nucleic acids, including molecular beacons (MBs) and RNA aptamers.[145] The most notable fluorescence RNA aptamer is Spinach developed in Jaffrey's lab.[146] Spinach is an RNA mimic of GFP. It binds to a *p*-HBI derivative, 3,5-difluoro-4-hydroxybenzylidene imidazolinone (DFHBI) and fluoresce with high quantum yield (0.72). Being smaller, Spinach has found a range of applications similar to, but wider than FPs. The innate

aptamer feature allows it to interact with nucleic acids, ions, and small molecules as well (**Figure I-16a**).[147-151] Slightly different, MBs are single-stranded DNAs that consist of a stem-loop structure doubly labeled with a fluorophore and a quencher group on each end, which remain in a dark state (**Figure I-16b**). Target binding induces conformational changes and opens up the hairpin folding, resulting in fluorescence turn-on. MBs are more flexible for rational engineering on different parts, and have many uses including real-time PCR.[152] Notably, nucleic acids also found tremendous usage in fluorescence *in situ* hybridization (FISH).[153]

It is also noteworthy to mention that, there is a growing interest in fluorescent antibody labeling, that achieves site-specific labeling based on the highly specific antigen-antibody recognition.[154] Different approaches have been taken to reduce the size of labeled fluorochromes. Examples include: single-chain variable fragment (scFv)-fused FPs, or fluorobodies;[155] and F_{ab}LEM (F_{ab} live endogenous modification), which uses monovalent antigen-binding fragment (F_{ab}) domain to conjugate fluorochromes.[156, 157] scFvs have been further developed into fluorogen activating proteins (FAPs) via direct evolution, which bind to a nonfluorescent dye and increase fluorescence.

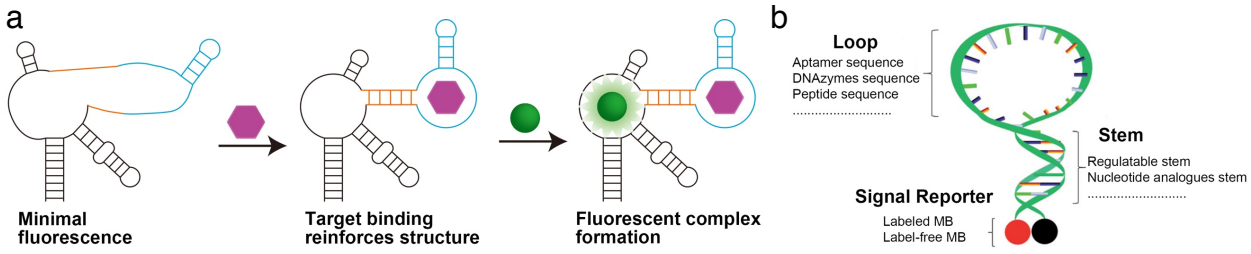


Figure 0-16 Schematic representations of nucleic acids-based imaging probes. (a) Spinach sensor, comprising Spinach (black), a transducer (orange), and a target-binding aptamer (blue). Target (purple) binding to the aptamer promotes stabilization of the transducer stem, enabling Spinach to fold and activate DFHBI (green) fluorescence. (b) General structure of molecular beacons.

I.2.2.3 Multimodality fluorescence imaging and intraoperative imaging guided cancer surgery

Fluorescence molecular imaging (FMI) is expanding its new roles from microscopic imaging into mesoscopic and macroscopic imaging. Typical imaging depth of conventional microscopy is usually about 10 μm. Because biological samples are not completely transparent, scattering of photos happens and limits the microscopic studies of tissues and whole-body animals. The imaging depth is determined by a physical parameter called mean free path (MFP) of a photon, which is the average distance a photon travels between two consecutive scattering events.[158] Confocal and two- or multiphoton microscopic techniques, by confining the average angle of scattered photons, have been developed to reach longer transport mean free path (TMFP) and further imaging depth (~ 1 mm) with different temporal resolutions.[159] Because of the weaker scattering in NIR region than in the visible and UV regions, recent research efforts have been put to develop NIR emitters (see **Section I.4**). Nevertheless, compared to other optic imaging techniques (e.g., SPECT, PET, CT, MRI), the reachable distance of FMI is still limited. Hybrid fluorescence molecular tomography (hFMT) has been developed to image the fluorescence distribution in tissues and small animals. It is a diffuse optical tomography that uses multi-angle optical illumination to collect fluorescence and excitation photons from different projections. hFMT allows three-dimensional and quantitative imaging with depth up to 1 cm.[160] Another trend is to develop imaging agents that couple multiple optical imaging systems.[161-163] For example, Chen's group has

designed an iron oxide NP doped with Cy5.5 and ^{64}Cu-DOTA to realize PET/MR/NIRF triple-modality imaging of U87MG xenograft mouse tumor model.[164]

A new cutting-edge field of multimodal fluorescence imaging applications is intraoperative fluorescence-guided surgery (FGS). The molecular-level of resolution of FMI is superior to all existing portable optical imaging systems.[159] It provides FMI as an ideal tool for indicating the remaining tumor cells in the surgical margin (the surrounding areas of the resection site) during a tumor removal in clinical operations. This is utterly important for the patient's survival and prognosis, given that a follow-up salvage surgery or adjuvant chemo-/radio-therapy usually cannot mitigate the tumor recurrence.[165] This fluorescence guide for surgery is termed by Tsien as "live molecular navigation".[166] Currently there are only two synthetic dyes approved by both FDA and EMA for FGS: indocyanine green (ICG) and fluorescein sodium. Methylene blue (MB) is approved by FDA but not EMA. 5-Aminolevulinic acid (5-ALA) is the precursor of the fluorescent protoporphyrin IX in certain tumor cells and is also approved by both.[167] A growing number of studies have focused on NIR-FGS to identify new fluorescent reagents, since NIR light is inherently safe in terms of laser illumination power and is invisible to human eyes, and thus does not alter the appearance of the surgical area.[167-174] A few FGS instrumentations are already approved by regulation authorities or under clinical trials. Interested readers are directed to the excellent perspective by Nguyen and Tsien.[166]

It is important to note, new agents that incorporate more sophisticated functionalities are emerging in the rapid growing area of multimodality fluorescence bioimaging, such as photosensitizing-based chromophore/fluorophore-assisted light

inactivation (CALI/FALI) and photodynamic/photothermal therapy (PDT/PTT),[175-178] PPI-based optogenetics,[179-182] and photoacoustic microscopy/ tomography (PAM/PAT).[183-185] Nevertheless, the detailed discussion is beyond the scope of this dissertation.

I.3 Site-specific labeling methods for *in vivo* fluorescence imaging

It is pivotal to label fluorescent probes to a specific cohort of targets of interest on a molecular level, to enable the imaging, sensing, and more sophisticated functions. Inarguably, the most commonly used site-specific labeling method is based on genetically addressable FPs. With recent advances in genome engineering (e.g., ZFN, CRISPR and TALEN), FP fusions can be expressed under the target protein's native promoter.[186, 187] However, facilitated by combinatorial synthesis and modern synthetic methodologies, synthetic dyes are much more structurally diverse.[188, 189] They have shown greater flexibility in modulating absorption/emission wavelengths, extinction coefficients, fluorescence quantum yields, photostability, and other physical characteristics such as fluorescence lifetime, singlet-triplet interconversion, to achieve more profound applications.[190-194] Thus, various posttranslational site-specific labeling methodologies have been developed to accommodate the exogenous dyes for *in vivo* imaging.[195-198]

I.3.1 Covalent enzymatic labeling

The idea to label POIs by enzymatic reactions is spurred by the fact that the cell utilizes protein posttranslational modification to diversify the structures and functions of biomolecules.[199] In this context, a number of posttranslational modification enzymes have been developed for protein labeling. These include transglutaminase (TGase),[200-203] sortase,[204-207] farnesyltransferase,[208, 209] biotin ligase (BL),[210-212] N-myristoyl transferase

(NMT),[213-215] formylglycine-generating enzyme (FGE),[216-218] phosphopantetheinyl transferase (PPTase),[219, 220] to name a few. However, these approaches generally require over-expression of non-bioorthogonal enzymes and sequential two-substrate enzymatic reactions, limiting their labeling specificity and kinetics. Bioorthogonal self-labeling enzymes have been developed in this context. They are engineered to stop the enzymatic cleavage of substrate before releasing, thus increasing the enzymatic kinetics and labeling specificity. Representative self-labeling enzymatic tags are SNAP/CLIP-tag, and HaloTag.

SNAP-tag is engineered human O^6-alkylguanine-DNA alkyl transferase (hAGT). hGAT is a 21 kDa DNA repair protein that catalyzes the irreversible alkyl group transfer of O^6-alkylguanine- or O^6-benzylguanine-DNA to its active site Cys residue.[221] hGAT mutants have been screened from direct evolution and yielded SNAP, with a 50-fold enhanced enzymatic activity over O^6-benzylguanine (BG).[222] This feature has been exploited for site-specific labeling of POI by transferring dye-functionalized BG derivative

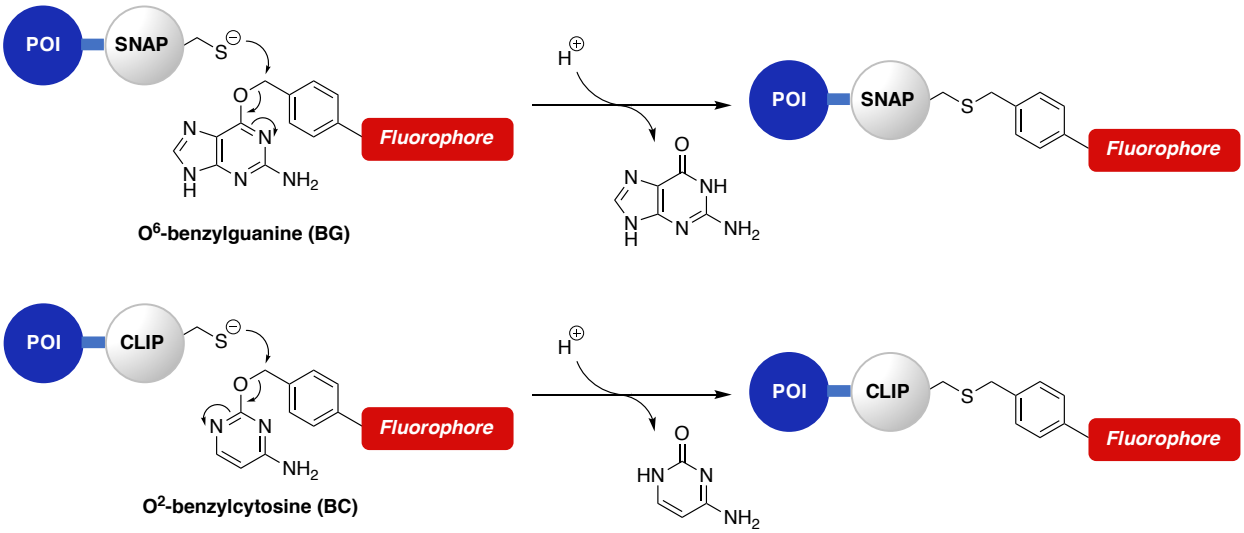
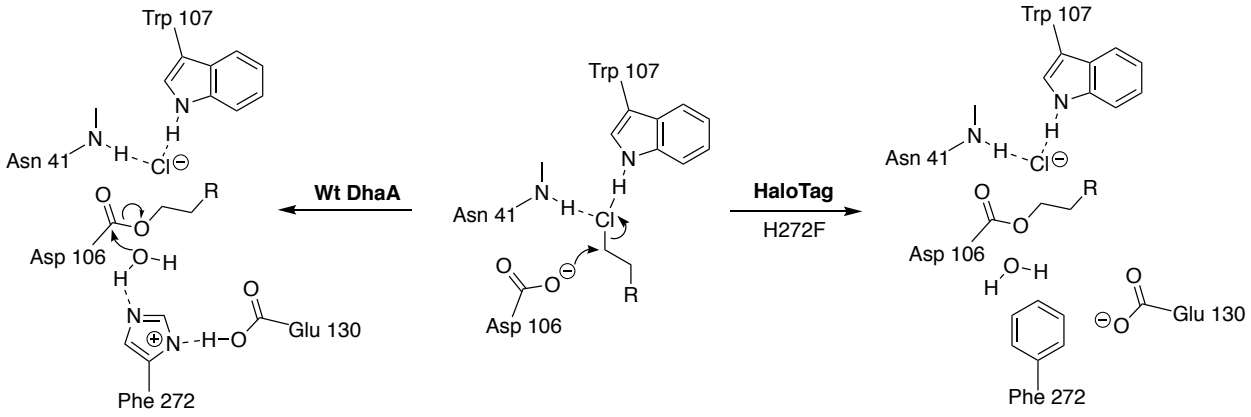


Figure 0-17 Schematic labeling reactions of SNAP/CLIP-tags.

to its genetic SNAP fusion. Slightly different, CLIP-tag is also engineered from hAGT via a combination of phage display and yeast surface display. Substrate specificity of SNAP-tag and CLIP-tag is orthogonal (**Figure I-17**). SNAP-tag only reacts with BG while CLIP-tag specifically reacts with O^2-benzylcytosine (BC). This orthogonality has been shown useful in simultaneous protein labeling and two-color imaging.[223] SNAP/CLIP-tags have been become an indispensable tool in the field of bioimaging and have realized super-resolution STORM imaging.[224, 225]

HaloTag is engineered from bacterial haloalkane dehalogenase (DhaA), and is a suicidal covalent ligand-binding protein similar to SNAP/CLIP-tags. As shown in **Scheme I-3**, the terminal chloride is removed by nucleophilic displacement with Asp106 of DhaA, and followed by an etherification between the hydrocarbon chain and the hydroxyl that forms a covalent intermediate. In the wild-type DhaA, the ester is further hydrolyzed by the base catalysis promoted by His272. A Phe272 mutation stops the hydrolysis and traps the intermediate as a stable covalent adduct.[226] HaloTag also has fast labeling kinetics and can be used simultaneously with SNAP/CLIP-tags.[227]



Scheme 0-3 Mechanistic representation of HaloTag, showing H272F mutation to trap fluorophore-labeled intermediate as a stable covalent adduct. R represents the labeling fluorophore.

I.3.2 Noncovalent affinity labeling

There is no clear boundary between covalently self-modified enzymatic tags and tags that are based on ligand-protein affinity. The ligands for the latter system can be designed to have covalent bond formation with a residue in proximity. Nevertheless, for the latter type, the affinity-based ligand-protein interactions remain as the major driving force for the site-specific recognition. As an example of proximity-induced affinity tag, Cornish and co-workers have developed TMP-tag based on the nanomolar noncovalent binding affinity of trimethoprim (TMP) with *E. coli* dihydrofolate reductase (eDHFR).[228] DHFR was fused to POI and labeled with a cell-permeable TMP heterodimer, which consists of TMP, a fluorophore, and a covalently linked acrylamide group. Upon binding, TMP brought the acrylamide close to an active cysteine residue just outside the pocket. A sequential Michael addition of the cysteine with this α,β-system covalently anchored

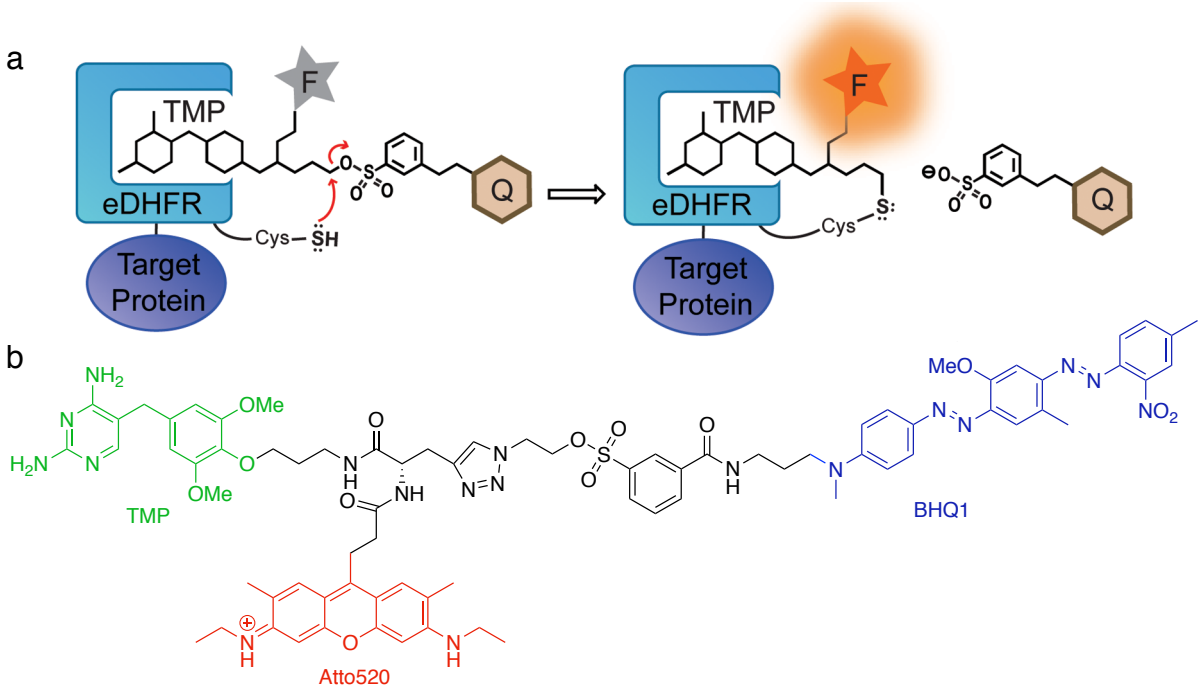


Figure 0-18 Fluorogenic TMP-tag. (a) Cartoon of the trimeric TMP-quencher-fluorophore to be cleaved in a proximity-induced S_N2 reaction. (b) Structure of TMP-BHQ1-Atto520.

the fluorophore to eDHFR. The labeling kinetics was increased to an 8-min half-time by rationally engineering the optimal distance between the acrylamide and the active Cys.[229] FRET-quenching was further introduced to the TMP ligand and made the system fluorogenic (**Figure I-18**).[230-232]

SNAP/CLIP-, Halo-, and TMP-tags are able to incorporate a variety of fluorescent dyes. Nonetheless, they normally require extensive wash steps to remove excess free fluorochromes to distinguish the bound and unbound probes. A more recent trend is to develop fluorogenic probes that remain in a dark state until site-specific binding happens. As a generic methodology, a quencher moiety can be conjugated to the fluorescent probe and quench the fluorescence either through FRET or PeT. These quencher groups can be removed by nucleophilic substitution coupled with the covalent labeling in a similar pattern to the third-generation of TMP-tag described before.[233] A more thorough discussion is presented in **Section I.20**.

Kikuchi and co-workers have developed photoactive yellow protein (PYP)-tag based on this principle. PYP is a 14-kDa, water-soluble protein derived from purple bacteria, which does not exist in animal body. It naturally binds to the CoA thioester of 4-hydroxycinnamic acid through transthioesterification with Cys69. Importantly, this natural ligand can be modified to a structural analog, 4-hydroxycoumarin, with the high binding affinity. A covalently-linked fluorophore to the 4-hydroxycoumarin derivative can associate with it under polar environment and have FRET-quenching. The fluorophore emission will be turned on after the transthioesterification that breaks the association. Alternatively, the PYP ligand can simultaneously be linked to a quencher and an emitter

to realize the same function.[233, 234] A more fluorescent 4-dimethylamino coumarin has been developed as a dual-function ligand for both binding and fluorescence, so that the coumarin fluorescence can be turned on directly after transthioesterification, negating the need to couple an exogenous fluorophore.[235] pK_a modulation of the thioester leaving group together with the charge optimization surrounding the binding cavity has further improved the transthioesterification kinetics (**Figure I-19**).[236] The PYP ligand has also been modified to accommodate more enzymatic substrate to demonstrate improved fluorogenicity.[237]

It is noteworthy to mention that, recently Gautier and co-workers have combined direct evolution using yeast display and fluorescence-activated cell sorting (FACS) to engineer PYP into a Yellow Fluorescence-Activating and absorption-Shifting Tag (Y-FAST). Instead of 4-hydroxycinnamic acid or coumarin, Y-FAST binds to 4-hydroxybenzylidene-rhodanine (HBR) or 4-hydroxy-3-methylbenzylidene-rhodanine (HMBR) in a reversible manner. Y-FAST distinguishes from PYP in two ways after ligand

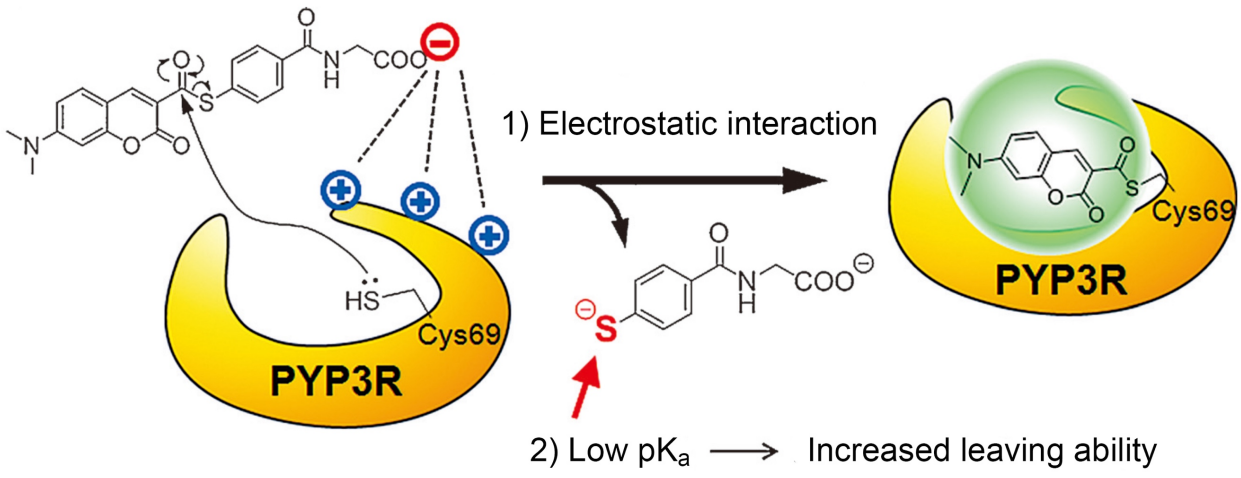


Figure 0-19 Design of the PYP-tag mutant PYP3R and its fluorogenic probe, with a focus on electrostatic interactions and the pK_a value of the leaving group. Copied from ref [236].

binding: 1) a significant increase in QY of H(M)BR; 2) a large red-shift in absorption due to phenol deprotonation (**Figure I-20a**).[238] This negates the need of covalently coupled quencher or fluorophore moieties of the ligands. The residence time of HBR and HMBR are 60 ms and 160 ms, respectively. This enables the Y-FAST labeling as instantaneous, highly dynamic, and fully reversible. Shown in **Figure I-20b**, a rapid labeling on-off cycle was demonstrated by exchanging ligand-free medium of the cells labeled with Y-FAST. A follow-up study reports the second generation of Y-FAST-tag that extends the emission into far-red/NIR region by elongating the π-conjugation of HBR analogues.[239]

Adopting similar strategies, a number of protein affinity-based labeling tags have been engineered, for instance, TEM-1, a class A β-lactamase, and CCD, a cephalosporin-based probe.[240] It is worth noting that the scope of protein hosts is not limited by substrate-

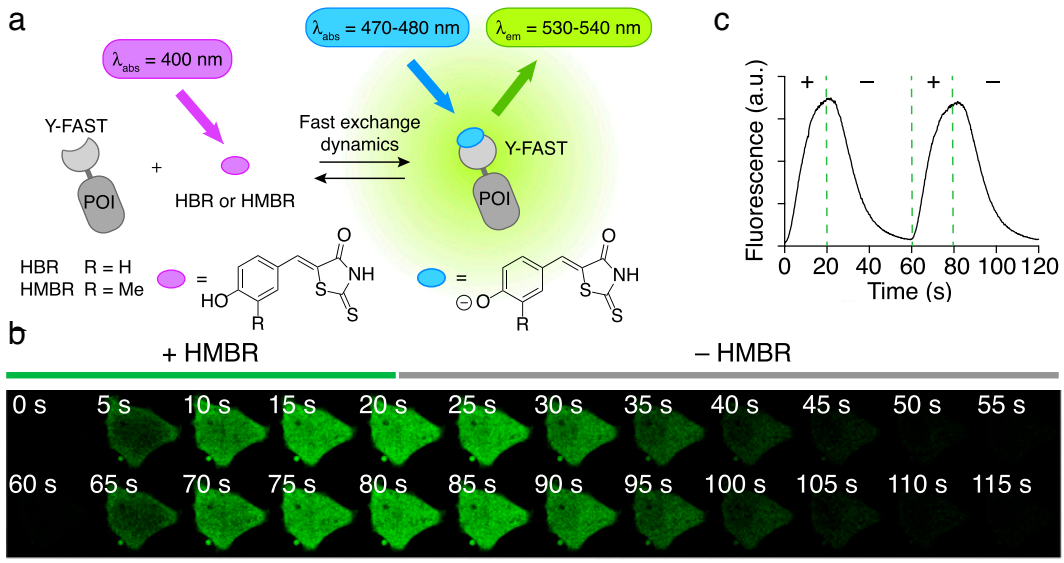


Figure 0-20 Y-FAST-tag. (a) Schematic showing the spectral changes during Y-FAST binding: spectral shift and QY increase. (b) Confocal time lapse showing two cycles of labeling/unlabeling (Ex/Em 488/493-575 nm) of HeLa cells expressing Y-FAST. Cells were repeatedly incubated with HMBR-containing culture medium for 20 s and HMBR-free culture medium for 40 s. HMBR concentration was 5 μM. (c) Temporal evolution of the cell fluorescence upon addition (+) and removal (-) of HMBR. Images and plots copied from ref [238].

specific enzymes and photoreceptor (i.e., PYP). As mentioned in **Section I.2.2.2**, scFv has also been engineered to bind a diverse set of fluorogenic dyes.[241, 242] These fluorogen-activating proteins (FAPs) bind their ligands with nanomolar affinity. Conceptually, the ligands are designed to be ionic and do not show fluorescence in polar environment. Shown in **Figure I-21** are representative examples: thiazole orange (TO) and malachite green (MG). The high affinity binding results not only in the increase of QY, but also in the red-shift of spectra and increase of extinction coefficients.[243] With multi-functionalized MG ester and corresponding scFvs, these no-wash FAP-tags have been applied in far-red imaging, super-resolution imaging, and multicolor imaging.[244-248]

I.3.3 Bioorthogonal chemical labeling

The site-specific labeling tags described in **Section I.3.1** and **I.3.2** are all protein-based, albeit indispensable, their relative large size (up to ~ 200 amino acids) may elicit concerns of disturbing the POIs. In contrast, bioorthogonal chemistry relies on the "click" reactions fusing the probe and a specialized functional group on POI, and can decrease the size perturbation. The field of bioorthogonal chemistry has witnessed an explosive development since the term was coined by Bertozzi in 2003.[249, 250]

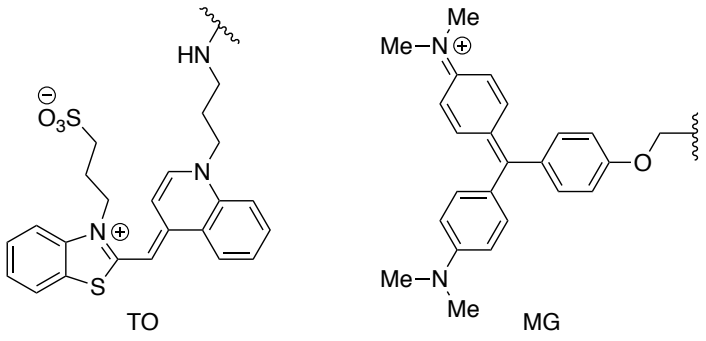
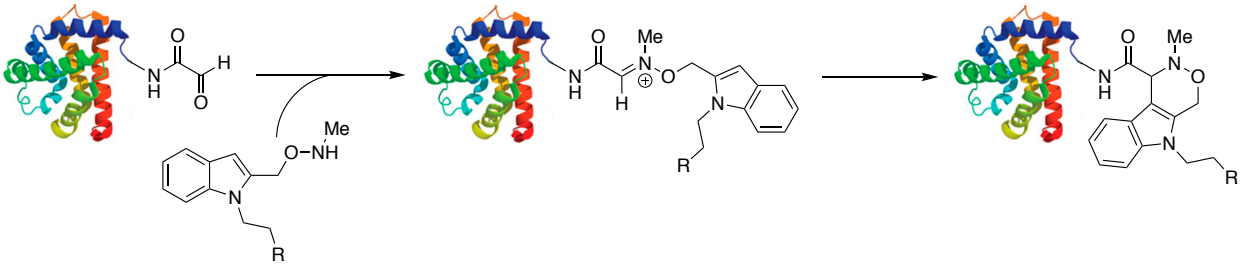


Figure 0-21 Fluorogenic ligands of FAP: thiazole orange (TO) and malachite green (MG).

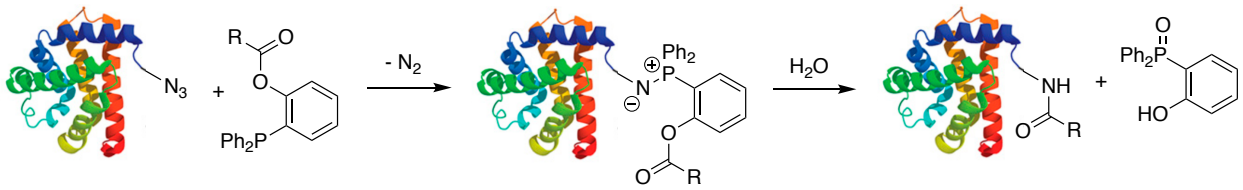
A number of modification methods were established based on the nucleophilic nature of lysine, cysteine, tyrosine, and tryptophan. Reagent scope encloses aldehyde, ketone, olefin, sulfonamide, phenol, aniline, diazomethine, etc., via either acidic/basic catalysis, or transition metal catalyzed coupling.[251] Among a variety of N-terminus modifications, a well-recognized method is the native chemical ligation (NCL), which is a rapid irreversible intramolecular S-N acyl transfer on thioesters by N-terminal amine.[252]

One early example of click reaction is hydrazide/oxime-ligation, which utilizes an oxyamine or hydrazine group to condense with an aldehyde or ketone group under either acidic or basic physiological conditions.[253, 254] However, the application is limited by the difficulty of introducing aldehyde groups to POIs. A recent example is a variant of Pictet-Spengler ligation.[255] The oxyiminium formed between the aldehyde and an oxyamine undergoes an intramolecular C-C bond formation with the indole nucleophilic C_β and formed a stable oxacarboline product (**Scheme I-4**).

Being small, kinetically stable under physiological conditions, and essentially absent from biological systems, the azide group has found many uses in biorthogonal click reactions. A classic example is the Staudinger ligation. Taking the prototype of Staudinger reduction, which starts from the phosphine nucleophilic attack of the azide, followed by N_2 release to yield an aza-ylide, Staudinger ligation is designed with an ortho-



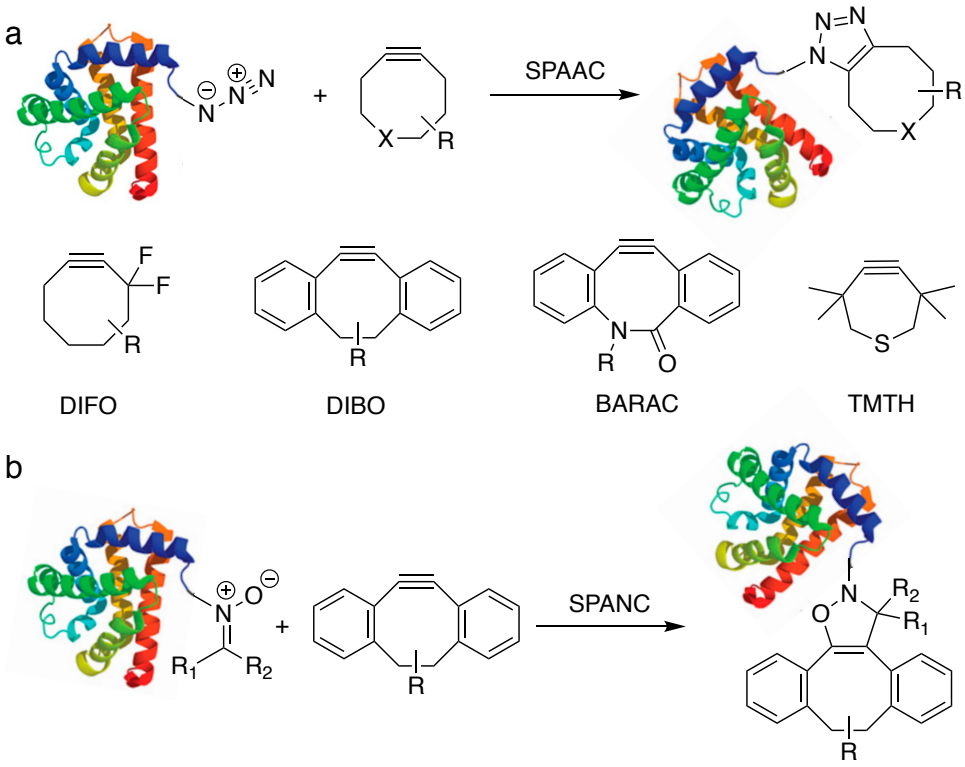
Scheme 0-4 Pictet–Spengler ligation of an aldehyde with a tryptamine nucleophile.



Scheme 0-5 Traceless Staudinger ligation.

ester group on the phosphine reagent to trap the reactive ylide and form a stable amide bond through intramolecular cyclization.[256] A "traceless" version is also developed by inverting the ester to release the phosphine oxide (**Scheme I-5**).[257] Azide-based Huisgen [3+2] cycloaddition has also been modified to a copper(I) catalyzed variant that proceeds without the requirement of high temperature and pressure.[258] Against the common thought that the cyclization is triggered by copper actylide via a six-membered copper(III) metallacycle, this copper-catalyzed alkyne-azide cycloaddition (CuAAC) mechanistically proceeds with a stepwise C-N bond formation catalyzed by a dicopper complex while the monomeric copper actylide is unreactive.[259, 260] Recently, CalFluor, a universal motif utilizing PeT quenching of azide was reported for CuAAC to cover across the visible spectrum.[261]

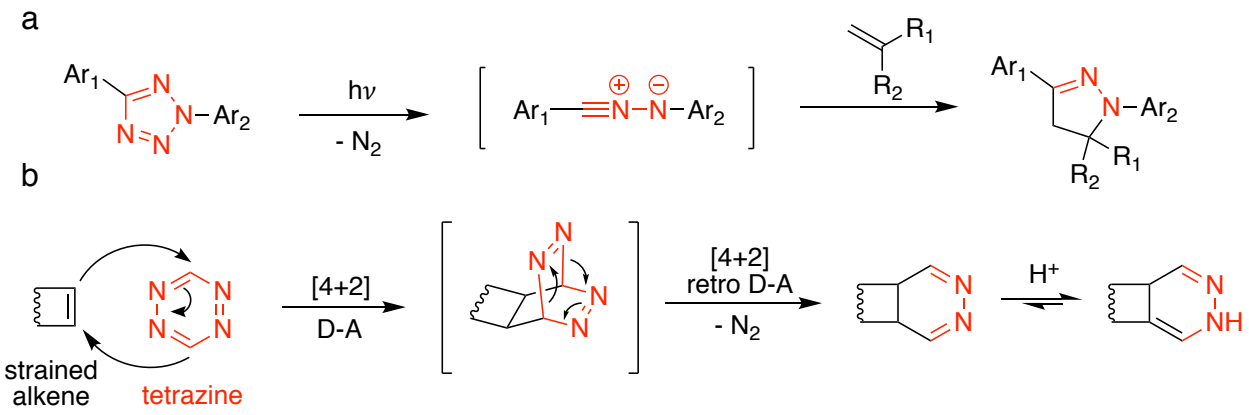
In terms of *in vivo* labeling, CuAAC is not ideal due to its high cellular toxicity and the low performance of the Cu(I) catalyst. A copper-free [3+2] strain-promoted alkyne-azide cycloaddition (SPAAC) was developed, driven by the ring strain-release of cyclooctyne.[262] Shown in **Scheme I-6a**, more electronically and/or sterically modified cyclooctyne derivatives were synthesized to optimize the SPAAC kinetics.[263-266] The triple bond in DIBO can be further modified into a cyclopropenone and unmasked by photo-activation.[267] Another closely related [3+2] cycloaddition is the strain-promoted alkyne-nitrone cycloaddition (SPANC, **Scheme I-6b**). The more reactive nitrone is used and



Scheme 0-6 [3+2] cycloadditions. (a) SPAAC and representative cyclooctyenes. (b) SPANC. R is a labeling fluorophore.

shows 3.9 $M^{-1}\cdot s^{-1}$ second-order rate constant in model reactions, almost 3-fold faster than the azide counterpart. However, the nitrone introduction to POI is not easy to implement.[268] Strained alkenes have also been applied in strain-promoted [3+2] cycloaddition, such as oxanorbornadiene derivatives. They are relatively easy to synthesize, but usually suffer from slow reaction kinetics and low specificity.[269]

An intriguing photoinducible [3+2] cycloaddition of alkene is the alkene-tetrazole photoclick cycloaddition (**Scheme I-7a**). Diarytetrazole can undergo a UV-activated reverse [3+2] reaction to release N_2 and form a nitrile-imine *in situ*, consequently furnishing a [3+2] product with labeled exogenous alkenes.[270] Comparatively, this photoclick cycloaddition is fast, and has intrinsic fluorogenicity since tetrazole itself is an



Scheme 0-7 (a) Tetrazole-alkene photoclick cycloaddition. (b) IEDDA tetrazine-alkene cycloaddition.

efficient PeT quencher.[271] A potential concern is the cross-reactivity with endogenous alkenes.

Recently the Inverse-Electron-Demand Diels-Alder (IEDDA) cycloaddition has drawn much attention (**Scheme I-7b**).[272, 273] Strained *trans*-cyclooctene is paired with tetrazene in this IEDDA and is 9 orders of magnitude faster in rate than internal *cis*-olefins.[274] The rate constant highly depends on the electronics of the dienophile.[275] To date, electron-rich norbornenes, cyclopropenes, bicyclo[6.1.0]nonynes, and even unstrained styrenes have all successfully made use of this labeling method.[276-278] Similar to tetrazole, tetrazene also serves as a PeT quencher for the purpose of fluorophore labeling.

Other click reactions are still emerging, e.g., redox-activated chemical tagging (ReACT),[279] photochemical thiol-ene reaction,[209] chemoselective rapid azo-coupling reaction (CRACR),[280] and the phospha-Michael addition.[281] Recently, one-pot triazole click reaction has also been realized on the DNA level.[282] Even Pd-catalyzed C-H

activation and Ru-catalyzed olefin metathesis have seen growing use in bioorthogonal labeling. Readers are referred to these extensive review articles.[283-285]

I.3.4 Labeling approaches with short oligomer tags

Despite the versatility of systems to incorporate various fluorochromes into targeting biomolecules, bioorthogonal labeling strategies are often complicated by the introduction of uncanonical amino acids (UAAs), which bear the synthetic functional groups needed by the chemical transformations. Expressing UAAs on POIs is not trivial. It requires the implementation of artificial tRNAs and corresponding recombinant enzyme cassette to exploit cell machinery,[286] which can in turn elicit the concern of functional perturbation of the targeted cells. To circumvent this, several strategies have been developed to use small oligomeric peptides and/or nucleic acids as labeling tags (for example, the RNA aptamer Spinach discussed in **Section I.2.2.2**).

Recently, Ting's lab has engineered the *E. coli* enzyme lipoic acid ligase (LplA) capable of covalently ligating 7-hydroxycoumarin to a 13-residue LplA acceptor peptide (LAP).[287] This PRIME (PRobe Incorporation Mediated by Enzymes) method has found

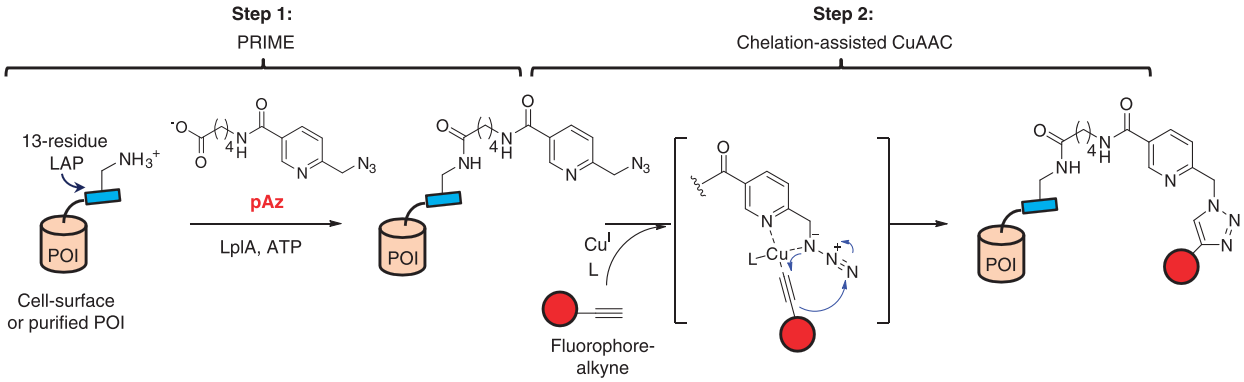
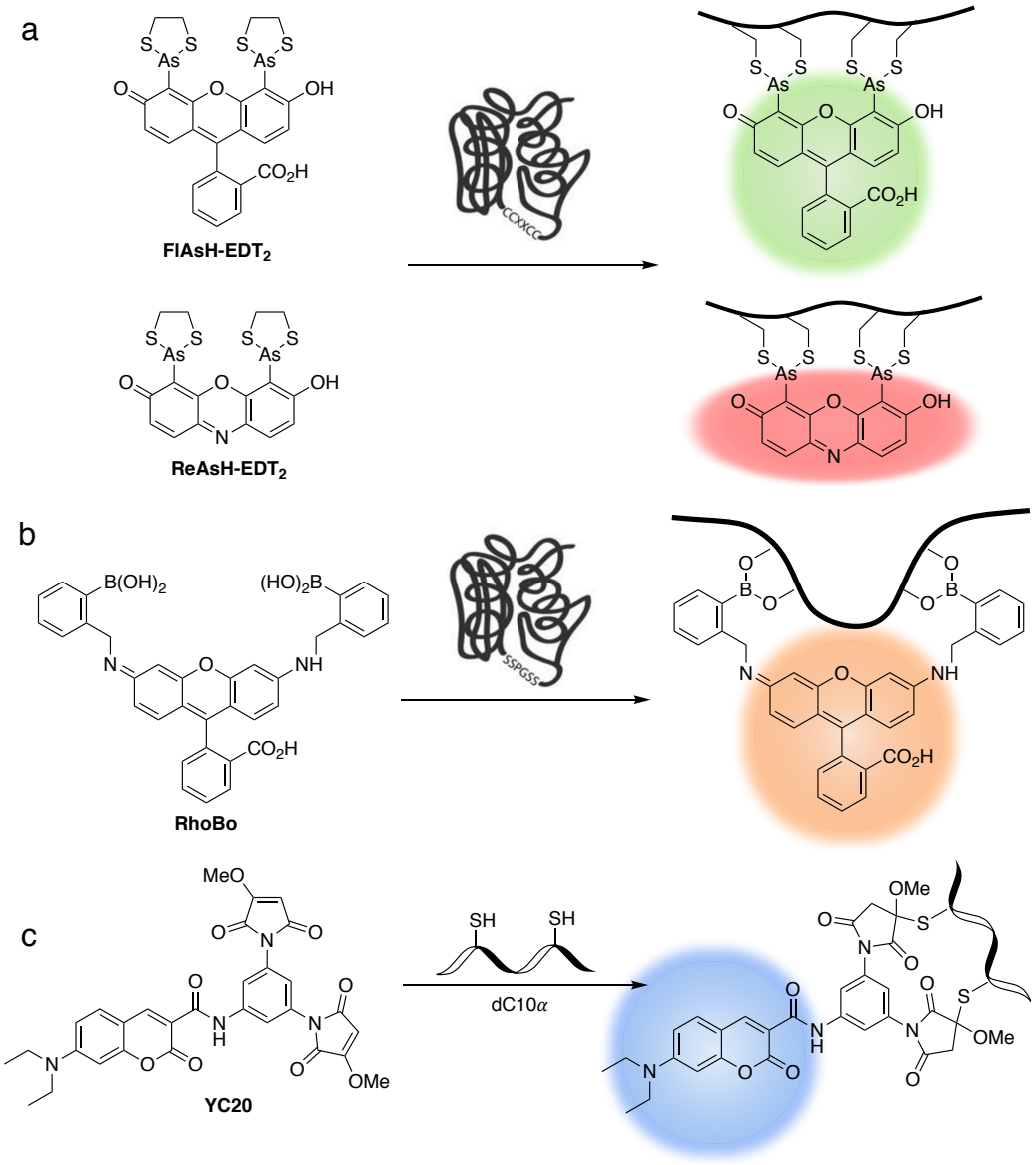


Figure 0-22 Two-step labeling scheme of site-specific protein labeling via PRIME and chelation-assisted CuAAC. In the first step, W37VLplA covalently attaches a copper-chelating picolyl azide (pAz) onto genetically fused LAP. In step two, CuAAC selectively derivatizes pAz with a probe-conjugated terminal alkyne.

use in single molecular nanoscopy and PPI studies.[288, 289] It is worth noting that, LplA can be engineered to recognize azidoalkanoic acid instead of lipoic acid. This opens an avenue to couple CuAAC with PRIME to avoid potential steric collisions between large fluorochromes and enzyme active site (**Figure I-22**).[289-292]



Scheme 0-8 Labeling approaches based on short peptides. (a) FlAsH and ReAsH with tetracysteine motif. (b) Bis-boronic acid RhoBo with tetraserine motif. (c) Dimaleimide coumarin YC20 with vicinal dicysteine motif.

To date, the smallest labeling tag is the tetracysteine motif of biarsenical FlAsH/ReAsH tags (**Scheme I-8a**). First developed in Tsien's lab, four cysteines were placed at the *i*, *i* + 1, *i* + 4, and *i* + 5 positions of an α-helix to facilitate the binding with two trivalent arsenics of 4',5'-bis(1,3,2-dithioarsolan-2-yl)fluorescein bis-ethanedithiol adduct (FlAsH-EDT_2). The QY of nonfluorescent FlAsH-EDT_2 can be increased by > 50,000-fold after dithiol transposition with the tetracysteine motif.[293] Soon after its debut, the biarsenical label was modified extensively, both its chemical structure and the peptide motif, to optimize the affinity of the biarsenics with tetracysteine and increase the contrast between specific and nonspecific staining.[294-297] Although these biarsenics are limited by their reductive nature, they have found widespread applications across various fields.[298-300] Most recently, *ab initio* calculations and excited-state lifetime measurement were conducted to elucidate the origin of rotamer-restricted fluorogenicity of these biarsenical labels.[301]

Similar strategies were adopted to develop other short peptide motifs for site-specific labeling. Schepartz and co-workers reported a bis-boronic acid probe that shows high affinity to a tetraserine motif and negates the use of cytotoxic arsenic (**Scheme I-8b**).[302] By coupling a dimaleimide PeT quencher to a coumarin, Keillor and co-workers have developed a fluorogen that can have turn-on fluorescence after the Michael addition with a vicinal dithiol peptide (**Scheme I-8c**).[303, 304] It could be envisioned that aided by directed evolution, new vicinity-induced multi-transposition tags will emerge in the near future.

I.4 Ongoing pursuit of far-red/near-infrared fluorochromes

For modern biomedical fluorescence imaging, especially *in vivo* imaging, the two pillars are the imaging resolution and the imaging depth. The former has witnessed the third revolutionary wave in microscopy, which was recognized by the 2014 Nobel Prize in Chemistry jointly awarded to Eric Betzig, Stefan W. Hell, and William E. Moerner, for "the development of super-resolved fluorescence microscopy".[305] The latter one, however, is embracing the continuous advancement of NIR emitters. Deeper tissue is transparent to NIR light for two reasons: 1) physically the longer the wavelength, the less scattering; 2) physiologically, haemoglobins and water are the major absorbers in visible and infrared regions, respectively, while having the lowest absorption coefficients in the NIR-I region (650 – 900 nm, **Figure I-23**).[306] Fluorophores suitable for NIR-I imaging have drawn much attention during the past decade. Recently, a number of inorganic and nanomaterials have also been explored in use of NIR-II (1,000 – 1,700 nm) imaging.[307]

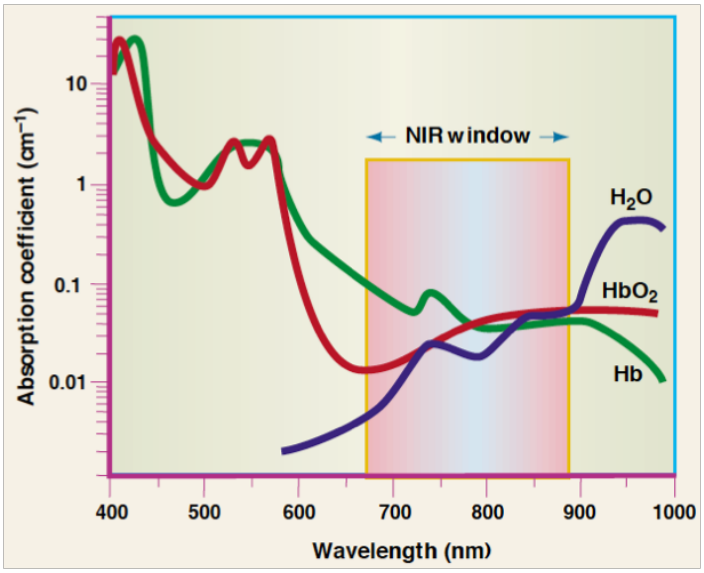


Figure 0-23 The ideal NIR window for in vivo imaging, showing minimal light absorption by haemoglobin (Hb, green), oxyhaemoglobin (HbO_2, red) (<650 nm) and water (>900 nm). Copied from ref [306].

I.4.1 Far-red and NIR FPs

Discussed in **Section I.1.2**, DsRed-like chromophores have extended conjugation through acylimines at residue 65. Actually, DsRed has been used as the parent template for a variety of autocatalytic far-red FPs.[18, 19] Representative examples are mKate/2, eqFP650/670, TagRFP657/675, mNeptune, mPlum, and mCardinal, to name a few.[47, 53, 308-310] Their emission maxima are all close to, or beyond 650 nm. The red-shift is based on several strategies, including extended π-conjugation, chromophore isomerization, increased chromophore planarity, hydrogen-bonding to the acylimine oxygen, ground-

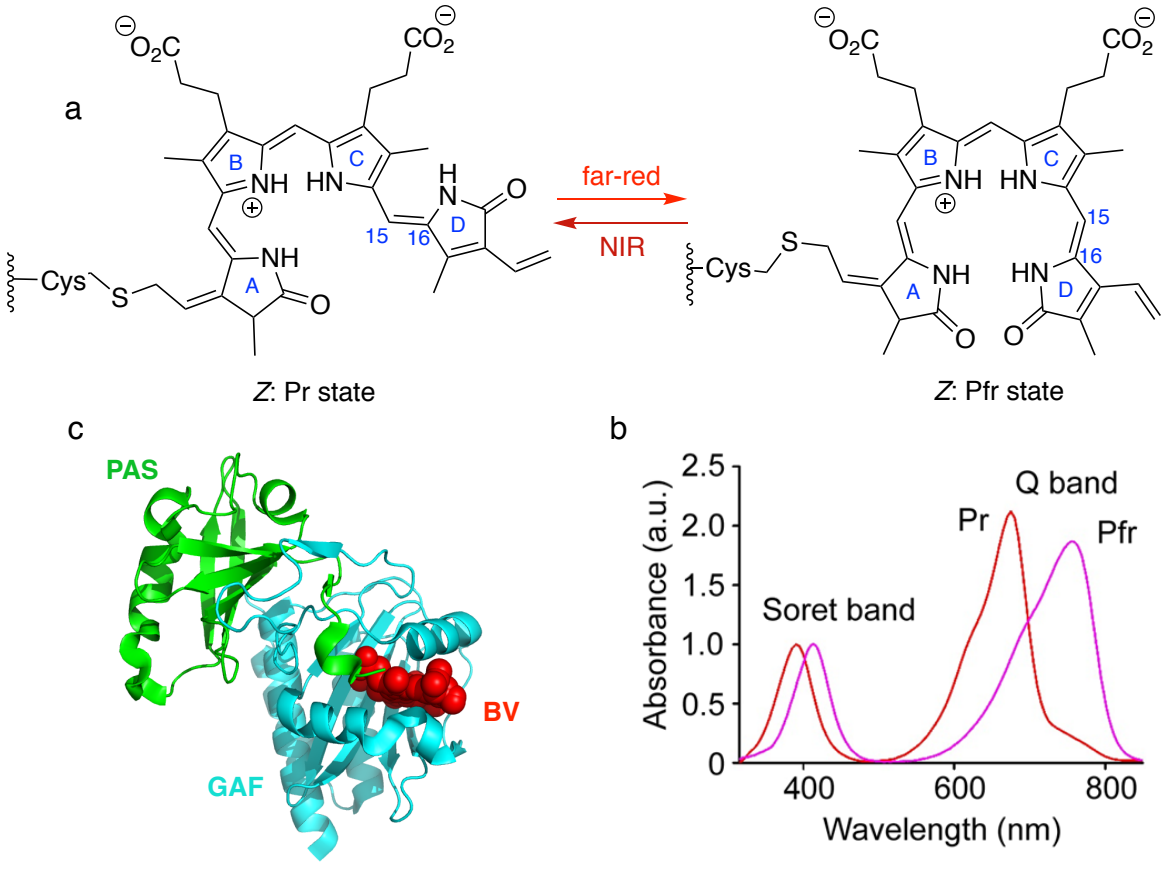
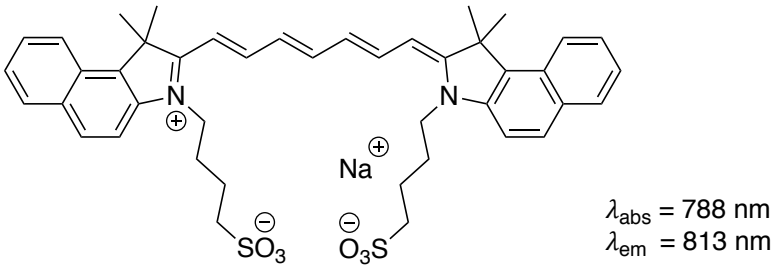


Figure 0-24 Phytochrome-derived BV-binding FP. (a) Scheme showing Z/E isomerization between Pr and Pfr states of BV adduct. (b) Absorption spectra of Pr and Pfr states. Q band is the major absorption. Soret band is the pyrrole absorption. (c) A truncated PAS-GAF NIR FP (PDB ID: 4XTQ).

state destabilization and excited-state stabilization, and increased environment polarity.[20, 310, 311]

Phytochromes from plant, fungi, and bacteria provide another source of NIR FPs. Their natural function as photoreceptors are to absorb far-red and NIR light and regulate light response. Taking bacteria phytochromes (BphP) as an example, they consist of the PAS, GAF, and PHY domains which are topologically conservative throughout species.[312] BphP binds biliverdin IXα (BV) in the GAF domain via a thioetherification between the active Cys residue and the terminal alkene on the A ring of BV's tetrapyrrole.[313] The embedded chromophore can undergo a light-triggered *Z/E* isomerization at the C_{15}-C_{16} double bond, namely, the Pr and Pfr states. The Pr states absorbs light at 660 – 700 nm, whereas the Pfr state absorbs light at 740 – 770 nm (**Figure I-24**). Substantial mutagenesis has halted this *Z/E* isomerization to yield permanently fluorescent NIR FPs. Because of the ubiquitous existence of BV in mammalian cells, the current developed NIR FPs are all from BphPs.[54, 314, 315] Numerous structural and activity studies have elucidated the essential functions of each domain.[316] With these understandings, novel NIR FPs are engineered based on truncating BphPs to either single GAF domain for small monomeric FPs (e.g., GAF-FP),[56] or to PAS-GAF domains for dimeric FPs (e.g., IFPs



Indocyanine green (ICG)

Figure 0-25 Indocyanine green (ICG).

from *Dr*BphP, and iRFPs from *Rp*BphP).[54, 55] By engineering the tethered PHY domain, photoactivatable and photoswitchable NIR FPs are also developed and are used in SRM. Assisted with FACS and random mutagenesis, blue- and red-shifted NIR FPs have emerged across the NIR region.[317] A recent report even shows Sandercyanin, a BV-binding protein from walleye skin mucus, capable of being excited at UV-blue region and emitting in the far-red/NIR region.[64]

I.4.2 NIR organic dyes

For a long time, NIR organic dyes have been sought for various applications including biomedical imaging and biosensing.[318, 319] The classical approach of synthetic dyes to reach NIR window is by extending the π-conjugation. One representative is the ICG approved by FDA for intraoperative fluorescence-guided surgery (**Figure I-25**, see **Section I.2.2.3**). Recent progress in developing NIR dye have been focused on extending conjugation (i.e., either by fusing (hetero)aromatics, or by introduing more electron-diffused heteroatom), affecting bond length alternation, modulating intramolecular charge transfer, and other effects including intramolecular hydrogen bonding and molecular stacking.

I.4.2.1 Polymethine dyes

Classical cyanine dyes are a family of organic dyes having odd number of carbons in a conjugated polymethine chain with two ends of nitrogen-containing heterocycles. A characteristic polymethine framework does not have significant bond length alternation between each carbon unit. Cyanines commonly feature sharp absorption bands and high extinction coefficients. Their polymethine chain lengths and nitrogen-containing terminal

groups can vary.[320] According to Brooker,[321] symmetrical cyanines are *non-convergent* series, which means the absorption and emission wavelength shifts with the increasing number of vinylene group (termed "vinylene shift") are essentially equal (~ 100 nm). While asymmetrical cyanines are *convergent* series and their vinylene shifts become smaller with the increasing length of methine conjugation. Cyanine dyes are well developed throughout the decades. To approach the NIR window, heptamethine cyanines with different terminal groups and rigidified polymethine backbones are synthesized (**Figure**

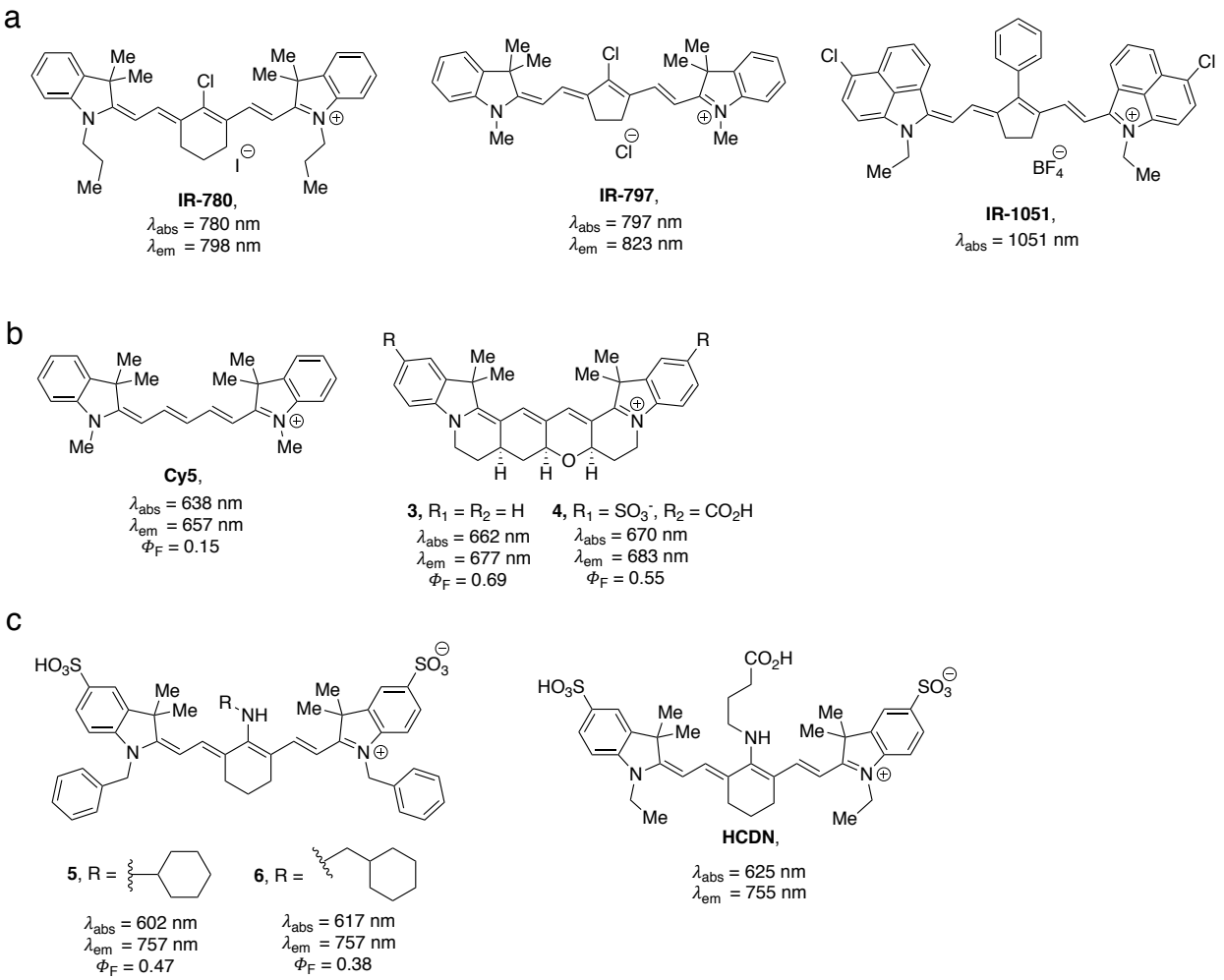


Figure 0-26 Representative non-convergent polymethine cyanines. (a) Cyanines with various rigidified heptamethine backbones and terminal groups. (b) Conformation-restrained pentamethine cyanines. (c) Large Stokes shift heptamethine cyanines.

I-26a).[322-324] However, the quantum yield is usually correlated to a dramatic loss with the increasingly red-shifted absorption. Recent efforts have conformationally restrained cyanines for increased stability and quantum yield, however the restrained heptamethine has not been synthesized as of yet (**Figure I-26b**).[325] Interestingly, it was found an amine substitution on position 4 of the polymethine leads to a significant blue-shift in absorption,

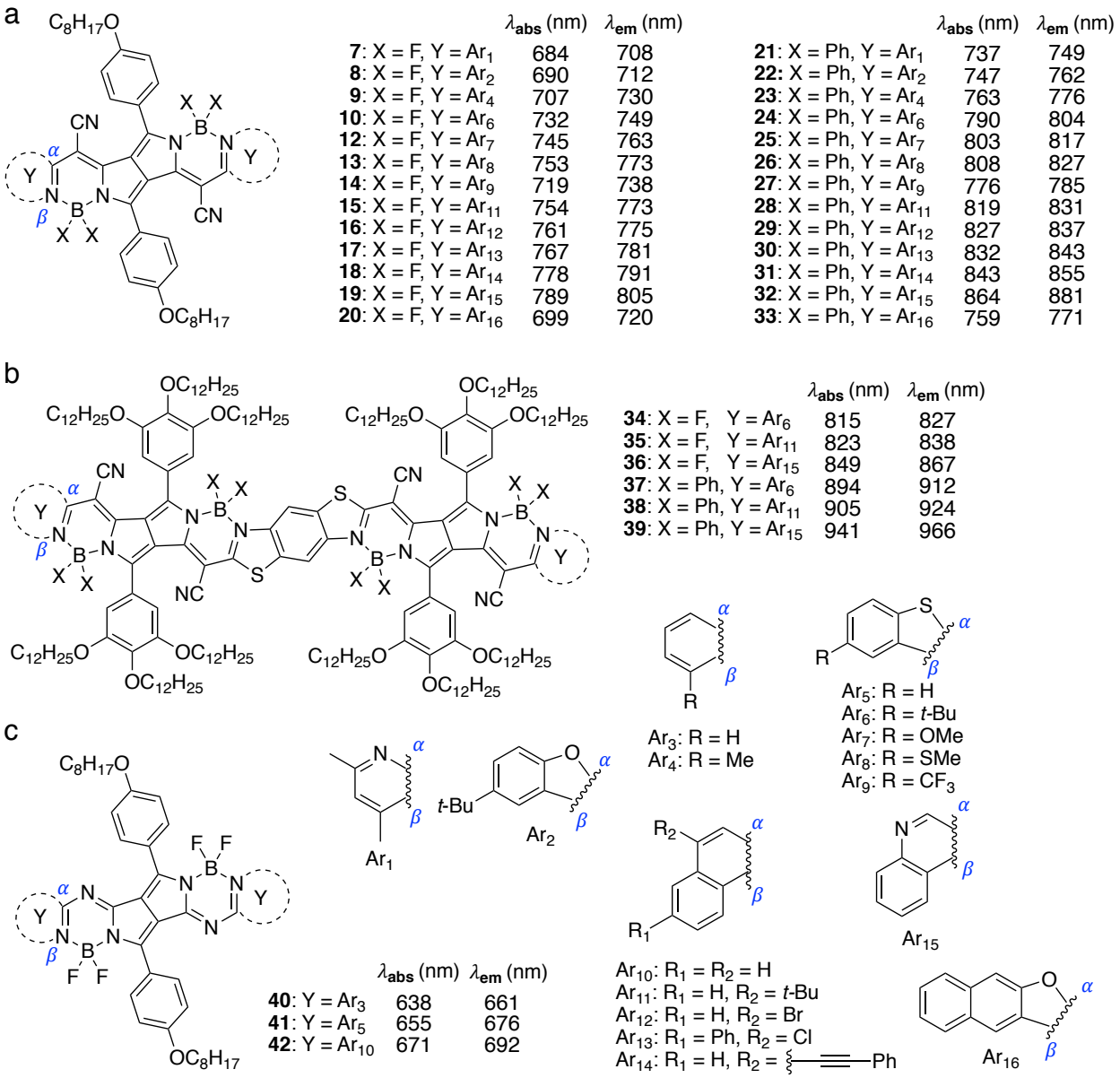


Figure 0-27 Chemical structures of PPCy dyes. (a) Standard PPCys. (b) Further-extended PPCys. (c) PPCy aza-BODIPY analogues.

without affecting emission wavelength, which is advantageous for imaging purpose due to the large Stokes shift (**Figure I-26c**).[326-328]

Polymethine dyes are not restricted to traditional cyanines. Essentially, they are characterized with methine chains of degenerated bond length alternation. Developed by Daltrozzo's and Zumbusch's groups, pyrrolopyrrole (PPCy) is a new class of polymethine dyes. Their pyrrolopyrrole core is an effective cyanine-type mimicry, and is almost exclusively synthesized via the condensation of diketopyrrolopyrroles with α-substituted acetonitriles.[329] PPCys often show sharp emission bands in the NIR region with high extinction coefficients and exceptional fluorescence quantum yields (**Figure I-27a**).[329-333] Their boron chelation between the nitrogen atoms of the pyrrolopyrrole and terminal aryl groups rigidifies the conformation and renders them with excellent light and thermal stability. Further π-extended PPCys fused with benzobisthiazoles have been synthesized and show extremely large extinction coefficients and close to NIR-II emission (**Figure I-27b**).[334] As the boron chelate is structurally similar to BODIPY dyes (*vide infra*), PPCy aza-BODIPY analogues have also been synthesized and exhibit close to NIR-I fluorescence (**Figure I-27c**).[335]

Boron dipyrromethene (BODIPY), or 4,4-difluoro-4-bora-3*a*,4*a*-diaza-*s*-indacene, is one of the most frequently investigated family of fluorescent compounds. With many commercially available BODIPYs, new structural entities are still emerging for both NIR emitting and functional sensing.[336-338] As shown in **Figure I-28a**, BODIPYs can be regarded as a rigid and cross-conjugated cyanines. Being similar in many aspects, they have sharp absorption and emission spectra and usually small Stokes shifts, with a

superior advantage in stability. Although common BODIPYs emit in the visible range, their potential in easy structural modification have stimulated numerous derivatizations at all seven carbons.[339] It is known that the replacement of C8 with a nitrogen atom can effectively red-shift the spectra, possibly because of the higher electron density of

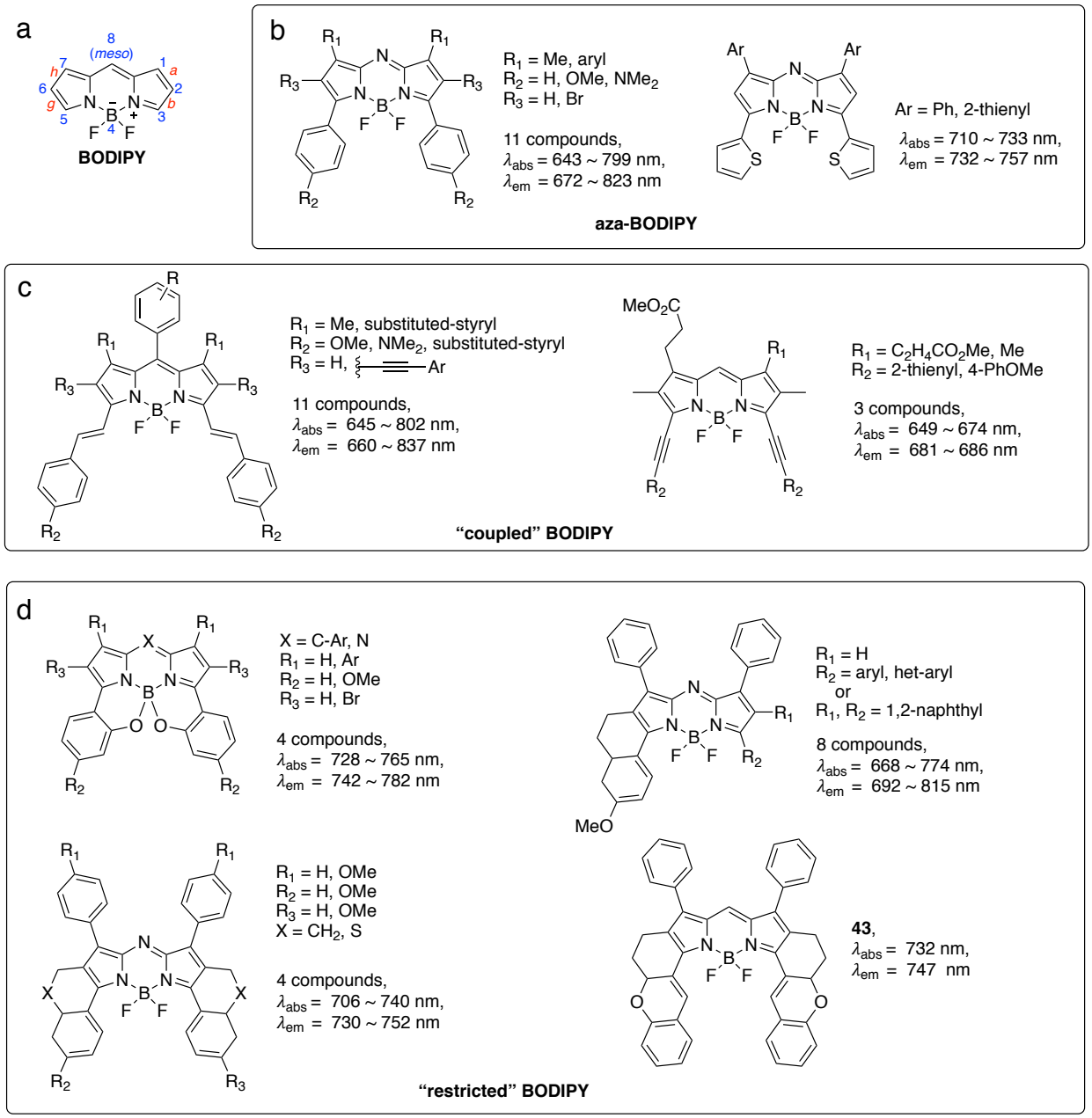


Figure 0-28 NIR BODIPYs. (a) BODIPY framework. (b) aza-BODIPYs. (c) "coupled" BODIPYs. (d) "restricted" BODIPYs.

nitrogen at the *meso* position that facilitates stronger resonance. Recent synthetic advances have allowed further development of these “aza-BODIPYs” with moderate to high QY in the NIR-I region (**Figure I-28b**).[340-343] Another common strategy is to extend the conjugation by coupling multiple aryl groups on the dipyrromethene framework. It has been shown that 3-/5- disubstitution is more impactful than 2-/6- or 1-/7- diarylation (**Figure I-28c**).[344-346] However, these 3,5-diaryl-BODIPYs usually have diminished

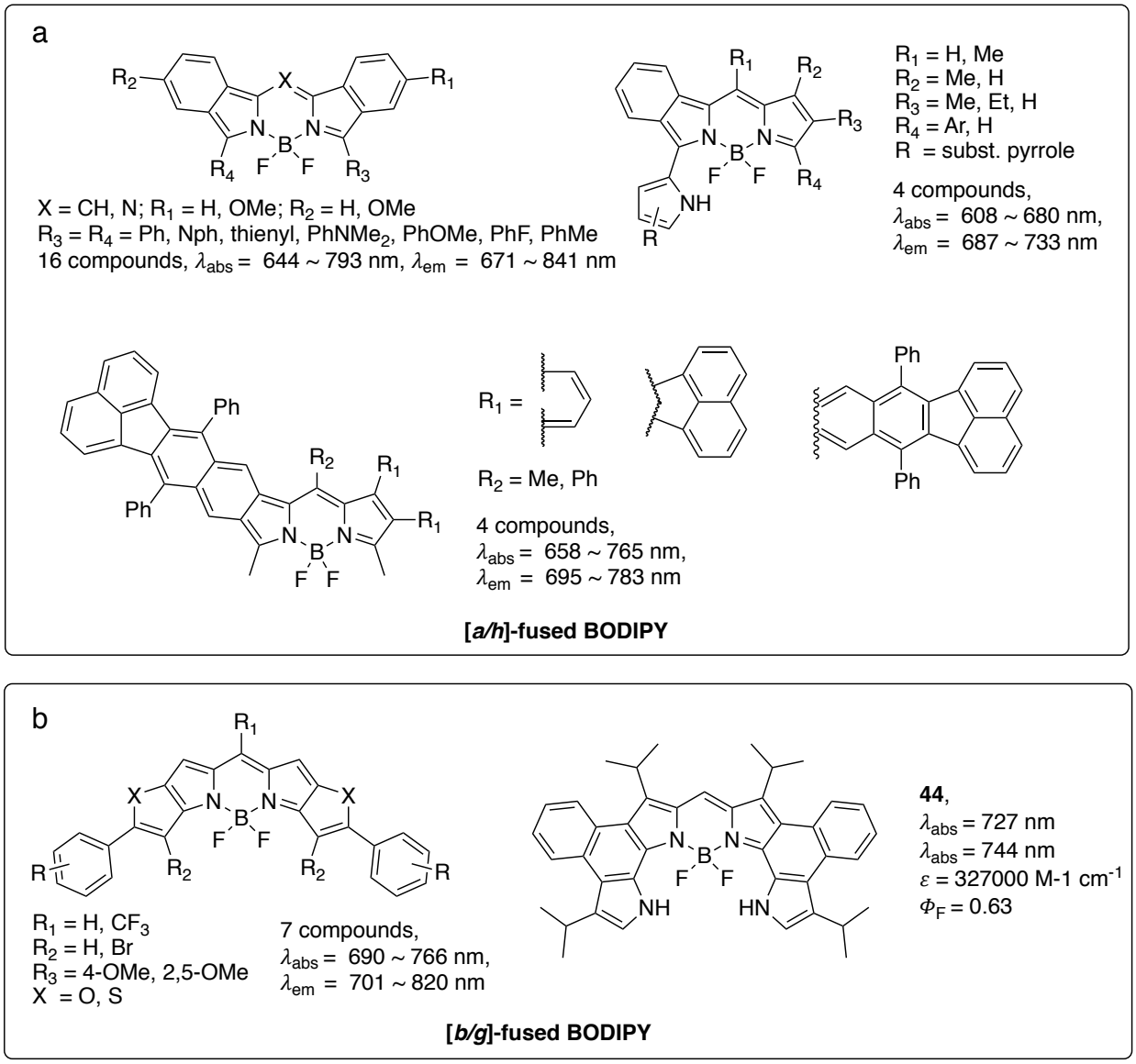


Figure 0-29 NIR ring-fused BODIPYs. (a) [a/h]-fused BODIPYs. (b) [b/g]-fused BODIPYs.

extinction coefficients and quantum yields, probably due to the free rotation of the aryl groups.[347, 348] The facile solution is to increase molecular rigidity by fusing the "coupled" aryl groups to the pyrrole framework (**Figure I-28d**). A bathochromic shift together with slight increase in extinction coefficient was observed when 3,5-diaryl were locked either through chalcogen (e.g., O, S) or ethylene unit.[349] A good example is shown by 3,4,4*a*-trihydroxanthene-fused BODIPY (**43**), which shows over 100 nm bathochromic shift compare to the styryl BODIPY analogue.[350] Difluorides on boron have also been substituted by ortho-phenolates on the coupling aryls to form boronate.[351] The similar "restriction" approach has been applied to aza-BODIPY.[352] Besides the π-extension through position 1-/7- and 3-/5- via rotatable bonds, a prominent and more challenging direction is to build conjugation through [*a*/*h*] or [*b*/*g*] fused aromatic rings.[353-355] The idea is to have π-extension and at the same time to take advantage of BODIPY's high rigidity for high QY. However, the optical properties are usually difficult to estimate due to the unpredictable ring fusion effects. It has been shown that among a vast number of *a/h*- or *b/g*-fused BODIPYs, those with conjugation extended through heterocyclics as furano, pyrrolo, and thieno-fused BODIPYs are the most effective red-shifted ones (**Figure I-29**).[340, 356-362] It is noteworthy to mention that a recently published naphtopyrrole-fused BODIPY (**44**) has shown extraordinary optical properties.[363]

I.4.2.2 Donor-Acceptor NIR dyes

Squaraines are a family of dye transitioning from polymethine type to donor-acceptor type. They have an electron-withdrawing cyclobutanone in the center and two electron-donating groups on the edge, while their resonance-stabilized zwitterionic

structure still presents traits of polymethine.[364] Squaraines have sharp spectra, extremely large extinction coefficient, and high stability.[365] They have been widely used in imaging, nonlinear optics, photovoltaics, and photodynamic therapy.[366] Their inherent strong intramolecular charge transfer character (donor-acceptor-donor sandwich, D-A-D) makes them quite polarity-sensitive. By adding strong electron-donors or extending the π-conjugation, the band gap can be effectively lowered and results in bathochromic shift to

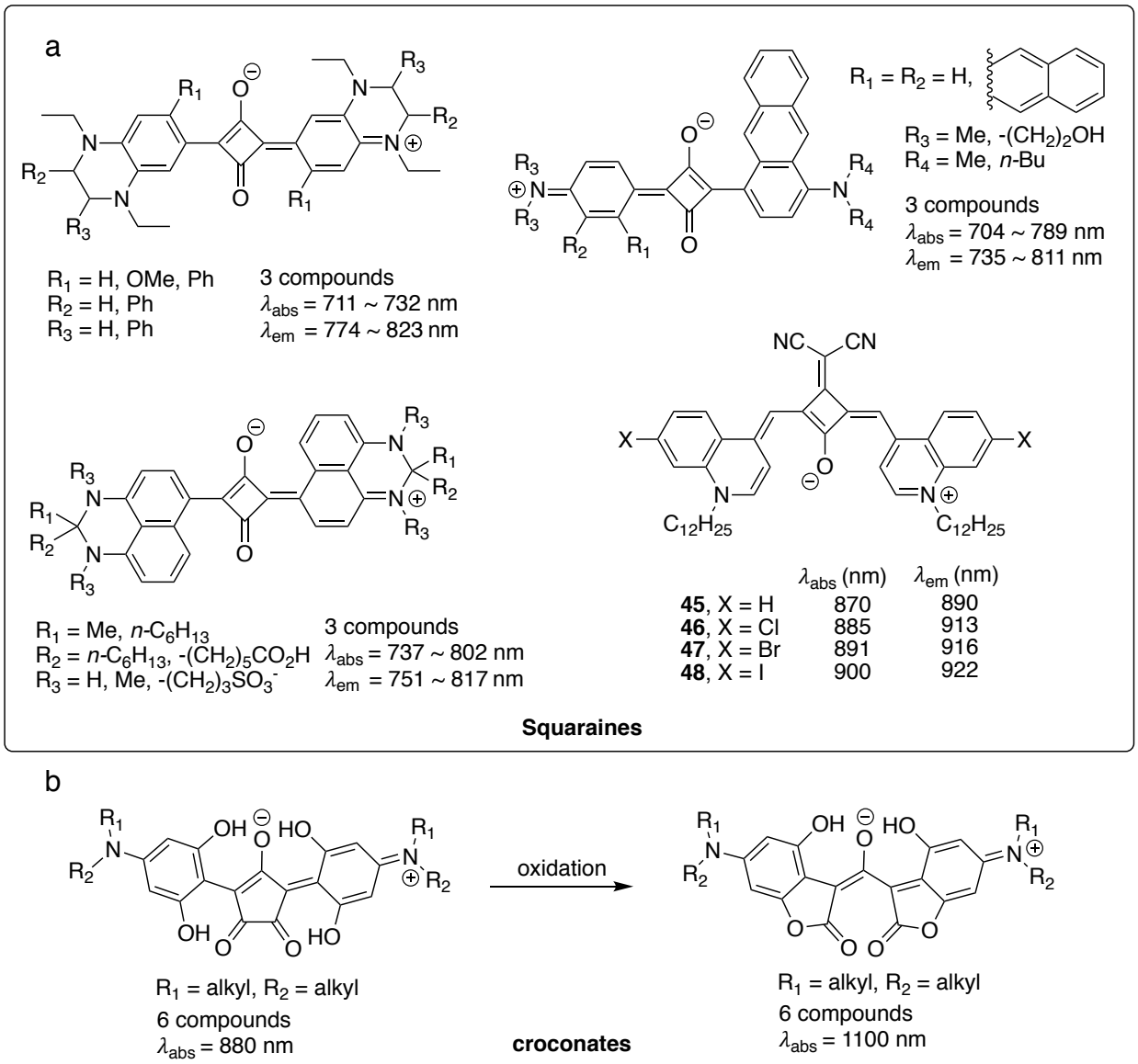


Figure 0-30 (a) NIR fluorescent squaraines. (b) NIR-II absorptive croconates. Scheme shows mesoionic oxidation.

NIR region (**Figure I-30a**).[367] Recent advances in squaraine synthesis have enabled the assembly of various heterocyclic groups on the squaric acid core, including symmetric and asymmetric squaraines.[368-373] An interesting expansion of the zwitterionic core is the croconic acid, which provides an even stronger electron acceptor and hence lowers the band gap more efficiently. Alkyl croconates, albeit not fluorescent, can absorb into NIR-I and are easily red-shifted to 1.1 μm with a mesoionic form after quick oxidation (**Figure I-30b**).[374, 375]

Xanthene is another important type of dye framework with one monomethine bridging two aromatic rings. Commonly seen examples include fluoresceins, pyronins, rhodamines, and the meso-nitrogen derivative resorufins. Except for fluoresceins, these dyes easily reach the far-red region of visible spectrum (e.g. Atto dyes and some of the AlexaFluors).[376] However, although bearing the methine unit and an electron donor-acceptor pair on two sides, the majority of red xanthenes (i.e., rhodamines and pyronines) do not display ICT-type environment sensitivity, with asymmetric resorufins (e.g., Nile red and Nile blue) as the only exceptions. Typically, the spectra of rhodamines are not sensitive towards the aryl group coupling as discussed in the BODIPY case. Currently

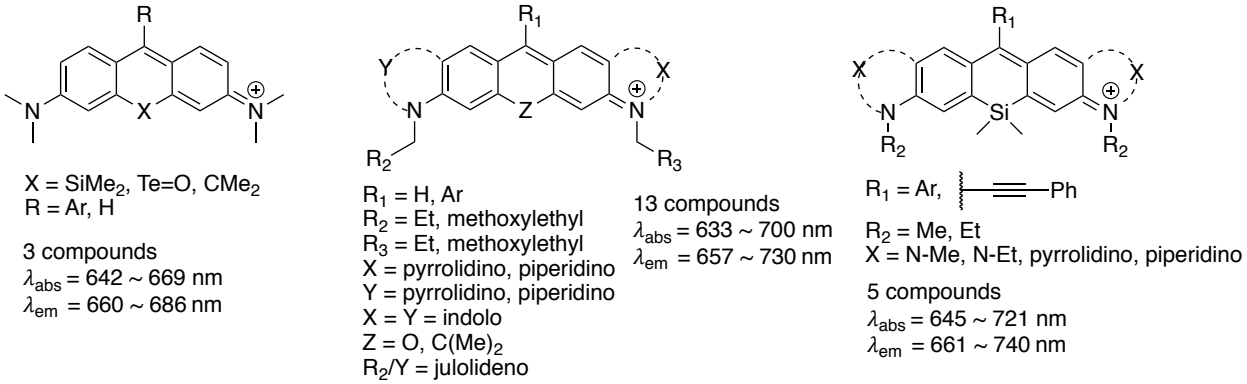


Figure 0-31 Restricted and C10-replaced rhodamines.

applied strategies to induce bathochromic shifts in rhodamines include conformational restrictions on both rings and amine lone pairs, and meso-replacement with the first three rows of group 14, 15 and 16 elements.[377-379] Proper alkylation on the nitrogen atoms will increase the rotational barrier and suppress the twisted intramolecular charge transfer process (TICT) in the excited states, and result in spectral bathochromic shifts.[380] Modifications include fused aliphatic (e.g., pyrrolidine, julolidene) and aromatic rings, nonetheless, with limited improvement in bathochromic shifts. A recent trend in rhodamine and pyronin is to replace C10 with more diffused elements (Si, Ge, Se, Te) and couple with extended π-conjugation to realize NIR emission (**Figure I-31**).[381-387]

It is noteworthy to mention here, though mostly found use in organic optic materials, highly fused poly-heteroaromatics with properly embedded electron donor and acceptor

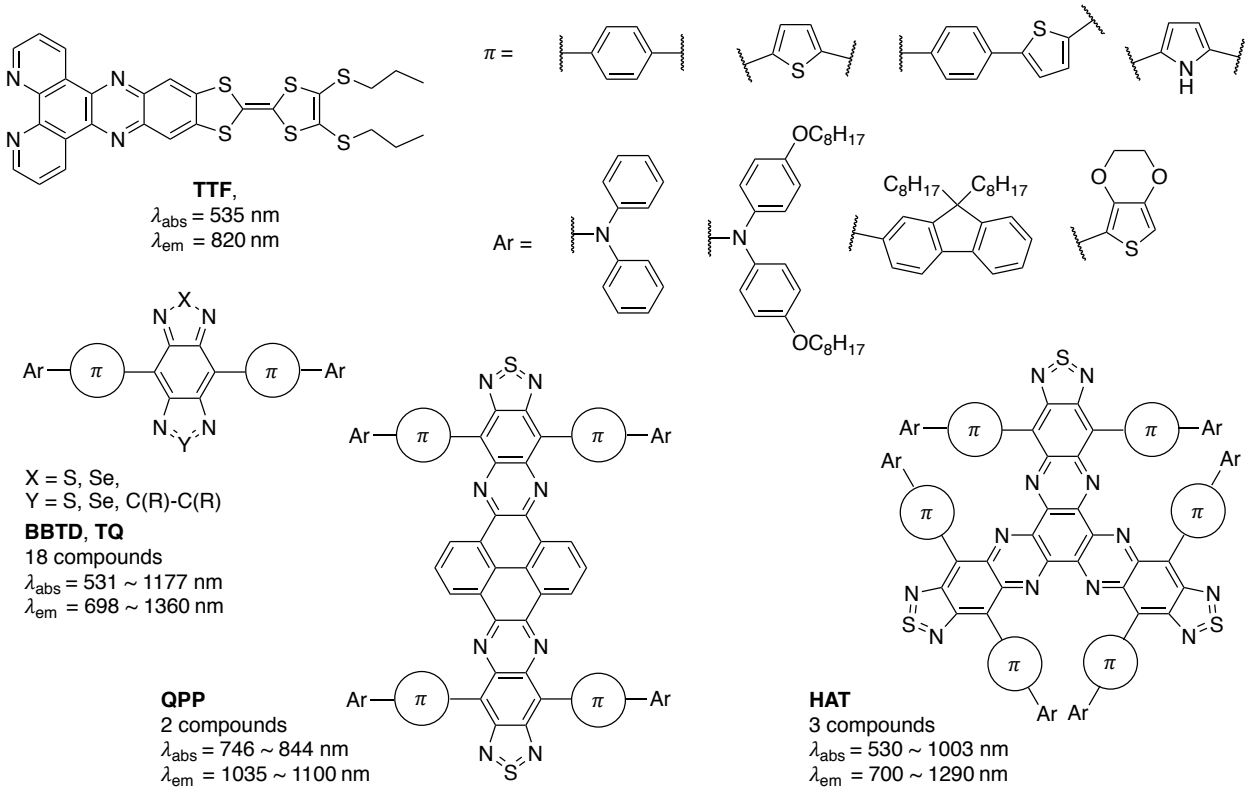


Figure 0-32 Representative NIR D-A-D type of dyes.

moieties have been successfully developed into D-π-A or D-π-A-π-D NIR-I/II dyes. Examples include tetrathiafulvalenes (TTF),[388] benzothiadiazoles (BTD),[389] benzobisthiadiazoles (BBTD) and Se homologues,[390-393] phenothiazines,[394] thiadiazoloquinoxalines (TQ),[395, 396] hexaazatriphenylene (HAT),[397, 398] and quinoxalino[2',3',9,10]phenanthro [4,5-abc]phenazines (QPP).[399] These core frameworks are usually coupled to electron-rich pyrrole, fluorene, thiophene, or diphenylaniline spacers to obtain lengthy resonating system hence low band gaps (**Figure I-32**). Although these dyes are typically large and highly hydrophobic, most recently Dai and coworkers

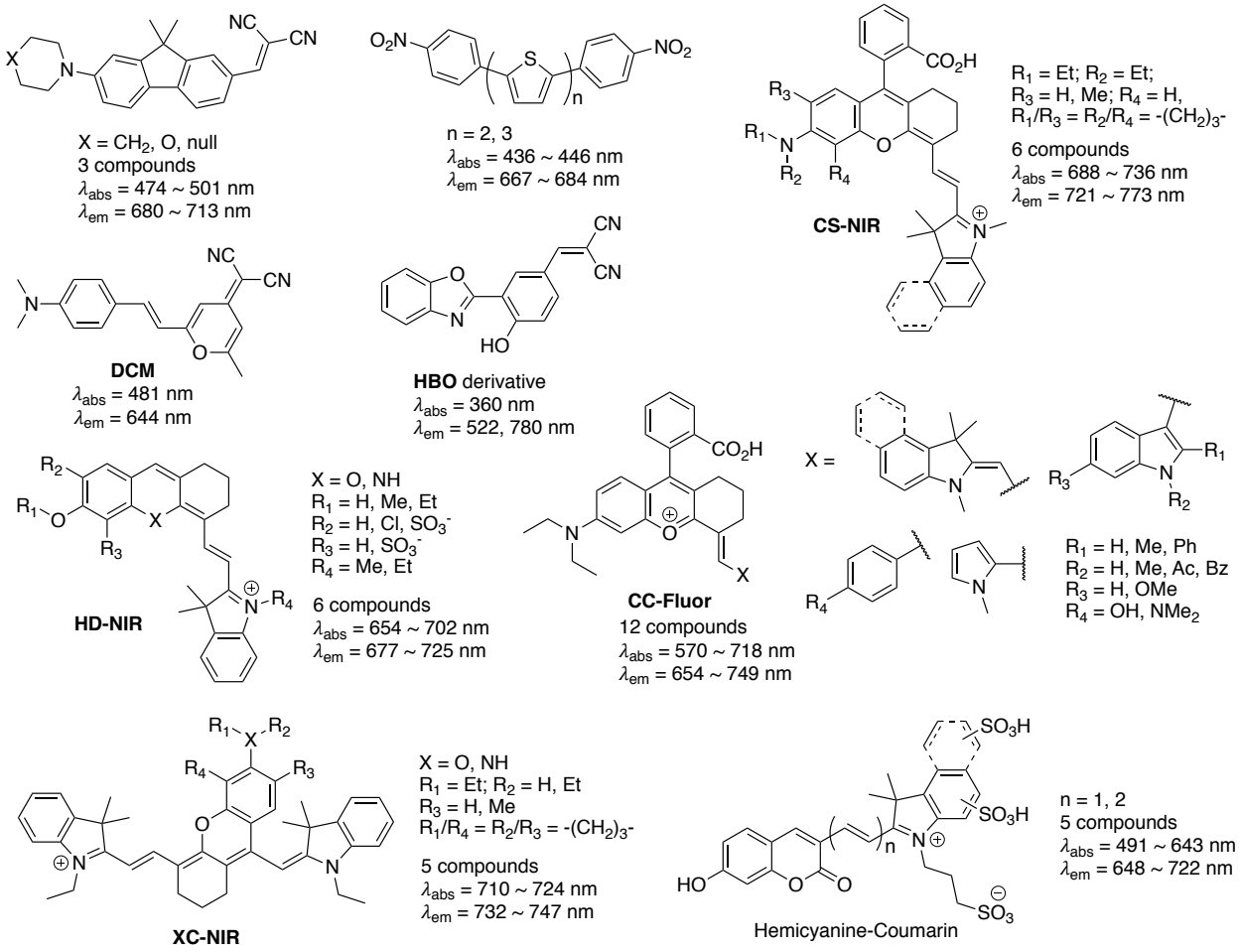


Figure 0-33 Selected ICT dyes and D-A hybrids.

have PEGylated a BBTD dye (CH1055) and successfully achieved micrometer-scale resolution of NIR-II imaging in live mouse.[400]

Donor-acceptor type of interactions are not limited to these gigantic polyheterocyclic dyes, essentially any molecule facilitating ICT process has this band gap lowering feature.[239, 401] Small molecules such as donor-acceptor conjugated fluorenes and oligothiophenes have shown great bathochromic shift to NIR-I edge in responding to environment polarity change.[402, 403] Recently, the old laser dye dicyanomethylene-4*H*-pyran (DCM) has drawn much attention for NIR applications.[79, 404-406] Another widely applied design is to couple two red dyes together to install D-A interaction. For instance, 2-(2'-hydroxyphenyl)-benzoxazole (HBO) has been coupled to a dicyanovinylene fragment to realize two well-separated emission maxima, with one into the NIR region that features a characteristic proton transfer event of the phenol in the excited state.[407]

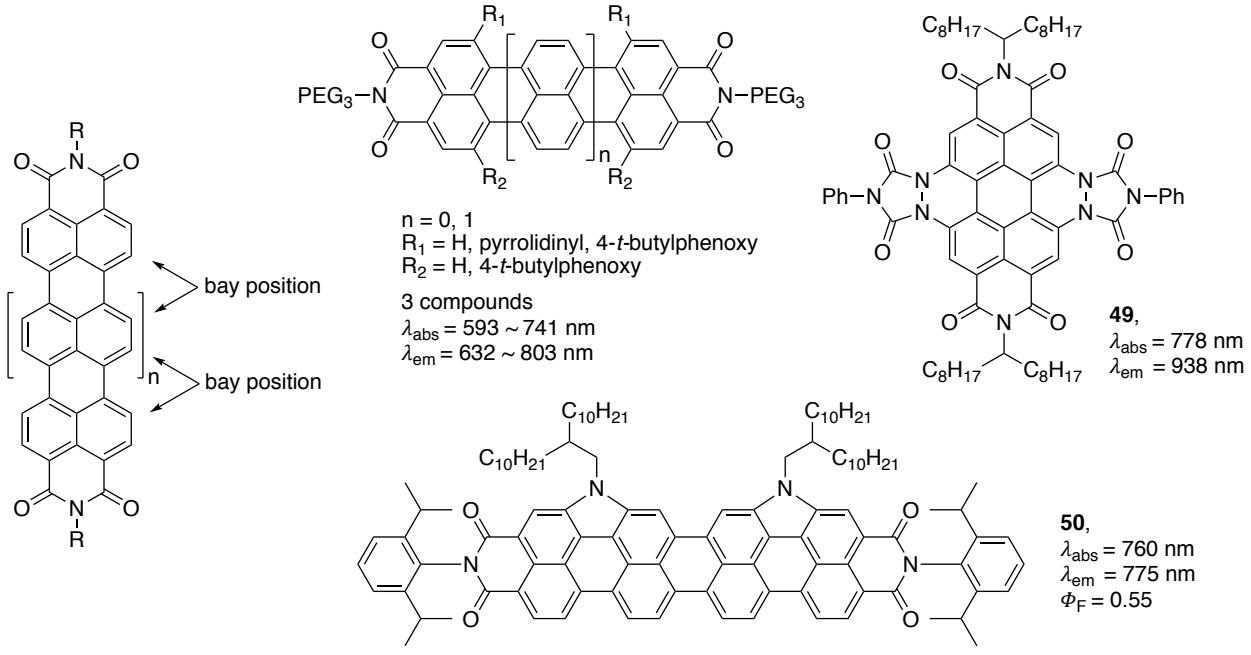


Figure 0-34 Selected NIR rylenes.

Other examples include indocyanine-coupled xanthene and coumarin dyes (**Figure I-33**).[408-412]

I.4.2.3 Other NIR dyes

Polyenes can also be pushed into NIR region simply by extending conjugation, though the wavelength shift is not as significant as polymethine dyes (see **I.4.2.1**) with increasing number of π-spacers. Rylenes are a family of rigid polymeric naphthalenes coupled through α-carbons. The diimides at the terminals consist of a pull-pull system. NIR-I emission can be easily approached with the installment of multiple naphthalene units ($n \geqq 2$).[413, 414] Another strategy to effectively lower the band gap is by inserting donor groups at the bay position without lengthy extensions (**Figure I-34**).[415] It has been shown recently that an asymmetric donor installed at the long axis yields a quarterrylene (**50**) with large extinction coefficient (259,540 M^{-1} cm^{-1}) and excellent quantum yield (0.55 at 775 nm).[416]

Structured as conjugate close-ring polypyrroles, porphyrinoids are receiving attention as a new type NIR emitter. Common core structures of porphyrinoids include porphyrin, phthalocyanine, and expanded ones such as hexaphyrin and rubyrin (**Figure I-35**).[417] These polycyclics usually have very bathochromic spectra extending into the NIR

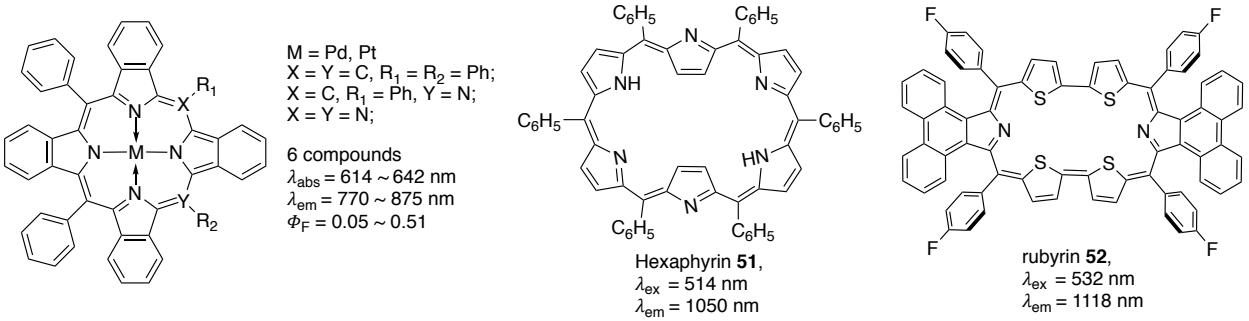


Figure 0-35 Selected NIR porphyrinoids.

region. One certain advantage of porphyrinoids is that they can be excited at their short-wavelength Soret bands (λ_{abs} = 500 ~ 600 nm) and emit into NIR-II region. Their fluorescence intensity is usually affected by metal-ligand charge transfer (MLCT) when they complex with transition metals. This feature has been extensively exploited in designing NIR metal sensors.[418, 419] The most common metals are palladium and platinum.[420] Not limited to these two, other close-shell and open-shell metals can also form complexes and more often result in NIR phosphorescence. A more detailed discussion is not fitting the scope here; the reader is directed to Armaroli's recent review.[421]

As a closing remark, it is noteworthy to point out that the approaches to NIR emission should not be limited to intramolecular π-electron dispersion. A rising field is the aggregation-induced emission (AIE).[422] Using the iconic AIEgen tetraphenylene (TPE) as an example, the aggregation stops the free rotations of the phenyl groups and strong emission occurs due to the suppressed nonradiative decay. TPE can be easily modified to couple with a dicyanovinylene acceptor through a thiophene spacer, which results in a significant bathochromic shift in TPE emission (**53**, **Figure I-36a**).[423] Alternatively, red fluorophores can be engineered into AIEgens such that the band gap is further lowered

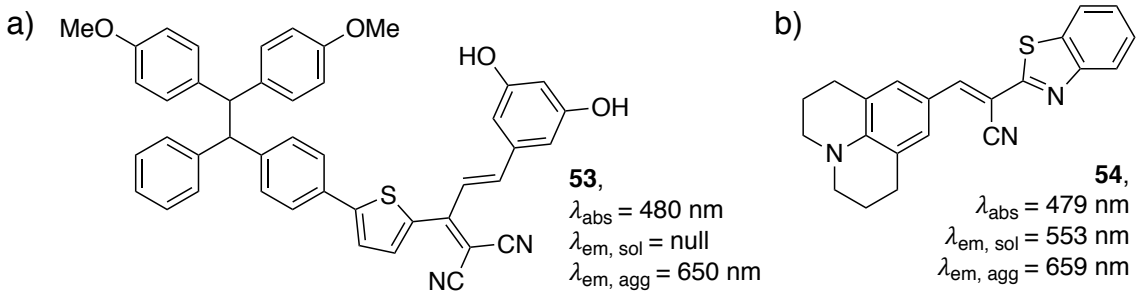


Figure 0-36 Examples of NIR AIEgen. (a) Red-shifted TPE emission by extended conjugation. (b) Aggregation-induced bathochromic shift in emission.

by excimer-induced intermolecular π-electron dispersion, hence realizing NIR emission (**54**, **Figure I-36b**).[424]

REFERENCES

REFERENCES

1. Hooke, R. *Micrographia: or some physiological descriptions of minute bodies made by magnifying glasses with observations and inquiries thereupon.* (Royal Society; London; **1665**).

2. Prasher, D.C., Eckenrode, V.K., Ward, W.W., Prendergast, F.G. & Cormier, M.J. Primary structure of the Aequorea victoria green-fluorescent protein. *Gene* **1992**, 111, 229-233.

3. Chalfie, M., Tu, Y., Euskirchen, G., Ward, W. & Prasher, D. Green fluorescent protein as a marker for gene expression. *Science* **1994**, 263, 802-805.

4. Matz, M.V. et al. Fluorescent proteins from nonbioluminescent Anthozoa species. *Nat. Biotechnol.* **1999**, 17, 969-973.

5. Newman, R.H., Fosbrink, M.D. & Zhang, J. Genetically encodable fluorescent biosensors for tracking signaling dynamics in living cells. *Chem. Rev.* **2011**, 111, 3614-3666.

6. Subach, O.M., Cranfill, P.J., Davidson, M.W. & Verkhusha, V.V. An enhanced monomeric blue fluorescent protein with the high chemical stability of the chromophore. *PLoS One* **2011**, 6, e28674.

7. Dedecker, P., De Schryver, F.C. & Hofkens, J. Fluorescent proteins: shine on, you crazy diamond. *J. Am. Chem. Soc.* **2013**, 135, 2387-2402.

8. Wilson, T. & Hastings, J.W. Bioluminescence. *Annu. Rev. Cell Dev. Biol.* **1998**, 14, 197-230.

9. Zimmer, M. Green Fluorescent Protein (GFP): Applications, Structure, and Related Photophysical Behavior. *Chem. Rev.* **2002**, 102, 759-782.

10. Heim, R., Prasher, D.C. & Tsien, R.Y. Wavelength mutations and posttranslational autoxidation of green fluorescent protein. *Proc. Natl. Acad. Sci. U. S. A.* **1994**, 91, 12501-12504.

11. Zhang, L., Patel, H.N., Lappe, J.W. & Wachter, R.M. Reaction progress of chromophore biogenesis in green fluorescent protein. *J. Am. Chem. Soc.* **2006**, 128, 4766-4772.

12. Barondeau, D.P., Putnam, C.D., Kassmann, C.J., Tainer, J.A. & Getzoff, E.D. Mechanism and energetics of green fluorescent protein chromophore synthesis

revealed by trapped intermediate structures. *Proc. Natl. Acad. Sci. U. S. A.* **2003**, 100, 12111-12116.

13. Sniegowski, J.A., Lappe, J.W., Patel, H.N., Huffman, H.A. & Wachter, R.M. Base catalysis of chromophore formation in Arg96 and Glu222 variants of green fluorescent protein. *J. Biol. Chem.* **2005**, 280, 26248-26255.

14. Sniegowski, J.A., Phail, M.E. & Wachter, R.M. Maturation efficiency, trypsin sensitivity, and optical properties of Arg96, Glu222, and Gly67 variants of green fluorescent protein. *Biochem. Biophys. Res. Commun.* **2005**, 332, 657-663.

15. Shagin, D.A. et al. GFP-like proteins as ubiquitous metazoan superfamily: evolution of functional features and structural complexity. *Mol. Biol. Evol.* **2004**, 21, 841-850.

16. Labas, Y.A. et al. Diversity and evolution of the green fluorescent protein family. *Proc. Natl. Acad. Sci. U. S. A.* **2002**, 99, 4256-4261.

17. Chudakov, D.M., Matz, M.V., Lukyanov, S. & Lukyanov, K.A. Fluorescent proteins and their applications in imaging living cells and tissues. *Physiol. Rev.* **2010**, 90, 1103-1163.

18. Verkhusha, V.V. & Lukyanov, K.A. The molecular properties and applications of Anthozoa fluorescent proteins and chromoproteins. *Nat. Biotechnol.* **2004**, 22, 289-296.

19. Subach, F.V., Piatkevich, K.D. & Verkhusha, V.V. Directed molecular evolution to design advanced red fluorescent proteins. *Nat. Methods* **2011**, 8, 1019-1026.

20. Subach, F.V. & Verkhusha, V.V. Chromophore transformations in red fluorescent proteins. *Chem. Rev.* **2012**, 112, 4308-4327.

21. Strack, R.L., Strongin, D.E., Mets, L., Glick, B.S. & Keenan, R.J. Chromophore formation in DsRed occurs by a branched pathway. *J. Am. Chem. Soc.* **2010**, 132, 8496-8505.

22. Subach, O.M. et al. Structural characterization of acylimine-containing blue and red chromophores in mTagBFP and TagRFP fluorescent proteins. *Chem. Biol.* **2010**, 17, 333-341.

23. Pakhomov, A.A. & Martynov, V.I. Chromophore aspartate oxidation-decarboxylation in the green-to-red conversion of a fluorescent protein from Zoanthus sp. 2. *Biochemistry* **2007**, 46, 11528-11535.

24. Quillin, M.L. et al. Kindling fluorescent protein from Anemonia sulcata: dark-state structure at 1.38 A resolution. *Biochemistry* **2005**, 44, 5774-5787.

25. Gurskaya, N.G., Savitsky, A.P., Yanushevich, Y.G., Lukyanov, S.A. & Lukyanov, K.A. Color transitions in coral's fluorescent proteins by site-directed mutagenesis. *BMC Biochem.* **2001**, 2, 6.

26. Remington, S.J. et al. zFP538, a yellow-fluorescent protein from Zoanthus, contains a novel three-ring chromophore. *Biochemistry* **2005**, 44, 202-212.

27. Pletneva, N.V. et al. Three-dimensional structure of yellow fluorescent protein zYFP538 from Zoanthus sp. at the resolution 1.8 Å. *Russ. J. Bioorg. Chem.* **2007**, 33, 390-398.

28. Karasawa, S., Araki, T., Nagai, T., Mizuno, H. & Miyawaki, A. Cyan-emitting and orange-emitting fluorescent proteins as a donor/acceptor pair for fluorescence resonance energy transfer. *Biochem. J* **2004**, 381, 307-312.

29. Kikuchi, A. et al. Structural characterization of a thiazoline-containing chromophore in an orange fluorescent protein, monomeric Kusabira Orange. *Biochemistry* **2008**, 47, 11573-11580.

30. Mizuno, H. et al. Photo-induced peptide cleavage in the green-to-red conversion of a fluorescent protein. *Mol. Cell.* **2003**, 12, 1051-1058.

31. Ormo, M. et al. Crystal structure of the Aequorea victoria green fluorescent protein. *Science* **1996**, 273, 1392-1395.

32. Tomosugi, W. et al. An ultramarine fluorescent protein with increased photostability and pH insensitivity. *Nat. Methods* **2009**, 6, 351-353.

33. Mena, M.A., Treynor, T.P., Mayo, S.L. & Daugherty, P.S. Blue fluorescent proteins with enhanced brightness and photostability from a structurally targeted library. *Nat. Biotechnol.* **2006**, 24, 1569-1571.

34. Ai, H.W., Shaner, N.C., Cheng, Z., Tsien, R.Y. & Campbell, R.E. Exploration of new chromophore structures leads to the identification of improved blue fluorescent proteins. *Biochemistry* **2007**, 46, 5904-5910.

35. Subach, O.M. et al. Conversion of red fluorescent protein into a bright blue probe. *Chem. Biol.* **2008**, 15, 1116-1124.

36. Rizzo, M.A., Springer, G.H., Granada, B. & Piston, D.W. An improved cyan fluorescent protein variant useful for FRET. *Nat. Biotechnol.* **2004**, 22, 445-449.

37. Goedhart, J. et al. Bright cyan fluorescent protein variants identified by fluorescence lifetime screening. *Nat. Methods* **2010**, 7, 137-139.

38. Markwardt, M.L. et al. An improved cerulean fluorescent protein with enhanced brightness and reduced reversible photoswitching. *PLoS One* **2011**, 6, e17896.

39. Yang, T.T., Cheng, L. & Kain, S.R. Optimized codon usage and chromophore mutations provide enhanced sensitivity with the green fluorescent protein. *Nucleic Acids Res.* **1996**, 24, 4592-4593.

40. Cubitt, A.B., Woollenweber, L.A. & Heim, R. in Chapter 2: Understanding Structure—Function Relationships in the Aequorea victoria Green Fluorescent Protein. *Green Fluorescent Proteins*. Methods in Cell Biology. Vol. 58. (eds. K.F. Sullivan & S.A. Kay), 19-30 (Academic Press; **1998**).

41. Evdokimov, A.G. et al. Structural basis for the fast maturation of Arthropoda green fluorescent protein. *EMBO Rep.* **2006**, 7, 1006-1012.

42. Sarkisyan, K.S. et al. Green fluorescent protein with anionic tryptophan-based chromophore and long fluorescence lifetime. *Biophys. J.* **2015**, 109, 380-389.

43. Nagai, T. et al. A variant of yellow fluorescent protein with fast and efficient maturation for cell-biological applications. *Nat. Biotechnol.* **2002**, 20, 87-90.

44. Kremers, G.J., Goedhart, J., van Munster, E.B. & Gadella, T.W., Jr. Cyan and yellow super fluorescent proteins with improved brightness, protein folding, and FRET Forster radius. *Biochemistry* **2006**, 45, 6570-6580.

45. Hoi, H. et al. An engineered monomeric Zoanthus sp. yellow fluorescent protein. *Chem. Biol.* **2013**, 20, 1296-1304.

46. Shaner, N.C. et al. Improved monomeric red, orange and yellow fluorescent proteins derived from Discosoma sp. red fluorescent protein. *Nat. Biotechnol.* **2004**, 22, 1567-1572.

47. Merzlyak, E.M. et al. Bright monomeric red fluorescent protein with an extended fluorescence lifetime. *Nat. Methods* **2007**, 4, 555-557.

48. Kredel, S. et al. mRuby, a bright monomeric red fluorescent protein for labeling of subcellular structures. *PLoS One* **2009**, 4, e4391.

49. Bindels, D.S. et al. mScarlet: a bright monomeric red fluorescent protein for cellular imaging. *Nat. Methods* **2017**, 14, 53-56.

50. Wang, L., Jackson, W.C., Steinbach, P.A. & Tsien, R.Y. Evolution of new nonantibody proteins via iterative somatic hypermutation. *Proc. Natl. Acad. Sci. U. S. A.* **2004**, 101, 16745-16749.

51. Lin, M.Z. et al. Autofluorescent proteins with excitation in the optical window for intravital imaging in mammals. *Chem. Biol.* **2009**, 16, 1169-1179.

52. Shcherbo, D. et al. Far-red fluorescent tags for protein imaging in living tissues. *Biochem. J* **2009**, 418, 567-574.

53. Shcherbo, D. et al. Near-infrared fluorescent proteins. *Nat. Methods* **2010**, 7, 827-829.

54. Shcherbakova, D.M. & Verkhusha, V.V. Near-infrared fluorescent proteins for multicolor in vivo imaging. *Nat. Methods* **2013**, 10, 751-754.

55. Yu, D. et al. An improved monomeric infrared fluorescent protein for neuronal and tumour brain imaging. *Nat. Commun.* **2014**, 5, 3626.

56. Rumyantsev, K.A. et al. Minimal domain of bacterial phytochrome required for chromophore binding and fluorescence. *Sci. Rep.* **2015**, 5, 18348.

57. Zapata-Hommer, O. & Griesbeck, O. Efficiently folding and circularly permuted variants of the Sapphire mutant of GFP. *BMC Biotechnol.* **2003**, 3, 5.

58. Kogure, T. et al. A fluorescent variant of a protein from the stony coral Montipora facilitates dual-color single-laser fluorescence cross-correlation spectroscopy. *Nat. Biotechnol.* **2006**, 24, 577-581.

59. Piatkevich, K.D. et al. Monomeric red fluorescent proteins with a large Stokes shift. *Proc. Natl. Acad. Sci. U. S. A.* **2010**, 107, 5369-5374.

60. Piatkevich, K.D., Malashkevich, V.N., Almo, S.C. & Verkhusha, V.V. Engineering ESPT pathways based on structural analysis of LSSmKate red fluorescent proteins with large Stokes shift. *J. Am. Chem. Soc.* **2010**, 132, 10762-10770.

61. Shcherbakova, D.M., Hink, M.A., Joosen, L., Gadella, T.W. & Verkhusha, V.V. An orange fluorescent protein with a large Stokes shift for single-excitation multicolor FCCS and FRET imaging. *J. Am. Chem. Soc.* **2012**, 134, 7913-7923.

62. Yang, J. et al. mBeRFP, an improved large stokes shift red fluorescent protein. *PLoS One* **2013**, 8, e64849.

63. Chu, J. et al. A bright cyan-excitable orange fluorescent protein facilitates dual-emission microscopy and enhances bioluminescence imaging in vivo. *Nat. Biotechnol.* **2016**, 34, 760-767.

64. Ghosh, S. et al. Blue protein with red fluorescence. *Proc. Natl. Acad. Sci. U. S. A.* **2016**, 113, 11513-11518.

65. Patterson, G.H. & Lippincott-Schwartz, J. A photoactivatable GFP for selective photolabeling of proteins and cells. *Science* **2002**, 297, 1873-1877.

66. Grotjohann, T. et al. Diffraction-unlimited all-optical imaging and writing with a photochromic GFP. *Nature* **2011**, 478, 204-208.

67. Gurskaya, N.G. et al. Engineering of a monomeric green-to-red photoactivatable fluorescent protein induced by blue light. *Nat. Biotechnol.* **2006**, 24, 461-465.

68. McKinney, S.A., Murphy, C.S., Hazelwood, K.L., Davidson, M.W. & Looger, L.L. A bright and photostable photoconvertible fluorescent protein. *Nat. Methods* **2009**, 6, 131-133.

69. McEvoy, A.L. et al. mMaple: a photoconvertible fluorescent protein for use in multiple imaging modalities. *PLoS One* **2012**, 7, e51314.

70. Ando, R., Mizuno, H. & Miyawaki, A. Regulated fast nucleocytoplasmic shuttling observed by reversible protein highlighting. *Science* **2004**, 306, 1370-1373.

71. Andresen, M. et al. Photoswitchable fluorescent proteins enable monochromatic multilabel imaging and dual color fluorescence nanoscopy. *Nat. Biotechnol.* **2008**, 26, 1035-1040.

72. Brakemann, T. et al. A reversibly photoswitchable GFP-like protein with fluorescence excitation decoupled from switching. *Nat. Biotechnol.* **2011**, 29, 942-947.

73. Tiwari, D.K. et al. A fast- and positively photoswitchable fluorescent protein for ultralow-laser-power RESOLFT nanoscopy. *Nat. Methods* **2015**, 12, 515-518.

74. Acharya, A. et al. Photoinduced Chemistry in Fluorescent Proteins: Curse or Blessing? *Chem. Rev.* **2017**, 117, 758-795.

75. Zhang, J., Campbell, R.E., Ting, A.Y. & Tsien, R.Y. Creating new fluorescent probes for cell biology. *Nat. Rev. Mol. Cell Biol.* **2002**, 3, 906-918.

76. Shaner, N.C., Steinbach, P.A. & Tsien, R.Y. A guide to choosing fluorescent proteins. *Nat. Methods* **2005**, 2, 905-909.

77. Megason, S.G. & Fraser, S.E. Imaging in systems biology. *Cell* **2007**, 130, 784-795.

78. Balla, T. Green light to illuminate signal transduction events. *Trends Cell Biol.* **2009**, 19, 575-586.

79. Wu, X. et al. In vivo and in situ tracking cancer chemotherapy by highly photostable NIR fluorescent theranostic prodrug. *J. Am. Chem. Soc.* **2014**, 136, 3579-3588.

80. Chen, Z. et al. Highly accurate fluorogenic DNA sequencing with information theory-based error correction. *Nat. Biotechnol.* **2017**, 35, 1170-1178.

81. Houtsmuller, A.B. in Fluorescence Recovery after Photobleaching: Application to Nuclear Proteins. *Microscopy Techniques*. (ed. J. Rietdorf), 177-199 (Springer Berlin Heidelberg; Berlin, Heidelberg; **2005**).

82. Fritzsche, M. & Charras, G. Dissecting protein reaction dynamics in living cells by fluorescence recovery after photobleaching. *Nat. Protoc.* **2015**, 10, 660-680.

83. Lippincott-Schwartz, J., Altan-Bonnet, N. & Patterson, G.H. Photobleaching and photoactivation: following protein dynamics in living cells. *Nat. Cell Biol.* **2003**, Suppl, S7-14.

84. Dunn, G.A., Dobbie, I.M., Monypenny, J., Holt, M.R. & Zicha, D. Fluorescence localization after photobleaching (FLAP): a new method for studying protein dynamics in living cells. *J. Microsc.* **2002**, 205, 109-112.

85. Ishikawa-Ankerhold, H.C., Ankerhold, R. & Drummen, G.P.C. Advanced Fluorescence Microscopy Techniques—FRAP, FLIP, FLAP, FRET and FLIM. *Molecules* **2012**, 17, 4047-4132.

86. Terskikh, A. "Fluorescent Timer": Protein That Changes Color with Time. *Science* **2000**, 290, 1585-1588.

87. Subach, F.V. et al. Monomeric fluorescent timers that change color from blue to red report on cellular trafficking. *Nat. Chem. Biol.* **2009**, 5, 118-126.

88. Förster, T. Zwischenmolekulare Energiewanderung und Fluoreszenz. *Ann. Phys.* **1948**, 437, 55-75.

89. Miyawaki, A. et al. Fluorescent indicators for Ca2+ based on green fluorescent proteins and calmodulin. *Nature* **1997**, 388, 882-887.

90. Piston, D.W. & Kremers, G.J. Fluorescent protein FRET: the good, the bad and the ugly. *Trends Biochem. Sci* **2007**, 32, 407-414.

91. Van Munster, E.B. & Gadella, T.W., Jr. ϕFLIM: a new method to avoid aliasing in frequency-domain fluorescence lifetime imaging microscopy. *J. Microsc.* **2004**, 213, 29-38.

92. Kim, S.A., Heinze, K.G., Waxham, M.N. & Schwille, P. Intracellular calmodulin availability accessed with two-photon cross-correlation. *Proc. Natl. Acad. Sci. U. S. A.* **2004**, 101, 105-110.

93. Baudendistel, N., Muller, G., Waldeck, W., Angel, P. & Langowski, J. Two-hybrid fluorescence cross-correlation spectroscopy detects protein-protein interactions in vivo. *ChemPhysChem* **2005**, 6, 984-990.

94. Bacia, K., Kim, S.A. & Schwille, P. Fluorescence cross-correlation spectroscopy in living cells. *Nat. Methods* **2006**, 3, 83-89.

95. Mo, G.C.H. et al. Genetically encoded biosensors for visualizing live-cell biochemical activity at super-resolution. *Nat. Methods* **2017**, 14, 427-434.

96. Kerppola, T.K. Visualization of molecular interactions by fluorescence complementation. *Nat. Rev. Mol. Cell Biol.* **2006**, 7, 449-456.

97. Kerppola, T.K. Design and implementation of bimolecular fluorescence complementation (BiFC) assays for the visualization of protein interactions in living cells. *Nat. Protoc.* **2006**, 1, 1278-1286.

98. Michnick, S.W., Ear, P.H., Manderson, E.N., Remy, I. & Stefan, E. Universal strategies in research and drug discovery based on protein-fragment complementation assays. *Nat. Rev. Drug Discovery* **2007**, 6, 569-582.

99. Morell, M., Espargaro, A., Aviles, F.X. & Ventura, S. Study and selection of in vivo protein interactions by coupling bimolecular fluorescence complementation and flow cytometry. *Nat. Protoc.* **2008**, 3, 22-33.

100. Hanson, G.T. et al. Green Fluorescent Protein Variants as Ratiometric Dual Emission pH Sensors. 1. Structural Characterization and Preliminary Application†. *Biochemistry* **2002**, 41, 15477-15488.

101. McAnaney, T.B., Park, E.S., Hanson, G.T., Remington, S.J. & Boxer, S.G. Green Fluorescent Protein Variants as Ratiometric Dual Emission pH Sensors. 2. Excited-State Dynamics. *Biochemistry* **2002**, 41, 15489-15494.

102. Bizzarri, R. et al. Development of a novel GFP-based ratiometric excitation and emission pH indicator for intracellular studies. *Biophys. J.* **2006**, 90, 3300-3314.

103. Bagar, T., Altenbach, K., Read, N.D. & Bencina, M. Live-Cell imaging and measurement of intracellular pH in filamentous fungi using a genetically encoded ratiometric probe. *Eukaryot. Cell* **2009**, 8, 703-712.

104. Zhang, X. et al. Highly photostable, reversibly photoswitchable fluorescent protein with high contrast ratio for live-cell superresolution microscopy. *Proc. Natl. Acad. Sci. U. S. A.* **2016**, 113, 10364-10369.

105. Tao, R. et al. Genetically encoded fluorescent sensors reveal dynamic regulation of NADPH metabolism. *Nat. Methods* **2017**, 14, 720-728.

106. Chan, J., Dodani, S.C. & Chang, C.J. Reaction-based small-molecule fluorescent probes for chemoselective bioimaging. *Nat. Chem.* **2012**, 4, 973-984.

107. Mohr, G.J. Chromo- and fluororeactands: indicators for detection of neutral analytes by using reversible covalent-bond chemistry. *Chem. Eur. J.* **2004**, 10, 1082-1090.

108. Wu, J. et al. Chromogenic/Fluorogenic Ensemble Chemosensing Systems. *Chem. Rev.* **2015**, 115, 7893-7943.

109. You, L., Zha, D. & Anslyn, E.V. Recent Advances in Supramolecular Analytical Chemistry Using Optical Sensing. *Chem. Rev.* **2015**, 115, 7840-7892.

110. Hettie, K.S., Klockow, J.L. & Glass, T.E. Three-input logic gates with potential applications for neuronal imaging. *J. Am. Chem. Soc.* **2014**, 136, 4877-4880.

111. Hammers, M.D. et al. A Bright Fluorescent Probe for H2S Enables Analyte-Responsive, 3D Imaging in Live Zebrafish Using Light Sheet Fluorescence Microscopy. *J. Am. Chem. Soc.* **2015**, 137, 10216-10223.

112. Hu, J.J. et al. Fluorescent Probe HKSOX-1 for Imaging and Detection of Endogenous Superoxide in Live Cells and In Vivo. *J. Am. Chem. Soc.* **2015**, 137, 6837-6843.

113. Cho, D.G. & Sessler, J.L. Modern reaction-based indicator systems. *Chem. Soc. Rev.* **2009**, 38, 1647-1662.

114. Li, X., Gao, X., Shi, W. & Ma, H. Design strategies for water-soluble small molecular chromogenic and fluorogenic probes. *Chem. Rev.* **2014**, 114, 590-659.

115. Tang, Y. et al. Development of fluorescent probes based on protection-deprotection of the key functional groups for biological imaging. *Chem. Soc. Rev.* **2015**, 44, 5003-5015.

116. Madsen, J. et al. Nile Blue-based nanosized pH sensors for simultaneous far-red and near-infrared live bioimaging. *J. Am. Chem. Soc.* **2013**, 135, 14863-14870.

117. Wu, L., Li, X., Huang, C. & Jia, N. Dual-Modal Colorimetric/Fluorescence Molecular Probe for Ratiometric Sensing of pH and Its Application. *Anal. Chem.* **2016**, 88, 8332-8338.

118. Sun, Y.Q. et al. A mitochondria-targetable fluorescent probe for dual-channel NO imaging assisted by intracellular cysteine and glutathione. *J. Am. Chem. Soc.* **2014**, 136, 12520-12523.

119. Brewer, T.F. & Chang, C.J. An Aza-Cope Reactivity-Based Fluorescent Probe for Imaging Formaldehyde in Living Cells. *J. Am. Chem. Soc.* **2015**, 137, 10886-10889.

120. Roth, A., Li, H., Anorma, C. & Chan, J. A Reaction-Based Fluorescent Probe for Imaging of Formaldehyde in Living Cells. *J. Am. Chem. Soc.* **2015**, 137, 10890-10893.

121. Umezawa, K., Yoshida, M., Kamiya, M., Yamasoba, T. & Urano, Y. Rational design of reversible fluorescent probes for live-cell imaging and quantification of fast glutathione dynamics. *Nat. Chem.* **2017**, 9, 279-286.

122. Thomas, S.W., 3rd, Joly, G.D. & Swager, T.M. Chemical sensors based on amplifying fluorescent conjugated polymers. *Chem. Rev.* **2007**, 107, 1339-1386.

123. Feng, X., Liu, L., Wang, S. & Zhu, D. Water-soluble fluorescent conjugated polymers and their interactions with biomacromolecules for sensitive biosensors. *Chem. Soc. Rev.* **2010**, 39, 2411-2419.

124. Kim, H.N., Guo, Z., Zhu, W., Yoon, J. & Tian, H. Recent progress on polymer-based fluorescent and colorimetric chemosensors. *Chem. Soc. Rev.* **2011**, 40, 79-93.

125. Liu, H.Y. et al. Quinoxaline-Based Polymer Dots with Ultrabright Red to Near-Infrared Fluorescence for In Vivo Biological Imaging. *J. Am. Chem. Soc.* **2015**, 137, 10420-10429.

126. Lee, M.H., Kim, J.S. & Sessler, J.L. Small molecule-based ratiometric fluorescence probes for cations, anions, and biomolecules. *Chem. Soc. Rev.* **2015**, 44, 4185-4191.

127. Peterka, D.S., Takahashi, H. & Yuste, R. Imaging voltage in neurons. *Neuron* **2011**, 69, 9-21.

128. Miller, E.W. Small molecule fluorescent voltage indicators for studying membrane potential. *Curr. Opin. Chem. Biol.* **2016**, 33, 74-80.

129. Miller, E.W. et al. Optically monitoring voltage in neurons by photo-induced electron transfer through molecular wires. *Proc. Natl. Acad. Sci. U. S. A.* **2012**, 109, 2114-2119.

130. Woodford, C.R. et al. Improved PeT molecules for optically sensing voltage in neurons. *J. Am. Chem. Soc.* **2015**, 137, 1817-1824.

131. Huang, Y.L., Walker, A.S. & Miller, E.W. A Photostable Silicon Rhodamine Platform for Optical Voltage Sensing. *J. Am. Chem. Soc.* **2015**, 137, 10767-10776.

132. Stabley, D.R., Jurchenko, C., Marshall, S.S. & Salaita, K.S. Visualizing mechanical tension across membrane receptors with a fluorescent sensor. *Nat. Methods* **2011**, 9, 64-67.

133. Blakely, B.L. et al. A DNA-based molecular probe for optically reporting cellular traction forces. *Nat. Methods* **2014**, 11, 1229-1232.

134. Chang, Y. et al. A General Approach for Generating Fluorescent Probes to Visualize Piconewton Forces at the Cell Surface. *J. Am. Chem. Soc.* **2016**, 138, 2901-2904.

135. Reisch, A. & Klymchenko, A.S. Fluorescent Polymer Nanoparticles Based on Dyes: Seeking Brighter Tools for Bioimaging. *Small* **2016**, 12, 1968-1992.

136. Wolfbeis, O.S. An overview of nanoparticles commonly used in fluorescent bioimaging. *Chem. Soc. Rev.* **2015**, 44, 4743-4768.

137. Peng, H.S. & Chiu, D.T. Soft fluorescent nanomaterials for biological and biomedical imaging. *Chem. Soc. Rev.* **2015**, 44, 4699-4722.

138. Qu, J.B. et al. Inherently fluorescent polystyrene microspheres for coating, sensing and cellular imaging. *Colloids Surf., B* **2017**, 152, 475-481.

139. Trofymchuk, K., Reisch, A., Shulov, I., Mely, Y. & Klymchenko, A.S. Tuning the color and photostability of perylene diimides inside polymer nanoparticles: towards biodegradable substitutes of quantum dots. *Nanoscale* **2014**, 6, 12934-12942.

140. Ding, D., Li, K., Liu, B. & Tang, B.Z. Bioprobes based on AIE fluorogens. *Acc. Chem. Res.* **2013**, 46, 2441-2453.

141. Wagh, A. et al. Polymeric nanoparticles with sequential and multiple FRET cascade mechanisms for multicolor and multiplexed imaging. *Small* **2013**, 9, 2129-2139.

142. Andreiuk, B. et al. Fluorescent Polymer Nanoparticles for Cell Barcoding In Vitro and In Vivo. *Small* **2017**, 13, 1701582.

143. le Masne de Chermont, Q. et al. Nanoprobes with near-infrared persistent luminescence for in vivo imaging. *Proc. Natl. Acad. Sci. U. S. A.* **2007**, 104, 9266-9271.

144. Miao, Q. et al. Molecular afterglow imaging with bright, biodegradable polymer nanoparticles. *Nat. Biotechnol.* **2017**, 35, 1102-1110.

145. Zheng, J. et al. Rationally designed molecular beacons for bioanalytical and biomedical applications. *Chem. Soc. Rev.* **2015**, 44, 3036-3055.

146. Paige, J.S., Wu, K.Y. & Jaffrey, S.R. RNA mimics of green fluorescent protein. *Science* **2011**, 333, 642-646.

147. Paige, J.S., Nguyen-Duc, T., Song, W. & Jaffrey, S.R. Fluorescence imaging of cellular metabolites with RNA. *Science* **2012**, 335, 1194.

148. Song, W., Strack, R.L. & Jaffrey, S.R. Imaging bacterial protein expression using genetically encoded RNA sensors. *Nat. Methods* **2013**, 10, 873.

149. Strack, R.L., Disney, M.D. & Jaffrey, S.R. A superfolding Spinach2 reveals the dynamic nature of trinucleotide repeat-containing RNA. *Nat. Methods* **2013**, 10, 1219-1224.

150. Song, W., Strack, R.L., Svensen, N. & Jaffrey, S.R. Plug-and-play fluorophores extend the spectral properties of Spinach. *J. Am. Chem. Soc.* **2014**, 136, 1198-1201.

151. Strack, R.L., Song, W. & Jaffrey, S.R. Using Spinach-based sensors for fluorescence imaging of intracellular metabolites and proteins in living bacteria. *Nat. Protoc.* **2014**, 9, 146-155.

152. Ding, C. 'Other' applications of single nucleotide polymorphisms. *Trends Biotechnol.* **2007**, 25, 279-283.

153. Mellis, I.A., Gupte, R., Raj, A. & Rouhanifard, S.H. Visualizing adenosine-to-inosine RNA editing in single mammalian cells. *Nat. Methods* **2017**, 14, 801-804.

154. Specht, E.A., Braselmann, E. & Palmer, A.E. A Critical and Comparative Review of Fluorescent Tools for Live-Cell Imaging. *Annu. Rev. Physiol.* **2017**, 79, 93-117.

155. Kaiser, P.D., Maier, J., Traenkle, B., Emele, F. & Rothbauer, U. Recent progress in generating intracellular functional antibody fragments to target and trace cellular components in living cells. *Biochim. Biophys. Acta* **2014**, 1844, 1933-1942.

156. Sato, Y. et al. Genetically encoded system to track histone modification in vivo. *Sci. Rep.* **2013**, 3, 2436.

157. Stasevich, T.J. et al. Regulation of RNA polymerase II activation by histone acetylation in single living cells. *Nature* **2014**, 516, 272-275.

158. Ntziachristos, V. Going deeper than microscopy: the optical imaging frontier in biology. *Nat. Methods* **2010**, 7, 603-614.

159. Fernandez-Suarez, M. & Ting, A.Y. Fluorescent probes for super-resolution imaging in living cells. *Nat. Rev. Mol. Cell Biol.* **2008**, 9, 929-943.

160. Ntziachristos, V., Tung, C.H., Bremer, C. & Weissleder, R. Fluorescence molecular tomography resolves protease activity in vivo. *Nat. Med.* **2002**, 8, 757-760.

161. Olson, E.S. et al. Activatable cell penetrating peptides linked to nanoparticles as dual probes for in vivo fluorescence and MR imaging of proteases. *Proc. Natl. Acad. Sci. U. S. A.* **2010**, 107, 4311-4316.

162. Chi, C. et al. Intraoperative imaging-guided cancer surgery: from current fluorescence molecular imaging methods to future multi-modality imaging technology. *Theranostics* **2014**, 4, 1072-1084.

163. Ni, D. et al. Dual-targeting upconversion nanoprobes across the blood-brain barrier for magnetic resonance/fluorescence imaging of intracranial glioblastoma. *ACS Nano* **2014**, 8, 1231-1242.

164. Xie, J. et al. PET/NIRF/MRI triple functional iron oxide nanoparticles. *Biomaterials* **2010**, 31, 3016-3022.

165. Nguyen, Q.T. et al. Surgery with molecular fluorescence imaging using activatable cell-penetrating peptides decreases residual cancer and improves survival. *Proc. Natl. Acad. Sci. U. S. A.* **2010**, 107, 4317-4322.

166. Nguyen, Q.T. & Tsien, R.Y. Fluorescence-guided surgery with live molecular navigation--a new cutting edge. *Nat. Rev. Cancer* **2013**, 13, 653-662.

167. Vahrmeijer, A.L., Hutteman, M., van der Vorst, J.R., van de Velde, C.J. & Frangioni, J.V. Image-guided cancer surgery using near-infrared fluorescence. *Nat. Rev. Clin. Oncol.* **2013**, 10, 507-518.

168. Perlitz, C. et al. Comparison of two tricarbocyanine-based dyes for fluorescence optical imaging. *J. Fluoresc.* **2005**, 15, 443-454.

169. van de Ven, S. et al. A novel fluorescent imaging agent for diffuse optical tomography of the breast: first clinical experience in patients. *Mol. Imaging Biol.* **2010**, 12, 343-348.

170. Schaafsma, B.E. et al. The clinical use of indocyanine green as a near-infrared fluorescent contrast agent for image-guided oncologic surgery. *J. Surg. Oncol.* **2011**, 104, 323-332.

171. van Dam, G.M. et al. Intraoperative tumor-specific fluorescence imaging in ovarian cancer by folate receptor-alpha targeting: first in-human results. *Nat. Med.* **2011**, 17, 1315-1319.

172. Jafari, M.D. et al. The use of indocyanine green fluorescence to assess anastomotic perfusion during robotic assisted laparoscopic rectal surgery. *Surg. Endosc.* **2013**, 27, 3003-3008.

173. van der Vorst, J.R. et al. Near-infrared fluorescence-guided resection of colorectal liver metastases. *Cancer* **2013**, 119, 3411-3418.

174. Jewell, E.L. et al. Detection of sentinel lymph nodes in minimally invasive surgery using indocyanine green and near-infrared fluorescence imaging for uterine and cervical malignancies. *Gynecol. Oncol.* **2014**, 133, 274-277.

175. Bulina, M.E. et al. Chromophore-assisted light inactivation (CALI) using the phototoxic fluorescent protein KillerRed. *Nat. Protoc.* **2006**, 1, 947-953.

176. Hoffman-Kim, D., Diefenbach, T.J., Eustace, B.K. & Jay, D.G. in Chromophore-Assisted Laser Inactivation. *Methods in Cell Biology*. Vol. 82, 335-354 (Academic Press; **2007**).

177. He, J. et al. A genetically targetable near-infrared photosensitizer. *Nat. Methods* **2016**, 13, 263-268.

178. Jung, H.S. et al. A Mitochondria-Targeted Cryptocyanine-Based Photothermogenic Photosensitizer. *J. Am. Chem. Soc.* **2017**, 139, 9972-9978.

179. Glantz, S.T. et al. Functional and topological diversity of LOV domain photoreceptors. *Proc. Natl. Acad. Sci. U. S. A.* **2016**, 113, E1442-1451.

180. Kaberniuk, A.A., Shemetov, A.A. & Verkhusha, V.V. A bacterial phytochrome-based optogenetic system controllable with near-infrared light. *Nat. Methods* **2016**, 13, 591-597.

181. Repina, N.A., Rosenbloom, A., Mukherjee, A., Schaffer, D.V. & Kane, R.S. At Light Speed: Advances in Optogenetic Systems for Regulating Cell Signaling and Behavior. *Annu. Rev. Chem. Biomol. Eng.* **2017**, 8, 13-39.

182. Rost, B.R., Schneider-Warme, F., Schmitz, D. & Hegemann, P. Optogenetic Tools for Subcellular Applications in Neuroscience. *Neuron* **2017**, 96, 572-603.

183. Frenette, M. et al. Shining light on the dark side of imaging: excited state absorption enhancement of a bis-styryl BODIPY photoacoustic contrast agent. *J. Am. Chem. Soc.* **2014**, 136, 15853-15856.

184. Yao, J. et al. Multiscale photoacoustic tomography using reversibly switchable bacterial phytochrome as a near-infrared photochromic probe. *Nat. Methods* **2015**, 13, 67-73.

185. Reinhardt, C.J., Zhou, E.Y., Jorgensen, M.D., Partipilo, G. & Chan, J. A Ratiometric Acoustogenic Probe for in Vivo Imaging of Endogenous Nitric Oxide. *J. Am. Chem. Soc.* **2018**, 140, 1011-1018.

186. Gaj, T., Gersbach, C.A. & Barbas, C.F., 3rd ZFN, TALEN, and CRISPR/Cas-based methods for genome engineering. *Trends Biotechnol.* **2013**, 31, 397-405.

187. Pennisi, E. The CRISPR craze. *Science* **2013**, 341, 833-836.

188. Vendrell, M., Zhai, D., Er, J.C. & Chang, Y.T. Combinatorial strategies in fluorescent probe development. *Chem. Rev.* **2012**, 112, 4391-4420.

189. de Moliner, F., Kielland, N., Lavilla, R. & Vendrell, M. Modern Synthetic Avenues for the Preparation of Functional Fluorophores. *Angew. Chem. Int. Ed.* **2017**, 56, 3758-3769.

190. Xiong, X. et al. Thermally activated delayed fluorescence of fluorescein derivative for time-resolved and confocal fluorescence imaging. *J. Am. Chem. Soc.* **2014**, 136, 9590-9597.

191. Grimm, J.B. et al. A general method to improve fluorophores for live-cell and single-molecule microscopy. *Nat. Methods* **2015**, 12, 244-250.

192. Kawasumi, K. et al. Thermally Activated Delayed Fluorescence Materials Based on Homoconjugation Effect of Donor-Acceptor Triptycenes. *J. Am. Chem. Soc.* **2015**, 137, 11908-11911.

193. Cheng, Y. et al. Unparalleled Ease of Access to a Library of Biheteroaryl Fluorophores via Oxidative Cross-Coupling Reactions: Discovery of Photostable NIR Probe for Mitochondria. *J. Am. Chem. Soc.* **2016**, 138, 4730-4738.

194. Grimm, J.B. et al. A general method to fine-tune fluorophores for live-cell and in vivo imaging. *Nat. Methods* **2017**, 14, 987-994.

195. Marks, K.M. & Nolan, G.P. Chemical labeling strategies for cell biology. *Nat. Methods* **2006**, 3, 591-596.

196. Sunbul, M. & Yin, J. Site specific protein labeling by enzymatic posttranslational modification. *Org. Biomol. Chem.* **2009**, 7, 3361-3371.

197. Crivat, G. & Taraska, J.W. Imaging proteins inside cells with fluorescent tags. *Trends Biotechnol.* **2012**, 30, 8-16.

198. Dean, K.M. & Palmer, A.E. Advances in fluorescence labeling strategies for dynamic cellular imaging. *Nat. Chem. Biol.* **2014**, 10, 512-523.

199. Rashidian, M., Dozier, J.K. & Distefano, M.D. Enzymatic labeling of proteins: techniques and approaches. *Bioconjugate Chem.* **2013**, 24, 1277-1294.

200. Griffin, M., Casadio, R. & Bergamini, C.M. Transglutaminases: nature's biological glues. *Biochem. J* **2002**, 368, 377-396.

201. Lin, C.W. & Ting, A.Y. Transglutaminase-catalyzed site-specific conjugation of small-molecule probes to proteins in vitro and on the surface of living cells. *J. Am. Chem. Soc.* **2006**, 128, 4542-4543.

202. Tominaga, J. et al. An enzymatic method for site-specific labeling of recombinant proteins with oligonucleotides. *Chem. Commun.* **2007**, 401-403.

203. Oteng-Pabi, S.K., Pardin, C., Stoica, M. & Keillor, J.W. Site-specific protein labelling and immobilization mediated by microbial transglutaminase. *Chem. Commun.* **2014**, 50, 6604-6606.

204. Popp, M.W., Antos, J.M., Grotenbreg, G.M., Spooner, E. & Ploegh, H.L. Sortagging: a versatile method for protein labeling. *Nat. Chem. Biol.* **2007**, 3, 707-708.

205. Tanaka, T., Yamamoto, T., Tsukiji, S. & Nagamune, T. Site-specific protein modification on living cells catalyzed by Sortase. *ChemBioChem* **2008**, 9, 802-807.

206. Antos, J.M. et al. Site-specific N- and C-terminal labeling of a single polypeptide using sortases of different specificity. *J. Am. Chem. Soc.* **2009**, 131, 10800-10801.

207. Guimaraes, C.P. et al. Site-specific C-terminal and internal loop labeling of proteins using sortase-mediated reactions. *Nat. Protoc.* **2013**, 8, 1787-1799.

208. Duckworth, B.P., Zhang, Z., Hosokawa, A. & Distefano, M.D. Selective labeling of proteins by using protein farnesyltransferase. *ChemBioChem* **2007**, 8, 98-105.

209. Chen, Y.X., Triola, G. & Waldmann, H. Bioorthogonal chemistry for site-specific labeling and surface immobilization of proteins. *Acc. Chem. Res.* **2011**, 44, 762-773.

210. Chen, I., Howarth, M., Lin, W. & Ting, A.Y. Site-specific labeling of cell surface proteins with biophysical probes using biotin ligase. *Nat. Methods* **2005**, 2, 99.

211. Howarth, M., Takao, K., Hayashi, Y. & Ting, A.Y. Targeting quantum dots to surface proteins in living cells with biotin ligase. *Proc. Natl. Acad. Sci. U. S. A.* **2005**, 102, 7583-7588.

212. Howarth, M. & Ting, A.Y. Imaging proteins in live mammalian cells with biotin ligase and monovalent streptavidin. *Nat. Protoc.* **2008**, 3, 534-545.

213. Heal, W.P. et al. Site-specific N-terminal labelling of proteins in vitro and in vivo using N-myristoyl transferase and bioorthogonal ligation chemistry. *Chem. Commun.* **2008**, 480-482.

214. Heal, W.P., Wickramasinghe, S.R., Leatherbarrow, R.J. & Tate, E.W. N-Myristoyl transferase-mediated protein labelling in vivo. *Org. Biomol. Chem.* **2008**, 6, 2308-2315.

215. Heal, W.P., Wright, M.H., Thinon, E. & Tate, E.W. Multifunctional protein labeling via enzymatic N-terminal tagging and elaboration by click chemistry. *Nat. Protoc.* **2011**, 7, 105-117.

216. Carrico, I.S., Carlson, B.L. & Bertozzi, C.R. Introducing genetically encoded aldehydes into proteins. *Nat. Chem. Biol.* **2007**, 3, 321-322.

217. Rush, J.S. & Bertozzi, C.R. New aldehyde tag sequences identified by screening formylglycine generating enzymes in vitro and in vivo. *J. Am. Chem. Soc.* **2008**, 130, 12240-12241.

218. Liu, J. et al. An Efficient Site-Specific Method for Irreversible Covalent Labeling of Proteins with a Fluorophore. *Sci. Rep.* **2015**, 5, 16883.

219. Yin, J., Liu, F., Li, X. & Walsh, C.T. Labeling proteins with small molecules by site-specific posttranslational modification. *J. Am. Chem. Soc.* **2004**, 126, 7754-7755.

220. Yin, J., Lin, A.J., Golan, D.E. & Walsh, C.T. Site-specific protein labeling by Sfp phosphopantetheinyl transferase. *Nat. Protoc.* **2006**, 1, 280-285.

221. Keppler, A. et al. A general method for the covalent labeling of fusion proteins with small molecules in vivo. *Nat. Biotechnol.* **2003**, 21, 86-89.

222. Juillerat, A. et al. Directed evolution of O6-alkylguanine-DNA alkyltransferase for efficient labeling of fusion proteins with small molecules in vivo. *Chem. Biol.* **2003**, 10, 313-317.

223. Gautier, A. et al. An engineered protein tag for multiprotein labeling in living cells. *Chem. Biol.* **2008**, 15, 128-136.

224. Maurel, D. et al. Cell-surface protein-protein interaction analysis with time-resolved FRET and snap-tag technologies: application to GPCR oligomerization. *Nat. Methods* **2008**, 5, 561-567.

225. Jones, S.A., Shim, S.-H., He, J. & Zhuang, X. Fast, three-dimensional super-resolution imaging of live cells. *Nat. Methods* **2011**, 8, 499.

226. Los, G.V. et al. HaloTag: a novel protein labeling technology for cell imaging and protein analysis. *ACS Chem. Biol.* **2008**, 3, 373-382.

227. Erhart, D. et al. Chemical development of intracellular protein heterodimerizers. *Chem. Biol.* **2013**, 20, 549-557.

228. Gallagher, S.S., Sable, J.E., Sheetz, M.P. & Cornish, V.W. An in vivo covalent TMP-tag based on proximity-induced reactivity. *ACS Chem. Biol.* **2009**, 4, 547-556.

229. Chen, Z., Jing, C., Gallagher, S.S., Sheetz, M.P. & Cornish, V.W. Second-generation covalent TMP-tag for live cell imaging. *J. Am. Chem. Soc.* **2012**, 134, 13692-13699.

230. Wombacher, R. et al. Live-cell super-resolution imaging with trimethoprim conjugates. *Nat. Methods* **2010**, 7, 717-719.

231. Jing, C. & Cornish, V.W. A fluorogenic TMP-tag for high signal-to-background intracellular live cell imaging. *ACS Chem. Biol.* **2013**, 8, 1704-1712.

232. Liu, W. et al. A rapid and fluorogenic TMP-AcBOPDIPY probe for covalent labeling of proteins in live cells. *J. Am. Chem. Soc.* **2014**, 136, 4468-4471.

233. Hori, Y. & Kikuchi, K. Protein labeling with fluorogenic probes for no-wash live-cell imaging of proteins. *Curr. Opin. Chem. Biol.* **2013**, 17, 644-650.

234. Hori, Y., Ueno, H., Mizukami, S. & Kikuchi, K. Photoactive yellow protein-based protein labeling system with turn-on fluorescence intensity. *J. Am. Chem. Soc.* **2009**, 131, 16610-16611.

235. Hori, Y. et al. Development of fluorogenic probes for quick no-wash live-cell imaging of intracellular proteins. *J. Am. Chem. Soc.* **2013**, 135, 12360-12365.

236. Hori, Y., Hirayama, S., Sato, M. & Kikuchi, K. Redesign of a Fluorogenic Labeling System To Improve Surface Charge, Brightness, and Binding Kinetics for Imaging the Functional Localization of Bromodomains. *Angew. Chem. Int. Ed.* **2015**, 54, 14368-14371.

237. Kamikawa, Y. et al. Design of a protein tag and fluorogenic probe with modular structure for live-cell imaging of intracellular proteins. *Chem. Sci.* **2016**, 7, 308-314.

238. Plamont, M.A. et al. Small fluorescence-activating and absorption-shifting tag for tunable protein imaging in vivo. *Proc. Natl. Acad. Sci. U. S. A.* **2016**, 113, 497-502.

239. Li, C. et al. Design and characterization of red fluorogenic push-pull chromophores holding great potential for bioimaging and biosensing. *Org. Biomol. Chem.* **2016**, 14, 9253-9261.

240. Mizukami, S., Hori, Y. & Kikuchi, K. Small-molecule-based protein-labeling technology in live cell studies: probe-design concepts and applications. *Acc. Chem. Res.* **2014**, 47, 247-256.

241. Ozhalici-Unal, H. et al. A rainbow of fluoromodules: a promiscuous scFv protein binds to and activates a diverse set of fluorogenic cyanine dyes. *J. Am. Chem. Soc.* **2008**, 130, 12620-12621.

242. Szent-Gyorgyi, C. et al. Fluorogen-activating single-chain antibodies for imaging cell surface proteins. *Nat. Biotechnol.* **2008**, 26, 235-240.

243. Bruchez, M.P. Dark dyes-bright complexes: fluorogenic protein labeling. *Curr. Opin. Chem. Biol.* **2015**, 27, 18-23.

244. Yan, Q. et al. Localization microscopy using noncovalent fluorogen activation by genetically encoded fluorogen-activating proteins. *ChemPhysChem* **2014**, 15, 687-695.

245. Telmer, C.A. et al. Rapid, specific, no-wash, far-red fluorogen activation in subcellular compartments by targeted fluorogen activating proteins. *ACS Chem. Biol.* **2015**, 10, 1239-1246.

246. Larsen, M.B., Hu, J., Frizzell, R.A. & Watkins, S.C. Simple image-based no-wash method for quantitative detection of surface expressed CFTR. *Methods* **2016**, 96, 40-45.

247. Naganbabu, M. et al. Multiexcitation Fluorogenic Labeling of Surface, Intracellular, and Total Protein Pools in Living Cells. *Bioconjugate Chem.* **2016**, 27, 1525-1531.

248. Saurabh, S., Perez, A.M., Comerci, C.J., Shapiro, L. & Moerner, W.E. Super-resolution Imaging of Live Bacteria Cells Using a Genetically Directed, Highly Photostable Fluoromodule. *J. Am. Chem. Soc.* **2016**, 138, 10398-10401.

249. Sletten, E.M. & Bertozzi, C.R. From mechanism to mouse: a tale of two bioorthogonal reactions. *Acc. Chem. Res.* **2011**, 44, 666-676.

250. Nikić, I., Kang, J.H., Girona, G.E., Aramburu, I.V. & Lemke, E.A. Labeling proteins on live mammalian cells using click chemistry. *Nat. Protoc.* **2015**, 10, 780.

251. Sletten, E.M. & Bertozzi, C.R. Bioorthogonal chemistry: fishing for selectivity in a sea of functionality. *Angew. Chem. Int. Ed.* **2009**, 48, 6974-6998.

252. Dawson, P.E., Muir, T.W., Clark-Lewis, I. & Kent, S.B. Synthesis of proteins by native chemical ligation. *Science* **1994**, 266, 776-779.

253. Zeng, Y., Ramya, T.N., Dirksen, A., Dawson, P.E. & Paulson, J.C. High-efficiency labeling of sialylated glycoproteins on living cells. *Nat. Methods* **2009**, 6, 207-209.

254. Yi, L. et al. A Highly Efficient Strategy for Modification of Proteins at the C Terminus. *Angew. Chem. Int. Ed.* **2010**, 49, 9417-9421.

255. Agarwal, P., van der Weijden, J., Sletten, E.M., Rabuka, D. & Bertozzi, C.R. A Pictet-Spengler ligation for protein chemical modification. *Proc. Natl. Acad. Sci. U. S. A.* **2013**, 110, 46-51.

256. Saxon, E. & Bertozzi, C.R. Cell surface engineering by a modified Staudinger reaction. *Science* **2000**, 287, 2007-2010.

257. Saxon, E., Armstrong, J.I. & Bertozzi, C.R. A "traceless" Staudinger ligation for the chemoselective synthesis of amide bonds. *Org. Lett.* **2000**, 2, 2141-2143.

258. Haldon, E., Nicasio, M.C. & Perez, P.J. Copper-catalysed azide-alkyne cycloadditions (CuAAC): an update. *Org. Biomol. Chem.* **2015**, 13, 9528-9550.

259. Worrell, B.T., Malik, J.A. & Fokin, V.V. Direct evidence of a dinuclear copper intermediate in Cu(I)-catalyzed azide-alkyne cycloadditions. *Science* **2013**, 340, 457-460.

260. Ziegler, M.S., Lakshmi, K.V. & Tilley, T.D. Dicopper Cu(I)Cu(I) and Cu(I)Cu(II) Complexes in Copper-Catalyzed Azide-Alkyne Cycloaddition. *J. Am. Chem. Soc.* **2017**, 139, 5378-5386.

261. Shieh, P. et al. CalFluors: A Universal Motif for Fluorogenic Azide Probes across the Visible Spectrum. *J. Am. Chem. Soc.* **2015**, 137, 7145-7151.

262. Agard, N.J., Prescher, J.A. & Bertozzi, C.R. A strain-promoted [3 + 2] azide-alkyne cycloaddition for covalent modification of biomolecules in living systems. *J. Am. Chem. Soc.* **2004**, 126, 15046-15047.

263. Baskin, J.M. et al. Copper-free click chemistry for dynamic in vivo imaging. *Proc. Natl. Acad. Sci. U. S. A.* **2007**, 104, 16793-16797.

264. Laughlin, S.T., Baskin, J.M., Amacher, S.L. & Bertozzi, C.R. In vivo imaging of membrane-associated glycans in developing zebrafish. *Science* **2008**, 320, 664-667.

265. Yao, J.Z. et al. Fluorophore targeting to cellular proteins via enzyme-mediated azide ligation and strain-promoted cycloaddition. *J. Am. Chem. Soc.* **2012**, 134, 3720-3728.

266. Gong, Y. & Pan, L. Recent advances in bioorthogonal reactions for site-specific protein labeling and engineering. *Tetrahedron Lett.* **2015**, 56, 2123-2132.

267. Poloukhtine, A.A., Mbua, N.E., Wolfert, M.A., Boons, G.J. & Popik, V.V. Selective labeling of living cells by a photo-triggered click reaction. *J. Am. Chem. Soc.* **2009**, 131, 15769-15776.

268. Ning, X. et al. Protein modification by strain-promoted alkyne-nitrone cycloaddition. *Angew. Chem. Int. Ed.* **2010**, 49, 3065-3068.

269. van Berkel, S.S. et al. Application of metal-free triazole formation in the synthesis of cyclic RGD-DTPA conjugates. *ChemBioChem* **2008**, 9, 1805-1815.

270. Wang, Y., Vera, C.I. & Lin, Q. Convenient synthesis of highly functionalized pyrazolines via mild, photoactivated 1,3-dipolar cycloaddition. *Org. Lett.* **2007**, 9, 4155-4158.

271. Song, W., Wang, Y., Qu, J., Madden, M.M. & Lin, Q. A photoinducible 1,3-dipolar cycloaddition reaction for rapid, selective modification of tetrazole-containing proteins. *Angew. Chem. Int. Ed.* **2008**, 47, 2832-2835.

272. Blackman, M.L., Royzen, M. & Fox, J.M. Tetrazine ligation: fast bioconjugation based on inverse-electron-demand Diels-Alder reactivity. *J. Am. Chem. Soc.* **2008**, 130, 13518-13519.

273. Devaraj, N.K. & Weissleder, R. Biomedical applications of tetrazine cycloadditions. *Acc. Chem. Res.* **2011**, 44, 816-827.

274. Thalhammer, F., Wallfahrer, U. & Sauer, J. Reaktivität einfacher offenkettiger und cyclischer dienophile bei Diels-Alder-reaktionen mit inversem elektronenbedarf. *Tetrahedron Lett.* **1990**, 31, 6851-6854.

275. Seitchik, J.L. et al. Genetically encoded tetrazine amino acid directs rapid site-specific in vivo bioorthogonal ligation with trans-cyclooctenes. *J. Am. Chem. Soc.* **2012**, 134, 2898-2901.

276. Lang, K. et al. Genetically encoded norbornene directs site-specific cellular protein labelling via a rapid bioorthogonal reaction. *Nat. Chem.* **2012**, 4, 298-304.

277. Peng, T. & Hang, H.C. Site-Specific Bioorthogonal Labeling for Fluorescence Imaging of Intracellular Proteins in Living Cells. *J. Am. Chem. Soc.* **2016**, 138, 14423-14433.

278. Shang, X. et al. Fluorogenic protein labeling using a genetically encoded unstrained alkene. *Chem. Sci.* **2017**, 8, 1141-1145.

279. Lin, S. et al. Redox-based reagents for chemoselective methionine bioconjugation. *Science* **2017**, 355, 597-602.

280. Addy, P.S., Erickson, S.B., Italia, J.S. & Chatterjee, A. A Chemoselective Rapid Azo-Coupling Reaction (CRACR) for Unclickable Bioconjugation. *J. Am. Chem. Soc.* **2017**, 139, 11670-11673.

281. Lee, Y.J., Kurra, Y. & Liu, W.R. Phospha-Michael Addition as a New Click Reaction for Protein Functionalization. *ChemBioChem* **2016**, 17, 456-461.

282. Kukwikila, M., Gale, N., El-Sagheer, A.H., Brown, T. & Tavassoli, A. Assembly of a biocompatible triazole-linked gene by one-pot click-DNA ligation. *Nat. Chem.* **2017**, 9, 1089-1098.

283. Lim, R.K. & Lin, Q. Bioorthogonal chemistry: recent progress and future directions. *Chem. Commun.* **2010**, 46, 1589-1600.

284. Lang, K. & Chin, J.W. Cellular incorporation of unnatural amino acids and bioorthogonal labeling of proteins. *Chem. Rev.* **2014**, 114, 4764-4806.

285. Patterson, D.M., Nazarova, L.A. & Prescher, J.A. Finding the right (bioorthogonal) chemistry. *ACS Chem. Biol.* **2014**, 9, 592-605.

286. Thyer, R., Robotham, S.A., Brodbelt, J.S. & Ellington, A.D. Evolving tRNA(Sec) for efficient canonical incorporation of selenocysteine. *J. Am. Chem. Soc.* **2015**, 137, 46-49.

287. Uttamapinant, C. et al. A fluorophore ligase for site-specific protein labeling inside living cells. *Proc. Natl. Acad. Sci. U. S. A.* **2010**, 107, 10914-10919.

288. Slavoff, S.A., Liu, D.S., Cohen, J.D. & Ting, A.Y. Imaging protein-protein interactions inside living cells via interaction-dependent fluorophore ligation. *J. Am. Chem. Soc.* **2011**, 133, 19769-19776.

289. Liu, D.S., Phipps, W.S., Loh, K.H., Howarth, M. & Ting, A.Y. Quantum dot targeting with lipoic acid ligase and HaloTag for single-molecule imaging on living cells. *ACS Nano* **2012**, 6, 11080-11087.

290. Uttamapinant, C. et al. Site-specific protein labeling using PRIME and chelation-assisted click chemistry. *Nat. Protoc.* **2013**, 8, 1620.

291. Hauke, S. et al. Two-step protein labeling utilizing lipoic acid ligase and Sonogashira cross-coupling. *Bioconjugate Chem.* **2014**, 25, 1632-1637.

292. Plaks, J.G., Falatach, R., Kastantin, M., Berberich, J.A. & Kaar, J.L. Multisite clickable modification of proteins using lipoic acid ligase. *Bioconjugate Chem.* **2015**, 26, 1104-1112.

293. Griffin, B.A., Adams, S.R. & Tsien, R.Y. Specific covalent labeling of recombinant protein molecules inside live cells. *Science* **1998**, 281, 269-272.

294. Adams, S.R. et al. New Biarsenical Ligands and Tetracysteine Motifs for Protein Labeling in Vitro and in Vivo: Synthesis and Biological Applications. *J. Am. Chem. Soc.* **2002**, 124, 6063-6076.

295. Martin, B.R., Giepmans, B.N., Adams, S.R. & Tsien, R.Y. Mammalian cell-based optimization of the biarsenical-binding tetracysteine motif for improved fluorescence and affinity. *Nat. Biotechnol.* **2005**, 23, 1308-1314.

296. Cao, H., Chen, B., Squier, T.C. & Mayer, M.U. CrAsH: a biarsenical multi-use affinity probe with low non-specific fluorescence. *Chem. Commun.* **2006**, 2601-2603.

297. Spagnuolo, C.C., Vermeij, R.J. & Jares-Erijman, E.A. Improved photostable FRET-competent biarsenical-tetracysteine probes based on fluorinated fluoresceins. *J. Am. Chem. Soc.* **2006**, 128, 12040-12041.

298. Hoffmann, C. et al. A FlAsH-based FRET approach to determine G protein-coupled receptor activation in living cells. *Nat. Methods* **2005**, 2, 171-176.

299. Adams, S.R. & Tsien, R.Y. Preparation of the membrane-permeant biarsenicals FlAsH-EDT2 and ReAsH-EDT2 for fluorescent labeling of tetracysteine-tagged proteins. *Nat. Protoc.* **2008**, 3, 1527-1534.

300. Hoffmann, C. et al. Fluorescent labeling of tetracysteine-tagged proteins in intact cells. *Nat. Protoc.* **2010**, 5, 1666-1677.

301. Walker, A.S., Rablen, P.R. & Schepartz, A. Rotamer-Restricted Fluorogenicity of the Bis-Arsenical ReAsH. *J. Am. Chem. Soc.* **2016**, 138, 7143-7150.

302. Halo, T.L., Appelbaum, J., Hobert, E.M., Balkin, D.M. & Schepartz, A. Selective recognition of protein tetraserine motifs with a cell-permeable, pro-fluorescent bis-boronic acid. *J. Am. Chem. Soc.* **2009**, 131, 438-439.

303. Chen, Y. et al. Coumarin-based fluorogenic probes for no-wash protein labeling. *Angew. Chem. Int. Ed.* **2014**, 53, 13785-13788.

304. Wang, Y. et al. Development of a red fluorescent light-up probe for highly selective and sensitive detection of vicinal dithiol-containing proteins in living cells. *Chem. Sci.* **2016**, 7, 518-524.

305. Stelzer, E.H. Better imaging through chemistry. *Cell* **2014**, 159, 1243-1246.

306. Weissleder, R. A clearer vision for in vivo imaging. *Nat. Biotechnol.* **2001**, 19, 316-317.

307. Hong, G., Antaris, A.L. & Dai, H. Near-infrared fluorophores for biomedical imaging. *Nat. Biomed. Eng.* **2017**, 1, 0010.

308. Shcherbo, D. et al. Bright far-red fluorescent protein for whole-body imaging. *Nat. Methods* **2007**, 4, 741-746.

309. Subach, F.V. et al. Red fluorescent protein with reversibly photoswitchable absorbance for photochromic FRET. *Chem. Biol.* **2010**, 17, 745-755.

310. Hense, A., Nienhaus, K. & Nienhaus, G.U. Exploring color tuning strategies in red fluorescent proteins. *Photochem. Photobiol. Sci.* **2015**, 14, 200-212.

311. Ng, H.L. & Lin, M.Z. Structure-guided wavelength tuning in far-red fluorescent proteins. *Curr. Opin. Struct. Biol.* **2016**, 39, 124-133.

312. Rockwell, N.C. & Lagarias, J.C. A brief history of phytochromes. *ChemPhysChem* **2010**, 11, 1172-1180.

313. Shcherbakova, D.M. et al. Molecular Basis of Spectral Diversity in Near-Infrared Phytochrome-Based Fluorescent Proteins. *Chem. Biol.* **2015**, 22, 1540-1551.

314. Filonov, G.S. et al. Bright and stable near-infrared fluorescent protein for in vivo imaging. *Nat. Biotechnol.* **2011**, 29, 757-761.

315. Shcherbakova, D.M. et al. Bright monomeric near-infrared fluorescent proteins as tags and biosensors for multiscale imaging. *Nat. Commun.* **2016**, 7, 12405.

316. Chernov, K.G., Redchuk, T.A., Omelina, E.S. & Verkhusha, V.V. Near-Infrared Fluorescent Proteins, Biosensors, and Optogenetic Tools Engineered from Phytochromes. *Chem. Rev.* **2017**, 117, 6423-6446.

317. Rodriguez, E.A. et al. A far-red fluorescent protein evolved from a cyanobacterial phycobiliprotein. *Nat. Methods* **2016**, 13, 763-769.

318. Yuan, L., Lin, W., Zheng, K., He, L. & Huang, W. Far-red to near infrared analyte-responsive fluorescent probes based on organic fluorophore platforms for fluorescence imaging. *Chem. Soc. Rev.* **2013**, 42, 622-661.

319. Guo, Z., Park, S., Yoon, J. & Shin, I. Recent progress in the development of near-infrared fluorescent probes for bioimaging applications. *Chem. Soc. Rev.* **2014**, 43, 16-29.

320. Bricks, J.L., Kachkovskii, A.D., Slominskii, Y.L., Gerasov, A.O. & Popov, S.V. Molecular design of near infrared polymethine dyes: A review. *Dyes Pigm.* **2015**, 121, 238-255.

321. Brooker, L.G.S. Absorption and Resonance in Dyes. *Rev. Mod. Phys.* **1942**, 14, 275-293.

322. Descalzo, A.B. & Rurack, K. On the signalling pathways and Cu(II)-mediated anion indication of N-meso-substituted heptamethine cyanine dyes. *Chem. Eur. J.* **2009**, 15, 3173-3185.

323. Kiyose, K. et al. Molecular design strategies for near-infrared ratiometric fluorescent probes based on the unique spectral properties of aminocyanines. *Chem. Eur. J.* **2009**, 15, 9191-9200.

324. Redy-Keisar, O., Kisin-Finfer, E., Ferber, S., Satchi-Fainaro, R. & Shabat, D. Synthesis and use of QCy7-derived modular probes for the detection and imaging of biologically relevant analytes. *Nat. Protoc.* **2013**, 9, 27.

325. Michie, M.S. et al. Cyanine Conformational Restraint in the Far-Red Range. *J. Am. Chem. Soc.* **2017**, 139, 12406-12409.

326. Peng, X. et al. Heptamethine cyanine dyes with a large stokes shift and strong fluorescence: a paradigm for excited-state intramolecular charge transfer. *J. Am. Chem. Soc.* **2005**, 127, 4170-4171.

327. Bertolino, C.A., Caputo, G., Barolo, C., Viscardi, G. & Coluccia, S. Novel heptamethine cyanine dyes with large Stoke's shift for biological applications in the near infrared. *J. Fluoresc.* **2006**, 16, 221-225.

328. Pascal, S. et al. Expanding the polymethine paradigm: evidence for the contribution of a bis-dipolar electronic structure. *J. Phys. Chem. A* **2014**, 118, 4038-4047.

329. Kaur, M. & Choi, D.H. Diketopyrrolopyrrole: brilliant red pigment dye-based fluorescent probes and their applications. *Chem. Soc. Rev.* **2015**, 44, 58-77.

330. Fischer, G.M., Ehlers, A.P., Zumbusch, A. & Daltrozzo, E. Near-infrared dyes and fluorophores based on diketopyrrolopyrroles. *Angew. Chem. Int. Ed.* **2007**, 46, 3750-3753.

331. Fischer, G.M., Isomaki-Krondahl, M., Gottker-Schnetmann, I., Daltrozzo, E. & Zumbusch, A. Pyrrolopyrrole cyanine dyes: a new class of near-infrared dyes and fluorophores. *Chem. Eur. J.* **2009**, 15, 4857-4864.

332. Fischer, G.M. et al. Asymmetric PPCys: strongly fluorescing NIR labels. *Chem. Commun.* **2010**, 46, 5289-5291.

333. Fischer, G.M., Klein, M.K., Daltrozzo, E. & Zumbusch, A. Pyrrolopyrrole Cyanines: Effect of Substituents on Optical Properties. *Eur. J. Org. Chem.* **2011**, 2011, 3421-3429.

334. Fischer, G.M., Daltrozzo, E. & Zumbusch, A. Selective NIR chromophores: bis(pyrrolopyrrole) cyanines. *Angew. Chem. Int. Ed.* **2011**, 50, 1406-1409.

335. Shimizu, S., Iino, T., Araki, Y. & Kobayashi, N. Pyrrolopyrrole aza-BODIPY analogues: a facile synthesis and intense fluorescence. *Chem. Commun.* **2013**, 49, 1621-1623.

336. Ulrich, G., Goeb, S., De Nicola, A., Retailleau, P. & Ziessel, R. Chemistry at boron: synthesis and properties of red to near-IR fluorescent dyes based on boron-substituted diisoindolomethene frameworks. *J. Org. Chem.* **2011**, 76, 4489-4505.

337. Ni, Y. & Wu, J. Far-red and near infrared BODIPY dyes: synthesis and applications for fluorescent pH probes and bio-imaging. *Org. Biomol. Chem.* **2014**, 12, 3774-3791.

338. Chen, H. et al. A General Strategy Toward Highly Fluorogenic Bioprobes Emitting across the Visible Spectrum. *J. Am. Chem. Soc.* **2017**, 139, 10157-10163.

339. Lu, H., Mack, J., Yang, Y. & Shen, Z. Structural modification strategies for the rational design of red/NIR region BODIPYs. *Chem. Soc. Rev.* **2014**, 43, 4778-4823.

340. Gresser, R., Hummert, M., Hartmann, H., Leo, K. & Riede, M. Synthesis and characterization of near-infrared absorbing benzannulated aza-BODIPY dyes. *Chem. Eur. J.* **2011**, 17, 2939-2947.

341. Grossi, M. et al. Mechanistic insight into the formation of tetraarylazadipyrromethenes. *J. Org. Chem.* **2012**, 77, 9304-9312.

342. Zhang, X., Yu, H. & Xiao, Y. Replacing phenyl ring with thiophene: an approach to longer wavelength aza-dipyrromethene boron difluoride (Aza-BODIPY) dyes. *J. Org. Chem.* **2012**, 77, 669-673.

343. Wu, D. & O'Shea, D.F. Synthesis and properties of BF2-3,3'-dimethyldiarylazadipyrromethene near-infrared fluorophores. *Org. Lett.* **2013**, 15, 3392-3395.

344. Burghart, A. et al. 3,5-Diaryl-4,4-difluoro-4-bora-3a,4a-diaza-s-indacene (BODIPY) Dyes: Synthesis, Spectroscopic, Electrochemical, and Structural Properties. *J. Org. Chem.* **1999**, 64, 7813-7819.

345. Buyukcakir, O., Bozdemir, O.A., Kolemen, S., Erbas, S. & Akkaya, E.U. Tetrastyryl-Bodipy dyes: convenient synthesis and characterization of elusive near IR fluorophores. *Org. Lett.* **2009**, 11, 4644-4647.

346. Leen, V. et al. 1,7-Disubstituted boron dipyrromethene (BODIPY) dyes: synthesis and spectroscopic properties. *J. Org. Chem.* **2011**, 76, 8168-8176.

347. Dost, Z., Atilgan, S. & Akkaya, E.U. Distyryl-boradiazaindacenes: facile synthesis of novel near IR emitting fluorophores. *Tetrahedron* **2006**, 62, 8484-8488.

348. Jiao, L. et al. Long wavelength red fluorescent dyes from 3,5-diiodo-BODIPYs. *Org. Biomol. Chem.* **2010**, 8, 2517-2519.

349. Chen, J., Burghart, A., Derecskei-Kovacs, A. & Burgess, K. 4,4-Difluoro-4-bora-3a,4a-diaza-s-indacene (BODIPY) dyes modified for extended conjugation and restricted bond rotations. *J. Org. Chem.* **2000**, 65, 2900-2906.

350. Jiang, X.D., Gao, R., Yue, Y., Sun, G.T. & Zhao, W. A NIR BODIPY dye bearing 3,4,4a-trihydroxanthene moieties. *Org. Biomol. Chem.* **2012**, 10, 6861-6865.

351. Loudet, A. et al. B,O-chelated azadipyrromethenes as near-IR probes. *Org. Lett.* **2008**, 10, 4771-4774.

352. Zhao, W. & Carreira, E.M. Conformationally Restricted Aza-BODIPY: Highly Fluorescent, Stable Near-Infrared Absorbing Dyes. *Chem. Eur. J.* **2006**, 12, 7254-7263.

353. Loudet, A. & Burgess, K. BODIPY dyes and their derivatives: syntheses and spectroscopic properties. *Chem. Rev.* **2007**, 107, 4891-4932.

354. Okujima, T. et al. Synthesis of π-expanded BODIPYs and their fluorescent properties in the visible–near–infrared region. *Tetrahedron* **2010**, 66, 6895-6900.

355. Umezawa, K., Citterio, D. & Suzuki, K. New trends in near-infrared fluorophores for bioimaging. *Anal. Sci.* **2014**, 30, 327-349.

356. Goeb, S. & Ziessel, R. Convenient synthesis of green diisoindolodithienylpyrromethene-dialkynyl borane dyes. *Org. Lett.* **2007**, 9, 737-740.

357. Donyagina, V.F., Shimizu, S., Kobayashi, N. & Lukyanets, E.A. Synthesis of N,N-difluoroboryl complexes of 3,3′-diarylazadiisoindolylmethenes. *Tetrahedron Lett.* **2008**, 49, 6152-6154.

358. Umezawa, K., Nakamura, Y., Makino, H., Citterio, D. & Suzuki, K. Bright, color-tunable fluorescent dyes in the visible-near-infrared region. *J. Am. Chem. Soc.* **2008**, 130, 1550-1551.

359. Umezawa, K., Matsui, A., Nakamura, Y., Citterio, D. & Suzuki, K. Bright, color-tunable fluorescent dyes in the Vis/NIR region: establishment of new "tailor-made" multicolor fluorophores based on borondipyrromethene. *Chem. Eur. J.* **2009**, 15, 1096-1106.

360. Awuah, S.G., Polreis, J., Biradar, V. & You, Y. Singlet oxygen generation by novel NIR BODIPY dyes. *Org. Lett.* **2011**, 13, 3884-3887.

361. Lu, H., Shimizu, S., Mack, J., Shen, Z. & Kobayashi, N. Synthesis and spectroscopic properties of fused-ring-expanded aza-boradiazaindacenes. *Chem. Asian J.* **2011**, 6, 1026-1037.

362. Yu, C. et al. Isoindole-BODIPY dyes as red to near-infrared fluorophores. *Chem. Eur. J.* **2012**, 18, 6437-6442.

363. Sarma, T., Panda, P.K. & Setsune, J. Bis-naphthobipyrrolylmethene derived BODIPY complex: an intense near-infrared fluorescent dye. *Chem. Commun.* **2013**, 49, 9806-9808.

364. Qian, G. & Wang, Z.Y. Near-infrared organic compounds and emerging applications. *Chem. Asian J.* **2010**, 5, 1006-1029.

365. Karpenko, I.A. et al. Squaraine as a bright, stable and environment-sensitive far-red label for receptor-specific cellular imaging. *Chem. Commun.* **2015**, 51, 2960-2963.

366. Sreejith, S., Carol, P., Chithra, P. & Ajayaghosh, A. Squaraine dyes: a mine of molecular materials. *J. Mater. Chem.* **2008**, 18, 264-274.

367. Ajayaghosh, A. Chemistry of squaraine-derived materials: near-IR dyes, low band gap systems, and cation sensors. *Acc. Chem. Res.* **2005**, 38, 449-459.

368. Basheer, M.C. et al. Design and synthesis of squaraine based near infrared fluorescent probes. *Tetrahedron* **2007**, 63, 1617-1623.

369. Umezawa, K., Citterio, D. & Suzuki, K. A Squaraine-based Near-infrared Dye with Bright Fluorescence and Solvatochromic Property. *Chem. Lett.* **2007**, 36, 1424-1425.

370. Umezawa, K., Citterio, D. & Suzuki, K. Water-soluble NIR Fluorescent Probes Based on Squaraine and Their Application for Protein Labeling. *Anal. Sci.* **2008**, 24, 213-217.

371. Chandrasekaran, Y., Dutta, G.K., Kanth, R.B. & Patil, S. Tetrahydroquinoxaline based squaraines: Synthesis and photophysical properties. *Dyes Pigm.* **2009**, 83, 162-167.

372. Mayerhoffer, U., Fimmel, B. & Wurthner, F. Bright near-infrared fluorophores based on squaraines by unexpected halogen effects. *Angew. Chem. Int. Ed.* **2012**, 51, 164-167.

373. Hu, L., Yan, Z. & Xu, H. Advances in synthesis and application of near-infrared absorbing squaraine dyes. *RSC Adv.* **2013**, 3, 7667-7676.

374. Langhals, H. An unexpectedly simple NIR dye for 1.1 microm with a central mesoionic structure. *Angew. Chem. Int. Ed.* **2003**, 42, 4286-4288.

375. Tian, M. et al. Discovery of novel dyes with absorption maxima at 1.1 microm. *J. Am. Chem. Soc.* **2003**, 125, 348-349.

376. Kolmakov, K. et al. Far-Red Emitting Fluorescent Dyes for Optical Nanoscopy: Fluorinated Silicon-Rhodamines (SiRF Dyes) and Phosphorylated Oxazines. *Chem. Eur. J.* **2015**, 21, 13344-13356.

377. Grimm, J.B. et al. Bright photoactivatable fluorophores for single-molecule imaging. *Nat. Methods* **2016**, 13, 985-988.

378. Grimm, J.B., Brown, T.A., Tkachuk, A.N. & Lavis, L.D. General Synthetic Method for Si-Fluoresceins and Si-Rhodamines. *ACS Cent. Sci.* **2017**, 3, 975-985.

379. Ikeno, T., Nagano, T. & Hanaoka, K. Silicon-substituted Xanthene Dyes and Their Unique Photophysical Properties for Fluorescent Probes. *Chem. Asian J.* **2017**, 12, 1435-1446.

380. Liu, X. et al. Aziridinyl Fluorophores Demonstrate Bright Fluorescence and Superior Photostability by Effectively Inhibiting Twisted Intramolecular Charge Transfer. *J. Am. Chem. Soc.* **2016**, 138, 6960-6963.

381. Kolmakov, K. et al. A Versatile Route to Red-Emitting Carbopyronine Dyes for Optical Microscopy and Nanoscopy. *Eur. J. Org. Chem.* **2010**, 2010, 3593-3610.

382. Koide, Y., Urano, Y., Hanaoka, K., Terai, T. & Nagano, T. Evolution of group 14 rhodamines as platforms for near-infrared fluorescence probes utilizing photoinduced electron transfer. *ACS Chem. Biol.* **2011**, 6, 600-608.

383. Koide, Y. et al. A reversible near-infrared fluorescence probe for reactive oxygen species based on Te-rhodamine. *Chem. Commun.* **2012**, 48, 3091-3093.

384. Koide, Y. et al. Development of NIR fluorescent dyes based on Si-rhodamine for in vivo imaging. *J. Am. Chem. Soc.* **2012**, 134, 5029-5031.

385. Wang, T. et al. Spirolactonized Si-rhodamine: a novel NIR fluorophore utilized as a platform to construct Si-rhodamine-based probes. *Chem. Commun.* **2012**, 48, 8781-8783.

386. Lukinavicius, G. et al. A near-infrared fluorophore for live-cell super-resolution microscopy of cellular proteins. *Nat. Chem.* **2013**, 5, 132-139.

387. Pastierik, T., Sebej, P., Medalova, J., Stacko, P. & Klan, P. Near-infrared fluorescent 9-phenylethynylpyronin analogues for bioimaging. *J. Org. Chem.* **2014**, 79, 3374-3382.

388. Jia, C. et al. An experimental and computational study on intramolecular charge transfer: a tetrathiafulvalene-fused dipyridophenazine molecule. *Chem. Eur. J.* **2007**, 13, 3804-3812.

389. Velusamy, M., Thomas, K.R.J., Lin, J.T. & Wen, Y.S. Benzo[1,2,5]selenadiazole bridged amines: electro-optical properties. *Tetrahedron Lett.* **2005**, 46, 7647-7651.

390. Ono, K., Tanaka, S. & Yamashita, Y. Benzobis(thiadiazole)s Containing Hypervalent Sulfur Atoms: Novel Heterocycles with High Electron Affinity and Short Intermolecular Contacts between Heteroatoms. *Angew. Chem. Int. Ed.* **1994**, 33, 1977-1979.

391. Karikomi, M., Kitamura, C., Tanaka, S. & Yamashita, Y. New Narrow-Bandgap Polymer Composed of Benzobis(1,2,5-thiadiazole) and Thiophenes. *J. Am. Chem. Soc.* **1995**, 117, 6791-6792.

392. Qian, G. et al. Band Gap Tunable, Donor–Acceptor–Donor Charge-Transfer Heteroquinoid-Based Chromophores: Near Infrared Photoluminescence and Electroluminescence. *Chem. Mater.* **2008**, 20, 6208-6216.

393. Qian, G. et al. Simple and Efficient Near-Infrared Organic Chromophores for Light-Emitting Diodes with Single Electroluminescent Emission above 1000 nm. *Adv. Mater.* **2009**, 21, 111-116.

394. Yao, L. et al. Highly efficient near-infrared organic light-emitting diode based on a butterfly-shaped donor-acceptor chromophore with strong solid-state fluorescence and a large proportion of radiative excitons. *Angew. Chem. Int. Ed.* **2014**, 53, 2119-2123.

395. Yang, Y. et al. Near infrared organic light-emitting devices based on donor-acceptor-donor oligomers. *Appl. Phys. Lett.* **2008**, 93, 163305.

396. Qian, G. et al. Synthesis and Application of Thiadiazoloquinoxaline-Containing Chromophores as Dopants for Efficient Near-Infrared Organic Light-Emitting Diodes. *J. Phys. Chem. C* **2009**, 113, 1589-1595.

397. Ishi-i, T., Murakami, K., Imai, Y. & Mataka, S. Light-harvesting and energy-transfer system based on self-assembling perylene diimide-appended hexaazatriphenylene. *Org. Lett.* **2005**, 7, 3175-3178.

398. Secondo, P. & Fages, F. Design and synthesis of bismacrocyclic hexaazatriphenylene derivatives. *Org. Lett.* **2006**, 8, 1311-1314.

399. Luo, M. et al. Rational design, synthesis, and optical properties of film-forming, near-infrared absorbing, and fluorescent chromophores with multidonors and large heterocyclic acceptors. *Chem. Eur. J.* **2009**, 15, 8902-8908.

400. Antaris, A.L. et al. A small-molecule dye for NIR-II imaging. *Nat. Mater.* **2016**, 15, 235-242.

401. Thooft, A.M., Cassaidy, K. & VanVeller, B. A Small Push-Pull Fluorophore for Turn-on Fluorescence. *J. Org. Chem.* **2017**, 82, 8842-8847.

402. Hachiya, S., Asai, K. & Konishi, G.-i. Environment-responsive multicolor fluorescent dyes based on nitrophenyl or nitrophenylethynyl oligothiophene derivatives: correlation between fluorescence and π-conjugation length. *Tetrahedron Lett.* **2013**, 54, 3317-3320.

403. Shaya, J., Fontaine-Vive, F., Michel, B.Y. & Burger, A. Rational Design of Push-Pull Fluorene Dyes: Synthesis and Structure-Photophysics Relationship. *Chem. Eur. J.* **2016**, 22, 10627-10637.

404. Hammond, P.R. Laser dye DCM, its spectral properties, synthesis and comparison with other dyes in the red. *Opt. Commun.* **1979**, 29, 331-333.

405. Tong, H. et al. Color-tunable, aggregation-induced emission of a butterfly-shaped molecule comprising a pyran skeleton and two cholesteryl wings. *J. Phys. Chem. B* **2007**, 111, 2000-2007.

406. Huang, X., Guo, Z., Zhu, W., Xie, Y. & Tian, H. A colorimetric and fluorescent turn-on sensor for pyrophosphate anion based on a dicyanomethylene-4H-chromene framework. *Chem. Commun.* **2008**, 5143-5145.

407. Chen, W., Wright, B.D. & Pang, Y. Rational design of a NIR-emitting Pd(II) sensor via oxidative cyclization to form a benzoxazole ring. *Chem. Commun.* **2012**, 48, 3824-3826.

408. Richard, J.A., Massonneau, M., Renard, P.Y. & Romieu, A. 7-hydroxycoumarin-hemicyanine hybrids: a new class of far-red emitting fluorogenic dyes. *Org. Lett.* **2008**, 10, 4175-4178.

409. Yuan, L., Lin, W., Yang, Y. & Chen, H. A unique class of near-infrared functional fluorescent dyes with carboxylic-acid-modulated fluorescence ON/OFF switching: rational design, synthesis, optical properties, theoretical calculations, and applications for fluorescence imaging in living animals. *J. Am. Chem. Soc.* **2012**, 134, 1200-1211.

410. Yuan, L. et al. A unique approach to development of near-infrared fluorescent sensors for in vivo imaging. *J. Am. Chem. Soc.* **2012**, 134, 13510-13523.

411. Chen, H., Lin, W., Cui, H. & Jiang, W. Development of unique xanthene-cyanine fused near-infrared fluorescent fluorophores with superior chemical stability for biological fluorescence imaging. *Chem. Eur. J.* **2015**, 21, 733-745.

412. Wei, Y. et al. Design of NIR Chromenylium-Cyanine Fluorophore Library for "Switch-ON" and Ratiometric Detection of Bio-Active Species In Vivo. *Anal. Chem.* **2016**, 88, 1842-1849.

413. Nolde, F. et al. Synthesis and modification of terrylenediimides as high-performance fluorescent dyes. *Chem. Eur. J.* **2005**, 11, 3959-3967.

414. Heek, T., Wurthner, F. & Haag, R. Synthesis and optical properties of water-soluble polyglycerol-dendronized rylene bisimide dyes. *Chem. Eur. J.* **2013**, 19, 10911-10921.

415. Langhals, H. An approach to novel NIR dyes utilising α-effect donor groups. *Dyes Pigm.* **2003**, 59, 109-116.

416. Jiao, C. et al. Bis-N-annulated quaterrylenebis(dicarboximide) as a new soluble and stable near-infrared dye. *Org. Lett.* **2009**, 11, 4508-4511.

417. Wu, D. et al. A core-modified rubyrin with meso-aryl substituents and phenanthrene-fused pyrrole rings: a highly conjugated near-infrared dye and Hg2+ probe. *Angew. Chem. Int. Ed.* **2008**, 47, 193-197.

418. Zhu, X.J., Fu, S.T., Wong, W.K., Guo, J.P. & Wong, W.Y. A near-infrared-fluorescent chemodosimeter for mercuric ion based on an expanded porphyrin. *Angew. Chem. Int. Ed.* **2006**, 45, 3150-3154.

419. Zhu, X., Fu, S., Wong, W.-K. & Wong, W.-Y. A near-infrared fluorescent chemodosimeter for silver(I) ion based on an expanded porphyrin. *Tetrahedron Lett.* **2008**, 49, 1843-1846.

420. Borisov, S.M., Zenkl, G. & Klimant, I. Phosphorescent platinum(II) and palladium(II) complexes with azatetrabenzoporphyrins-new red laser diode-compatible indicators for optical oxygen sensing. *ACS Appl. Mater. Interfaces* **2010**, 2, 366-374.

421. Barbieri, A., Bandini, E., Monti, F., Praveen, V.K. & Armaroli, N. The Rise of Near-Infrared Emitters: Organic Dyes, Porphyrinoids, and Transition Metal Complexes. *Top. Curr. Chem.* **2016**, 374, 47.

422. Yan, L., Zhang, Y., Xu, B. & Tian, W. Fluorescent nanoparticles based on AIE fluorogens for bioimaging. *Nanoscale* **2016**, 8, 2471-2487.

423. Yuan, Y., Xu, S., Cheng, X., Cai, X. & Liu, B. Bioorthogonal Turn-On Probe Based on Aggregation-Induced Emission Characteristics for Cancer Cell Imaging and Ablation. *Angew. Chem. Int. Ed.* **2016**, 55, 6457-6461.

424. Han, G., Kim, D., Park, Y., Bouffard, J. & Kim, Y. Excimers beyond pyrene: a far-red optical proximity reporter and its application to the label-free detection of DNA. *Angew. Chem. Int. Ed.* **2015**, 54, 3912-3916.

DEVELOPING DYE-HCRBPII COMPLEXES INTO NO-WASH BACKGROUND-FREE NEAR-INFRARED TAGS VIA PHOTOSWITCHING.

In **0** we described the broad scope of available FP variants that cover the entire visible spectrum. These FPs are sufficiently bright and have been applied in a variety of biomedical research fields. Tsien's review article provides an excellent guide on how to select the optimal FP for a specific experiment.[1] Nonetheless, FPs still have certain pitfalls that may affect the physiology of the POIs or have interference on the experiments due to their suboptimal features.[2, 3]

For example, the Stokes shifts of FPs are usually small. And small Stokes shifts will have significant overlap in the absorption and emission spectra, resulting in self-quenching, or the re-absorption of the emitted photons by adjacent FP molecules. Therefore, the imaging depth and overall emission brightness are severely limited. The emission wavelength of FPs is also a concern. As discussed in **Section I.4**, near-infrared light is more advantageous for deep tissue and whole body imaging. In the anthozoan family, DsRed derived FPs can emit into far-red but not NIR. Recently biliverdin-binding phytochrome derived NIR FPs have emerged to solve the problem, however, with limited brightness. Because the fluorophore is formed either innately or upon binding with exogenous factors, its maturation time can vary from a couple of minutes to several hours, depending on the FP that is chosen. This mild-to-slow maturation time also limits their application in the real-time imaging of transient biological events. Moreover, the requirement of molecular oxygen in the fluorophore maturation of metazoan FPs (see **Section I.1.1**) also limits their use in some anaerobic experiment settings.[4] Besides, the

metazoan FPs share a size of ~ 240 amino acids, and the phytochrome FPs are commonly larger than 55 kDa. Although extensive efforts have been put to develop monomeric FPs, their large sizes and the intrinsic oligomerizing nature lead to the concern of POI perturbation.[5] Recently, it was observed by Landgraf *et al.* that fused FPs will also cause the mislocalization of POIs.[6]

Fluorescent protein tags can be generated by introducing exogenous fluorophores into the protein binding pocket to furnish a complex tag, such as the bilirubin-binding UnaG derived from Japanese eel muscle,[7] and the biliverdin-binding NIR phytochromes (**Section I.4.1**). Similar strategies have been discussed in **Section I.3.2**. The combination of genetically addressable protein tags with photophysically and/or photochemically tunable synthetic ligands should open a wide window for the development of novel imaging tags.

I.5 Preliminary work towards the hCRBPII-based fluorescent tag

In 2012, our group reported the wavelength regulation of all-*trans*-retinal when bound to the type II human cellular retinoid binding protein (hCRBPII).[8] hCRBPII complexes with retinal through the imine formation of its active lysine 108 and the aldehyde group of retinal. The complex is protonated under physiological pH to form an iminium, or protonated Schiff base (PSB). The absorption wavelength of this retinylidene PSB can span from 425 nm to 644 nm by mutating the highlighted key residues in **Figure II-1**. The ligand-protein interactions that lead to the wide wavelength span are attributed to the collective effect of electrostatic perturbation and steric restraints produced by either polar or bulky residues. The tight binding pocket also provides highly reserved water

molecules to mediate specific hydrogen-bonding networks that further maneuver the ligand-protein interaction. hCRBPII can also tolerate a high level of mutations and maintain its correct fold.[9] In this context, by replacing all-*trans*-retinal with different synthetic dyes, hCRBPII can serve as a robust platform to design novel fluorescent complexes based on various fluorophore-protein interactions. Besides, hCRBPII has certain advantages over FPs and previously discussed protein-based tags. It is 133 amino acids and about 15 KDa in weight, only half of metazoan FPs. The ligand conjugation is not oxygen dependent. Both traits can complement the current fluorescent tagging methodologies.

As a proof of concept, the merocyanine **MCRA** was synthesized to conjugate hCRBPII and type II cellular retinoic acid binding protein (CRABPII), which is also a small

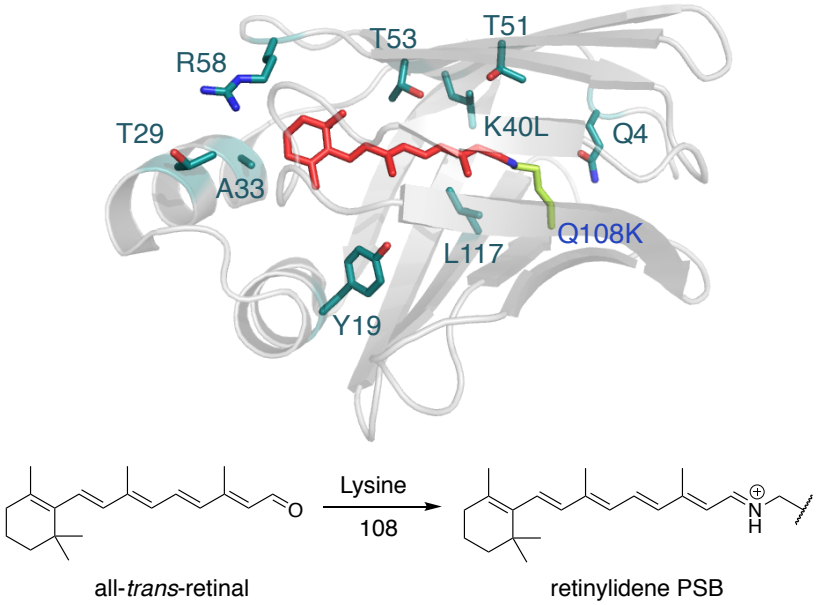


Figure 0-1 Crystal structure of hCRBPII KL mutant complexed with all-*trans*-retinal. Retinal is shown in red. The active lysine residue Q108K is shown in light green. Other key residues engineered to regulate the absorption wavelength of the bound retinylidene are shown in teal, with oxygen atoms colored red and nitrogen atoms colored blue (PDB ID: 4EXZ). The scheme shows the iminium (PSB) formation between lysine 108 and retinal aldehyde.

cytosolic lipid binding protein and is a structural homologue of hCRBPII but with a deeper binding cavity.[10] Structurally, **MCRA** has a polyenal tail that is similar to retinal (highlighted blue in **Figure II-2**). **MCRA** binds to both proteins through the similar iminium formation. The formed PSB contains two nitrogens connected through a pentamethine chain that is similar to Cy5 dye (highlighted red in **Figure II-2**). The optical features were examined with a variety of mutants. The use of these complexes as potential fluorescent imaging tags was demonstrated by fluorescence imaging with both *E. coli* and mammalian cells. With extensive protein engineering, the binding time of **MCRA** to hCRBPII mutants can be shortened to less than 1 minute. The optimized imaging condition is to use 250 nM **MCRA** as the staining concentration for HeLa, U2OS, and COS-7 cells and incubate at 37 °C for 1 min,[11] then wash with DPBS to remove excess **MCRA**. Imaging of subcellular compartments such as nuclei and cytosol have been realized by targeting the hCRBPII mutant with signaling peptides like nucleus-localizing sequence (NES) and nucleus-

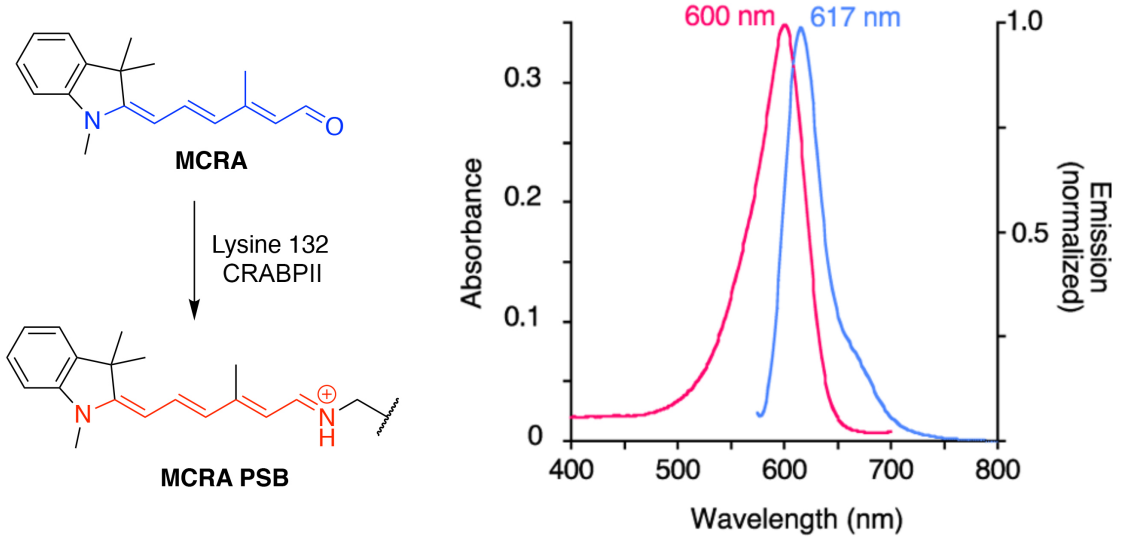


Figure 0-2 Structure of **MCRA** and its schematic PSB formation with active lysine 132 of CRABPII. The absorption (red) and emission (blue) spectra are of the R132K:R111L (KL) mutant complex with **MCRA**.

exclusion sequence (NES). We were also able to show that the binding rate and pK_a can be manipulated by the rational mutagenesis of hCRBPII.[11]

To this end, the concept of developing fluorescent tags based on the small cytosolic hCRBPII protein proved successful. hCRBPII shows potential as a robust platform for this purpose. However, in view of practical application, this is just the beginning. As represented by the CRABPII-KL mutant in **Figure II-2**, the absorption maxima of the **MCRA** complexes with either hCRBPII or CRABPII are centered around 600 nm, no matter the nature of mutations in the binding cavity.[12] Another issue is that they often show Stokes shifts smaller than 30 nm. Furthermore, incubating **MCRA** for a prolonged time leads to non-specific fluorescence background at the same emission wavelength.[11] This background cannot be diminished by extra washing steps and is generated from the non-specific binding of **MCRA** with other proteins in the cell. In this context, novel fluorescent ligands are needed to overcome these issues and meet the requirements of real-world live cell imaging experiments.

I.6 The requirements of a successful fluorescence imaging tag

As an opening remark to the development of novel hCRBPII-based imaging tags, the major requirements from different perspectives can be summarized as followed.

Photophysically, a successful system needs to exhibit high extinction coefficient and high fluorescence quantum yield. The product of these two determines the absolute brightness, which is the overarching goal for an imaging tag. A large Stokes shift is also desired. As previously discussed, the large Stokes shift can prevent self-absorption of the emitting photons and effectively increase the overall imaging depth into the cell or tissue.

In addition, well separated excitation and emission wavelengths can avoid crosstalk between the excitation light source and the emission detector in the microscope setup. The third photophysical requirement is the far-red and/or NIR wavelengths. The redder the light, the less scattering is observed in the biological tissue. Moreover, the NIR window provides the longest light penetration depth due to the minimal absorption of haemoglobins and water, as described in **Section I.4**. And the least energy-intense far-red/NIR excitation light can assure the minimal phototoxicity to the living cells or tissues. Together, these features can secure the highest tissue transparency for fluorescence imaging.

Chemically, labeling specificity is the major concern. Different from genetically encoded FPs, tags requiring the supplementation of exogenous synthetic ligands always face this challenge. The off-target labeling will cause non-specific fluorescence signals from proteins other than POIs. The other portion of non-specific fluorescence background comes from the excess dyes or fluorophores that reside in either the hydrophobic compartments or the hydrophilic environments, depending on their chemical natures. To overcome this, extensive washing steps are normally required in a typical dye-staining fluorescence imaging experiment to remove the excess dyes after incubation. These time-consuming washing steps can damage the biological sample, increase the complexity of the experiment, and prevent the signal capture of transient biological events. In this context, fluorogenicity, or the ability to activate fluorescence after labeling, are much desired to enable no-wash imaging experiments.

Another important photochemical feature of an advanced imaging tag is the “on/off” switchability of the fluorescence. Extended from the fluorogenicity, if the fluorescence can be turned on and off iteratively by fast photochemical transformations, then the spatiotemporal control of the fluorescence signals can be realized. More importantly, the controllable “on/off” switchability is the key requirement of the tags applied in localization-based super-resolution microscopic technologies like PALM and STORM.[13] Other important chemical features of the tag are fast labeling kinetics and high photostability. In combination with fluorogenicity, the former one enables the fast imaging of biological events. The latter one is essential for allowing the proper imaging duration with the tag.

Mentioned last but not trivial, biologically the dye should elicit least cytotoxicity and high cell permeability. The size of the tag needs to be small so as not to interfere with regular biological functionalities of the tagged POIs. hCRBPII certainly is advantageous in this perspective.

I.7 Early attempts in finding fluorescent ligands for hCRBPII

What is the optimal fluorophoric ligand of hCRBPII that can meet so many requirements as described in **Section I.6**? There is no clear answer. It is extremely challenging to predict which molecular scaffold will be fluorescent before its synthesis and examination. Even with the same scaffold, different substituents can lead to drastically different fate of fluorescence. Very recently, the Japan OLED firm Kyulux has secured the license of Harvard’s machine learning AI *Molecular Space Shuttle* for the high throughput virtual screening of potential chemical candidates for thermally activated delayed fluorescence (TADF). This AI, developed by a collaborative team between Harvard,

Samsung, and MIT, combines the state-of-art TD-DFT calculation and machine learning, and is set up on a space of 1.6 million molecules. It can screen for candidates with optimal TADF features such as singlet-triplet energy barrier, radiative rate, and thus EQE.[14] Unfortunately, it is not feasible to duplicate this approach for the design of suitable sets of fluorescent ligands for hCRBPII with our current computational capacity.

Considering the shape and size of all-*trans*-retinal that is embedded inside hCRBPII mutants, the spatial volume of the binding cavity is tight and limited (**Figure II-3**). As described in **Section I.4.2**, the regular NIR dyes are large scaffolds except for polymethine cyanines. However, as exemplified by **MCRA**, the highly resonating cyanine scaffold distributes the positive charge almost homogenously along the chain and has the least bond alternation. The result is minimized dipole moment change when the molecule is excited from S_0 to S_1, thus featuring the characteristically small Stoke shift.

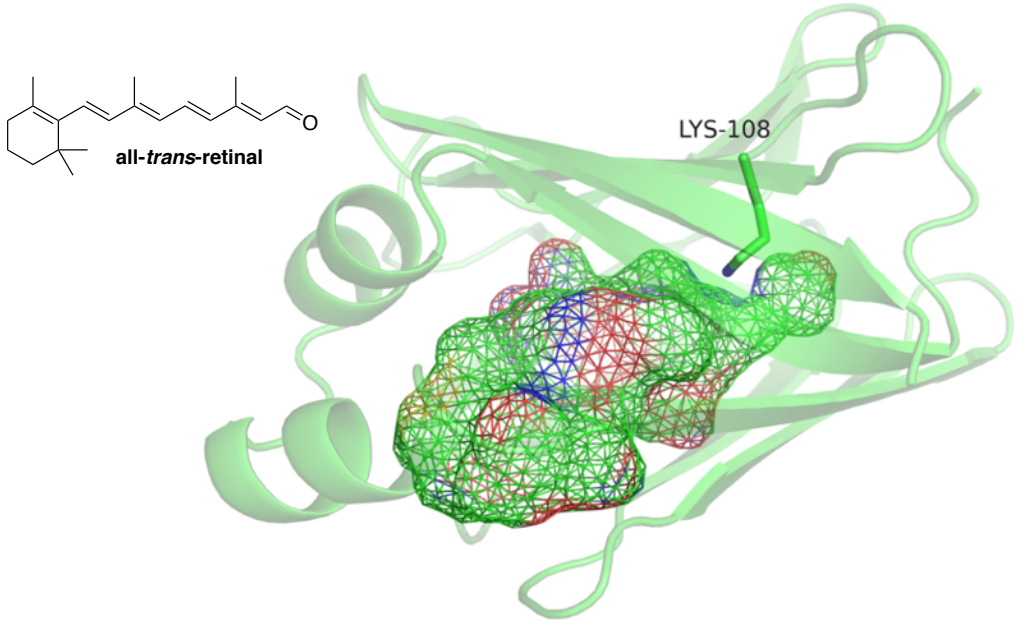
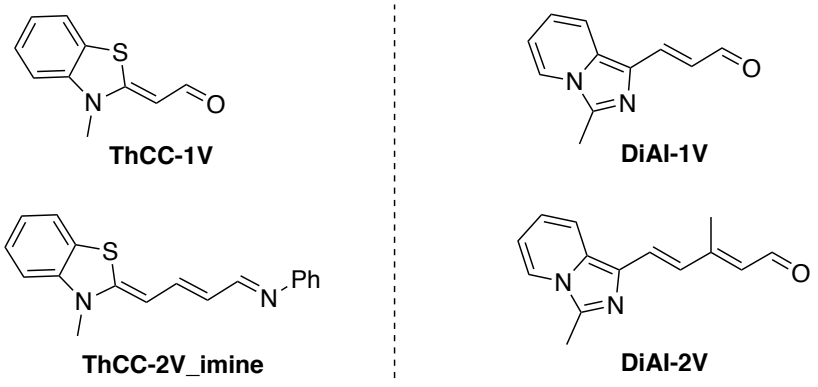


Figure 0-3 Crystal structure of hCRBPII-KL (Q108K:K40L) mutant, highlighting the cavity for ligand binding (meshed cages). PDB ID: 4EXZ. The bound all-*trans*-retinal is deleted for clarity.

As an important structural feature of retinal, the vinylene group conjugated with aldehyde can be essential for setting the correct binding trajectory. The π-extension leads to an expected red-shift, for both the absorption and emission wavelengths as long as the main scaffold is fluorescent. Keep these in mind, the first attempt of modifying the **MCRA** structure for increased Stokes shift was to make isoelectronic structures of the indolinium head group of **MCRA**. Shown in **Scheme II-1**, the first series to be tested is the thiacarbocyanine (ThCC) **MCRA** analogue by substituting the indolium C3 to sulfur. **ThCC-1V** was synthesized by basic hydrolysis of the Vilsmeier-Haack product of 2,3-dimethylbenzothiazolium. However, due to very weak electrophilicity of the aldehyde group, none of the regular Grignard, Wittig, and Hornor-Wadsworth-Emmons (HWE) reactions were successful in extending the polymethine chain. Alternatively, the condensation between 2,3-dimethylbenzothiazolium and dianil malonaldehyde followed by basic hydrolysis afforded **ThCC-2V** phenylimine with 87% purity mixed with **ThCC-2V** aldehyde. Complete hydrolysis and further purification was not fruitful and only yielded degraded side products.



Scheme 0-1 Structures of thiacarbocyanines (**ThCC**s) and diazaindenes (**DiAl**s), with different number of vinylene insertions between the head group and the aldehyde.

The second series is the diazaindene-derived isoelectronic analogues of **ThCC**. **DiAI-1V** and **DiAI-2V** are synthesized by the HWE reaction of 1-formyl-3-methyl [2,3a]diazaindene followed with DIBAL reduction. These reactions yielded different ratio of *Z/E* isomers. Tremendous effort was invested for the purification of the final products. However, when **DiAI-2V** was bound to different hCRBPII mutants, the resulting absorption/emission spectra showed no significant differences from those of **MCRA**.

Table 0-1 Spectral features of selected **DiAI-2V**/hCRBPII complexes.

Entry	hCRBPII mutant	$\lambda_{abs,\ SB}$ (nm)	$\lambda_{em,\ SB}$ (nm)	$\lambda_{abs,\ PSB}$ (nm)	$\lambda_{em,\ PSB}$ (nm)	Φ_{PSB}[a]	$t_{1/2}$[b] (min)
1	Q108K:K40L:T51V:T53A:R58Y	-	-	594	621	7.1	n.d.[c]
2	Q108K:K40L:T51V:T53S:Y19W:R58W	-	-	597	619	9.2	577
3	Q108K:K40L:T51V:T53S:Y19W:R58W:T29L	-	-	597	619	8.1	n.d.
4	Q108K:K40L:T51V:T53S:Y19W:R58W:L117E	-	-	530 (500)[d]	597	5.3	5.5
5	Q108K:K40L:T51V:T53S:Y19W:R58W:L117D	-	-	498 (530)	600	n.d.	n.d.
6	Q108K:K40L:T51V:T53S:Y19W:R58W:L117N	-	-	548	600	n.d.	n.d.
7	Q108K:K40L:T51V:T53S:Y19W:R58W:L119E	-	-	585	615	n.d.	n.d.
8	Q108K:K40L:T51V:T53S:Y19W:R58W:V62N	436	n.d.	591	618	7.3	n.d.
9	Q108K:K40L:T51V:T53S:Y19W:R58W:V62S	-	-	592	618	8.4	n.d.
10	Q108K:K40L:T51V:T53S:Y19W:R58W:V62E	-	-	585	617	5.7	40
11	Q108K:K40L:T51V:T53S:Y19W:R58W:V62N:L117E	443	n.d.	530	598	3.2	n.d.
12	Q108K:K40L:T51V:T53S:Y19W:R58W:V62E:L117E	443	n.d.	530	597	2.5	n.d.
13	Q108K:K40L:T51V:T53S:V62E	435	578	587	612	n.d.	n.d.
14	Q108K:K40L:T51V:T53S:L117E	440	n.d.	563	600	n.d.	n.d.
15	Q108K:K40L:T51A:T53S:V62E	439	604	583 (633)	611 (644)[e]	n.d.	n.d.
16	Q108K:K40L:T51A:T53S:V62N	-	-	631 (590)	644	18.1	n.d.
17	Q108K:K40L:T53S:V62E	438	n.d.	561	602	n.d.	n.d.
18	Q108K:K40L:T51C:T53S:V62N	-	-	579	613	n.d.	n.d.

[a]Relative quantum yield measurement in percentage. Referenced against Oxazine-170. [b]Ligand-mutant binding half-time, in PBS buffer (pH 7.3) at 23 °C. Exponential rising fits were used to derive $t_{1/2}$ with protein concentration at 20 μM and ligand concentration of 10 μM. [c]n.d.: not determined. [d]Wavelengths of absorption shoulders. [e]Emission maximum, excited at shoulder absorption wavelength.

Summarized in **Table II-1**, most of the tested mutants exhibited small Stokes shifts with nearly identical absorption and emission maxima of those of **MCRA**. The absorption maxima are mostly centered around 600 nm, and the Stokes shifts are about 30 ~ 50 nm. Nevertheless, special attention should be paid to some mutant complexes. When residue 117 is mutated to acidic glutamate in hCRBPII, the corresponding complexe shows a blue-shifted absorption maximum at 530 nm (entry 4 in **Table II-1**). Similarly, the 117D mutant (entry 5) also has the same hypsochromic effect but with the shoulder absorption becoming the maximum. The increased Stokes shift could be due to the electrostatic induction or potential hydrogen-bonding induced by 117E/D. Nonetheless, there is no further structural information for a clear conclusion.

Another important observation is highlighted with entry 13 and 15. As shown, when residue 62 is mutated to glutamate, a significant portion of **DiAI-2V** Schiff base (SB) is formed with absorption maximum around 440 nm. Similar behavior is also observed with some V62N and/or L117E mutants. The SB emission of these two mutants are 578 nm and 604 nm, respectively. Compared with the PSB emission wavelengths centered around 610 nm, the SB emissions are too red-shifted and resemble emission from a PSB with Stokes shifts greater than 140 nm. Although currently there is no regular SB emission to compare with, it is reasonable to hypothesize that the abnormally large Stokes shifts are rising from excited-state hydrogen bonding process of the imine nitrogen atom. Further observation and evidence will be discussed in **0**.

The live cell imaging performance of **DiAI-2V** was tested in HeLa cells. hCRBPII mutant Q108K:K40L:T51V:T53S:Y19W:R58W:L117E (KLVSWW:L117E) was chosen for

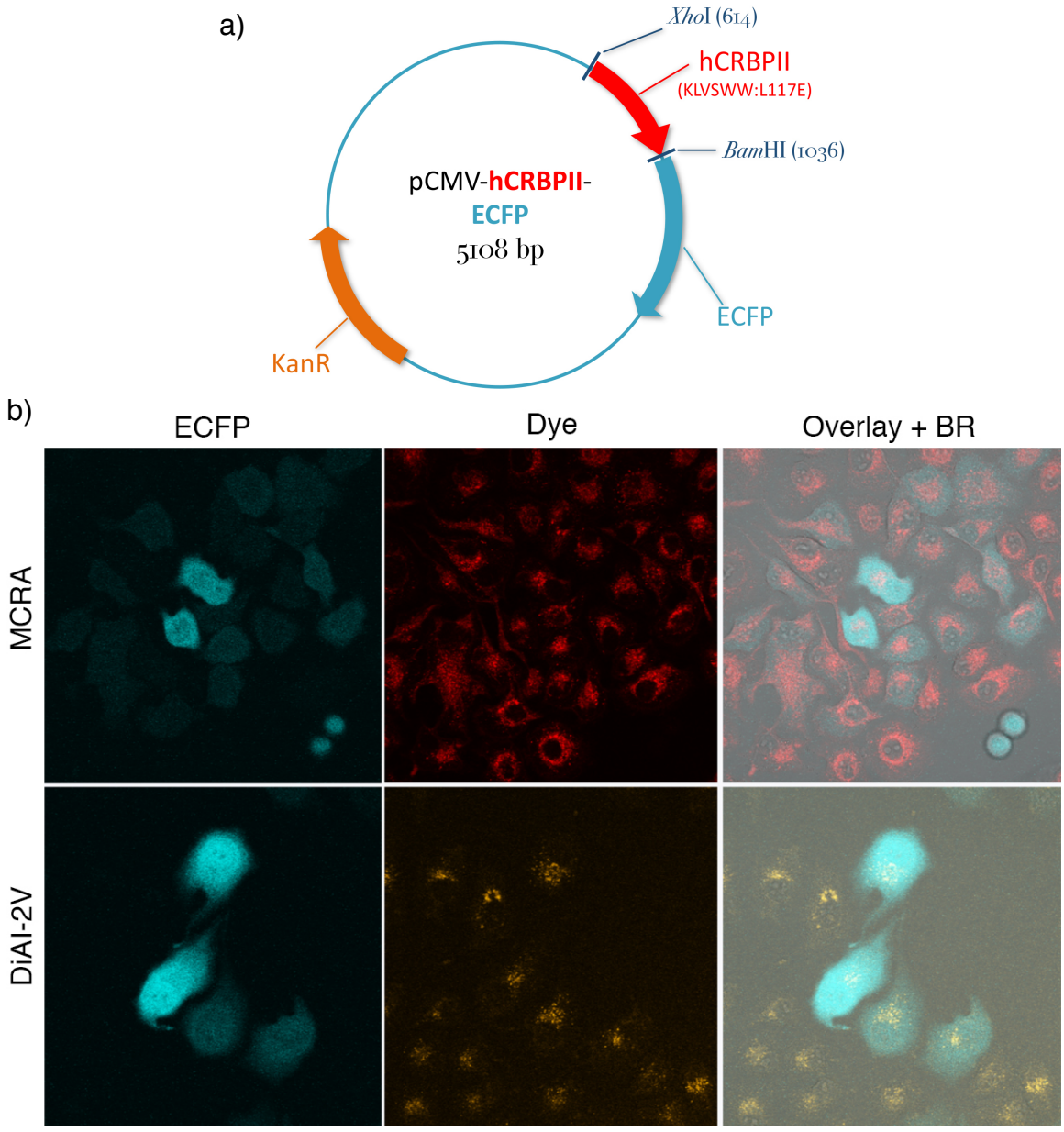


Figure 0-4 Live cell imaging with DiAI-2V and MCRA for performance testing. a) Clone map of hCRBPII mutant KLVSWW:L117E in ECFG-GalT vector. b) Comparison of images of DiAI-2V and MCRA complexed with KLVSWW:L117E in HeLa cells. Cells were stained with 250 nM of each dye and incubated for 10 min at 37 °C. Cells were washed with DPBS twice before imaging. ECFP channel: λex = 458 nm, BP 475-525. MCRA channel: λex = 594 nm, LP 615. DiAI-2V channel: λex = 514 nm, LP 560. BR: bright-field.

imaging because of its fast complex formation ($t_{½}$ = 5.5 min). The KLVSWW:L117E gene was cloned into an pECFP-N1 vector and inserted before the ECFP sequence (**Figure II-4a**). The hybrid construct was then expressed in HeLa cells by transient transfection.

As shown in **Figure II-4b**, **DiAI-2V** was tested against **MCRA**. The ECFP fluorescence was used as an internal reference for the whole cell staining. However, both **MCRA** and **DiAI-2V** showed significant non-specific background after 10 min incubation. As observed in the dye channels, **MCRA** mostly stains mitochondria and **DiAI-2V** predominantly stains cell nuclei. To this end, it can be concluded that **DiAI-2V** is not a suitable dye for the hCRBPII imaging purpose. It is limited by the low quantum yield, low brightness, orange emission color, relatively small Stokes shift, and most importantly, the lack of specific labeling aptitude. Thus, further structural modification and imaging optimization was not pursued.

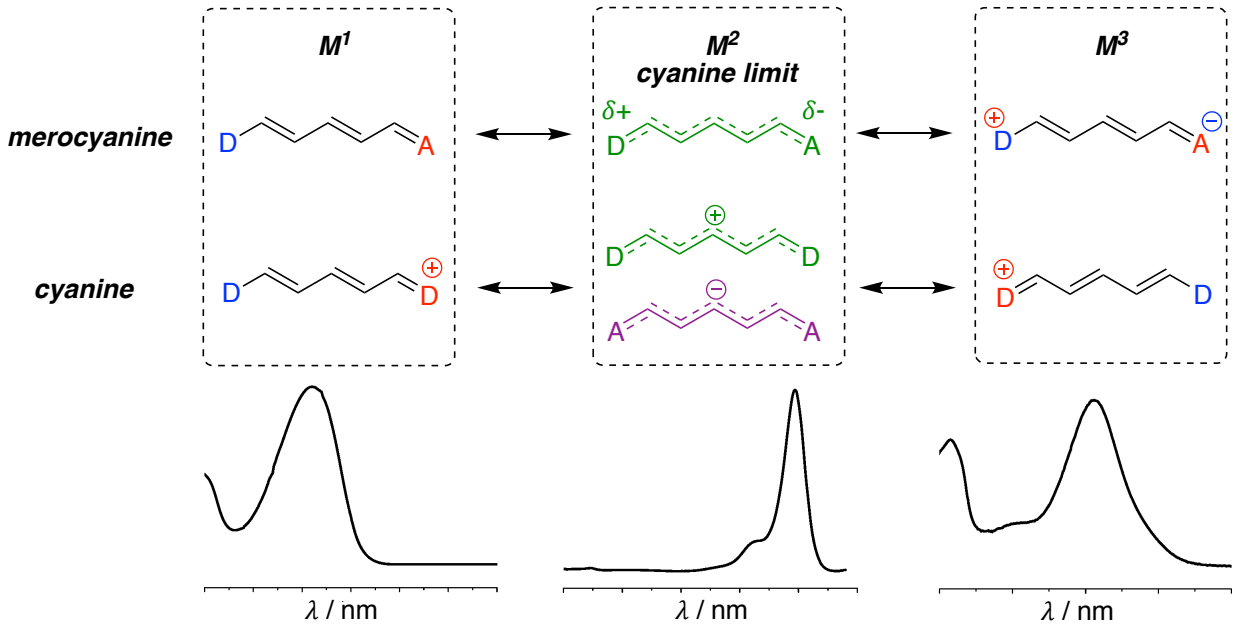


Figure 0-5 Different resonance forms proposed for push-pull chromophores and related shape of the absorption spectra. The charge distribution along the push-pull systems of merocyanines and cyanines are depicted by three states: M^1 (neutral for merocyanine, zwitterionic for cyanine), M^2 (least bond length alteration), and M^3 (bipolar for merocyanine, inverted zwitterionic for cyanine). Merocyanines are featured by one electron rich amine group (D, donor) and one more electronegative terminal group (A, acceptor) on either ends of the push-pull chain. Typical cyanines bear one neutral amine (D) and one charged iminium (A) on either ends of the push-pull chain.

I.8 Approach to NIR emission with large Stokes shift

Before devising new dye scaffold to reach large Stokes shift, it is important to understand the underlying reason for the small Stokes shift observed with **MCRA**. As discussed in the beginning of **Section I.7**, the evenly-dispersed charge along the polymethine chain determines the small Stokes shift of cyanines and merocyanines. Shown in **Figure II-5**, the electron push-pull merocyanine and cyanine structures can have three resonance limiting forms: the neutral state ***M¹***, the zwitterionic state ***M³***, and the ***M²*** state or the "cyanine limit".[15] The "cyanine limit" is featured by the least bond length alternation. Its absorption spectrum is characterized by very red-shifted sharp intense band. In contrast, the bipolar ***M³*** state is featured by a very strong electron donor and acceptor fragments, and a complete intramolecular charge transfer (ICT) occurring in the excited state. This betaine structure has the opposite maximized bond length alternation. Because of the continuous symmetry breaking, it is characterized by the broad intense absorption and shows strong solvatochromism.[16, 17] This is the basis of ICT-generated large Stokes shift.

Further contemplating the ICT transition (**Figure II-6**), if strong electron donor and acceptor fragments are installed on the two sides of a π-spacer, the local excitation (LE) of the molecule can elicit a strong dipole moment pointing from the acceptor to the donor moiety. But if the ICT occurs, an opposite dipole moment can be induced by the pair of split charges, minimizing the overall change in the dipole moment.[18] This will commonly result in a smaller energy gap between S_1 and S_0, and hence a bathochromic shift in the emission wavelength. Because the LE happens before the ICT transition, the absorption

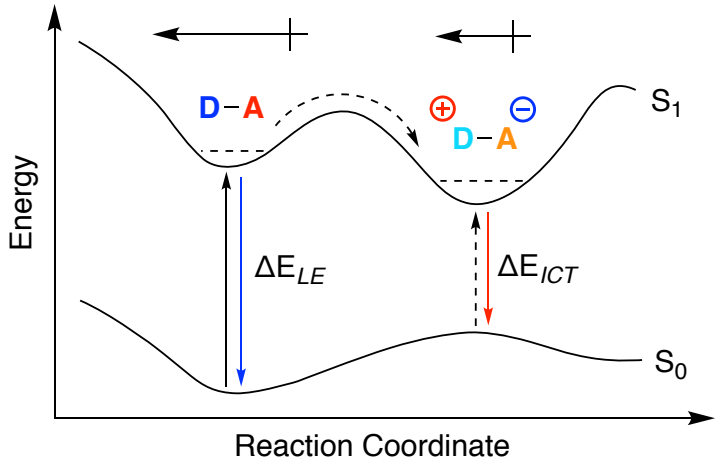
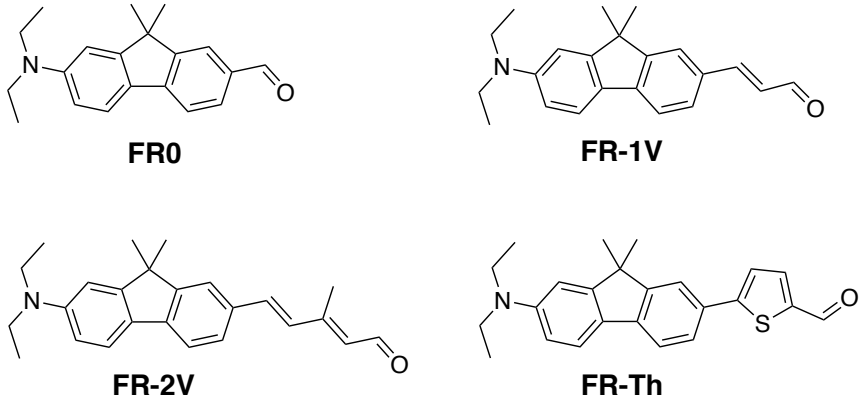


Figure 0-6 Schematic cross section of the ground state and the lowest excited singlet state potential hypersurfaces along the reaction coordinate corresponding to the ICT state model.

wavelength is not affected. This explains why the absorption maxima of solvatochromic compounds in various solvents are usually the same. Taking the solvent effect into consideration, the ICT state in S_1 can further be stabilized by the dipole moment reorientation of the surrounding solvent molecules to a different extent. Therefore, a positive solvatochromic (i.e., the emission wavelength shifts bathochromically with increasing solvent polarity) dye can have the most bathochromic shift in emission wavelength when in a polar solvent environment.[19] It should be noted that, the above discussion is limited to the planarized ICT (PLICT) transition.[20] Normally, if the donor and acceptor are not in the same plane in the excited state, a twisted ICT (TICT) can occur.[21] This TICT also results in large Stokes shift. But the larger the twist, the lower the fluorescence quantum yield, as the radiative decay becomes forbidden.[22]

Following this idea, a suitable dye scaffold to conjugate with hCRBPII for the far-red/NIR emission wavelength and large Stokes shift should feature a strong ICT character. Like enzymes, the cavity of hCRBPII is filled with highly ordered water molecule, making

a polar but not an aqueous environment. This environment could be expected to provide the bathochromic shift of the wavelength without a drastic quenching of fluorescence by highly exchangeable protons. Because of the difficulty to predict fluorescence properties, a feasible approach to get a candidate scaffold is to start with a bright ICT dye that has the potential to emit into the red wavelength region. An extensive literature research led to the selection of **FR0** scaffold for its extremely high quantum yield and relatively high extinction coefficient.[23] Shown in **Scheme II-2**, **FR0** has a simple structure. It has a diethylamino group as a strong electron donor, and a formyl group as a strong electron acceptor, spaced by a 9,9-dimethylfluorenyl fragment. The emission maximum of **FR0** spans from 434 nm to 573 nm in a variety of organic solvents ranging from non-polar toluene to very polar methanol. Different spacers were installed between the aldehyde group and the fluorenyl scaffold to red-shift the emission wavelength by extending the length of conjugation (**Scheme II-2**). Among these, **FR-1V** exhibits the optimal extinction coefficient, fluorescence quantum yield, and proper emission maxima (**Table II-2**). Although **FR-2V** is more red-shifted, its quantum yield is significantly decreased in various



Scheme 0-2 FR series of ICT dyes, derivatized from **FR0** with different lengths and types of π-spacers.

Table 0-2 Spectral features of **FR** dyes in different organic solvents.

	FR0			FR-1V		
	λ_{abs} (nm)	λ_{em} (nm)	Φ[a]	λ_{abs} (nm)	λ_{em} (nm)	Φ
Toluene	396	434	0.703	416	488	0.759
THF	392	470	0.802	414	537	0.796
Ethyl acetate	389	475	0.662	410	532	0.820
Dichloromethane	399	497	0.774	423	575	0.873
DMF	398	512	0.775	420	608	0.691
DMSO	402	526	0.763	425	614	0.725
Acetonitrile	393	523	0.745	415	605	0.638
Ethanol	396	556	0.664	420	633, 660	0.074
Methanol	396	573	0.445	420	669	0.024

	FR-2V			FR-Th		
	λ_{abs} (nm)	λ_{em} (nm)	Φ	λ_{abs} (nm)	λ_{em} (nm)	Φ
Toluene	428	559	0.675	417	503	0.879
THF	426	603	0.524	417	563	0.782
Ethyl acetate	422	600	0.555	412	561	0.770
Dichloromethane	435	634, 665	0.432	424	604	0.751
DMF	432	633, 669	0.167	424	663	0.473
DMSO	438	633, 672	0.175	429	672	0.278
Acetonitrile	425	630, 670	0.134	415	667	0.361
Ethanol	433	627, 667	0.021	419	604	0.027
Methanol	431	670	0.006	417	473	0.006

[a]Absolute fluorescence quantum yield measurement using Quantaurus-QY at room temperature.

solvents comparing to **FR-1V**, probably due to more rotational freedom along the polyene and increased vibrational levels. Besides, the yield of **FR-2V** is much lower than that of **FR-1V** due to more *Z/E* isomers and harder purification. When the diene spacer is locked by sulfur as a thiophene ring to furnish **FR-Th**, the emission maxima are blue-shifted and close to those of **FR-1V**, however with a much smaller extinction coefficient. More interestingly, from non-polar to polar aprotic solvents **FR-2V** and **FR-Th** exhibit positive solvatochromism, while a negative solvatochromism is observed when these two are dissolved in polar protic solvents like ethanol and methanol (i.e., the emission maxima are blue-shifted with increased solvent polarity). It is not clear at this stage the possible

photochemical transformation that leads to this phenomenon, but very likely the protonation is involved in the excited hypersurface. In this context, **FR-1V** stands out as the optimal candidate for further studies.

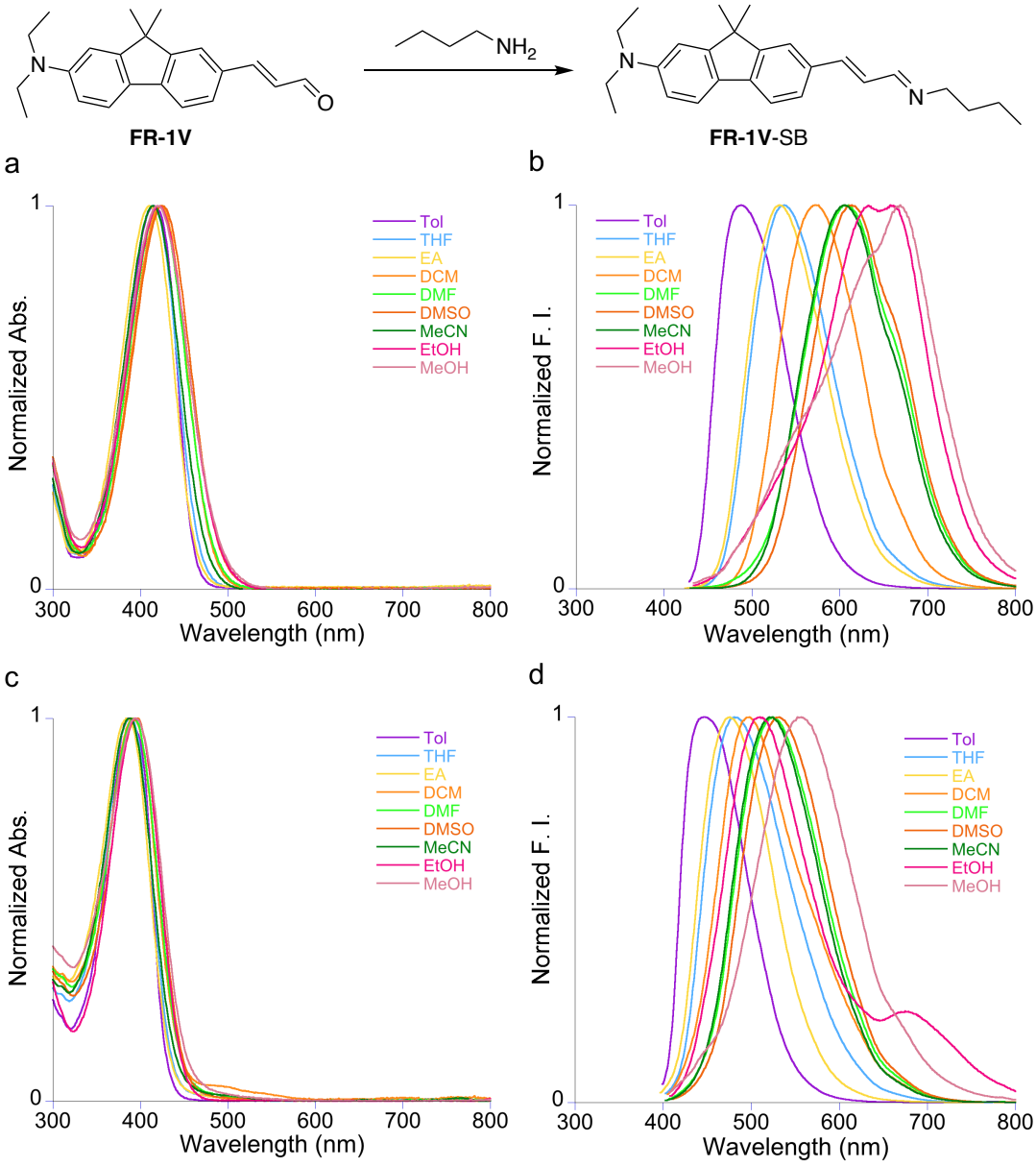


Figure 0-7 Normalized spectra of **FR-1V** in various solvents: (a) absorbance, (b) emission. Normalized spectra of **FR-1V**-SB (*n*-butylamine) in various solvents: (c) absorbance, (d) emission. Tol: toluene; THF: tetrahydrofuran; EA: ethyl acetate; DCM: dichloromethane; DMF: *N,N*-dimethyl formamide; DMSO: dimethyl sulfone; MeCN: acetonitrile; EtOH: ethanol; MeOH: methanol. Scheme shows the SB formation between **FR-1V** and *n*-butylamine.

As shown in **Table II-2**, the emission wavelength of **FR-1V** reaches the far-red/NIR region when dissolved in polar protic solvents, although we lack a direct comparison in aqueous solutions due to its very low solubility. Considering the previous discussion of ICT transition, it is expected that the electron withdrawing ability of the acceptor part will decrease when **FR-1V** forms imine with the active lysine 108 of hCRBPII. This is due to the replacement of oxygen to the less electronegative nitrogen and will lead to the hypsochromic shifts in both absorption and emission maxima to some extent. Following the same argument, the protonation of imine to iminium can effectively increase the electron withdrawing ability and further lower the band gap to reach more red-shifted wavelengths than those of the original **FR-1V** aldehyde.

To test this idea, *N*-butylamine is used as a surrogate of the active lysine 108 to bind with **FR-1V** and form the corresponding SB (**Figure II-7**). Spectral features are summarized in **Table II-3**. As expected, the *n*-butylimine exhibits hypsochromic shifts in both absorption and emission. The following up acidification of SB to PSB regains the bathochromic shifts as shown in **Figure II-8**. The absorption maximum is dramatically

Table 0-3 Spectral features of **FR-1V** and its SB in different solvents.

	FR-1V			**FR-1V**-SB[b]		
	λ_{abs} (nm)	λ_{em} (nm)	Φ[a]	λ_{abs} (nm)	λ_{em} (nm)	Φ
Toluene	416	488	0.759	386	447	0.622
THF	414	537	0.796	389	481	0.597
Ethyl acetate	410	532	0.820	384	476	0.595
Dichloromethane	423	575	0.873	391	498	0.685
DMF	420	608	0.691	393	525	0.658
DMSO	425	614	0.725	396	532	0.749
Acetonitrile	415	605	0.638	388	524	0.738
Ethanol	420	633, 660	0.074	394	510, 675	0.049
Methanol	420	669	0.024	393	557	0.065

[a]Absolute fluorescence quantum yield measurement. [b]*n*-butylimine.

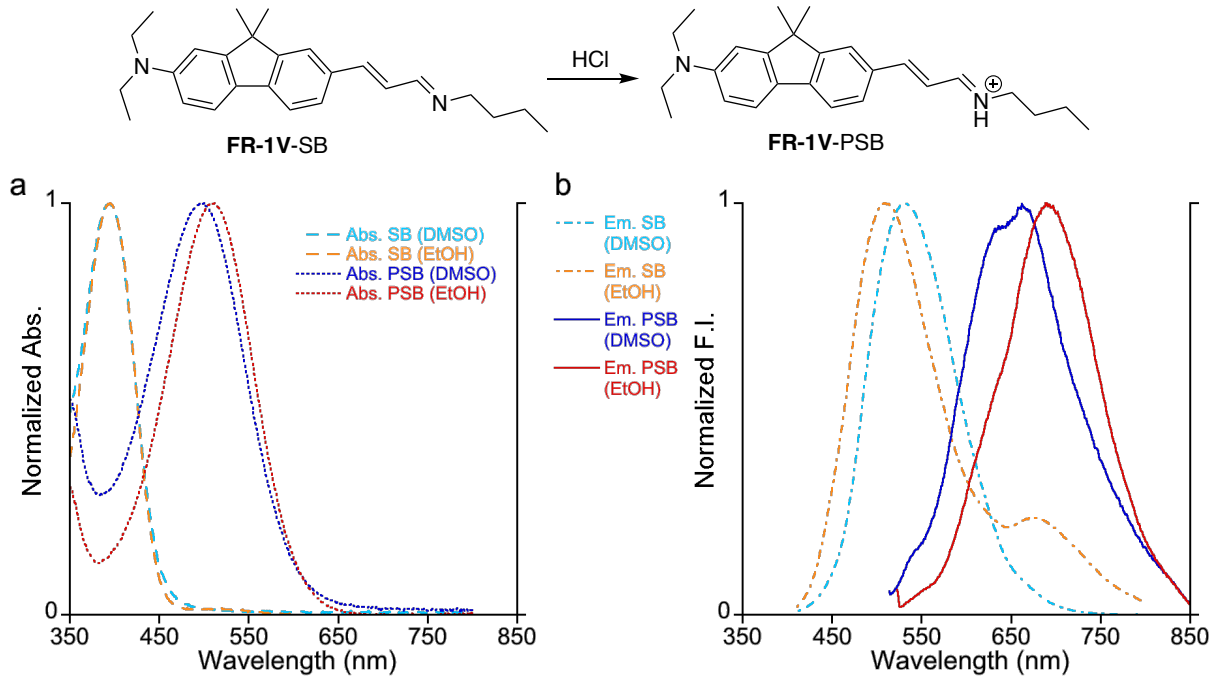


Figure 0-8 Comparison of (a) absorbance and (b) emission spectra of **FR-1V**-SB and **FR-1V**-PSB in DMSO and ethanol.

red-shifted from 396 nm to 496 nm in DMSO, and from 394 nm to 512 nm in ethanol, respectively. The emission maxima also display over 150 nm bathochromic shift into the NIR region (662 nm for DMSO and 690 nm for ethanol). The wavelengths are all redder than those of the original **FR-1V** (**Table II-4**).

We have so far proved the concept of employing ICT to approach NIR emission with large Stokes shift. The next move is to embedded **FR-1V** into hCRBPII and gain special functionalities while maintaining its optical properties.

Table 0-4 Wavelength comparison of **FR-1V** and its SB, PSB.

	FR-1V		**FR-1V**-SB		**FR-1V**-PSB	
	λ_{abs} (nm)	λ_{em} (nm)	λ_{abs} (nm)	λ_{em} (nm)	λ_{abs} (nm)	λ_{em} (nm)
DMSO	425	614	396	532	528	662
Ethanol	420	633, 660	394	510 (675)[a]	510	690

[a]Shoulder emission (see **0 Section I.14**).

I.9 Discovery of photochromic dye-hCRBPII complexes

As described in **Section I.7**, a large portion of the non-specific fluorescence background is from the non-selective imine formed between the dye's aldehyde group and non-target protein amine groups. It is inevitable to have these non-specific labeling due to the high reactivity of the aldehyde group, unless less reactive carbonyl is used instead. Therefore, to develop **FR-1V**-hCRBPII complexes into useful imaging tags, a different approach is needed to differentiate the emission of target hCRBPII complexes from other non-specific proteins.

In ethanol, the **FR-1V**-PSB (*n*-butyliminium) emission is 690 nm, but the SB emission is only at 510 nm. If there is a method to control the complexation of **FR-1V** exclusively as a PSB with hCRBPII and a SB with other proteins, then the background issue of off-target labeling can be solved by specifically imaging the PSB emission wavelength region. In addition, because of the large emission wavelength difference between **FR-1V** and its PSB, the fluorescence background from the extra dye residing in the hydrophobic cell compartments can be cut off simply by selecting the proper dichroic mirrors in the microscope. This will further enable a no-wash protocol for the live cell imaging. However, the initial **FR-1V** and hCRBPII mutants binding assays showed the formation of predominant SB while the PSB only forms as a limited fraction. Thus, we need an effective method to form PSB in favor of SB, preferably in a controllable manner.

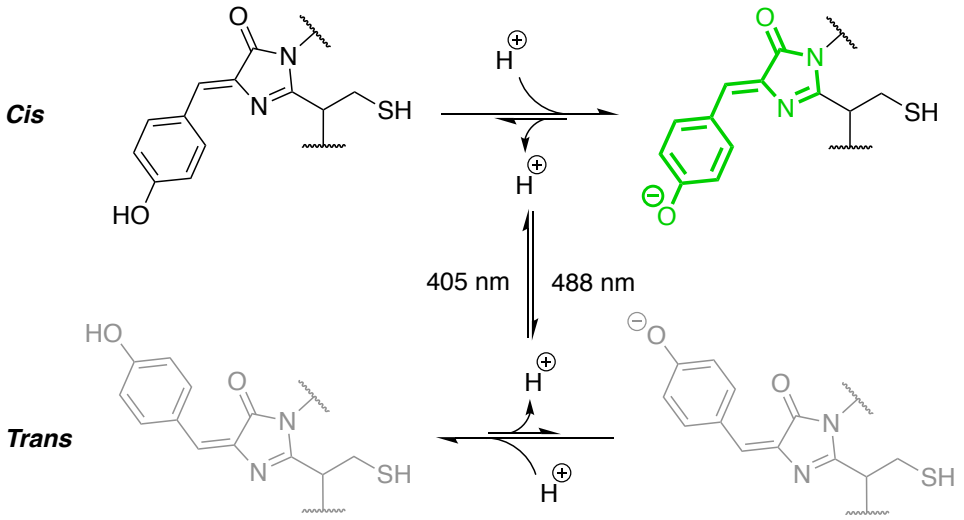
The switchable feature of the emitter fluorescence, or the ability to turn on and turn off the fluorescence, is the molecular basis of STORM and PALM. There are different structural approaches to attain this "on/off" switchability, for example, the spirocyclization,

double bond isomerization (either C=C, C=N, or N=N), and reversible redox addition.[13, 24-26] The most studied small molecular switches are the rapidly photoswitchable azobenzenes and perfluoronated diaryethenes.[25, 27-32] The former has been studied over a few decades, but it is usually limited by its fluorescence efficiency. The latter one is drawing more attention recently,[33-35] but is limited by its tunable optical features. On the contrary, the photoactivatable and photoswitchable FP rivals provides inspiration to modify our **FR-1V**/hCRBPII complexes for the desired light-switchable PSB emission.[36-38]

The PA-FPs and PS-FPs have different underlying switching mechanisms. For example, PA-GFP undergoes a Glu222 decaboxylation after photoexcitation and deprotonates its phenolic oxygen to turn on the green light.[39] Kaede undergoes a backbone breakage and introduces a double bond to conjugate the His65 (see **Section I.1.1**). Dreiklang undergoes a reversible hydration/dehydration cycle on the imidazolinone C2 position on 405/365 nm irradiations, respectively.[40] The most prominent RSFPs are the Dronpa and Padron (reversal of “dron” and “pa”).[41] Dronpa has an “on” state that absorbs at 503 nm and emits at 518 nm. It can be converted to a non-fluorescent “off” state by intense 488-nm irradiation. Thus, Dronpa keeps losing its “on” state emission because the same excitation simultaneously converts it to the “off” state. Hence, Dronpa is termed as a negatively photoswitchable RSFP (NS-RSFP). On the contrary, Padron has the opposite behavior and makes it a positively photoswitchable RSFP (PS-RSFP). An intense 503-nm irradiation can initiate the “off” to “on” transition. The same light can excite the “on” state that leads to fluorescence. The exact photoswitching mechanism is

still under debate. The exact sequence and time scale of each individual step is not well understood. Nevertheless, both experimental and computational studies have demonstrated an ultrafast photoinduced *cis-trans* isomerization of the chromophore that is followed by a rapid ground-state proton transfer (GSPT). This GSPT is accompanied by structural reorganization of both solvent and protein scaffold.[42] The two conformations can have ~ 1.5 pK_a shift and lead to different protonation states that are responsible for the dark and bright fluorescence (**Scheme II-3**).

The photoswitching mechanism of Dronpa and Padron is intriguing. If this process is recapitulated in **FR-1V**/hCRBPII complexes, the control of PSB formation will not be a problem. Besides, the photochemical isomerization will ensure the spatiotemporal control of fluorescence turn “on” and “off” in terms of the PSB NIR emission. In addition, the SB and PSB have a pK_a difference that is fitting the photoswitching pattern observed in



Scheme 0-3 Proposed mechanism for the *cis–trans* isomerization of the chromophore in Dronpa and Padron. Bright and dark states correspond to the *cis* and *trans* forms of the chromophore, respectively. The two forms are determined by the pK_a difference in the acid-base equilibrium. In Dronpa, the *cis* form is anionic and bright.

Dronpa and Padron. Consider the structure of **FR-1V** and hCRBPII complex, there are two double bonds: the imine C=N and the α, β-conjugate vinylene C=C.

Which double bond is prone to photoisomerization? The photoinduced *cis-trans* isomerization involves the reorganization of the protein scaffold. Thus, it is reasonable to find possible protein mutations to elicit the desired photoisomerization. The possible gestures of **FR-1V** inside hCRBPII after covalent imine formation were simulated using AutoDock Vina with a crystal structure of all-*trans*-retinal (ATR) and hCRBPII KL (Q108K:K40L) mutant complex. Shown in **Figure II-9**, **FR-1V** occupies almost the same spatial volume as ATR. The embedded depths are also similar. Amino acid residues within 5.5 Å distance to **FR-1V** scaffold are highlighted for mutagenesis screening.

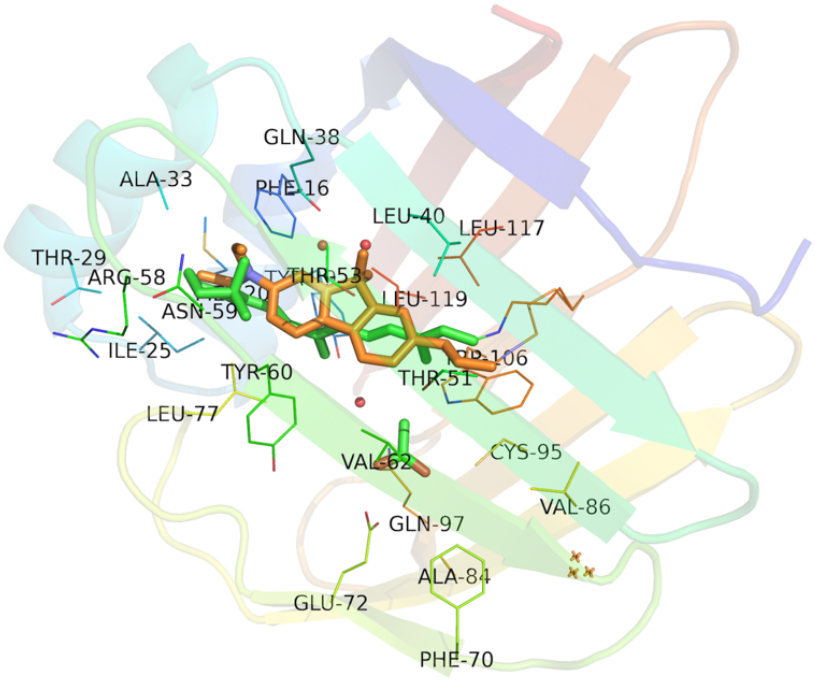


Figure 0-9 Flexible docking of **FR-1V** with all-*trans*-retinal bound hCRBPII KL mutant (PDB ID: 4EXZ). Green stick is the crystal structure of retinal. Orange stick is the pose of **FR-1V**. Docking was performed by AutoDock Vina. Residues within 5.5 Å distance to **FR-1V** are highlighted in line form.

By the time of hCRBPII mutagenesis and screening with **FR-1V**, a light-triggered photochromism was observed in the complexes of ATR with specific CRABPII mutants. In both solution and crystal cases, the ATR/CRABPII complexes can be iteratively converted between a colorless *trans*-SB form and a blue *cis*-PSB form (**Figure II-10a**).[43,44] As shown crystallograhically, the *cis*-PSB is first formed, followed by thermal isomerization to the *trans*-SB. It was further demonstrated in single crystals that the same cycle could be driven photochemically, with green light irradiation driving the *cis*-iminium to the *trans*-imine, and UV irradiation driving the photocycle in the opposite direction (**Figure II-10b**). The two forms are stable over a long-time period, enabling the

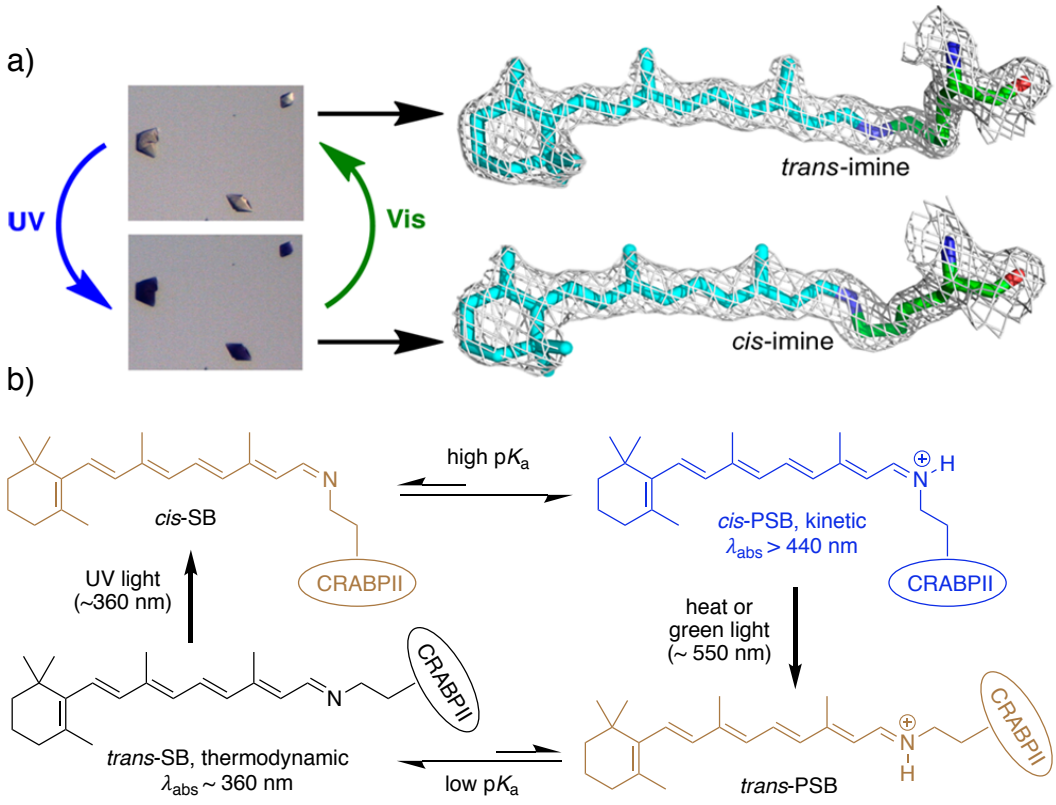


Figure 0-10 *Cis-trans* imine photoisomerization of all-*trans*-retinal bound CRABPII complexes. a) The iterative color switching of all-*trans* retinal/CRABPII complex under UV and green light irradiations. (PDB ID: 4YFP) b) Scheme illustrating the photocycle of retinylidene imine isomerization and the acid-base equilibrium of the thermodynamic SB and kinetic PSB. Figure and scheme are reproduced from ref [43].

determination of the pK_a difference between both states (~ 5 pK_a units). These observations were similar to those observed in Dronpa and Padron, and further affirmed the feasibility of finding suitable hCRBPII mutants to photoisomerize the **FR-1V**/hCRBPII complexes.

Listed in **Table II-5**, a non-exhaustive hCRBPII mutagenesis screening yields a panel of hCRBPII mutants that are capable of being photoswitched between two colorful states (see **Figure II-11** as represented by **FR-1V**/**ps4**). As denoted, the "OFF" state consists of mainly the SB species, and the "ON" state consists of mainly the PSB species. Although a clear conclusion cannot be drawn as to mutations are critical for the photoswitching phenomenon, however combination of T51V, T53S/C, and Y19W seem important for producing an efficient photoswitchable mutant. It should also be noted that,

Table 0-5 Selected **FR-1V**/hCRBPII mutants showing fluorescent photochromism.

Entry	hCRBPII mutant	"OFF"[a]		"ON"[b]			"ON/OFF" PSB Abs ratio[c]
		$\lambda_{abs,\ SB}$	$\lambda_{em,\ SB}$	$\lambda_{abs,\ PSB}$	$\lambda_{abs,\ PSB}$	$\lambda_{em,\ PSB}$	
ps1	Q108K:K40L:T51V:T53S	370	437	637	637	710	1.8
ps2	Q108K:K40L:Y19W:R58Y	395	455	568	572	674	1.2
ps3	Q108K:K40L:T51V:T53S:Y19W:R58L	380	439	625	629	702	4.4
ps4	Q108K:K40L:T51V:T53S:Y19W:R58Y	378	445	600	600	686	3.3
ps5	Q108K:K40L:T51V:T53S:Y19W:R58Y:S55Q	376	440	616	616	696	5.1
ps6	Q108K:K40L:T51V:T53S:Y19W:R58W:L77W	379	454	655	655	730	3.3
ps7	Q108K:K40L:T51V:T53C:Y19W:R58W:A33W	377	429	619	600	677	2.0
ps8	Q108K:K40L:T51V:T53S:Y19W:R58W:V62S	376	445	606	614	699	3.1
ps9	Q108K:K40L:T51V:T53S:Y19W:R58W:V62N	378	451	605	611	696	2.6

[a]"OFF" state is designated as the thermodynamic bound state of **FR-1V**/hCRBPII. It predominantly absorbs in the SB region, with a fractional absorption in the PSB region. [b]"ON" state is designated as the kinetic state of **FR-1V**/hCRBPII after photo-irradiation, showing a predominant absorption in the PSB region. Wavelengths are recorded in nanometers. [c]The ratio is measured by dividing the PSB absorption intensity of the "ON" state over that of the "OFF" state, as an indicator of the photoswitching ability.

the mutations do display a pronounced effect in tuning the emission wavelength of **FR-1V** as a result of its ICT character. Comparing the "ON" state PSB absorption and emission wavelengths between the mutants within **Table II-5**, one can see the absorption ranges from 572 – 655 nm, spanning 83 nanometers. The emission ranges from 674 – 730 nm with a span of 56 nanometers. Since the mutations impact the absorption more than the emission, one can conclude that the interactions between the mutants and **FR-1V** are not solely the result of solvatochromism. These can involve the potential hydrogen-bonding, the ground state and excited state deplanarization from molecular twisting, the *cis/trans* PSB isomerization in the ground state, or even protein reorganization.

Shown in **Figure II-11** are the absorption and emission spectra of the two photoswitching states of **FR-1V/ps4** as a representative of the photoswitching complexes listed in **Table II-5**. Here we term this complex as CrimFluor-1 (**CF-1**). After the thermal binding, **CF-1** shows an absorption with a major fraction at 378 nm and a minor fraction at 600 nm. A 5-second UV irradiation (using a ~ 365 nm handset or a Xenon lamp

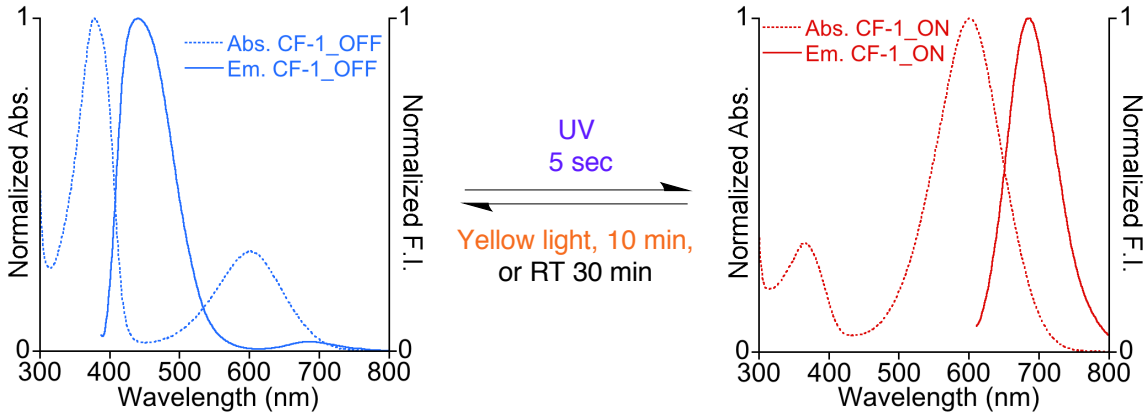
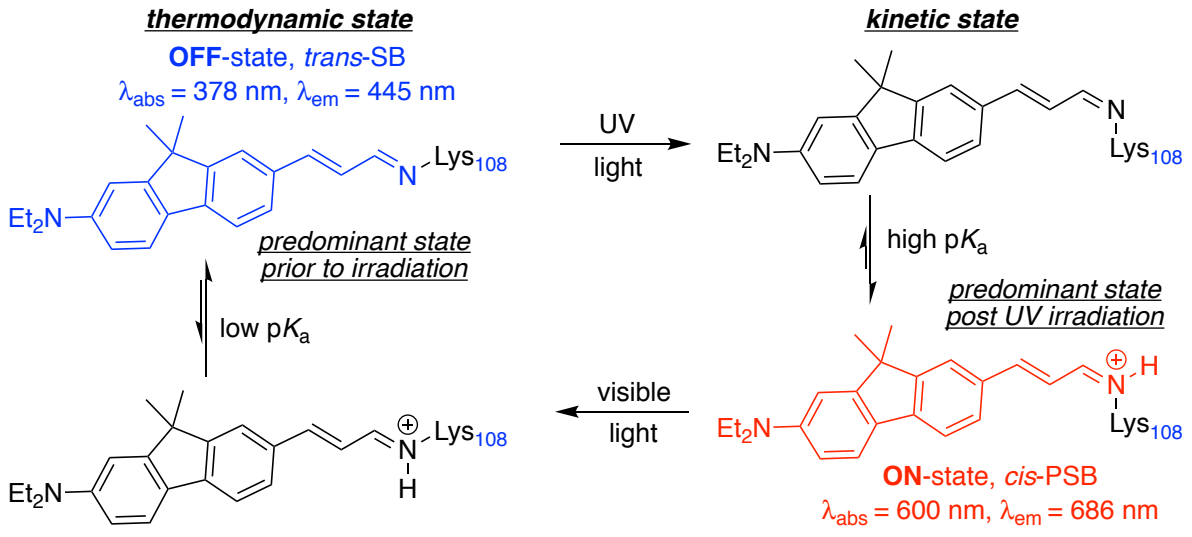


Figure 0-11 Normalized absorption and emission spectra of the two photoswitching states of **CF-1** (**FR-1V/ps4** complex). "OFF" state: the colorless thermal equilibrated state after binding. "ON" state: the blue-colored state after UV irradiation. The equilibrium illustrates the reversible switching under different conditions.

equipped with BP 300-400 band filter) can switch the thermal "OFF" state to a kinetic "ON" state that has a predominant absorption at 600 nm. Exciting the "OFF" state at 378 nm results in an intense 445-nm blue emission, with a tail at 686 nm (see **Section I.16**). The 600-nm excitation of the PSB maximum at the "ON" state gives a 686-nm emission. The ON-to-OFF switching can be driven either by a thermal process (30 min at room temperature in dark) or a photochemical process (10 min irradiation with yellow light). Because of the similarity to the ATR/CRABPII case, the photoswitching cycle is postulated to follow the same steps depicted in **Scheme II-4**. Initial binding of the fluorophore forms the thermodynamic *trans*-SB. UV irradiation isomerizes the fluorophore to a *cis*-SB. This *cis*-SB is quickly protonated to the NIR-emitting *cis*-PSB via GSPT due to its high pK_a. Yellow light irradiation or a thermal process can convert the kinetic *cis*-PSB to a more stable *trans*-PSB, which is subsequently deprotonated due to its low pK_a. We can surmise the change in the pK_a of the retinylidene as a function of the protein environment from crystal structures.



Scheme 0-4 Postulated photoswitching cycle of **CF-1**.

I.10 Developing CF-1 into a NIR tag for no-wash *in vivo* imaging

CF-1, or the **ps4** mutant, is chosen as the optimal candidate for the performance test as a NIR photoswitching tag for live cell imaging. Although **ps4** does not have the highest "ON"/"OFF" PSB photoswitching ratio, overall it exhibits fast binding rate (~ 20 min for completion, as compare to ~ 1 h of **ps5**) and high absorption coefficient and PSB quantum yield (comparing to **ps3**).

First, the binding rate of **ps4** and **FR-1V** was measured under pseudo-first order conditions. Shown in **Figure II-12a**, the initial addition of **FR-1V** displays an absorption at 420 nm as the free aldehyde residing in the hCRBPII binding cavity. A quick rise at 600 nm is observed within the first 20 min. This 600-nm PSB absorption then slowly transforms into the 378-nm SB absorption. Although it is not possible to rule out the simultaneous formation of the kinetic *cis*-PSB and thermodynamic *trans*-SB, however, based on the mechanism of proton-catalyzed imine condensation, it is reasonable to

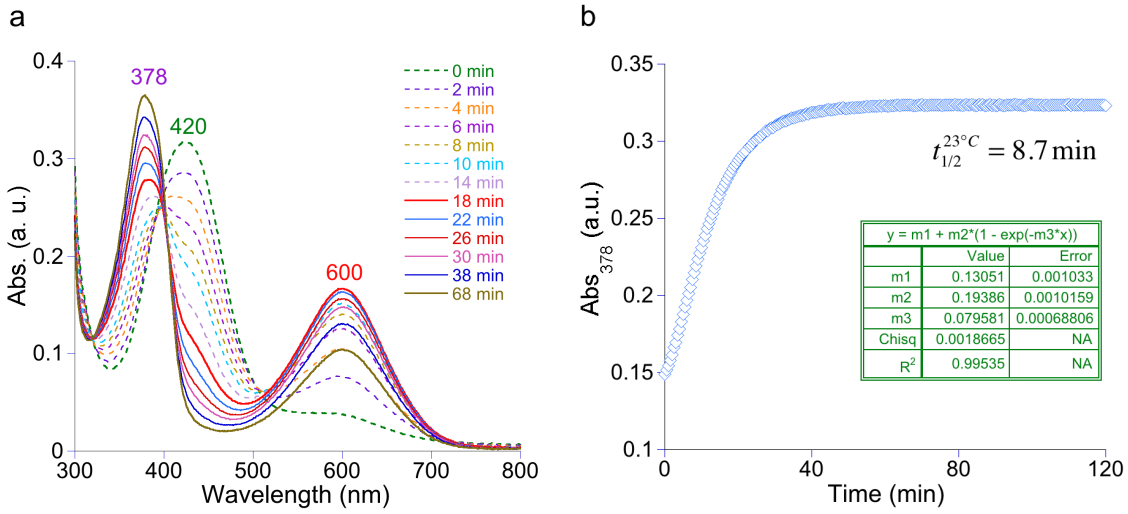


Figure 0-12 Binding of **ps4** (20 μM) and **FR-1V** in PBS buffer (pH 7.3) over time, incubated at 25 °C. (a) Stacked traces of absorbance spectra, **FR-1V** (7 μM); (b) Time-course absorbance spectrum monitored at 378 nm, **FR-1V** (6 μM). Data points were fitted to an exponential rise function.

hypothesize a stepwise process composed of the initial *cis*-PSB formation and subsequent thermal isomerization and deprotonation to *trans*-SB. Monitoring at the 378-nm SB absorption along the process, the intensity change perfectly follows an exponential increase as plotted in **Figure II-12b**, and gives a binding half-time of 8.7 min at 23 °C. This further supports the argument of the stepwise SB formation. If otherwise, a bi-exponential rise would be observed.

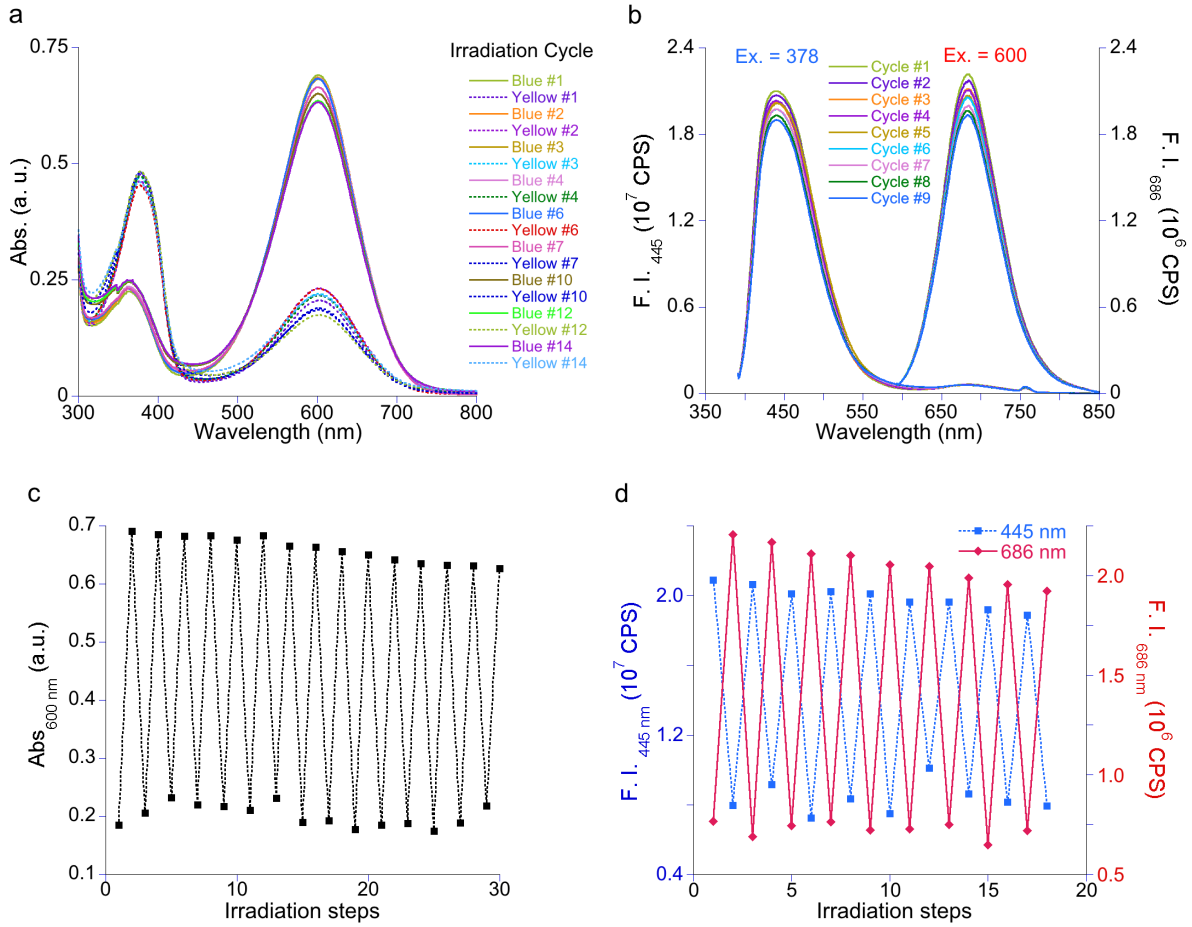


Figure 0-13 Switching fatigue resistance of **CF-1**. Stacked traces of (a) absorbance spectra, (b) emission spectra, over cycles of alternate UV and yellow light irradiations. For each cycle, excitation at 378 nm lasts 20 s with U-360 UV Bandpass filter (Blue); excitation at 600 nm lasts 15 min with Y-50 (500nm) Longpass filter (Yellow). (c) **CF-1** absorbance monitored at 600 nm, and (d) **CF-1** emission intensities monitored at the maxima of "OFF" and "ON" states in non-degassed solutions. 0.6% absorption and 1% emission intensities decreased per cycle. All measurements were in PBS (pH 7.3).

The next important property of a photoswitchable tag is its fatigue resistance, defined as the number of rounds it can be photoswitched before photodegradation. Shown in **Figure II-13**, a solution of **CF-1** was subjected to an iterative UV- and yellow-light irradiation. The absorption and emission intensities of the SB and PSB species are monitored at the corresponding wavelength maxima. To mimic the condition of real live cell experiment, the solution of **CF-1** was not degassed and supplemented with anti-fading additives. The spectra showed slight decreases in both absorption and emission after multiple rounds of light irradiation (0.6 % loss in absorption and 1 % loss in emission per cycle). This is possibly due to the oxidation of the conjugate imine moiety as observed in the heptamethine cyanines.[45] It should be noted that for the *in vitro* fatigue resistance measurement, a 500 W Xenon-Mercury lamp is used with two neutral density filters. The power density of the irradiation is much higher than that in a typical confocal microscopic

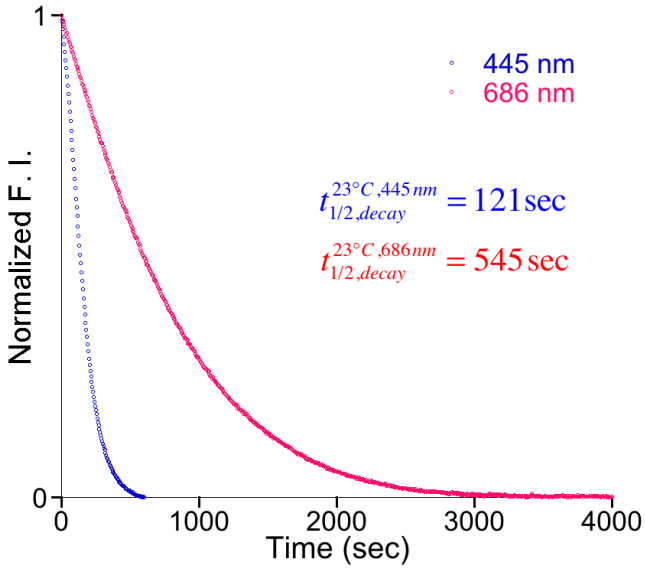


Figure 0-14 CF-1's emission switching time of the "OFF" and "ON" states. Monitored at the emission maxima under continuous excitation.

experiment. Overall, **CF-1** has demonstrated excellent photostability and fatigue resistance in a buffered environment.

The time duration of the NIR emission in the "ON" state was recorded by monitoring the 686-nm fluorescence intensity under continuous excitation. The intensity change is fitted to an exponential decrease that follows a first-order rate equation. The half-time is determined as 545 seconds for the PSB emission, and 121 seconds for the SB emission in the "OFF" state (**Figure II-14**). The length of the emission duration should suffice to image a 2048×2048 frame at the slowest line scanning rate under standard confocal microscopic setup.

A better understanding of the switching mechanism is necessary before **CF-1**'s application in live cell experiment. The OFF-to-ON photoswitching of **CF-1** is rapid and takes about 2-5 seconds. Limited by instrumentation, further investigation of the transient

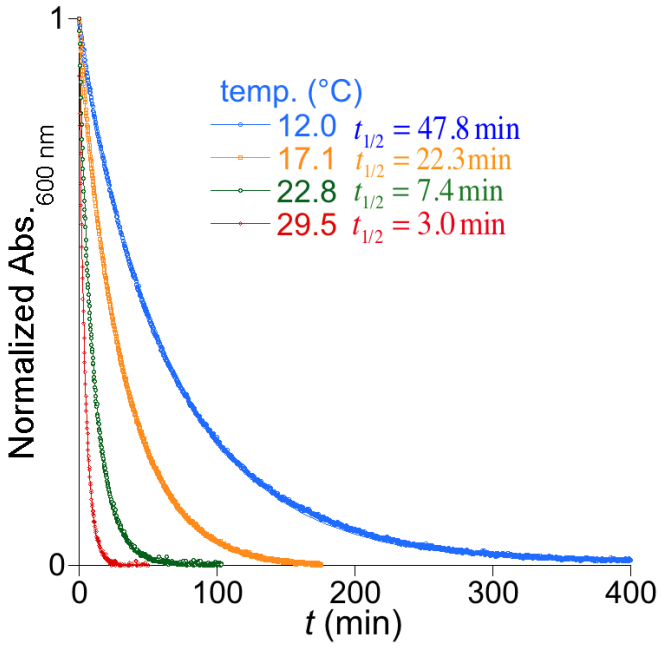


Figure 0-15 Temperature-dependent **CF-1** ON-to-OFF thermal switching, absorbance monitored at 600 nm.

events was not pursued. However, the ON-to-OFF switching is much slower. It can be driven both photochemically and thermally. This leads to the question as to what the ratio of the two kinetic rate constants is. To record the temperature effect on the thermal ON-to-OFF switching, a short UV irradiation was applied to a **CF-1** solution sample to secure a complete "ON" state before monitoring the 600-nm absorption decay in dark. The sample was kept at different temperatures using a coolant-driven thermostat. The temperature was monitored with a thermocouple sensor placed inside the solution. Nitrogen gas was continuously flowed over the cuvette surface to prevent any moisture condensation. As shown in **Figure II-15**, the thermal switching rate is temperature dependent. The thermal switching half-time were determined by fitting the intensity changes to the previously mentioned first-order exponential decay. Plotting these time constants over temperature according to the Arrhenius (**Equation II-1**, 1) and Eyring equations (**Equation II-1**, 2 and 3), we can derive the corresponding thermochemical coefficients. As calculated, the activation energy derived from the Arrhenius equation is 27.7 kcal·mol^{-1}, matching well with the enthalpy derived from the Eyring plot (27.1 kcal·mol^{-1}, **Figure II-16**). Following the conventional idea, the thermal switching should lead the kinetic PSB to a thermodynamically more stable state and that usually goes

$$k = Ae^{-E_a/RT} \quad \text{..... (1)}$$

$$k = \frac{k_B T}{h} e^{-\Delta G^*/RT} \quad \text{..... (2)}$$

$$\ln\frac{k}{T} = \frac{-\Delta H^*}{R}\frac{1}{T} + \ln\frac{k_B}{h} + \frac{\Delta S^*}{R} \quad \text{..... (3)}$$

Equation 0-1 Arrhenius and Eyring equations. (1) Arrhenius equation. (2) and (3) Eyring equations.

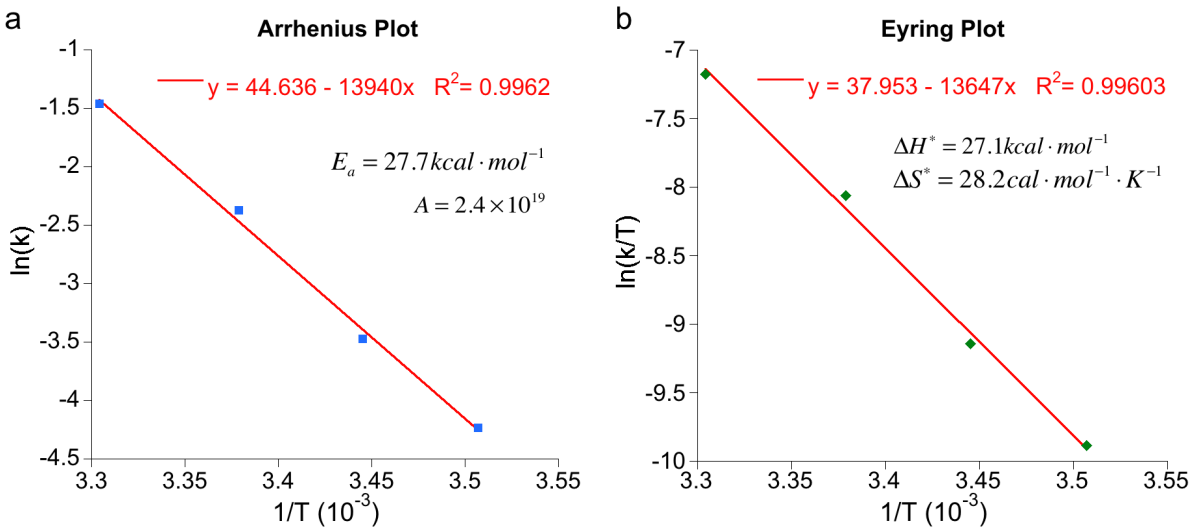


Figure 0-16 Thermal ON-to-OFF switching of **CF-1**. Rate constants plotted against temperature. (a) Arrhenius plot. (b) Eyring plot.

through an entropy decreasing process. However, it is interesting to obtain a positive entropy as 28.2 cal·mol^{-1}·K^{-1}. This might reflect the synergistic change in the protein scaffold along the switching process.

Knowing the thermodynamic constants of the ON-to-OFF thermal switching, we can deduce the photochemical contribution in the yellow light-assisted ON-to-OFF

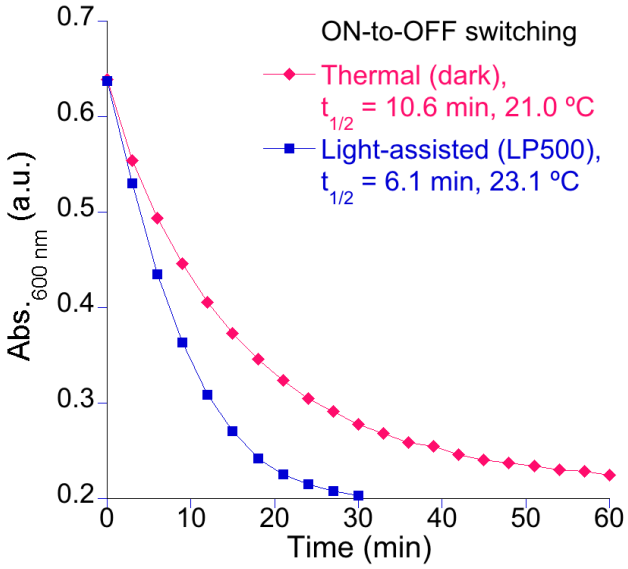


Figure 0-17 Thermal versus yellow light-assisted (LP 500 filter) ON-to-OFF switching of **CF-1**, monitored at absorption maximum. Data points collected at 3-min interval.

switching. Shown in **Figure II-17**, the light-assisted switching seems a lot faster than the dark thermal switching (6.1 min vs. 10.6 min). However, after adjusting for the small temperature difference, it appears that the photochemical rate constant only contributes to less than 20% of the whole switching process. On the other hand, it suggests that there is a large chemical space for accelerating the photochemical process.

In this photoswitching system, the key determinant for mitigating the non-specific fluorescence background is the NIR fluorescence of the kinetic PSB. The SB-PSB

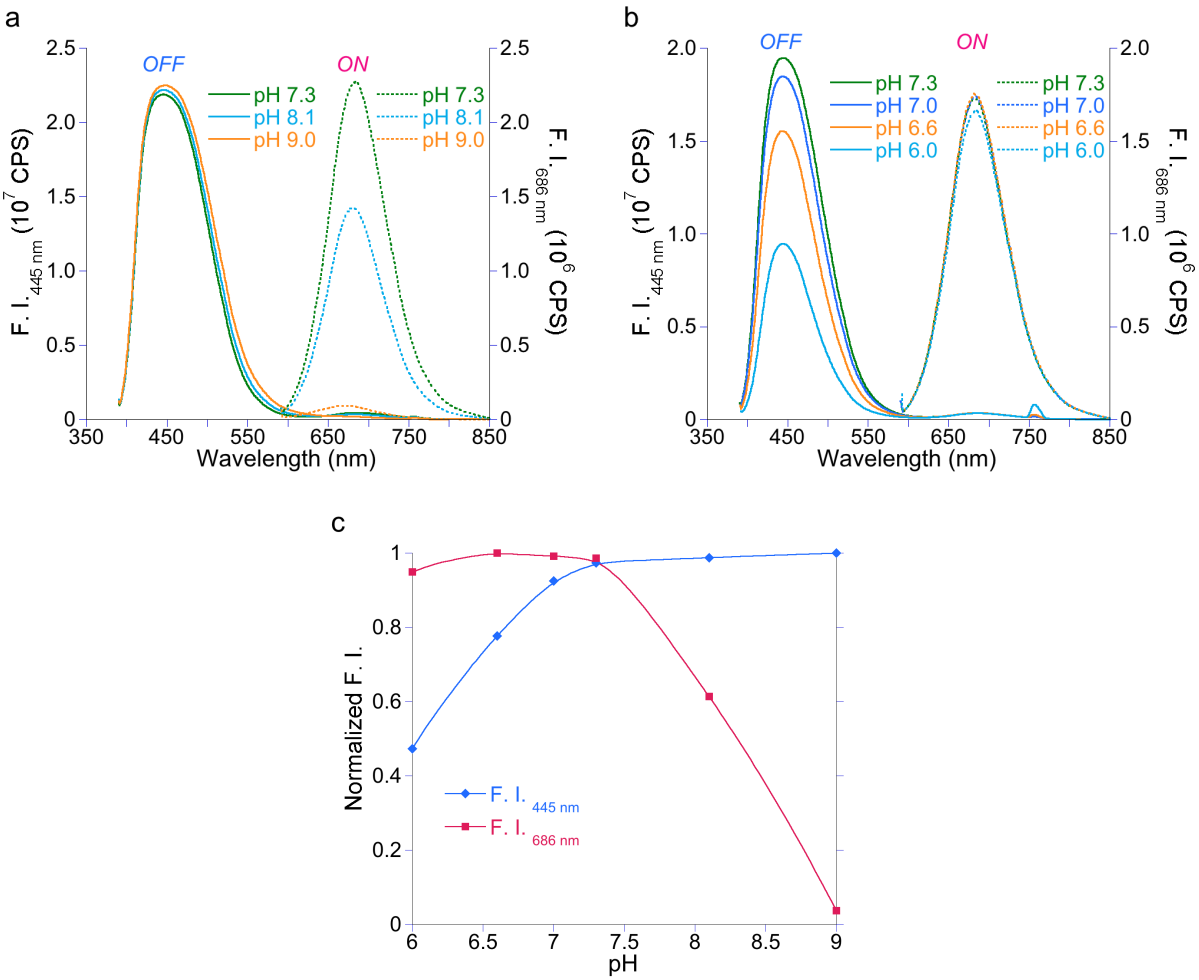


Figure 0-18 Working pH range of **CF-1**. Stacked traces of emission spectra of "OFF" (Ex. = 378 nm) and "ON" (Ex. = 600 nm) states: (a) pH 7 to 9; (b) pH 7 to 6. (c) pH-dependent fluorescence intensities of "OFF" and "ON" states, showing 80% intensities within pH 6.6 ~ 7.6 range.

equilibria is affected by the pH environment. Therefore, it is critical to know the proper pH range in which the *cis*-PSB can stay as a minor fraction before and as a major fraction after the photoswitching, or simply put, the working pH range. The SB emission in the "OFF" state and the PSB emission in the "ON" state were both recorded under various acidities. The fluorescence intensities at the corresponding maxima were plotted against the pH values (**Figure II-18**). Up to pH 7.6, **CF-1** retains 80% of its "ON"-state NIR emission. At low pH, the system is always on as the *trans*-SB is protonated to its PSB. Nevertheless, this will not be a problem for imaging under physiological conditions.

As an important fact for live cell experiments, the cytotoxicity of **FR-1V** was evaluated by the MTT assay. The MTT assay relies on the reduction of the yellow tetrazolium dye 3-(4,5-dimethylthiazol-2-yl)-2,5-diphenyltetrazolium bromide to a purple formazan by the mitochondrial reductase.[46] Quantification of the 550-nm absorbance can reflect the number of viable cells after being exposed to the chemical for a certain period

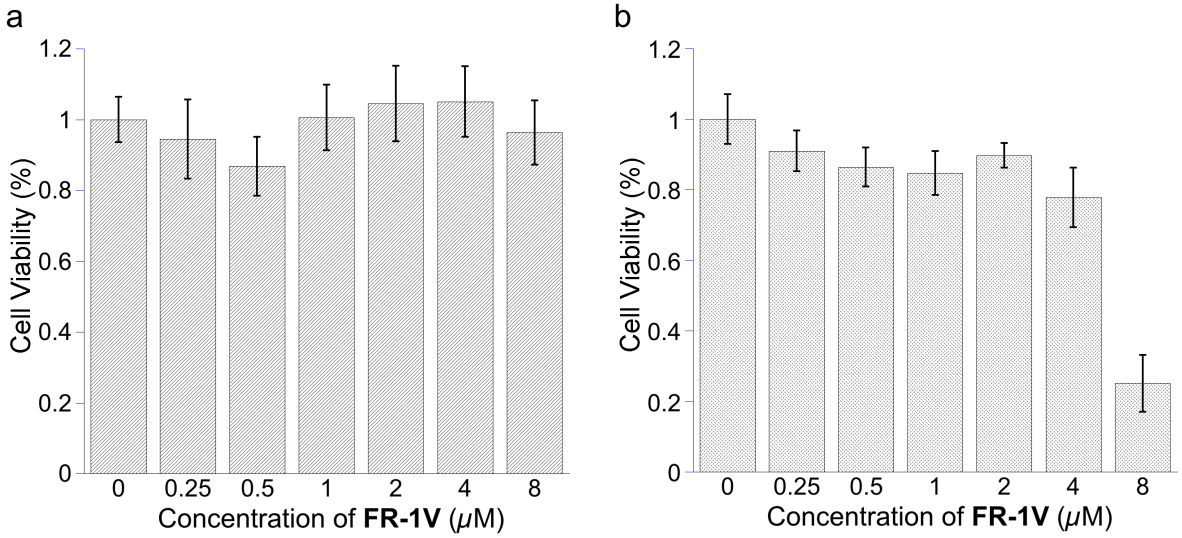


Figure 0-19 MTT assay of **FR-1V** in (a) HeLa and (b) U2OS cell lines. The absorbance was measured 550 nm, and corrected at 655 nm. Cells were treated with **FR-1V** for 24 h before MTT staining. Error bars represent the standard deviation of the readouts from (*n* = 6) cells.

of time. HeLa and U2OS cells were stained with a serial dilution of **FR-1V** stock solution and incubated for 24 h before the colorimetric measurement. As shown in **Figure II-19**, **FR-1V** does not elicit observable cytotoxicity up to 4 μM in U2OS and 8 μM in HeLa cell lines after 24 h. It should be noted that the typical time span of a confocal imaging experiment does not exceed a couple of hours. So, a concentration range of 0.5 ~ 2 μM **FR-1V** should be practical.

As discussed at the beginning of this chapter, one drawback of the FPs is their tendency to oligomerize. It has been shown in a variety of hCRBPII variants, mutations at certain specific positions can lead to a large number of domain-swapped dimers.[47] In the case of **CF-1** for its *in vivo* application, the same concern needs to be addressed. The propensity of **ps4** dimerization is evaluated by the size-exclusion chromatography of its over-expression in *E. coli*. As shown in **Figure II-20**, **ps4** remains monomeric in the

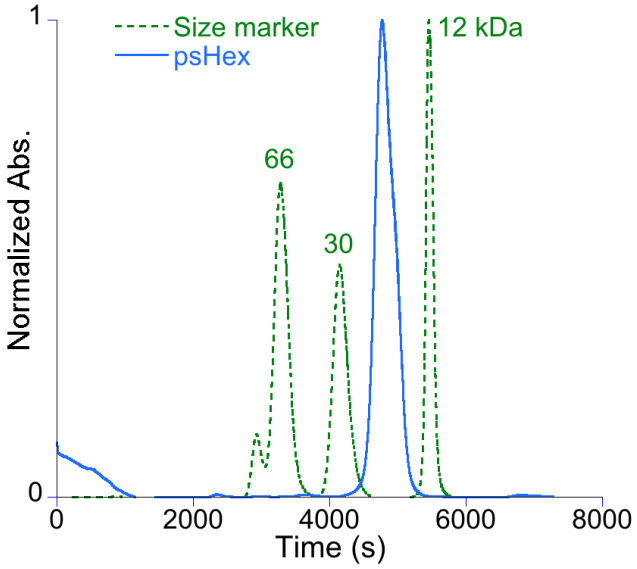


Figure 0-20 Size exclusion chromatography of hCRBPII mutant **ps4** expressed and purified from BL21(DE3)pLysS (buffer: 10 mM Tris·HCl, 2 M NaCl, pH 8.1) using a BioLogic DuoFlow QuadTec 10 system (Bio-Rad) equipped with a Superdex 120 16/600 GL size-exclusion column (GE Healthcare).

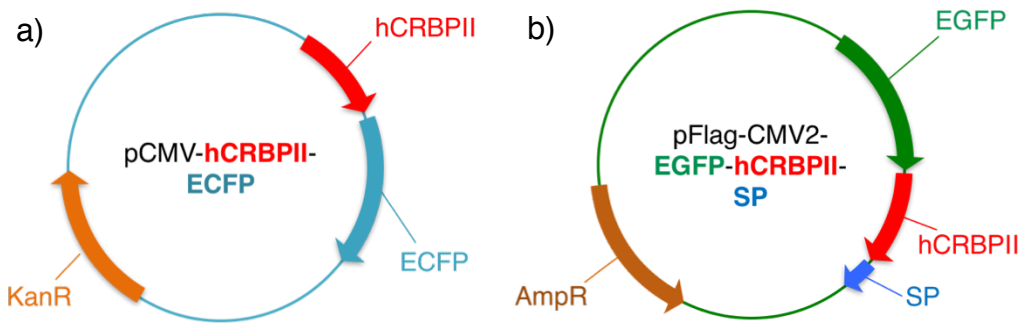


Figure 0-21 Schematic maps of the (a) hCRBPII-ECFP and (b) EGFP-hCRBPII-SP fusion constructs. SP: signaling peptides. SP = 3×NLS (nuclear localization sequence), NES (nuclear export sequence), and CAAX (prenylation tag).

extract solution up to millimolar concentration (20 mg/mL). Of course, *in vivo* assessment is necessary to confirm the pure monomeric nature of **ps4**.

To test the performance of **CF-1** *in vivo*, the **ps4** fusion constructs with ECFP and EGFP were cloned as illustrated in **Figure II-21**, respectively. Using the same ECFP-GalT vector of the hCRBPII-KLVSWW:L117E plasmid (**Figure II-4a**), the reporter ECFP was fused on the C-terminus of **ps4** for whole cell imaging. To target **ps4** at cell nuclei, cytosol, or plasma membranes, the signaling peptides NLS (nuclear localization sequence), NES (nuclear export sequence), and CAAX (prenylation tag) were fused to the C-terminus of **ps4**, respectively, with an N-terminal EGFP as the reporter gene.[48]

The proper **FR-1V** staining duration was first investigated. As determined in **Figure II-12b**, the *in vitro* binding half-time is 8.7 min at 23 °C. The binding in the living mammalian cells is accelerated if incubated at 37 °C. The nuclei-localized **ps4** was then transfected into U2OS cell lines and tested for **FR-1V** binding under different temperatures as monitored by the NIR PSB fluorescence. As expected, the binding rate increased at 37 °C. Shown in **Figure II-22b**, the **CF-1** complexation was completed within 5 min, and the system was switched to the "ON" state to present a bright NIR signal.

Surprisingly, when the cells were stained at 20 °C, **CF-1** did not form even with prolonged incubation up to 20 min (**Figure II-22a**). This gives us an extra handle to control the timing for labeling.

Both C- and N-terminal-fused **ps4** constructs were transfected and expressed in HeLa, U2OS, and HEK293 cancer cell lines to test the applicability of **CF-1**. Satisfactorily, in all cases the photoswitching feature and the "ON" state NIR emission were secured.

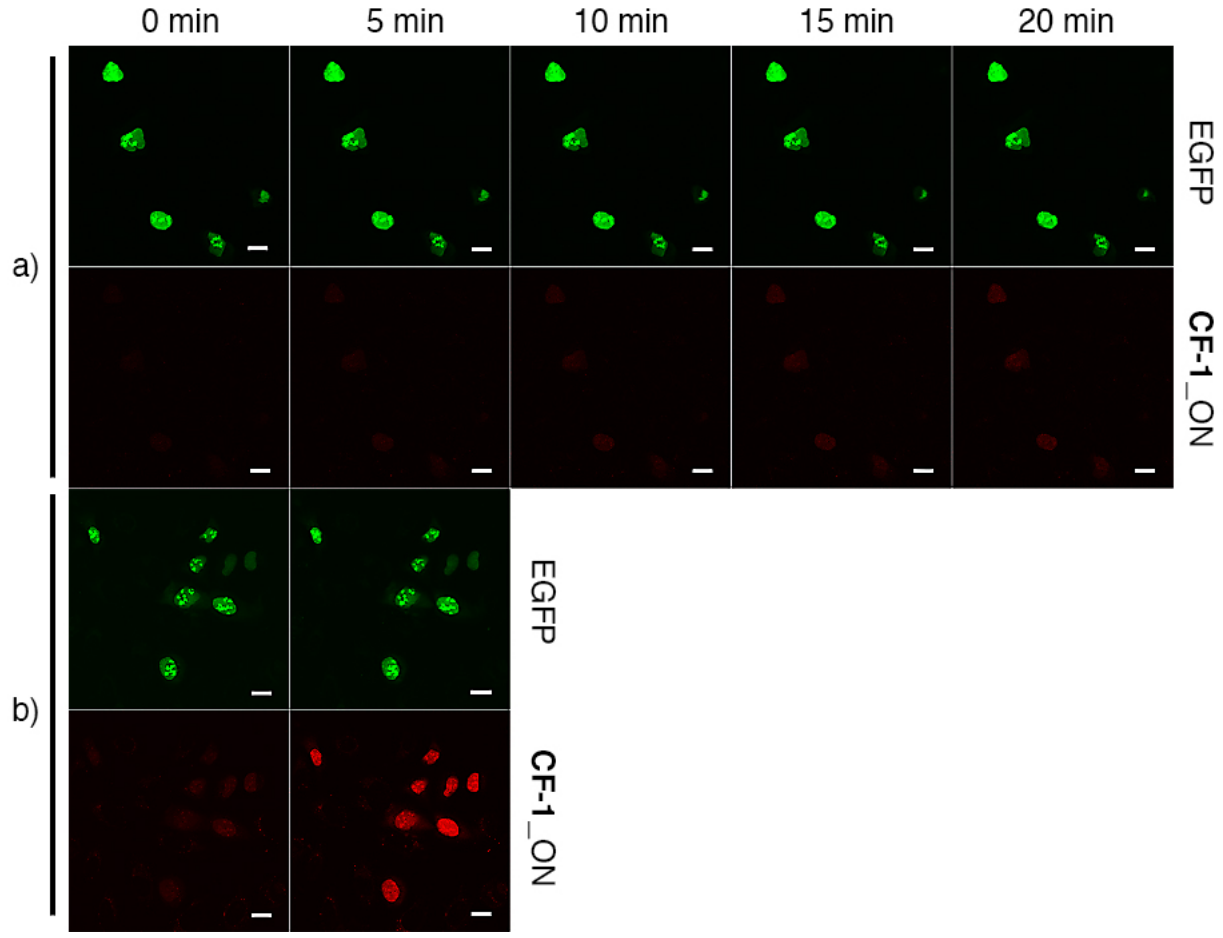


Figure 0-22 Time serial confocal fluorescence images of U2OS cells expressing construct pFlagCMV2-EGFP-**ps4**-3×NLS, stained with 1 μM **FR-1V** and incubated at (a) 20 °C, and (b) 37 °C. Channels: EGFP (Green), λ_{ex} = 488 nm, BP 505-530; **CF-1_ON** (Red), λ_{switch} = 405 nm, λ_{ex} = 594 nm, LP 650. Scale bar, 20 µm.

Typically, the cells were stained with **FR-1V** at a final concentration of 1 μM and incubated

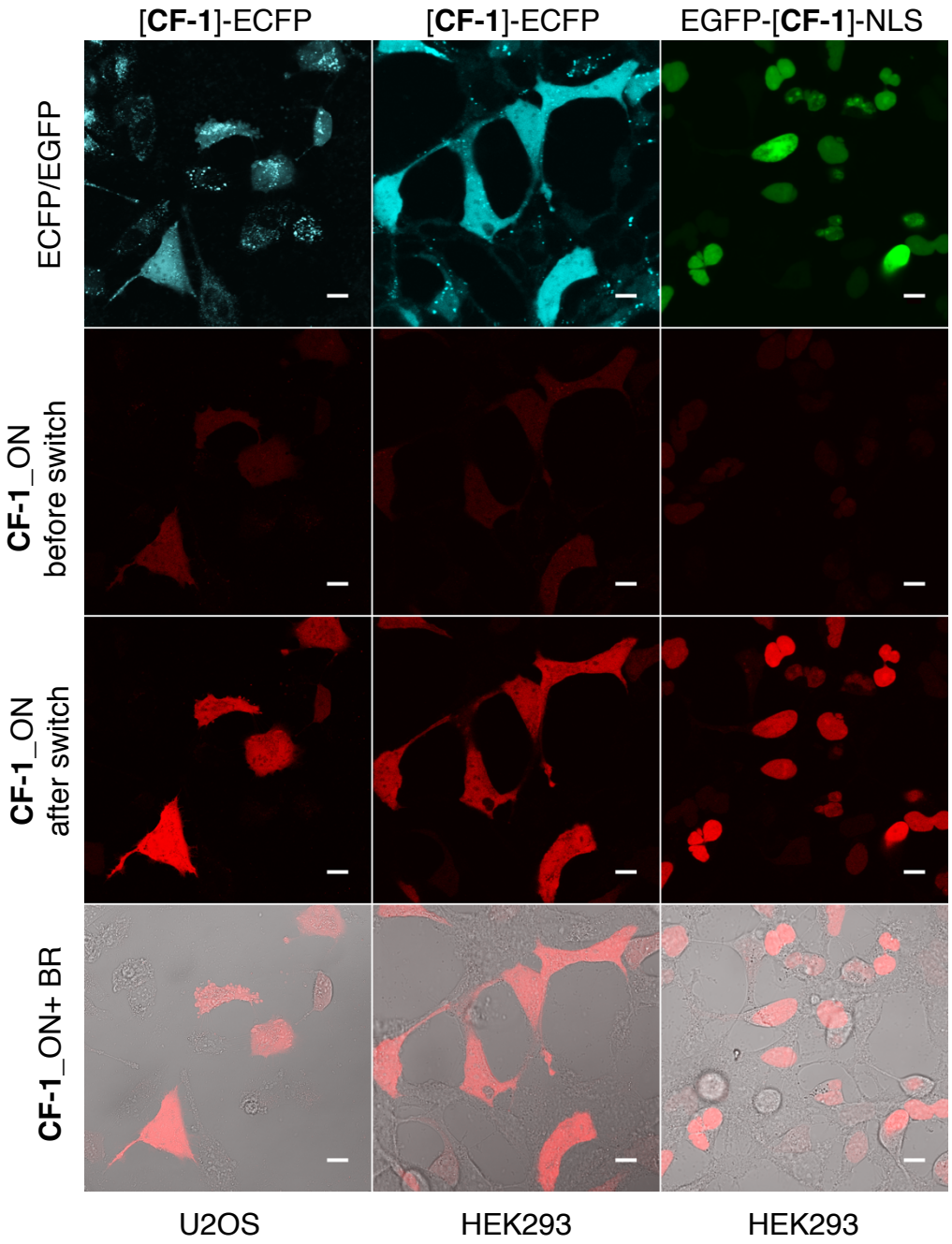


Figure 0-23 CF-1 labeling in U2OS and HEK293 cell lines. Left and middle column: cells expressing C-terminal ECFP, showing whole cell fluorescence. Right column: cells expressing N-terminal EGFP, showing nuclei-localized fluorescence. NLS = nuclear localization sequence. BR: bright-field. Channels: ECFP, λ_{ex} = 458 nm, BP 465-510IR; EGFP, λ_{ex} = 488 nm, BP 505-530; **CF-1**_ON, λ_{switch} = 405 nm, λ_{ex} = 594 nm, LP 650; Bright field, λ_{ex} = 488 nm. Cells were stained with 1 μM **FR-1V** and incubated at 37 °C for 5 min before imaging. No washing steps required. Scale bar, 20 µm.

at 37 °C for 5 min. The cells were then directly subjected to the confocal imaging without any washing steps. As can be seen in **Figure II-23**, the NIR channel (LP650) emission is more detectable in the ECFP construct than the EGFP construct. Presumably, this might

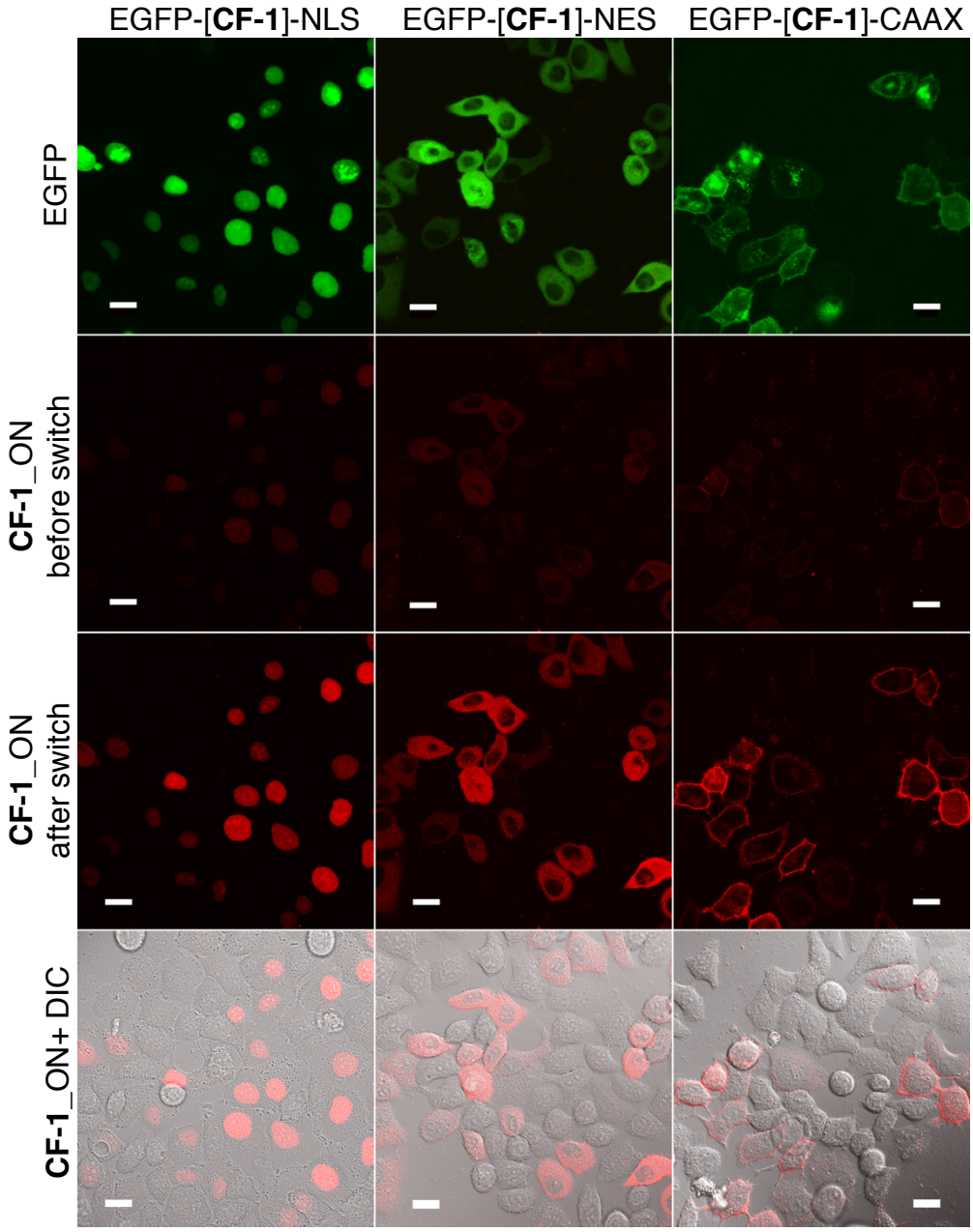


Figure 0-24 Compartmentalized **CF-1**_ON labeling in HeLa cells. (a) Labeling of different **CF-1** fusion proteins. NLS = nuclear localization sequence. NES = nuclear export sequence. CAAX = prenylation tag. DIC = differential interference contrast. Cells were stained with 2 μM **FR-1V** and incubated at 37 °C for 5 min before imaging. No washing steps required. Scale bar, 10 μm.

be due to the C-terminal instead of the N-terminal FP fusion that slightly changes the local pK_a of the **FR-1V** PSB in the hCRBPII cavity. The subcellular labeling of **CF-1** is demonstrated in HeLa cells (**Figure II-24**). The NIR fluorescence intensity has a 10-fold increase after a 1-sec 405-nm laser switching. In the case of plasma membrane labeling, **CF-1** is more advantageous than the reporter EGFP. It is observable that EGFP has intense fluorescence in places other than the plasma membrane, possibly due to the unwanted agglomeration. In contrast, **CF-1** does not show these off-target signals.

Looking at the NIR channel (LP650), it shows residual fluorescence before photoswitching. This signal comes from the small fraction of PSB in the "OFF" state. Closely examined, the NIR signal in the "OFF" state matches that in the "ON" state. It should be noted that this residual NIR fluorescence is not the non-specific background

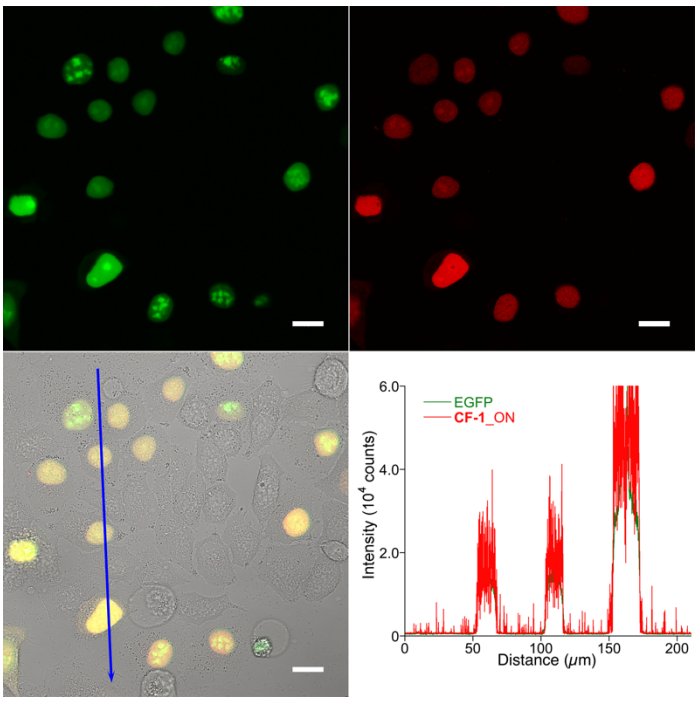


Figure 0-25 Labeling specificity of nuclei-localized **CF-1** in HeLa cells. Top left: EGFP channel; top right: **CF-1**_ON channel; bottom left: merged channels + brightfield; bottom right: line profiles of fluorescence intensities in two channels along the blue arrow in the merged image. Scale bars, 20 μm.

we commonly encounter due to off-target labeling and/or extra dye residing in the hydrophobic compartments. It is the specific signal from the labeled target. A fluorescence line profile is plotted to examine the labeling specificity of **CF-1** against the fused EGFP (**Figure II-25**). As shown, in each pixel along the blue arrow, the NIR fluorescence signal of **CF-1** is colocalized with the green fluorescence signal of EGFP, attesting the labeling specificity of **CF-1** as high as that of FPs.

I.11 Engineering ps4 into a truly fluorogenic tag for spatiotemporal imaging

Having demonstrated the imaging capability of **CF-1**, we next examined the possibility to further engineer **CF-1** as a fluorogenic tag without any residual PSB in the "OFF" state, so that a true "dark" NIR channel would be available before photoswitching. This would greatly increase the imaging contrast after photoswitching and would also allow for the spatiotemporal control of the NIR emission.

We hypothesized that the installation of more hydrophobic residues in the vicinity of the embedded **FR-1V** would destabilize the iminium (cationic species). This would have two potential consequences: 1) lessening or complete suppression of the residual PSB

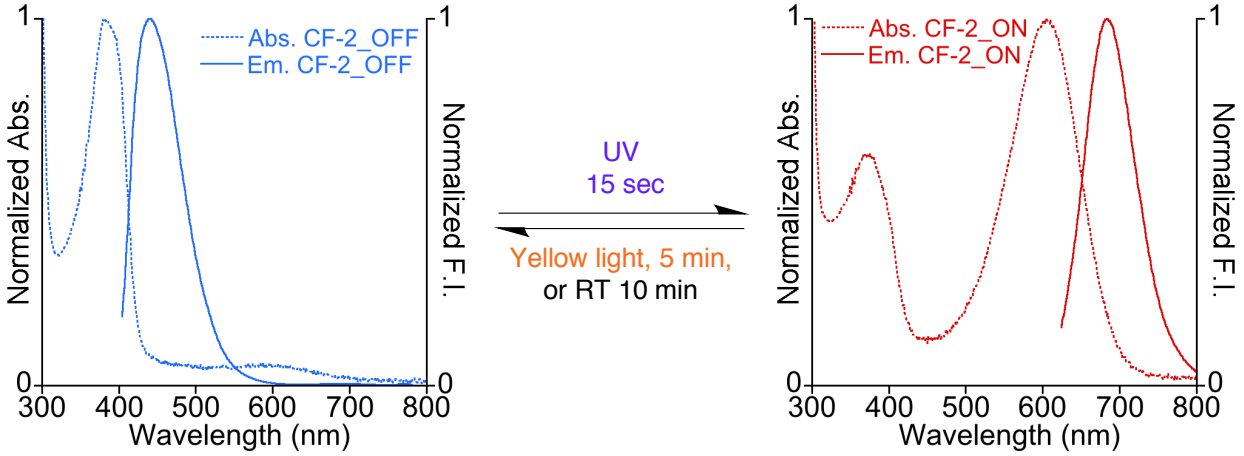


Figure 0-26 Normalized absorption and emission spectra of the two photoswitching states of **CF-2** (**FR-1V/ps5** complex).

absorption in the “OFF” state, and 2) an accelerated ON-to-OFF thermal switching rate, by increasing the electrostatic penalty for maintaining a charged species.

After several rounds of altering the **ps4** sequence (in collaboration with Dr. Setare Tahmasebi Nick), **ps5** (Q108K:K40L:T51V:T53S:Y19W:R58W:T29L:Q38L:Q128L) was identified. Illustrated in **Figure II-26**, the **FR-1V**/**ps5** complex (designated **CF-2**) showed negligible PSB absorption in its “OFF” state, while its absorption and emission maxima, QY and fatigue resistance were similar to those measured for **CF-1** (**Table II-6** and **Figure II-27**), but with a 6-fold increase in the *in vitro* ON-to-OFF thermal switching rate, and a 4.6-fold increased rate of complex formation (**Table II-6** and **Figure II-28**).

The N-terminal EGFP-fused **ps5** constructs with C-terminal signaling peptides were cloned and transfected into HeLa cells. The imaging protocol is similar to that of **CF-1**. Direct confocal imaging was taken after a quick staining with **FR-1V** for only 5 min at 37 °C, negating any washing step. Compared to the 1-sec OFF-to-ON switching of **CF-1**, **CF-2** takes 4 seconds to completely switch from “OFF” to “ON”. Nevertheless, in the

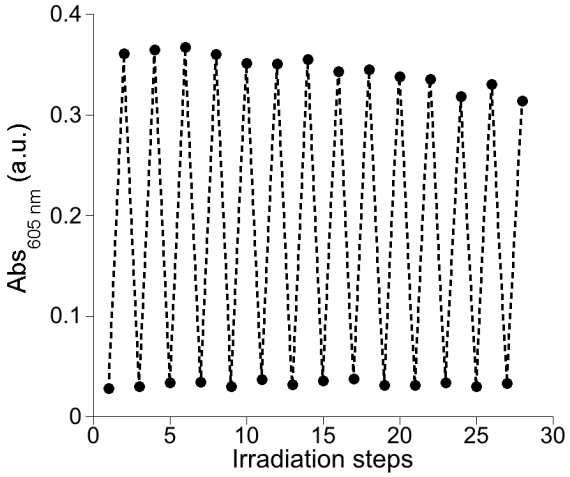


Figure 0-27 Switching fatigue resistance of **CF-2** monitored at 605 nm absorbance in PBS (pH 7.3). For each cycle, excitation at 378 nm lasts 20 s with U-360 UV Bandpass filter; excitation at 600 nm lasts 15 min with Y-50 (500 nm) Longpass filter.

Table 0-6 Feature comparison between **ps4** and **ps5**.

	Mutant	SB λ_{abs} / λ_{em}	PSB λ_{abs} / λ_{em}	QY[a]$_{SB}$	QY[a]$_{PSB}$	Binding $t_{1/2}$ (min)	ON → OFF[b] $t_{1/2}$ (min)
CF-1	ps4	378 / 445	600 / 686	0.46	0.16	8.7	7.4
CF-2	ps5	382 / 440	604 / 684	0.52	0.13	1.9	1.2

[a]Absolute quantum yields measured at pH 7.3. [b]Switching half-lives were measured in dark (thermal conversion) at 23 ºC.

compartmentalized imaging assays, a truly dark NIR channel is acquired before the photoswitching with a 405-nm laser (**Figure II-29**). A similar pixelated line-profile analysis of the colocalized EGFP and **CF-2** signals indicates the same level of labeling specificity (**Figure II-30**). The mean signal-to-background ratio (SBR) of the NIR fluorescence can be gauged in the "ON" state. Taking the nuclei-localized **CF-2** images as an example, the mean NIR emission intensity of multiple cell nuclei on different focal planes is divided by the mean background intensity of the dark areas to derive the mean SBR.[49] A remarkable SBR of 46 is achieved by this analysis (**Figure II-30**).

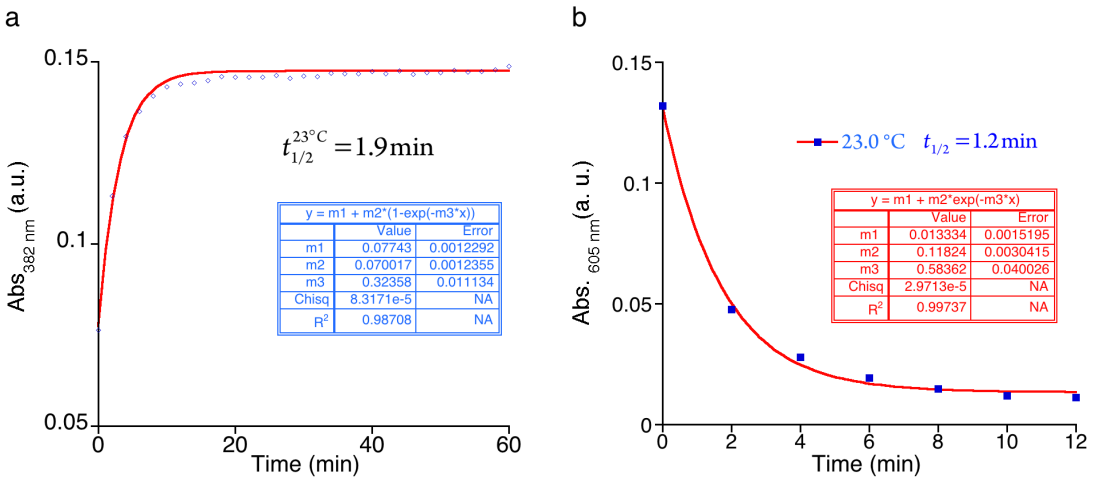


Figure 0-28 (a) Time-course absorbance spectrum monitored at 382 nm of **ps5** and **FR-1V** binding. Data points were fitted to an exponential rise function. (b) Time-course spectrum of **CF-2** ON-to-OFF thermal switching at 23 °C. Absorbance monitored at 605 nm. Data points were fitted to an exponential decay function.

The ON-to-OFF thermal switching rate is also investigated *in vivo* and compared between **CF-1** and **CF-2**. Basically, a short 405-nm laser irradiation was applied to switch the sample cells to the "ON" states. Then a selected region of interest (ROI) in the field

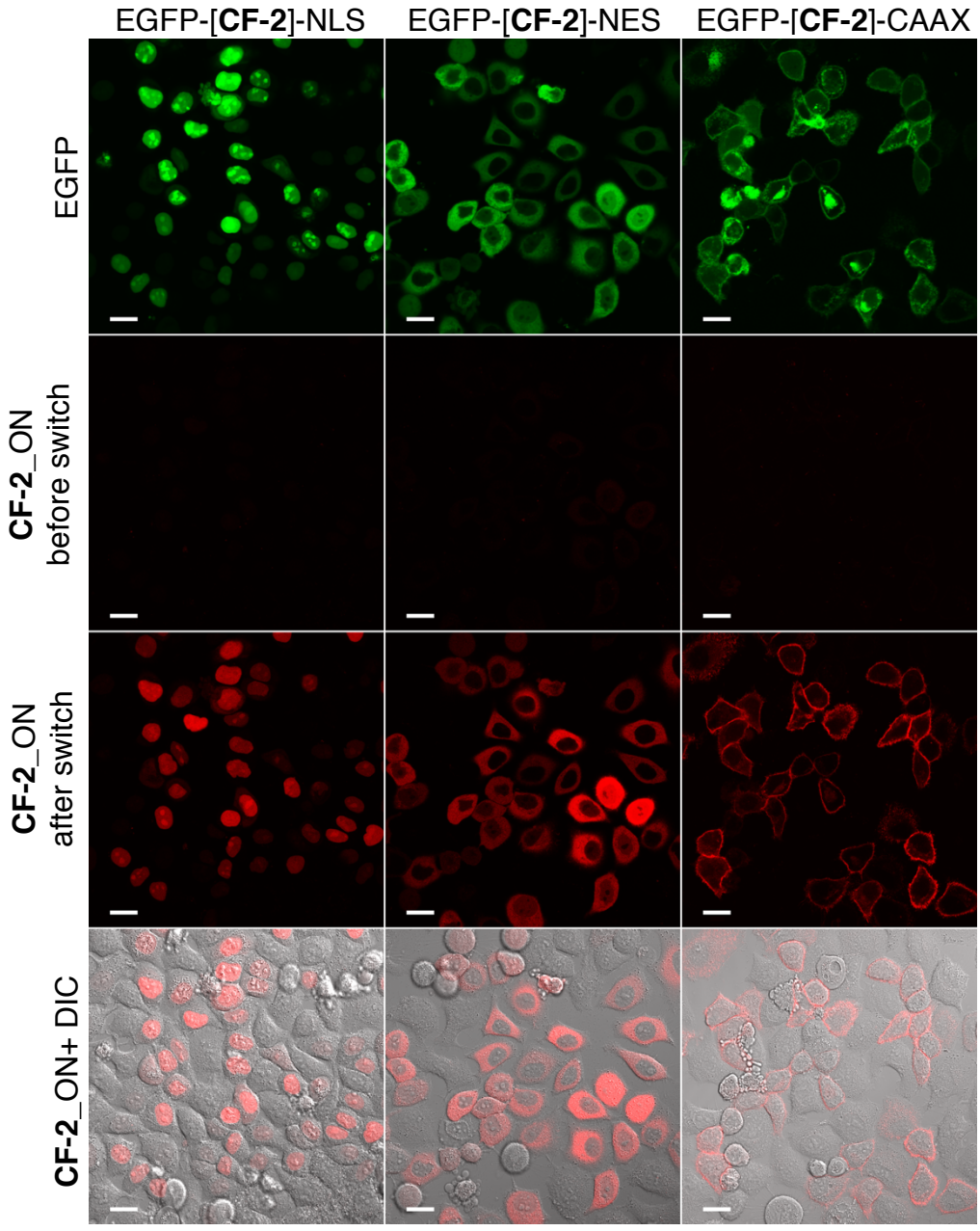


Figure 0-29 Compartmentalized **CF-2**_ON labeling in HeLa cells. Labeling of different **CF-2** fusion proteins. NLS = nuclear localization sequence. NES = nuclear export sequence. CAAX = prenylation tag. DIC = differential interference contrast. Cells were stained with 2 μM **FR-1V** and incubated at 37 °C for 5 min before imaging. No washing steps required. Scale bar, 10 μm.

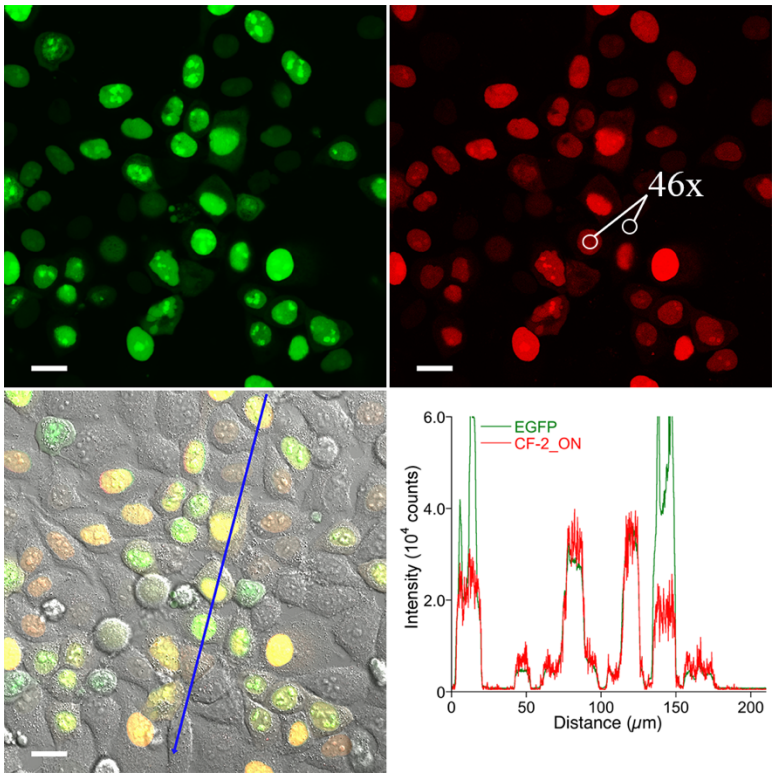


Figure 0-30 Labeling specificity of nuclei-localized **CF-2** in HeLa cells. Top left: EGFP channel; top right: **CF-2**_ON channel; bottom left: merged channels + DIC; bottom right: line profiles of fluorescence intensities in two channels along the blue arrow in the merged image. Scale bars, 20 μm. Circles and number indicating mean SBR *(n* = 440).

of view was monitored for the NIR emission intensity change. Compared to the *in vitro* rates, the ON-to-OFF switching is accelerated in the live cells even at 20 °C (**Figure II-31**). For **CF-1**, the half-time is shortened from 7.4 min to 2.7 min, while **CF-2** goes from 1.2 min to 0.68 min. The faster *in vivo* switching rate allows for iterative NIR fluorescence turn-on and turn-off in live cells. As demonstrated in **Figure II-32**, 10 switching cycles were performed with plasma membrane-labeled **CF-2** in HeLa cells, showing minimal loss of brightness.

As for the ultimate goal of controlling the NIR fluorescence in a spatiotemporal manner, nuclei-localized **CF-1** was first tested *in vivo*. After staining with **FR-1V**, the cells were kept in the "OFF" state. A selected cell nucleus was flashed with a 405-nm switching

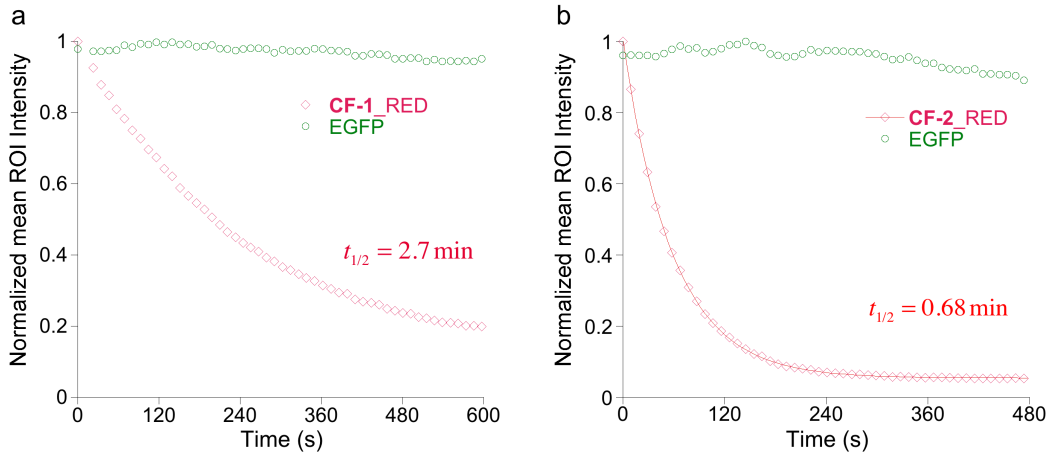


Figure 0-31 ON-to-OFF thermal switching kinetics of (a) **CF-1** and (b) **CF-2** in HeLa cells. Region of interest was excited continuously with 594 nm laser (1.63 μW). Mean ROI intensity was recorded every 6 sec.

laser in a crosshair mode. Unfortunately, the OFF-to-ON photoswitching of **CF-1** is ultrafast and ultra-sensitive. Even a 1-sec irradiation with the focused laser beam can

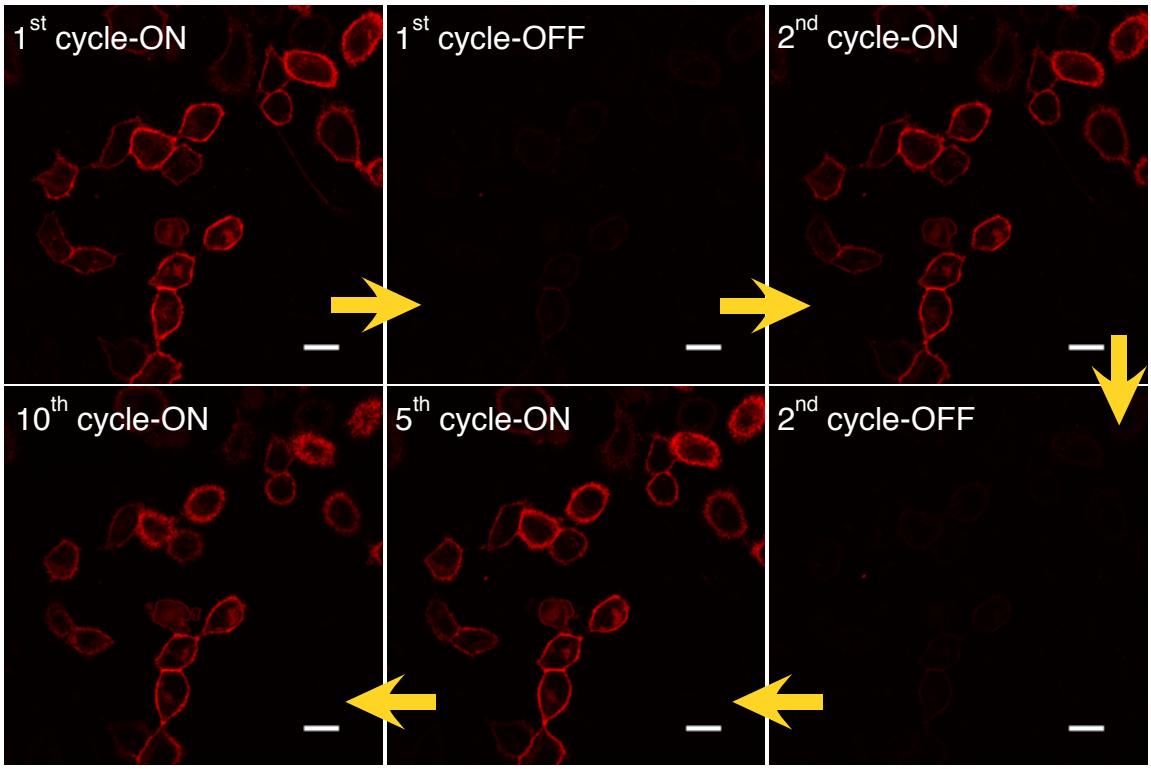


Figure 0-32 *In cellulo* NIR fluorescence (LP650) "ON/OFF" cycling of HeLa cells expressing EGFP-**ps5**-CAAX, showing 10 switching cycles. Arrows: OFF-to-ON, 405 nm laser 4 sec; ON-to-OFF, r.t. 3 min. Scale bar: 10 μm.

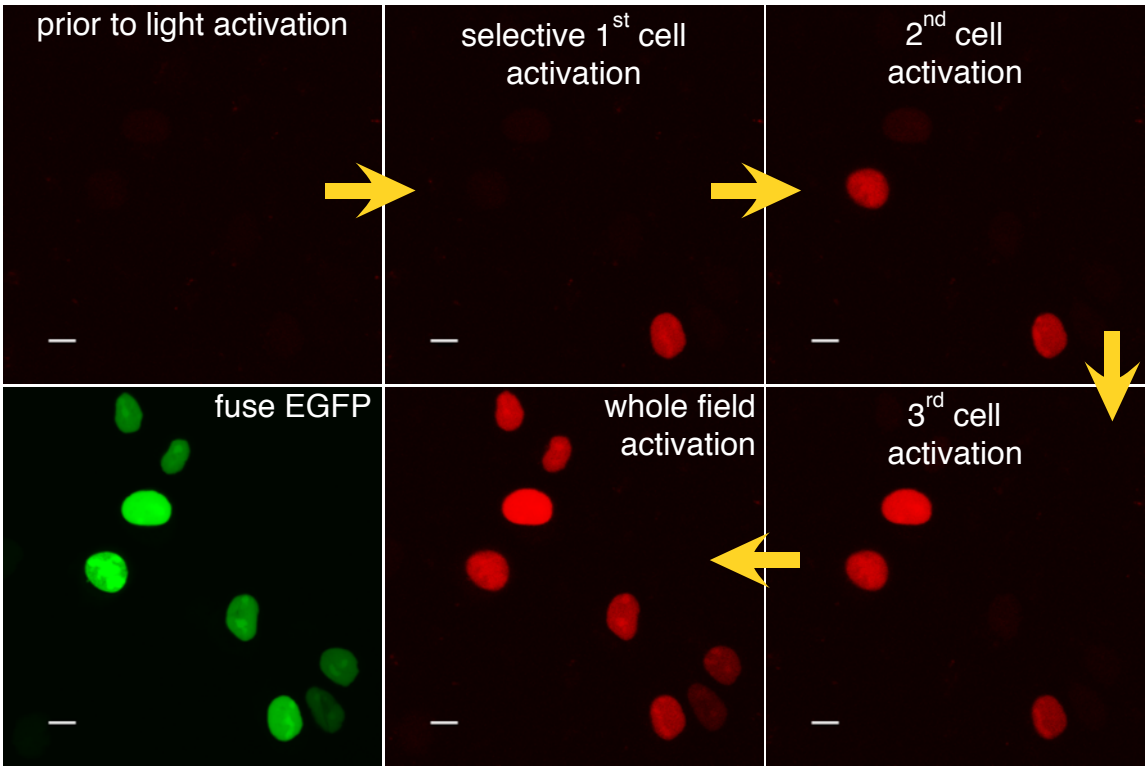


Figure 0-33 Spatiotemporal confocal imaging of HeLa cells, expressing nuclei-localized EGFP-fused **ps5**. Cells were stained with 2 μM **FR-1V** for 5 min at 37 °C and imaged without washing. Red channel: **CF-2**_ON. Following the arrows: before switch-on; 1st cell switch-on; 2nd cell switch-on; 3rd cell switch-on; whole field switch-on. Compare with green channel: colocalized reference EGFP. Scale bars, 10 μm.

switch "ON" the whole field of view. This also suggest the photoactivation rate is in the millisecond range. Mentioned earlier, **CF-2** has a slower OFF-to-ON switching rate. Luckily, this inhibits the whole field activation of **CF-2** under the same crosshair laser beam, and successfully leads to the spatiotemporal control of NIR fluorescence turn-on as showcased by the nuclei-localized **CF-2** (**Figure II-33**).

The comparison of **CF-1** and **CF-2** with some well-known far-red/NIR FPs are listed in **Table II-7**. The NIR brightness is quantified as the product of extinction coefficient at 635 nm and the fractional quantum yield in the range of 700 ~ 900 nm.[50] **CF-1** and **CF-**

Table 0-7 Comparison of **CF-1** and **CF-2** with other far-red/NIR FPs.[a]

	Katushka	E2-Crimson	mNeptune	eqFP650	eqFP670	CF-1 (ON)	CF-2 (ON)
Excitation peak (nm)	588	605	599	592	605	600	604
Emission peak (nm)	635	646	649	650	670	686	684
Fluorescence QY	0.34	0.12	0.18	0.24	0.06	0.16[c]	0.13[c]
ε_{max} ($M^{-1}\cdot cm^{-1}$)	65,000	58,500	57,500	65,000	70,000	50,500	35,700
Brightness (a.u.)[b]	22,100	7,080	10,350	15,600	4,200	8,080	4,641
ε_{635} ($M^{-1}\cdot cm^{-1}$)	1,700	12,640	7,900	4,300	15,700	37,550	27,940
Φ (700–900 nm)[d]	0.07	0.03	0.05	0.07	0.03	0.07	0.05
Brightness in NIR (a.u.)[e]	119	379	395	301	471	2,630	1,400
Relative NIR brightness	1	3.2	3.3	2.5	4.0	22.1	11.8

[a]Data of Katushka, E2-Crimson, mNeptune, eqFP650 and eqFP670 are from ref [50]. [b]Calculated as the product of molar extinction coefficient and quantum yield. [c]Absolute quantum yield measured in PBS at pH 7.3. [d]Calculated from the emission fraction between 700 nm and 900 nm. [e]Calculated as the product of molar extinction coefficient at 635 nm, and quantum yield in NIR.

2 have shown superior NIR brightness as 22-fold and 12-fold higher than that of Katushka (the dimeric parent of mKate), respectively.

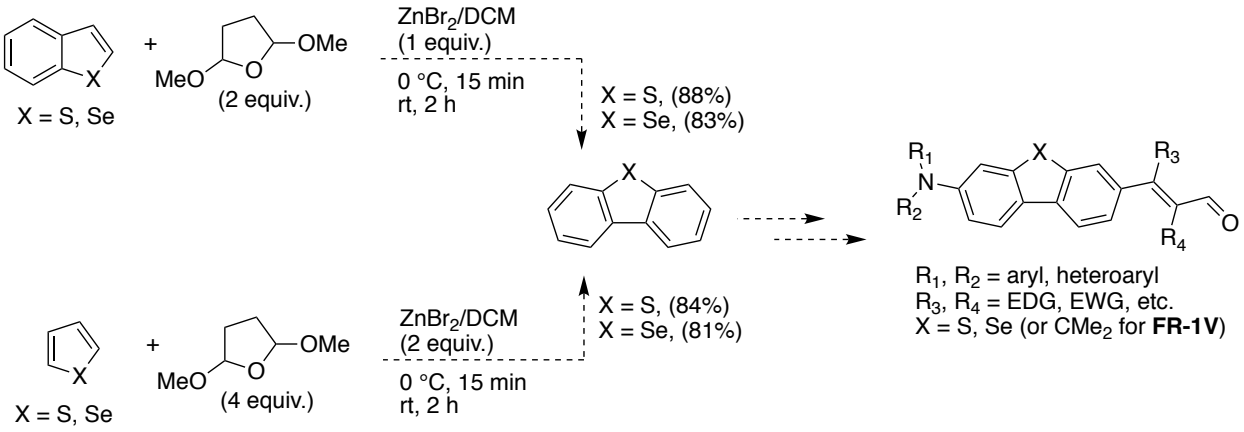
I.12 Conclusion and future research directions

To date, **CF-1** and **CF-2** are the first reported photoswitchable NIR tags that employ both a synthetic dye and a fusion protein. The design of CrimFluors accomplishes three complimentary goals towards a superior imaging platform, namely, 1) the use of ICT capable chromophores, 2) generation of a bathochromically-shifted PSB, and 3) the ability to photoactivably turn-on and turn-off the fluorescence signal. The use of ICT capable chromophores leads to “background-free” no-wash NIR fluorescence as a result of the large bathochromic shift of the chromophore upon protonation of the imine, which happens only when bound to the engineered protein, because non-specifically formed imines are not protonated under physiological conditions. The “ON/OFF” fluorescence switch is presumably a result of fluorophore photoisomerization. Compared to RSFPs, **CF-1** and **CF-2** have larger Stokes shifts and more red-shifted NIR fluorescence. Tested

in different cell lines, **CF-1** and **CF-2** can be turned to the "ON" state by a 405-nm laser with a 1 sec- and 3 sec- irradiation time, respectively, and both have good photostability. If optimal NIR brightness is required, then **CF-1** is an optimal choice. On the other hand, **CF-2** offers a complete dark state with a faster ON-to-OFF thermal switching rate. CrimFluors can complement current FPs for live cell imaging and are potential tags for bright deep-tissue imaging.

I.12.1 Future structural modification of FR-1V

One of the future research directions is further structural optimization of **FR-1V** for extended lifetimes of the emissive PSB species, such that the NIR brightness can be increased if the radiative decay constant does not alter much. Substitution on the α, β-conjugated double bond with electron-donating, electron-withdrawing, and steric functional groups are being attempted. The structural relationship with the photo-interconversion rates are under investigation. Hopefully, a faster ON-to-OFF photo-conversion rate can be obtained to enable a pure photo-controllable imaging tag for super-resolution microscopy.



Scheme 0-5 Potential derivatives of **FR-1V** for improving optical properties.

Another direction of modification is to replace the C9 of **FR-1V** fluorenyl to more electron-diffused S, Se, and Si. This type of substitution can increase the conjugation of the scaffold and may further lower the band gap of the derivative. Hopefully, the emissions of these derivatives can be further red-shifted into the long wavelength region of NIR-I, with the minimal trade-off in overall brightness and Stokes shift. One feasible synthetic route is given in **Scheme II-5** to construct the hetero-homologues of **FR-1V.** The core scaffolds can be furnished by benz-annulation of thiophene or selenophene with 2,5-dimethoxytetrahydrofuran.[51] The installment of the rest side chains should be similar to those of **FR-1V**.

I.12.2 FR-1V/hCRBPII as a dual-emission ratiometric pH probe

Now let's think in the opposite direction. What can we do with a non-switchable **FR-1V**/hCRBPII complex? Shown in **Table II-6** as an example, the "OFF" state has a common 450-nm SB emission with ~ 50% quantum yield. The strong fluorescence can also be utilized for a quantitative imaging measurement in addition to the NIR PSB emission. If the complex is not photoswitchable, then we can simply ascribe the ratio of the SB and PSB presented as per the acid-base equilibrium, whether it involves *cis-trans* isomerization or not. Therefore, a pH-dependent ratiometric fluorescence readout can be acquired based on the blue and NIR emissions from the equilibrated system.

Wavelength ratiometry is always a preferable method in sensing and imaging intermolecular interactions. Especially in UV/Vis and fluorescence spectrophotometry, wavelength ratiometry is clearly advantageous in comparison to simple intensity-based absorbance or emission detection by avoiding the misinterpretation from inconsistent

concentration of the pigment or emitter.[52] Compared to normal single-wavelength ratiometry, a dual-emission wavelength ratiometry has even more advantages.

For example, when the ratiometry is based on the single-wavelength fluorescence intensity ratio from two different excitation wavelengths, a potential problem is the light source power density fluctuation in the two excitation wavelengths, which will invalidate the ratiometric nature of the readout. On the other hand, a dual-emission wavelength ratiometry is self-calibrated. No matter what fluctuation may occur with the light source, it will reflect simultaneously in the dual-emission and cause no deviation in the readout.

Other than the compensation of light source fluctuation, a dual-emission sensing system can also simplify the readout if the two emission maxima are spectrally well-resolved. In this case, the deconvolution and integration of the fluorescence spectra is not necessary. Instead, the ratio can directly be derived from the intensities of the two emission maxima.

A single wavelength-emission ratiometry is based on the chemical transformation of the initial emitting species to a different emissive species elicited by the intermolecular interaction (e.g., pH change). If the two species have different extinction coefficients and fluorescence quantum yields and significant spectral overlap, it is almost impossible to do the spectral deconvolution. More often than not, the overall ratiometric intensity change is just described as a “black box”. The detailed mechanism is usually ignored on purpose, and a working curve is commonly plotted with experimental results used directly. However, if a dual-emission ratiometric system can be built on the straightforward acid-base

equilibrium, then a clear mathematical description can be derived instead of the “black box” working curve.

In view of this, a mutant-screening was carried out to find proper non-switchable candidates. A high PSB/SB absorbance ratio is desired because the PSB has a lower quantum yield than the SB, and the comparable brightness is essential to give a better dynamic range for the ratio readout. hCRBPII mutant **ph1** (Q108K:K40L:T51V:T53S:

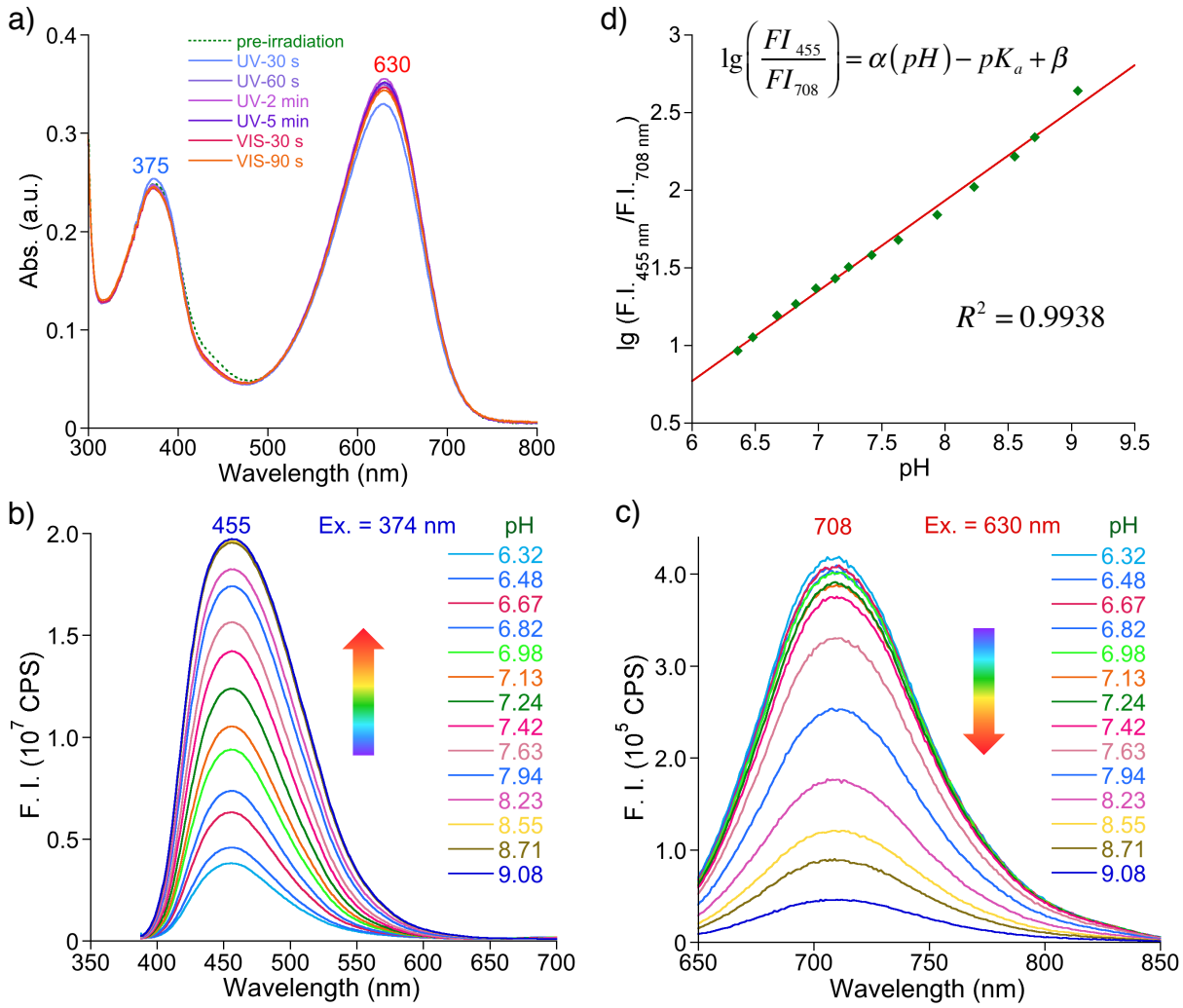


Figure 0-34 The prototype of a dual-emission ratiometric pH probe. a) Stacked traces of the absorption spectra of **FR-1V/ph1** (Q108K:K40L:T51V:T53S:V62E) complex upon iterative light irradiation. UV = U-360 UV Bandpass filter. VIS = Y-50 (500 nm) Longpass filter. Stacked traces of b) SB and c) PSB emission under different pH. d) The correlation of the logarithmic fluorescence ratio and pH. A linear function is presented.

V62E) was identified as the prototype for the dual-emission ratiometric pH probe. It has a PSB/SB absorbance ratio of 1.5. It does not show any photoswitching even under extended UV-light irradiation (**Figure II-34a**). As shown, the logarithmic ratio of the fluorescence intensity of its SB and PSB upon pH titration can be perfectly fitted to the linear function (**Figure II-34d**) derived from the acid-base equilibrium. Its probing capacity spans a broad pH range over 6.5 ~ 9. There is a 100-fold increase from the lower limit to the upper limit of the fluorescence intensity ratio. This provides a wide dynamic range and a high sensitivity.

The binding of **FR-1V** and **ph1** has a 3.1 min as the half-time. To apply this prototypic pH probe for live cell application, future work needs to be focused on increasing the quantum yields. Currently, it has a QY of 13% and 8% for SB and PSB, respectively. Another issue to address is the non-specific background, because the complex no longer has a mechanism to screen away off-target fluorescence.

I.13 Experimental section

Materials and general methods

All chemicals and solvents were purchased from Sigma-Aldrich and used without further purification. NMR (^{1}H, ^{13}C) spectra were recorded with Agilent DirectDrive2 500 MHz spectrometer and referenced with the residual ^{1}H peak from the deuterated solvents. HRMS (ESI) analysis was done by using a Waters Xevo G2-XS QTOF mass spectrometer (Agilent) and referenced against Polyethylene Glycol (PEG-400-600).

Site-directed mutagenesis and cloning

All DNA oligonucleotides used were purchased from Integrated DNA Technologies. Restriction endonucleases were purchased from New England BioLabs. PCR-amplified and restriction enzyme-digested DNA was purified by Wizard® SV Gel and PCR Clean-Up kit (Promega). All plasmids were amplified with QIAprep® Spin Miniprep Kit (QIAGEN). Ligation was performed with T4 DNA Ligase (New England BioLabs). All PCR and ligation products were transformed into XL1-Blue competent cells (Agilent), which were then plated onto LB-Amp/Tet agar. All site-directed mutagenesis PCR were performed using *PfuTurbo* DNA Polymerase (Agilent) following a standard TD-PCR protocol. All *E. Coli* constructs were in the pET-17b vector (Addgene). Mammalian constructs were generated through routine combination of PCR and restriction-enzyme cloning. Cloning-related PCRs were performed with Phusion® High-Fidelity DNA Polymerase (New England BioLabs). ECFP-coded construct was cloned by inserting hCRBPII sequence into the ECFP-GalT vector (Addgene) with XhoI and BamHI sites. EGFP-coded constructs were cloned by inserting hCRBPII into the pFlag-CMV2 vector (Sigma-Aldrich) with NotI and EcoRI sites. EGFP was inserted before hCRBPII with HindIII and NotI sites. Cell nucleus, cytosol, and plasma membrane were targeted by inserting triplicated-NLS (DPKKKRKV), NES (ELAEKLAGLDIN) and CAAX (GKKKKKKSKTKCVIM), respectively, after hCRBPII with EcoRI and BamHI sites.[48]

Protein expression and purification

hCRBPII mutants in pET-17b vector were expressed in *E. Coli* BL21(DE3)pLysS competent cells (Promega). The transformed cells were grown in LB growth medium

supplemented with 50 μg/mL ampicillin and 30 μg/mL chloramphenicol at 37 °C for 6 h, then induced with 1.0 mM IPTG and further grown at 23 °C for 18 h. The cells were harvested and lysed with Model 300 V/T Ultrasonic Homogenizer (BioLogics Inc.). hCRBPII protein in the supernatant was collected by ion exchange chromatography (Q Sepharose Fast Flow resin, GE Healthcare). The eluent was desalted by buffer exchange with Tris buffer (10 mM Tris·HCl, pH=8.0) using an ultrafiltration cell under nitrogen flow (~20 psi) through a 10,000 MW cutoff membrane (Ultrafiltration Membrane; material: regenerated cellulose; filter code: YM10; diameter 63.5 mm; NMWL: 10,000; Millipore™). Further purification was done by Bio-Rad BioLogic DuoFlow QuadTec 10 system or NGC Discover™ system equipped with SOURCE® 15Q column (GE Healthcare) using 10 mM Tris·HCl and 2 M NaCl at pH 8.1, followed by size exclusion chromatography with a Superdex 120 16/600 GL column (GE Healthcare).

UV/Vis and fluorescence spectroscopy

UV/Vis spectroscopy was performed with Cary 300 Bio UV-Visible Spectrophotometer (Varian) using 1-cm, 1.0-mL quartz microcuvettes (Starna Cells). Fluorescence spectroscopy was performed on a Fluorolog®-3 spectrofluorometer (Jobin Yvon, Horiba Scientific) with 1-cm, 3.5-mL quartz cuvettes or 1-cm, 1.0-mL quartz microcuvettes (Starna Cells). All measurements were taken at ambient temperature (23 ± 1 °C). Extinction coefficients are reported at λ_{max} (ε) as averages (n = 3). Protein samples (20 μM) were measured in PBS solutions. Normalized spectra were shown for clarity unless otherwise noted.

Protein extinction coefficient measurement

Protein extinction coefficients were measured as previously described by Gill and Vonhippel.[53] The theoretical extinction coefficient is calculated based on the following formula:

$$\varepsilon^{Theor} = a \times \varepsilon^{Trp} + b \times \varepsilon^{Tyr} + c \times \varepsilon^{Cys}$$

where a, b and c are the numbers of Trp Tyr and Cys residues, respectively, in the sequence of given mutant. The extinction coefficients of the three residues were determined at 280 nm previously (ε^{Trp} = 5690 $M^{-1} \cdot cm^{-1}$, ε^{Tyr} = 1280 $M^{-1} \cdot cm^{-1}$, ε^{Cys} = 120 $M^{-1} \cdot cm^{-1}$). The concentration of the protein can be measured in 6 M Guanidine·HCl solution (denaturing reagent) as per Lambert-Beer's Law:

$$Abs_{280,Den} = \varepsilon^{Theor} \times c \times l$$

where *l* is the cuvette path length, *c* is the concentration of the protein. The absorbance of the same amount of the protein was measured in PBS in the same cuvette. Thus, the experimental extinction coefficient of the protein can be derived by:

$$\varepsilon^{Exper} = \frac{Abs_{280,Nat}}{Abs_{280,Den}} \times \varepsilon^{Theor}$$

Absolute fluorescence quantum yield measurement

Absolute fluorescence quantum yields (Φ) were recorded at room temperature on a Quantaurus-QY C11347-11 (Hamamatsu Photonics K.K., Japan) equipped with a Xenon lamp and a monochromator as excitation light source, an integration sphere, and a multichannel back-thinned CCD detector. All samples were diluted with PBS solution or corresponding organic solvents ($A < 0.1$). Recorded values are average numbers ($n = 5$).

Relative fluorescence quantum yield measurement[54]

Relative quantum yields were determined with reference to the standard fluorescent dye Oxazine-170 (purchased from Across Organics, Lot# A0098689). For individual standard or dye-hCRBPII complex, the integrals of corrected emission spectra were plotted against the absorbance at the excitation wavelength at various concentrations. The obtained slopes of protein-fluorophore complexes were compared with that of the standard reference. The absorbance of all samples and reference were kept below 0.1 unit to prevent any potential scattering. According to Kasha-Vavilov's Rule, that generally the quantum yield is independent of the excitation wavelength,[55] all samples were excited at 565 nm to match the profile of Oxazine-170, and the emission data were collected from 575 nm to 800 nm. Temperature was kept constant at 20 °C during the course of measurement. The absolute quantum yield of Oxazine-170 was taken as 0.579 in ethanol.[56] The calculation of the sample quantum yield was corrected for the different refractive indices of ethanol (η=1.362, 20 °C)[57] and PBS (η=1.334)[58]:

$$\Phi_X = \Phi_{ST} \times \frac{Slope_X}{Slope_{ST}} \times \left(\frac{\eta_X}{\eta_{ST}} \right)^2$$

where the subscripts *ST* and *X* denote reference and sample, respectively, Φ is the fluorescence quantum yield, *Slope* is the gradient of the plot of integrated fluorescence intensity over absorbance, and η the refractive index of the solvent.

Dye-hCRBPII binding kinetics

Binding kinetics were measured at 23 °C. hCRBPII mutant (20 μM in PBS) was mixed with the fluorophore (0.8 ~ 1 equivalent) and increase in absorbance at the corresponding λ_{max} was recorded. Collected data points were fit with a first-order exponential rise function to determine the binding half-time as described below:

$$A = A_0 \times \left(1 - e^{-kt}\right) + c$$

where A is the absorbance at each time point, A_o is the final absorbance when the complex formation ends, k is the pseudo-first order rate constant, t is the time elapsed, and c is a varying constant which accounts for any time delay from the addition of the fluorophore to the point recording started.

Switching fatigue, working pH, and temperature-dependent measurements

For *in vitro* photoswitching fatigue resistance measurement, alternate illumination was performed by using an Hg(Xe) Arc lamp (Oriel™ Instruments) attenuated with two neutral-density filters (Edmund Optics Inc.). Samples in PBS solution were illuminated with U-360 UV Bandpass filter (Edmund Optics) for 20 sec to switch “ON”, and were illuminated with Y-50 (500nm) Longpass filter (Edmund Optics) for 15 min to switch “OFF”. A model MWTC Type-K thermocouple sensor (Omega Engineering Inc.) was used to record the temperature inside the microcuvette during temperature-dependent measurements. Fluorescence spectral change of samples in PBS solution were measured by titrating with 0.1 M HCl aqueous solution or 0.1 M NaOH aqueous solution. pH values were recorded with an accumet™ Basic pH meter (Fisher Scientific) equipped with a PerpHect™ ROSS™ Micro Combination pH electrode (Thermo Scientific Orion).

Mammalian cell culture and transfection

All cell lines were cultured at 37 °C with 5% CO_2 in Dulbecco's Modified Eagle's Medium (DMEM) supplemented with 1.0 mM sodium pyruvate (Life Technologies), 10% fetal bovine serum (FBS; BioWest), 1% penicillin, and 1% streptomycin (Life Technologies). All cell lines were used without authentication and mycoplasma detection, since the conclusions of this study made from the images acquired would not be affected. Cells were seeded 1 d before transfection on an ibidi μ-Slide 8 well coverslip (with ibiTreat). Transfection was performed at ~70% confluency with 1.0 μg of plasmid DNA using Lipofectamine™ 3000 reagent (Life Technologies) according to the manufacturer's protocol. The medium was replaced after 8 h. Cells were washed with Dulbecco's phosphate-buffered saline (DPBS; Life Technologies) twice after another 36 h incubation and incubated in Phenol Red-free RPMI 1640 medium (Life Technologies). Prior to confocal imaging, the fluorophore (in ethanol solution) was added to cells at a final concentration noted in text and incubated at 37 °C with 5% CO_2 for 5 min. All washing steps were omitted.

Confocal imaging

Images were acquired using a Zeiss 510 Meta ConfoCor 3 Laser Scanning Microscope configured on a Zeiss AxioObserver Z1 automated inverted microscope platform, equipped with Argon/2, Diode 405-30, and HeNe 594 laser sources. DIC images were acquired using a μ-Slide DIC lid (ibidi). Spatiotemporal "turn-on" images were taken with a Plan-Apochromat 63x/1.40 Oil DIC M27 objective, all other images were taken with

an EC Plan-Neofluar 40x/1.30 Oil DIC M27 objective. ZEN 2009 and LSM Image Browser software (Zeiss) were used to process images. Image acquisition used the following settings. ECFP: excitation 458 nm, main dichroic HFT 458, secondary dichroic NFT 545, and detection channel BP 465-510IR; EGFP: excitation 488 nm, main dichroic HFT 405/488, secondary dichroic NFT 545, and detection channel BP 505-530; DIC: excitation 488 nm, main dichroic HFT 405/488; Switching: excitation 405 nm; CF: excitation 594 nm, main dichroic HFT 488/594, secondary dichroic NFT 545, and detection channel LP 650. All images were scanned in line mode with bit depth of 16 and pixel size of 0.22 μm. Kalman averaging 4 was applied. When imaging CrimFluor_"OFF" and "ON", the identical microscope settings were used before and after photoswitching, and the signal intensities were compared within a normalized dynamic range. Signal-to-background ratio was determined by measuring the mean fluorescence intensity of nuclei relative to adjacent regions outside nuclei in four fields of view using Fiji (n = 440 areas as noted in text).[59]

Cell viability assay

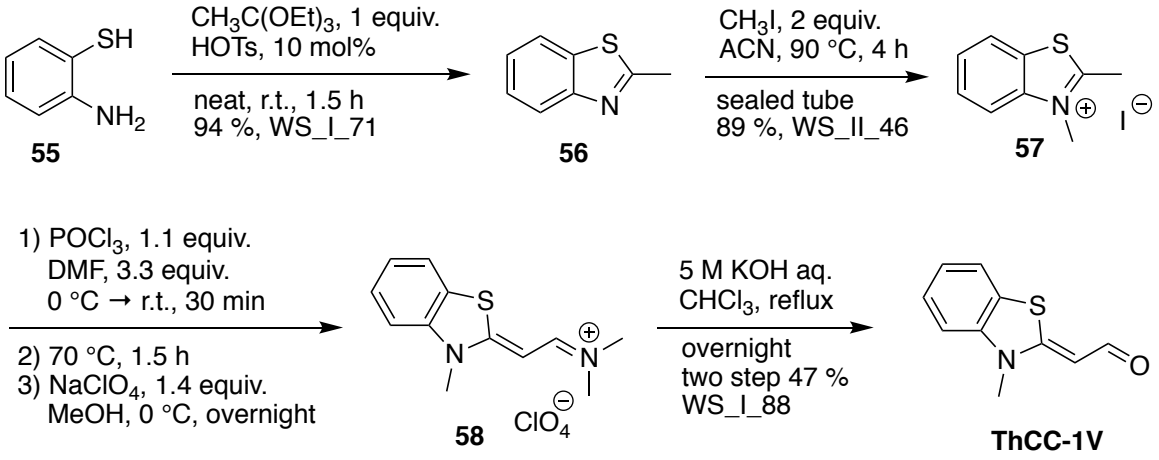
Cell viability was determined by using the tetrazolium dye 3-(4,5-dimethylthiazol-2-yl)-2,5-diphenyltetrazolium bromide (MTT, ThermoFisher Scientific).[46] HeLa or U2OS cells were seeded at 5,000 cells per well in a 96-well plate 1 d before the assay. When cells reached ~ 80% confluency, **FR-1V** was applied to cells (n = 6) at a series of concentrations to span the standard working condition of live cell experiments. Cells were then incubated at 37 °C for 24 h before addition of MTT, to examine the toxicity at a prolonged time span, although a typical confocal experiment would not last longer than a

few hours. The absorbance of dissolved formazan was recorded at 550 nm and referenced against 655 nm.

General synthetic procedures

Commercially available starting materials were obtained from Sigma-Aldrich and were used without further purification unless specified. All moisture sensitive reactions were carried out in flame-dried or oven-dried glassware under an atmosphere of nitrogen or argon. Unless otherwise mentioned, solvents were purified as follows: tetrahydrofuran (THF) and diethyl ether (Et_2O) were distilled freshly from the classical sodium/benzophenone ketyl still pot; dichloromethane (DCM), acetonitrile, and toluene were dried over CaH_2 and freshly distilled prior to use; dimethylsulfoxide (DMSO), dimethylformamide (DMF), and triethylamine (Et_3N) were distilled from CaH_2 and stored over activated molecular sieves. Chemical shifts were reported relative to the residual solvent peaks. (^{1}H-NMR: δ 7.26 ppm for $CDCl_3$, δ 3.31 ppm for CD_3OD, δ 2.50 ppm for DMSO-d_6, respectively. ^{13}C-NMR: δ 77.16 ppm for $CDCl_3$, δ 49.00 ppm for CD_3OD, δ 39.52 ppm for DMSO-d_6, respectively.) Analytical thin layer chromatography (TLC) was performed with pre-coated silica gel 60 F_{254} plates (Analtech, Inc.) Compounds in TLC were visualized upon UV irradiation and various staining techniques, i.e. *p*-anisaldehyde, potassium permanganate, phosphomolybdic acid in ethanol. Silica gel flash column chromatography was performed with Silicycle 40-60 Å (30 ~ 75 μM) silica gel.

Synthesis of ThCC



Scheme 0-6 Synthesis of **ThCC-1V**.

2-Methylbenzothiazole (56)[60]

p-Toluenesulfonic acid monohydrate (0.10 g, 0.50 mmol, 10 mol%) was added to a mixture of 2-aminothiophenol (**55**, 0.63 g, 5.0 mmol, 1.0 equiv.) and triethyl orthoacetate (0.81 g, 5.0 mmol, 1.0 equiv.). The mixture was stirred at room temperature for 1.5 h to reach full conversion. Cold water (10 mL) was added to the mixture under vigorous stirring. The resulting mixture was subjected to acid-base extraction with EtOAc (5 mL × 3). The combined organic layer was dried over Na_2SO_4 and concentrated *in vacuo* to afford a dim yellow oil as the product (0.70 g, 94% yield).

^{1}H-NMR (500 MHz, DMSO-d_6): δ (ppm) = 7.97 (d, J = 8.4 Hz, 1H), 7.83 (d, J = 8.4 Hz, 1H), 7.48 – 7.43 (m, 1H), 7.38 – 7.33 (m, 1H), 2.85 (s, 3H). ESI-MS calcd $[M+H]^+$: 150.04, found: 150.0.

2,3-Dimethylbenzothiazolium iodide (57)

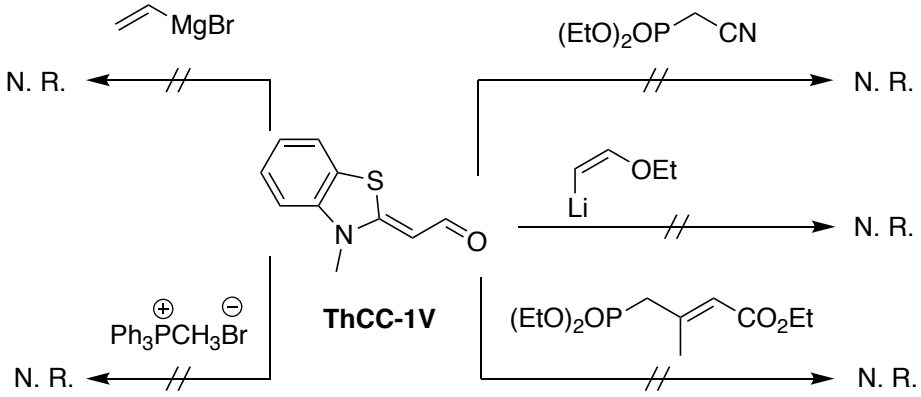
2-Methylbenzothiazole (**56**, 1.0 g, 6.7 mmol, 1.0 equiv.) was dissolved in acetonitrile (6 mL). Then iodomethane (1.9 g, 13.4 mmol, 2.0 equiv.) was added and the mixture was kept at 90 °C for 4 h in a sealed tube. After cooling to room temperature, the precipitate was collected by filtration, washed with dichloromethane (15 mL × 2), and dried *in vacuo* to afford a white solid (1.74 g) with 89% yield.

^{1}H-NMR (500 MHz, DMSO-d_6): δ (ppm) = 8.43 (d, J = 8.2 Hz, 1H), 8.29 (d, J = 8.5 Hz, 1H), 7.93 – 7.87 (m, 1H), 7.84 – 7.78 (m, 1H), 4.20 (s, 3H), 3.17 (s, 3H). ^{13}C-NMR (125 MHz, DMSO-d_6): δ (ppm) = 177.24, 141.55, 129.22, 128.67, 128.06, 124.44, 116.73, 36.13, 17.03. ESI-MS calcd $[M\text{-}Cl]^+$: 164.05, found: 164.0

2-Formylmethylene-3-methylbenzothiazoline (ThCC-1V)

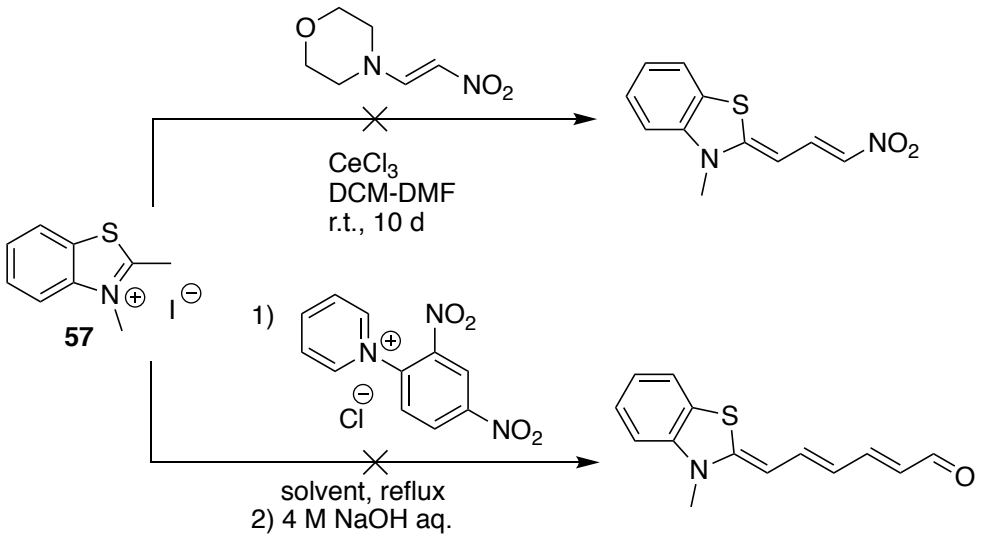
Phosphorous oxychloride (58 mg, 0.38 mmol, 1.1 equiv.) was dissolved in DMF (dry, 83 mg, 1.1 mmol, 3.3 equiv.) at 0 °C then warmed to room temperature. After 30 min, the resulting yellow solution was added dropwise to a solution of **57** (100 mg, 0.34 mmol, 1.0 equiv.) in DMF (dry, 1 mL) preheated to 70 °C over a period of 15 min. The reaction mixture was stirred for 1.5 h at 70 °C. The reaction mixture was cooled to room temperature, poured into methanol (3.5 mL) containing $NaClO_4$ (59 mg, 0.48 mmol, 1.4 equiv.), and chilled at -20 °C overnight. The precipitated deep red crystals **58** were filtered and stirred in a mixture of chloroform (15 mL) and NaOH aq. (5 M, 7.5 mL) under mild reflux overnight. The chloroform layer was separated and washed with water (2 × 5 mL), dried over Na_2SO_4 and concentrated *in vacuo*. The resulting oil was diluted with hexane (10 mL) and crystalized to afford yellow crystals as the final product (31 mg, 47% yield).

^{1}H-NMR (500 MHz, $CDCl_3$): δ (ppm) = 9.37 (s, 1H), 7.58 (d, J = 8.0 Hz, 1H), 7.37 (t, J = 7.3 Hz, 1H), 7.22 – 7.14 (m, 2H), 5.83 (s, 1H), 3.58 (s, 3H). ^{13}C-NMR (125 MHz, $CDCl_3$): δ (ppm) = 182.30, 160.46, 139.64, 126.79, 123.30, 122.59, 110.19, 90.72, 32.48. ESI-MS calcd $[M+H]^+$: 192.03, found: 192.0



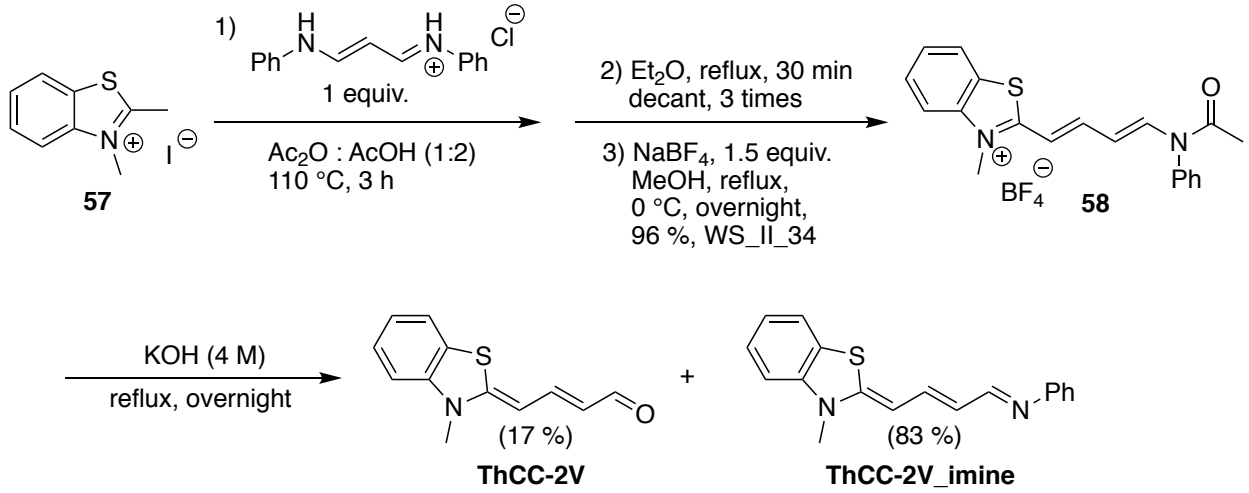
Scheme 0-7 Unsuccessful attempts for the nucleophilic elongation of **ThCC-1V.**

Attempts of direct olefination of the **ThCC-1V** aldehyde group were not successful. Probably due to its electron-rich nature, the aldehyde does not react with Wittig reagent, Grignard reagent, HWE phosphonates, or even the ethoxyvinyl lithium (**Scheme II-7**).



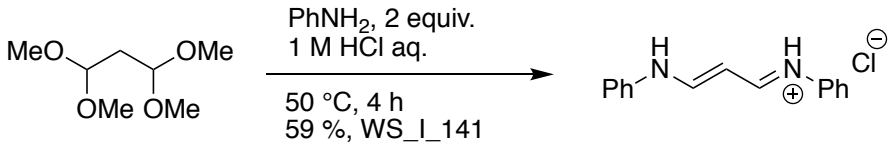
Scheme 0-8 Unsuccessful attempts for the electrophilic elongation of **57**.

In situ formation of the C2 vinylene of **57** and subsequent olefination via α-nitro enamine or *N*-dinitroaryl pyridinium mediated Zincke rearrangement were not successful either (**Scheme II-8**). The olefination was finally done via the malondialdehyde dianil condensation (**Scheme II-9**). However, the subsequent hydrolysis was not successful. It only yielded in a mixture of **ThCC-2V** and its phenylimine with a 17:83 ratio. Further optimization was not pursued.



Scheme 0-9 Attempted synthesis of **ThCC-2V** and its phenylimine.

Malondialdehyde dianil hydrochloride[61]



A solution of 1,1,3,3-tetramethoxypropane (2.0 g, 12 mmol, 1.0 equiv.) in hydrochloric acid (1 M, 20 mL) was heated to 50˚C. To it was added a solution of aniline (2.3 g, 24 mmol, 2.0 equiv.) in hydrochloric acid (1 M, 18 mL) in one portion. Upon addition, the mixture gradually turned orange. The reaction reached completion after 4 h. The

precipitate was collected by filtration, washed with ethyl acetate, and dried *in vacuo* to afford an orange solid (1.8 g) with 59% yield.

^{1}H-NMR (500 MHz, CD_3OD): δ (ppm) = 8.66 (d, J = 11.3 Hz, 2H), 7.49 – 7.43 (m, 4H), 7.38 – 7.33 (m, 4H), 7.31 – 7.25 (m, 2H), 6.23 (t, J = 11.7 Hz, 1H). ^{13}C-NMR (125 MHz, CD_3OD): δ (ppm) =159.86, 139.82, 131.17, 127.76, 118.75, 99.31. ESI-MS calcd $[M\text{-}Cl]^+$: 223.12, found: 223.1.

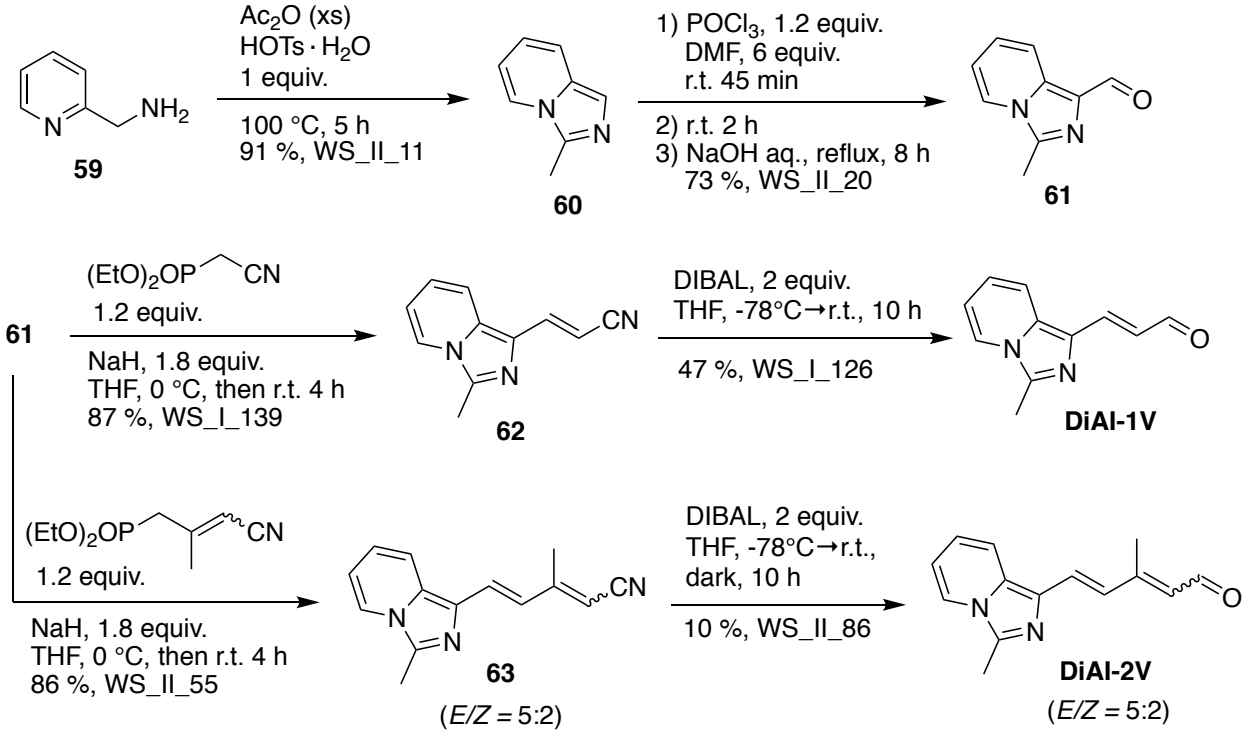
3-Methyl-2-((1*E*,3*E*)-4-(N-phenylacetamido)buta-1,3-dien-1-yl)benzothiazolium tetrafluoroborate (58)

2,3-Dimethylthiazolium iodide (**57**, 0.70 g, 2.4 mmol, 1 equiv.) was dissolved in a solution of AcOH and Ac_2O (2:1, 30 mL) and heated to 110 °C. Malondialdehyde dianil hydrochloride (0.70 g, 2.7 mmol, 1.1 equiv.) was then added into the solution in a portion wise manner over 30 min. The mixture was kept at 110 °C and vigorously stirred for additional 3 h. The resulting mixture was cooled to 60 °C and subjected to vacuum distillation (1.5 mbar) to remove the solvent. The slurry residue was mixed with Et_2O (20 mL) and refluxed for 30 min. The ethereal layer was decanted. Another portion of Et_2O (20 mL) was added, refluxed and decanted. The resulting solid was collected by filtration, dissolved into a solution of $NaBF_4$ (0.40 g, 3.6 mmol, 1.5 equiv., 20 mL of methanol), and crystalized at 0 °C overnight to afford red crystals as final product (0.98 g, 97% yield).

^{1}H-NMR (500 MHz, DMSO-d_6): δ (ppm) = 8.56 (d, J = 12.8 Hz, 1H), 8.32 (d, J = 8.0 Hz, 1H), 8.24 – 8.16 (m, 1H), 8.09 (d, J = 8.0 Hz, 1H), 7.81 – 7.76 (m, 1H), 7.70 (t, J = 7.6 Hz, 1H), 7.72 – 7.67 (m, 1H), 7.67 – 7.61 (m, 1H), 7.61-7.56 (m, 1H), 7.47 – 7.39 (m, 2H), 7.29 (d, J = 15.0 Hz, 1H), 5.43 (dd, J_1 = 13.3 Hz, J_2 = 11.4 Hz, 1H), 4.04 (s, 3H),

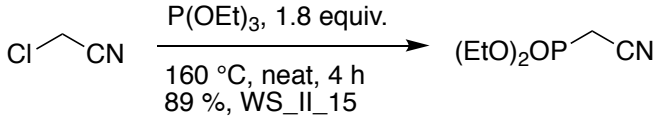
1.99 (s, 3H). ^{13}C-NMR (125 MHz, Acetone-d_6): δ (ppm) = 152.27, 145.50, 139.32, 131.42, 130.58, 130.25, 129.50, 129.00, 128.34, 124.61, 116.95, 112.54, 111.88, 36.24, 23.40. ESI-MS calcd $[M\text{-}Cl]^+$: 335.12, found: 335.0.

Synthesis of DiAl



Scheme 0-10 Synthesis of **DiAl**s.

(Diethylphosphono)acetonitrile[62]

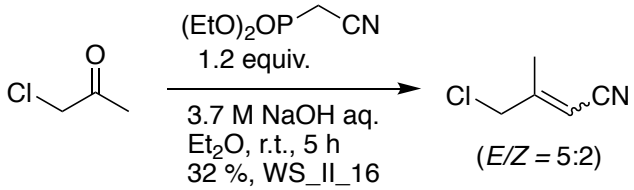


Triethyl phosphite (40 g, 0.24 mol, 1.8 equiv.) was heated to 160 ˚C. Chloroacetonitrile (10 g, 0.13 mol, 1.0 equiv.) was added at this temperature over a period of 1 h. The mixture was held for 3 more hours at 160 ˚C until gas evolvement was finished.

The mixture was distilled over a small Vigreux column (10 cm) under vacuum. The final fraction with b.p. 115 ~ 120 ˚C at 1.5 mbar was collected to afford a colorless oil (20.8 g) as the product (89% Yield).

^{1}H-NMR (500 MHz, $CDCl_3$): δ (ppm) = 4.26 – 4.20 (m, J_1 =7.0 Hz, J_2 = 1.0 Hz, 4H), 2.86 (d, J = 20.6 Hz, 2H), 1.37 (t, J = 7.0 Hz, 6H). ^{13}C-NMR (125 MHz, $CDCl_3$): δ (ppm) = 112.76 (d, J = 11.1 Hz), 64.06 (d, J = 6.9 Hz), 16.65 (d, J = 144.1 Hz), 16.42 (d, J = 5.9 Hz).

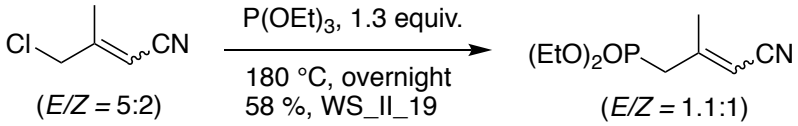
(2E/Z)-4-Chloro-3-methylbutyl-2-enenitrile[63]



Chloroacetone (5.0 g, 54 mmol, 1.0 equiv.) was added to a stirred solution of (diethylphosphono) acetonitrile (11.1 g, 62.7 mmol, 1.16 equiv.) in Et_2O (15 mL in a 100 mL three-necked round bottom flask fitted with a reflux condenser) at room temperature. Solution of NaOH (3.7 M, 17 mL, 1.2 equiv.) was added dropwise over 1 h at room temperature. The reaction mixture came to an ethereal reflux and turned orange. After an additional 4 h of stirring the two-phase mixture was separated. The aqueous phase was extracted with Et_2O (3 × 10 mL) and the combined organic layer was dried over Na_2SO_4, filtered and concentrated *in vacuo*. Vacuum distillation of the residual orange oil afforded a mixture of *cis*- and *trans*-4-chloro-3-methylbutyl-2-enenitrile (2.81 g, 32% yield, 50 ~ 60 °C at 1.5 mbar, *E/Z* = 5:2) as a colorless oil.

E/Z mixture: ^{1}H-NMR (500 MHz, $CDCl_3$): δ (ppm) = 5.52 (s, 1H), 5.29 (s, 1H), 4.27 (s, 2H), 4.07 (s, 2H), 2.15 (s, 3H), 2.06 (s, 3H). ^{13}C-NMR (125 MHz, $CDCl_3$): δ (ppm) =158.30, 158.01, 116.15, 115.36, 99.24, 99.00, 47.04, 44.41, 21.18, 19.27.

(2*E/Z*)-Diethyl (3-cyano-2-methylallyl)phosphonate[63]



(*E/Z* = 5:2) 58 %, WS_II_19 (*E/Z* = 1.1:1)

A neat mixture of triethyl phosphite (5.23 g, 31.5 mmol, 1.30 equiv.) and 4-chloro-3-methylbutyl-2-enenitrile (2.80 g, 24.2 mmol, 1.00 equiv.) in a 25 mL flask equipped with a stir bar was placed in a preheated bath at 180 °C. After stirring overnight, the mixture was allowed to cool to room temperature. Vacuum fractional distillation was employed and the mixture of geometric isomers of desired phosphonate was collected at 125 ~ 130 °C and 1.5 mbar to afforded 3.0 g (yield = 58%, *E/Z* = 1.1:1) as a colorless oil.

E/Z mixture: ^{1}H-NMR (500 MHz, $CDCl_3$): δ (ppm) = 5.25 – 5.28 (m, 2H), 4.09 – 4.19 (m, 8H), 2.96 (d, J = 23.7 Hz, 2H), 2.71 (d, J = 23.8 Hz, 2H), 2.19 (dd, J_1 = 3.3 Hz, J_2 = 0.9 Hz, 3H), 2.09 (dd, J_1 = 3.7 Hz, J_2 =1.6 Hz, 3H), 1.34 (t, J = 7.1 Hz, 6H), 1.32 (t, J = 7.1 Hz, 6H). ^{13}C-NMR (125 MHz, $CDCl_3$): δ (ppm) = 155.98 (d, J =11.2 Hz), 155.61 (d, J = 11.2 Hz), 116.50 (d, J = 5.4 Hz), 99.49 (d, J = 12.4 Hz), 99.06 (d, J = 12.4 Hz), 62.68 (d, J = 7.1 Hz), 62.62 (d, J = 7.1 Hz), 36.62 (d, J = 135.3 Hz), 34.87 (d, J = 135.3 Hz), 24.57 (d, J = 1.9 Hz), 22.62 (d, J = 3.1 Hz), 16.53 (d, J = 5.9 Hz), 16.51 (d, J = 5.7 Hz). ESI-MS calcd $[M+H]^+$: 218.09, found: 218.1.

3-Methyl [2,3a]diazaindene (60)

A solution of 2-picolylamine (**59**, 2.0 g, 18 mmol, 1.0 equiv.) and *p*-toluenesulfonic acid monohydrate (3.5 g, 18 mmol, 1 equiv.) in acetic anhydride (12 mL) was heated at 100 °C for 5 h. After cooling down to room temperature, the reaction mixture was poured into water (50 mL) and adjusted pH to 10 with 25% NaOH aqueous solution. Three portions of dichloromethane were used to extract the aqueous solution (3 × 20 mL). The combined organic layer was washed with brine and dried over Na_2SO_4. The removal of solvent afforded a brown oil (2.2 g, 91% yield).

^{1}H-NMR (500 MHz, $CDCl_3$): δ (ppm) = 7.66 (d, J_1 = 7 Hz, J_2 = 1 Hz, 1H), 7.40 (dt, J_1 = 9 Hz, J_2 = 1.1 Hz, J_3 = 1 Hz, 1H), 7.35 (s, 1H), 6.68 – 6.64 (m, J_1 = 9 Hz, J_2 = 6.8 Hz, 1H), 6.58 – 6.54 (m, 1H), 2.66 (s, 3H). ^{13}C-NMR (125 MHz, $CDCl_3$): δ (ppm) =134.84, 130.27, 120.58, 118.57, 117.81, 112.45, 12.48. ESI-MS calcd $[M+H]^+$: 133.07, found: 133.1.

1-Formyl-3-methyl [2,3a]diazaindene (61)

Phosphorous oxychloride (2.78 g, 18.2 mmol, 1.20 equiv.) was dissolved in DMF (dry, 6.64 g, 90.8 mmol, 6.00 equiv.) at 0 °C then warmed to room temperature. After 30 min, the formed yellow viscous reagent was added dropwise to a solution of **60** (2.0 g, 15 mmol, 1.0 equiv.) at 0 °C. A mud-like heavy suspension was immediately formed. The mixture was stirred vigorously at room temperature for 2 h, monitored by TLC (Hexane : EtOAc : Et_3N = 15 : 80 : 5). After complete conversion, NaOH aq. (5 M, 25 mL) and dichloromethane (30 mL) were added to the slurry. The mixture was allowed mild refluxed overnight. The organic layer was separated and combined with additional DCM extraction

(3 × 10 mL), dried over Na_2SO_4, and concentrated on rotavap. The crude was purified by flash silica gel chromatography to afford yellow solid (1.3 g, 73% yield).

^{1}H-NMR (500 MHz, $CDCl_3$): δ (ppm) = 10.07 (s, 1H), 8.27 (d, J = 9.2 Hz, 1H), 7.89 (dt, J_1 = 7.0 Hz, J_2 =1.0 Hz, 1H), 7.25 – 7.22 (m, 1H), 6.96 – 6.91 (m, 1H), 2.72 (s, 3H). ^{13}C-NMR (125 MHz, $CDCl_3$): δ (ppm) =185.27, 137.22, 129.43, 125.71, 121.78, 119.72, 118.85, 115.20, 12.65. ESI-MS calcd $[M+H]^+$: 161.06, found: 161.0.

(2*E*)-(3-methyl [2,3a]diazaindene-1-yl) acrylonitrile (62)

Sodium hydride (60 % in mineral oil, 101 mg, 2.53 mmol, 1.80 equiv.) was added to tetrahydrofuran (dry, 1.5 mL). The mixture was cooled to 0 °C. A solution of (diethylphosphono)acetonitrile (299 mg, 1.69 mmol, 1.20 equiv.) in tetrahydrofuran (dry, 1.0 mL) was then added dropwise to the NaH mixture under nitrogen. After hydrogen ceased evolving, a solution of **61** (225 mg, 1.41 mmol, 1.00 equiv.) in tetrahydrofuran (dry, 8 mL) was added in dropwise over 20 min. The reaction mixture was warmed to room temperature and kept for 4 h. The excess amount of phosphonate was quenched with distilled benzaldehyde (30 mg, 0.20 equiv.). The crude was concentrated *in vacuo* to obtain a mixture (*E/Z* = 6.7:1). It was further purified by flash chromatography (45% hexane, 50% CH_2Cl_2, 5% Et_3N), to afford yellow solid of *E*-isomer (223 mg, 87% yield).

^{1}H-NMR (500 MHz, $CDCl_3$): δ (ppm) = 7.73 (dd, J_1 = 7 Hz, J_2 = 1 Hz, 1H), 7.52 (dd, J_1 = 9 Hz, J_2 = 1 Hz, 1H), 7.51 (d, J = 15.8 Hz, 1H), 6.99 – 6.93 (m, 1H), 6.76 – 6.69 (m, 1H), 6.04 (d, J = 15.8 Hz, 1H), 2.67 (s, 3H). ^{13}C-NMR (125 MHz, $CDCl_3$): δ (ppm) =139.09,

137.94, 131.53, 125.72, 122.37, 122.01, 120.34, 117.05, 113.81, 89.45, 12.78. ESI-MS calcd $[M+H]^+$: 184.08, found: 184.1.

(*E*)-3-(3-methyl [2,3a]diazaindene-1-yl) acrylaldehyde (DiAl-1V)

To a solution of **62** (50 mg, 0.27 mmol, 1.0 equiv.) in THF (dry, 0.8 mL) was added DIBAL (1 M in hexane, 0.55 mL, 2.0 equiv.) at -78 °C under argon. The reaction mixture was then warmed to room temperature gradually. The resulting orange solution was stirred at rt for a further 10 h. The reaction was quenched with cold acetone (5 mL) at 0 °C. The aluminum emulsion was diluted with water (10 mL) and treated with saturated solution of Rochelle's salt. Extraction with DCM (4 × 10 mL) was employed after 30 min. The combined organic layer was dried and concentrated *in vacuo*. The crude was purified by flash chromatography (50% hexane, 45% DCM, 5% Et_3N) to afford yellow solid (24 mg, 47% yield).

^{1}H-NMR (500 MHz, $CDCl_3$): δ (ppm) = 9.64 (d, J = 8 Hz, 1H), 7.78 (d, J = 7 Hz, 1H), 7.66 (d, J = 9 Hz, 1H), 7.65 (d, J = 15.4 Hz, 1H), 7.03 (dd, J_1 = 9 Hz, J_2 = 9 Hz, 1H), 6.87 (dd, J = 15.4 Hz, 8 Hz, 1H), 6.78 (t, J = 7 Hz, 1H), 2.69 (s, 3H). ^{13}C-NMR (125 MHz, $CDCl_3$): δ (ppm) =193.42, 142.46, 138.28, 132.83, 126.21, 123.81, 122.89, 122.27, 117.58, 114.07, 12.81. ESI-MS calcd $[M+H]^+$: 187.08, found: 187.1.

(*2E/Z*)-(4*E*)-3-methyl-5-(3-methyl [2,3a]diazaindene-1-yl) penta-2,4-dienenitrile (63)

The procedure was similar to that for the preparation of **62**. Instead of (diethylphosphono) acetonitrile, (2*E/Z*)-diethyl (3-cyano-2-methylallyl)phosphonate (1.6 g,

7.5 mmol, 1.2 equiv.) was used to react with **61** (1.0 g, 6.2 mmol, 1.0 equiv.). Purification by flash chromatography (36% EtOAc, 61% hexane, 3% Et_3N) and subsequent crystallization in EtOAc afforded yellow crystals (1.2 g, 86% yield) with an isomer ratio of *E/Z* = 5:2. Further isolation of the two isomers was not fruitful. The whole procedure was carried out in dark under red light.

E/Z mixture: ^{1}H-NMR (500 MHz, $CDCl_3$): δ (ppm) = 7.73 – 7.66 (m, 1H), 7.66 – 7.62 (m, 1H'), 7.20 – 7.10 (m, 2H), 7.11 – 7.03 (m, 2H'), .6.91 – 6.81 (m, 1H, 1H'), 6.70 – 6.61 (m, 1H, 1H'), 5.27 (s, 1H), 5.07 (s, 1H'), 2.67 (s, 3H, 3H'), 2.29 (s, 3H), 2.14 (s, 3H'). ^{13}C-NMR (125 MHz, $CDCl_3$): δ (ppm) = 157.08, 156.66, 136.94, 130.27, 130.05, 127.65, 127.26, 127.19, 125.15, 124.13, 121.66, 121.59, 120.67, 120.38, 118.77, 118.07, 117.46, 113.33, 95.21, 93.54, 19.46, 16.54, 12.63, 12.60. ESI-MS calcd $[M+H]^+$: 224.11, found: 224.0.

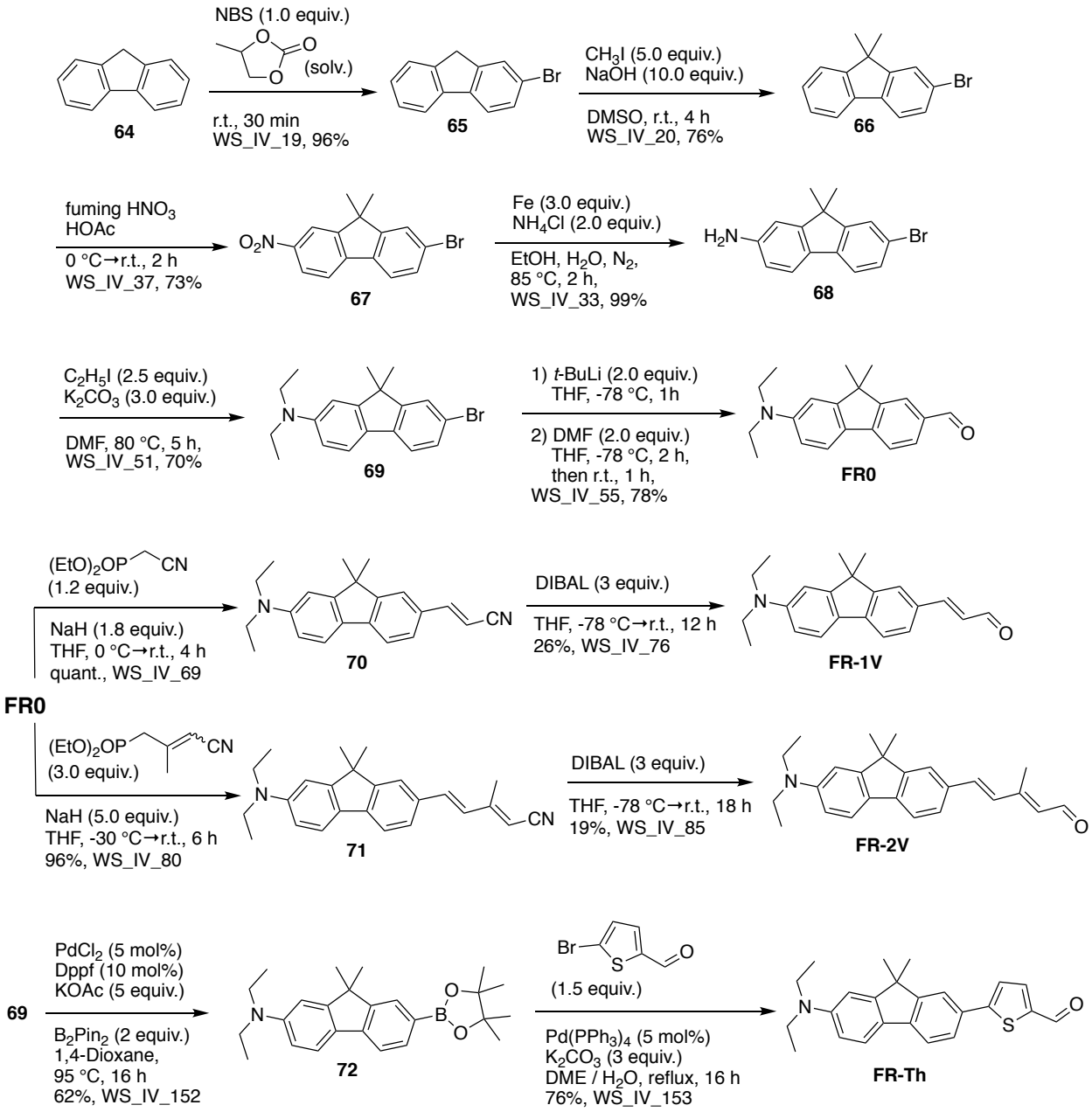
(*2E/Z*)-(4*E*)-3-methyl-5-(3-methyl [2,3a]diazaindene-1-yl) penta-2,4-dienal (DiAl-2V)

The DIBAL reduction procedure was similar to that for the preparation of **DiAl-1V**. 3 equivalents of DIBAL were used instead of 2 equiv. The whole procedure was performed in the dark room under red light. The crude was purified by dry column chromatography and Prep TLC to afford a deep red solid in as an *E/Z* mixture (12 mg, 10% yield, *E/Z* = 1:0.4, based on 1D-NOE). Further isolation was not fruitful even with Prep-HPLC. The two isomers quickly isomerize on silica and alumina.

E/Z mixture: ^{1}H-NMR (500 MHz, $CDCl_3$): δ (ppm) = 10.40 (d, J = 8.1 Hz, 1H), 10.11 (d, J = 8.1 Hz, 1H'), 7.69 (d, J = 7.2 Hz, 1H, 1H'), 7.58 (d, J = 9.2 Hz, 1H, 1H'), 7.29 –

7.24 (m, 1H, 1H'), .7.19 – 7.14 (m, 1H, 1H'), 6.89 – 6.83 (m, 1H, 1H'), 6.69 – 6.64 (m, 1H, 1H'), 6.11 (d, J = 8.2 Hz, 1H), 5.84 (d, J = 8.2 Hz, 1H'), 2.68 (s, 3H, 3H'), 2.40 (s, 3H), 2.22 (s, 3H'). ^{13}C-NMR (125 MHz, $CDCl_3$): δ (ppm) = 191.13, 190.51, 155.32, 137.04, 130.33, 128.26, 127.55, 127.32, 127.10, 125.72, 121.63, 120.65, 117.62, 117.59, 113.52, 29.69, 13.04, 12.58. 1D-NOE (500 MHz, $CDCl_3$): δ (ppm) = 2.40 (10.10). ESI-MS calcd $[M+H]^+$: 227.11, found: 227.0.

Synthesis of FR



Scheme 0-11 Synthesis of **FR**s.

2-bromo-9*H*-fluorene (65)[23]

Fluorene (4.98 g, 30.0 mmol) was dissolved in distilled propylene carbonate (60 mL) by heating up to 60°C shortly. NBS (5.34 g, 30.0 mmol) was then added to the

solution in portion over 2 h. The mixture was kept stirred at room temperature. The solution gradually turned yellow and formed precipitates. The reaction was monitored by TLC (hexane). The mixture was then poured into cold water (500 mL) and the precipitate was filtered to afford 7.07 g of an off-white solid (96% yield). The crude was used in the next reaction without crystallization.

^{1}H-NMR (500 MHz, $CDCl_3$), δ (ppm) = 7.76 (d, J = 6.6 Hz, 1H), 7.69 (s, 1H), 7.64 (d, J = 8.1 Hz, 1H), 7.54 (dt, J_1 = 7.3 Hz, J_2 = 1.0 Hz, 1H), 7.51 – 7.49 (m, 1H), 7.41 – 7.36 (m, 2H), 7.33 (td, J_1 = 7.4 Hz, J_2 = 1.2 Hz, 2H), 3.89 (s, 2H).

2-bromo-9,9-dimethyl-9*H*-fluorene (66)[23]

To a mixture of NaOH (4.00 g, 100 mmol) and DMSO (50 mL) was added **65** (2.45 g, 100 mmol). The mixture was stirred for 1 h at room temperature. A solution of iodomethane (7.10 g, 50.0 mmol) in DMSO (10 mL) was then added to the above mixture. The reaction mixture was stirred for another 4 h at room temperature and monitored by TLC (hexane). The mixture was poured into ice water (100 mL) and extracted with DCM (20 mL × 3). The crude product was purified by flash chromatography (hexane) to afford 2.10 g of a white solid (76% yield).

^{1}H-NMR (500 MHz, $CDCl_3$), δ (ppm) = 7.71 – 7.69 (m, 1H), 7.59 (d, J = 8 Hz, 1H) 7.57 – 7.54 (m, 1H), 7.48 – 7.46 (m, 1H), 7.44 – 7.42 (m, 1H), 7.36 – 7.34 (m, 2H), 1.49 (s, 6H).

2-bromo-9,9-dimethyl-7-nitro-9*H*-fluorene (67)[23]

To a solution of **66** (1.90 g, 6.96 mmol) in glacial acetic acid (40 mL) was added fuming nitric acid (6 mL) dropwise at 0 °C with vigorous stirring. The reaction mixture was stirred at room temperature after addition. A yellowish green precipitate formed in 30 min. The reaction mixture was poured into 200 mL water at the appearance of dinitro product (5% EtOAc-Hexane, Rf ~ 0.25). The precipitate was filtered, washed thoroughly with water, and recrystallized from acetonitrile (60 mL) to afford light yellow crystals (1.61 g, yield = 73%).

^{1}H-NMR (500 MHz, $CDCl_3$), δ (ppm) = 8.29 – 8.26 (m, 2H), 7.80 (d, J = 8 Hz, 1H) 7.68 – 7.66 (m, 1H), 7.64 (s, 1H), 7.56 – 7.54 (m, 1H), 1.55 (s, 6H).

7-bromo-9,9-dimethyl-9*H*-fluoren-2-amine (68)[23]

A mixture of **67** (2.50 g, 7.86 mmol), iron powder (1.32 g, 23.6 mmol, 3.0 equiv.), and ammonium chloride (840 mg, 15.7 mmol, 2.0 equiv.) in a co-solvent (90 mL of EtOH, 25 mL of H_2O) was heated to reflux (85 °C) and kept under mechanical stirring for 2 h. The reaction mixture was then neutralized with saturated $NaHCO_3$ solution to pH 8 and filtered. The filter cake was washed with ethanol to dissolve the product. The filtrate was combined and concentrated *in vacuo* to remove the ethanol. The product was extracted with DCM from the aqueous phase. The organic phase was dried with $NaSO_4$ and concentrated to afford a yellow crystalline solid (2.24 g, yield = 99%).

^{1}H-NMR (500 MHz, $CDCl_3$), δ (ppm) = 7.48 – 7.47 (m, 2H), 7.44-7.39 (m, 2H), 6.74 (d, J = 2.1 Hz, 1H), 6.67 (dd, J_1 = 8.0 Hz, J_2 = 2.2 Hz, 1H), 3.81 (s, 2H), 1.44 (s, 6H).

7-bromo-*N,N*-diethyl-9,9-dimethyl-9*H*-fluoren-2-amine (69)[23]

A mixture of **68** (2.00 g, 6.94 mmol), ethyl iodide (2.71 g, 17.3 mmol, 2.5 equiv.), potassium carbonate (2.88 g, 20.8 mmol, 3.0 equiv.) in DMF (20 mL) was heated at 80 °C for 5 h. The solvent was removed by distillation under reduced pressure. The resulting crude was poured into water and extracted with ethyl acetate. The organic phase was combined and dried, and concentrated *in vacuo.* The crude was purified by flash chromatography with 5% ethyl acetate in hexane to afford orange crystals (1.67 g, yield = 70%). ESI-MS calcd $[M+H]^+$: 344.09, found: 343.92.

^{1}H-NMR (500 MHz, $CDCl_3$), δ (ppm): 7.51 (d, J = 8 Hz, 1H), 7.44 (d, J = 2 Hz, 1H), 7.41 – 7.35 (m, 2H), 6.86 – 6.64 (m, 2H), 3.42 (q, J = 7.0 Hz, 4H), 1.44 (s, 6H), 1.21 (t, J = 7.0 Hz).

7-diethylamino-9,9-dimethyl-9*H*-fluorene-2-carbaldehyde (FR0)[23]

To a solution of **69** (500 mg, 1.45 mmol) in dry THF, *t*-BuLi (1.71 mL of 1.7 M solution in pentane, 2.0 equiv.) was added dropwise at -78 °C under argon. The reaction mixture was stirred for 1 h, and an orange suspension was formed. DMF (212 mg, 2.91 mmol, 2.0 equiv.) was added dropwise and the formed solution was stirred for additional 2 h at -78 °C. The reaction mixture was warmed to room temperature and stirred for 1 h. The reaction was quenched with 2 M HCl aq. and the pH was adjusted to 8. The solution was extracted with EtOAc. The combined organic phase was dried with Na_2SO_4 and evaporated *in vacuo*. The crude was purified by flash chromatography (5% EtOAc-Hexane) to yield **FR0** (330 mg, 78%) as a yellow solid.

^{1}H-NMR (500 MHz, $CDCl_3$), δ (ppm) = 9.98 (d, J = 0.8 Hz, 1H), 7.90 – 7.85 (m, 1H), 7.78 (dt, J_1 = 7.8 Hz, J_2 = 1.1 Hz, 1H), 7.68 – 7.59 (m, 2H), 6.73 – 6.66 (m, 2H), 3.46 (q, J = 7.1 Hz, 4H), 1.50 (s, 6H), 1.30 – 1.20 (m, 7H). ^{13}C-NMR (125 MHz, $CDCl_3$): δ (ppm) = 192.05, 157.33, 153.19, 148.99, 146.90, 133.41, 131.27, 125.20, 122.47, 122.35, 118.12, 110.87, 105.06, 46.62, 44.71, 27.24, 12.59.

(*E*)-3-(7-(diethylamino)-9,9-dimethyl-9*H*-fluoren-2-yl)acrylonitrile (70)

To a stirred suspension of NaH (13 mg, 0.31 mmol) in tetrahydrofuran (1.0 mL) was added a solution of (diethylphosphono)acetonitrile (36 mg, 0.21 mmol) in tetrahydrofuran (1 mL). The mixture was kept at 0 °C and stirred for 30 min. Then a solution of **FR0** (50 mg, 0.17 mmol) in dry tetrahydrofuran (3 mL) was added. The reaction mixture was stirred at ambient temperature for 4 h. The reaction mixture was then poured into cold water and extracted with ethyl acetate. The organic phase was dried and concentrated. Purification by flash chromatography (6% ethyl acetate in hexane) afforded 56 mg of a yellow solid (yield: quantitative).

^{1}H-NMR (500 MHz, $CDCl_3$), δ (ppm) = 7.55 (dd, J_1 = 15.4 Hz, J_2 = 8.1 Hz, 2H), 7.48 – 7.40 (m, 2H), 7.35 (dd, J_1 = 7.9 Hz, J_2 = 1.4 Hz, 1H), 6.73 – 6.64 (m, 2H), 5.88 – 5.79 (m, 1H), 3.45 (q, J = 7.1 Hz, 4H), 1.47 (s, 6H), 1.23 (t, J = 7.0 Hz, 6H). ^{13}C-NMR (125 MHz, $CDCl_3$): δ (ppm) = 156.45, 153.37, 151.25, 148.59, 143.76, 130.07, 127.46, 125.61, 121.81, 120.76, 119.10, 118.53, 110.81, 105.21, 93.00, 46.64, 44.71, 27.37, 12.61. ESI-HRMS: (calc.) (m/z) calcd for $C_{22}H_{24}N_2$ $[M+H]^+$ 317.2018, found 317.2019.

(*E*)-3-(7-(diethylamino)-9,9-dimethyl-9*H*-fluoren-2-yl)acrylaldehyde (FR-1V)

To a solution of compound **70** (50 mg, 0.16 mmol) in tetrahydrofuran (dry, 3 mL) was added DIBAL (1 M in THF, 0.50 mL) at -78 °C under argon. The reaction mixture was then allowed to warm to ambient temperature gradually and was stirred for 12 h. Cold methanol was added drop wise to quench reaction. The mixture was treated with saturate solution of Rochelle's salt and extracted with dichloromethane. The combined organic phase was dried and concentrated. Purification by flash chromatography (5% ethyl acetate in hexane) afforded 13 mg of an orange solid (26% yield).

^{1}H-NMR ($CDCl_3$, 500 MHz), δ (ppm) = 9.70 (d, J = 7.8 Hz, 1H), 7.61 – 7.47 (m, 5H), 6.78 – 6.66 (m, 3H), 3.46 (q, J = 7.1 Hz, 4H), 1.49 (s, 6H), 1.24 (t, J = 7.1 Hz, 6H). ^{13}C NMR ($CDCl_3$, 125 MHz), δ (ppm) = 193.83, 156.61, 154.07, 153.38, 148.64, 144.00, 130.54, 128.81, 126.43, 125.72, 122.01, 121.89, 118.59, 110.82, 105.22, 46.63, 44.72, 27.39, 12.63. ESI-HRMS (m/z) calcd for $C_{22}H_{25}NO$ $[M+H]^+$ 320.2014, found 320.2015.

(2*E*,4*E*)-5-(7-(diethylamino)-9,9-dimethyl-9*H*-fluoren-2-yl)-3-methylpenta-2,4-dienenitrile (71)

To a stirred suspension of NaH (102 mg, 2.56 mmol) in dry tetrahydrofuran (2.0 mL) was added a solution of (2*E/Z*)-diethyl (3-cyano-2-methylallyl)phosphonate (333 mg, 1.53 mmol) in dry tetrahydrofuran (1.0 mL). The mixture was kept at -30 °C and stirred for 1 h. Then a solution of **FR0** (0.15 g, 0.51 mmol) in dry tetrahydrofuran (5.0 mL) was added. The reaction mixture was stirred at ambient temperature for 6 h. The reaction mixture was then poured into cold water and extracted with ethyl acetate. The organic

phase was dried and concentrated. Purification by flash chromatography (5% ethyl acetate in hexane) afforded 174 mg of an orange solid (96% yield).

^{1}H-NMR ($CDCl_3$, 500 MHz), δ (ppm) = 7.53 (dd, J = 12.9, 8.2 Hz, 2H), 7.46 (d, J = 1.6 Hz, 1H), 7.37 (dd, J = 8.0, 1.6 Hz, 1H), 6.97 (d, J = 15.8 Hz, 1H), 6.88 – 6.81 (m, 1H), 6.72 – 6.63 (m, 2H), 5.33 – 5.29 (m, 1H), 3.44 (q, J = 7.0 Hz, 4H), 2.29 (d, J = 0.8 Hz, 3H), 1.47 (s, 6H), 1.22 (t, J = 7.1 Hz, 6H). ^{13}C NMR ($CDCl_3$, 125 MHz), δ (ppm) = 157.17, 156.15, 153.33, 148.23, 141.79, 136.90, 132.14, 127.17, 126.21, 126.13, 121.41, 120.75, 118.56, 118.28, 110.78, 105.43, 96.55, 46.61, 44.71, 27.47, 16.72, 12.63. ESI-HRMS (m/z) calcd for $C_{25}H_{29}N_2$ $[M+H]^+$ 357.2331, found 357.2349.

(2*E*,4*E*)-5-(7-(diethylamino)-9,9-dimethyl-9*H*-fluoren-2-yl)-3-methylpenta-2,4-dienal (FR-2V)

To a solution of compound **71** (0.15 g, 0.42 mmol) in dry THF (8.0 mL) was added DIBAL (1 M in THF, 1.3 mL) at -78 °C under argon. The reaction mixture was then allowed to warm to ambient temperature gradually and was stirred for 18 h. Cold methanol was added drop wise to quench the reaction. The mixture was treated with saturate solution of Rochelle's salt and extracted with dichloromethane. The combined organic phase was dried and concentrated. Purification by gravity silica chromatography and Prep-TLC (2% ethyl acetate in hexane) afforded 28 mg of a red solid (19% yield).

^{1}H-NMR ($CDCl_3$, 500 MHz), δ (ppm) = 10.17 (d, J = 8.2 Hz, 1H), 7.60 – 7.50 (m, 3H), 7.42 (dd, J_1 = 7.9 Hz, J_2 = 1.6 Hz, 1H), 7.16 (d, J = 16.0 Hz, 1H), 6.93 (dd, J_1 = 16.0 Hz, J_2 = 0.8 Hz, 1H), 6.74 – 6.65 (m, 1H), 6.15 – 6.08 (m, 1H), 3.45 (q, J = 7.1 Hz, 4H),

2.42 (d, J = 1.1 Hz, 3H), 1.50 (s, 6H), 1.23 (t, J = 7.1 Hz, 6H). ^{13}C NMR ($CDCl_3$, 125 MHz), δ (ppm) = 191.20, 156.22, 155.00, 153.36, 148.24, 141.84, 136.82, 132.51, 129.21, 129.12, 127.36, 126.25, 121.43, 120.82, 118.58, 110.78, 105.44, 46.62, 44.71, 27.48, 13.13, 12.64. ESI-HRMS (m/z) calcd for $C_{25}H_{30}NO$ $[M+H]^+$ 360.2327, found 360.2336.

_N,N_-diethyl-9,9-dimethyl-7-(4,4,5,5-tetramethyl-1,3,2-dioxaborolan-2-yl)-9_H_-fluoren-2-amine (72)

To a solution of **69** (0.20 g, 0.58 mmol) in dry 1,4-dioxane (30 mL) was added $PdCl_2$ (6.0 mg, 0.029 mmol, 5 mol%), Dppf (33 mg, 0.058 mmol, 10 mol%), B_2Pin_2 (295 mg, 1.16 mmol, 2.0 equiv.) and potassium acetate (285 mg, 2.90 mmol, 5.0 equiv.). The resulting mixture was flushed with argon, then heated to 95 °C and kept stirring for 16 h. The reaction was quenched with water after full conversion of the starting material monitored with TLC (10% EtOAc in Hexane). The mixture was extracted with EtOAc, and run through a silica pad to remove the palladium and Dppf. The combined organic phase was dried and concentrated *in vacuo*. The crude was purified by gradient chromatography with 100% Hexane to 5% EtOAc-Hexane. Crystallization in EtOAc afforded 140 mg of a pale yellow crystal (62% yield).

^{1}H-NMR ($CDCl_3$, 500 MHz), δ (ppm) = 7.80 (s, 1H), 7.76 (d, J = 7.5 Hz, 1H), 7.57 (t, J = 8.0 Hz, 2H), 6.71 (d, J = 2.3 Hz, 1H), 6.67 (dd, J_1 = 8.4 Hz, J_2 = 2.4 Hz, 1H), 3.44 (q, J = 7.1 Hz, 4H), 1.48 (s, 6H), 1.37 (s, 12H), 1.22 (t, J = 7.1 Hz, 6H). ^{13}C NMR ($CDCl_3$, 125 MHz), δ (ppm) = 156.28, 151.82, 148.17, 143.18, 133.96, 128.28, 126.86, 121.45,

117.71, 110.61, 105.50, 83.51, 46.65, 44.69, 27.43, 24.91, 23.42, 12.64. ESI-HRMS (m/z) calcd for $C_{25}H_{35}BNO_2$ $[M+H]^+$ 392.2761, found 392.2776.

5-(7-(diethylamino)-9,9-dimethyl-9*H*-fluoren-2-yl)thiophene-2-carbaldehyde (FR-Th)

To a solution of **72** (50 mg, 0.13 mmol) and 5-bromo-2-thiophene-carboxaldehyde (37 mg, 0.19 mmol, 1.5 equiv.) in DME (3.0 mL) was added $Pd(PPh_3)_4$ (8.0 mg, 6.4 μmol, 5 mol%) and potassium carbonate (53 mg, 0.38 mmol, 3.0 equiv.). Water (0.4 mL) was added as a co-solvent. The mixture was heated to reflux for 15 h. The resulting crude was run through a silica pad to remove palladium and extracted with EtOAc. The organic phase was dried and concentrated. The crude was purified by flash chromatography with 5% EtOAc in Hexane and crystalized in EtOAc to afford 29 mg of a bright-red crystal (76% yield).

^{1}H-NMR ($CDCl_3$, 500 MHz), δ (ppm) = 9.88 (s, 1H), 7.75 (d, J = 4.0 Hz, 1H), 7.66 – 7.55 (m, 4H), 7.42 (d, J = 4.0 Hz, 1H), 6.74 – 6.66 (m, 2H), 3.45 (q, J = 7.1 Hz, 4H), 1.51 (s, 6H), 1.24 (q, J = 7.1, 6.1 Hz, 6H). ^{13}C NMR ($CDCl_3$, 125 MHz), δ (ppm) = 182.65, 156.10, 155.91, 153.58, 148.32, 141.88, 141.28, 137.68, 129.44, 125.95, 125.62, 123.09, 121.49, 120.27, 118.74, 110.79, 105.39, 46.79, 44.71, 27.46, 12.63. ESI-HRMS (m/z) calcd for $C_{24}H_{26}NOS$ $[M+H]^+$ 376.1735, found 376.1729.

REFERENCES

REFERENCES

1. Shaner, N.C., Steinbach, P.A. & Tsien, R.Y. A guide to choosing fluorescent proteins. *Nat. Methods* **2005**, 2, 905-909.

2. McKinney, S.A., Murphy, C.S., Hazelwood, K.L., Davidson, M.W. & Looger, L.L. A bright and photostable photoconvertible fluorescent protein. *Nat. Methods* **2009**, 6, 131-133.

3. Durisic, N., Cuervo, L.L. & Lakadamyali, M. Quantitative super-resolution microscopy: pitfalls and strategies for image analysis. *Curr. Opin. Chem. Biol.* **2014**, 20, 22-28.

4. Costantini, L.M. & Snapp, E.L. Fluorescent Proteins in Cellular Organelles: Serious Pitfalls and Some Solutions. *DNA Cell Biol.* **2013**, 32, 622-627.

5. Zhang, M. et al. Rational design of true monomeric and bright photoactivatable fluorescent proteins. *Nat. Methods* **2012**, 9, 727-729.

6. Landgraf, D., Okumus, B., Chien, P., Baker, T.A. & Paulsson, J. Segregation of molecules at cell division reveals native protein localization. *Nat. Methods* **2012**, 9, 480-482.

7. Kumagai, A. et al. A Bilirubin-Inducible Fluorescent Protein from Eel Muscle. *Cell* **2013**, 153, 1602-1611.

8. Wang, W. et al. Tuning the Electronic Absorption of Protein-Embedded All-trans-Retinal. *Science* **2012**, 338, 1340-1343.

9. Gunasekaran, K., Hagler, A.T. & Gierasch, L.M. Sequence and structural analysis of cellular retinoic acid-binding proteins reveals a network of conserved hydrophobic interactions. *Proteins Struct. Funct. Bioinf.* **2004**, 54, 179-194.

10. Vasileiou, C. et al. Elucidating the exact role of engineered CRABPII residues for the formation of a retinal protonated Schiff base. *Proteins Struct. Funct. Bioinf.* **2009**, 77, 812-822.

11. Berbasova, T. in PhD Thesis. *Michigan State University* **2014**.

12. Yapici, I. et al. “Turn-On” Protein Fluorescence: In Situ Formation of Cyanine Dyes. *J. Am. Chem. Soc.* **2015**, 137, 1073-1080.

13. Dempsey, G.T., Vaughan, J.C., Chen, K.H., Bates, M. & Zhuang, X. Evaluation of fluorophores for optimal performance in localization-based super-resolution imaging. *Nat. Methods* **2011**, 8, 1027-1036.

14. Gómez-Bombarelli, R. et al. Design of efficient molecular organic light-emitting diodes by a high-throughput virtual screening and experimental approach. *Nat. Mater.* **2016**, 15, 1120-1127.

15. Dähne, S. & Radeglia, R. Revision der Lewis-Calvin-Regel zur charakterisierung vinyloger. Polyen- und polymethinähnlicher verbindungen. *Tetrahedron* **1971**, 27, 3673-3693.

16. Bouit, P.-A. et al. Continuous Symmetry Breaking Induced by Ion Pairing Effect in Heptamethine Cyanine Dyes: Beyond the Cyanine Limit. *J. Am. Chem. Soc.* **2010**, 132, 4328-4335.

17. Tolbert, L.M. & Zhao, X. Beyond the Cyanine Limit: Peierls Distortion and Symmetry Collapse in a Polymethine Dye. *J. Am. Chem. Soc.* **1997**, 119, 3253-3258.

18. Szydlowska, I., Kyrychenko, A., Nowacki, J. & Herbich, J. Photoinduced intramolecular electron transfer in 4-dimethylaminopyridines. *Phys. Chem. Chem. Phys.* **2003**, 5, 1032-1038.

19. Maksim, V.S., Vladimir, N.B. & Stefan, W.H. Fluorescent dyes with large Stokes shifts for super-resolution optical microscopy of biological objects: a review. *Methods Appl. Fluoresc.* **2015**, 3, 042004.

20. Haberhauer, G., Gleiter, R. & Burkhart, C. Planarized Intramolecular Charge Transfer: A Concept for Fluorophores with both Large Stokes Shifts and High Fluorescence Quantum Yields. *Chem. Eur. J.* **2016**, 22, 971-978.

21. Sasaki, S., Drummen, G.P.C. & Konishi, G.-i. Recent advances in twisted intramolecular charge transfer (TICT) fluorescence and related phenomena in materials chemistry. *J. Mater. Chem. C* **2016**, 4, 2731-2743.

22. Liu, X. et al. Aziridinyl Fluorophores Demonstrate Bright Fluorescence and Superior Photostability by Effectively Inhibiting Twisted Intramolecular Charge Transfer. *J. Am. Chem. Soc.* **2016**, 138, 6960-6963.

23. Kucherak, O.A., Didier, P., Mély, Y. & Klymchenko, A.S. Fluorene Analogues of Prodan with Superior Fluorescence Brightness and Solvatochromism. *J. Phys. Chem. Lett.* **2010**, 1, 616-620.

24. Fernández-Suárez, M. & Ting, A.Y. Fluorescent probes for super-resolution imaging in living cells. *Nat. Rev. Mol. Cell Biol.* **2008**, 9, 929-943.

25. Dugave, C. & Demange, L. Cis–Trans Isomerization of Organic Molecules and Biomolecules: Implications and Applications. *Chem. Rev.* **2003**, 103, 2475-2532.

26. Kwon, J. et al. RESOLFT nanoscopy with photoswitchable organic fluorophores. *Sci. Rep.* **2015**, 5, 17804.

27. Bossi, M., Belov, V., Polyakova, S. & Hell, S.W. Reversible Red Fluorescent Molecular Switches. *Angew. Chem. Int. Ed.* **2006**, 45, 7462-7465.

28. Cusido, J., Deniz, E. & Raymo, F.M. Fluorescent Switches Based on Photochromic Compounds. *Eur. J. Org. Chem.* **2009**, 2009, 2031-2045.

29. Herder, M. et al. Improving the Fatigue Resistance of Diarylethene Switches. *J. Am. Chem. Soc.* **2015**, 137, 2738-2747.

30. Jeong, Y.-C., Park, D.G., Lee, I.S., Yang, S.I. & Ahn, K.-H. Highly fluorescent photochromic diarylethene with an excellent fatigue property. *J. Mater. Chem.* **2009**, 19, 97-103.

31. Jeong, Y.-C., Yang, S.I., Ahn, K.-H. & Kim, E. Highly fluorescent photochromic diarylethene in the closed-ring form. *Chem. Commun.* **2005**, 2503-2505.

32. Uno, K. et al. In Situ Preparation of Highly Fluorescent Dyes upon Photoirradiation. *J. Am. Chem. Soc.* **2011**, 133, 13558-13564.

33. Fölling, J. et al. Synthesis and Characterization of Photoswitchable Fluorescent Silica Nanoparticles. *Small* **2008**, 4, 134-142.

34. Nevskyi, O., Sysoiev, D., Oppermann, A., Huhn, T. & Wöll, D. Nanoscopic Visualization of Soft Matter Using Fluorescent Diarylethene Photoswitches. *Angew. Chem. Int. Ed.* **2016**, 55, 12698-12702.

35. Roubinet, B. et al. Carboxylated Photoswitchable Diarylethenes for Biolabeling and Super-Resolution RESOLFT Microscopy. *Angew. Chem. Int. Ed.* **2016**, 55, 15429-15433.

36. Subach, F.V. et al. Red Fluorescent Protein with Reversibly Photoswitchable Absorbance for Photochromic FRET. *Chem. Biol.* **2010**, 17, 745-755.

37. Tiwari, D.K. et al. A fast- and positively photoswitchable fluorescent protein for ultralow-laser-power RESOLFT nanoscopy. *Nat. Methods* **2015**, 12, 515-518.

38. Zhang, X. et al. Highly photostable, reversibly photoswitchable fluorescent protein with high contrast ratio for live-cell superresolution microscopy. *Proc. Natl. Acad. Sci. U. S. A.* **2016**, 113, 10364-10369.

39. Lukyanov, K.A., Chudakov, D.M., Lukyanov, S. & Verkhusha, V.V. Photoactivatable fluorescent proteins. *Nat. Rev. Mol. Cell Biol.* **2005**, 6, 885-891.

40. Zhou, X.X. & Lin, M.Z. Photoswitchable fluorescent proteins: ten years of colorful chemistry and exciting applications. *Curr. Opin. Chem. Biol.* **2013**, 17, 682-690.

41. Acharya, A. et al. Photoinduced Chemistry in Fluorescent Proteins: Curse or Blessing? *Chem. Rev.* **2017**, 117, 758-795.

42. Warren, M.M. et al. Ground-state proton transfer in the photoswitching reactions of the fluorescent protein Dronpa. *Nat. Commun.* **2013**, 4, 1461.

43. Nosrati, M., Berbasova, T., Vasileiou, C., Borhan, B. & Geiger, J.H. A Photoisomerizing Rhodopsin Mimic Observed at Atomic Resolution. *J. Am. Chem. Soc.* **2016**, 138, 8802-8808.

44. Berbasova, T. et al. Light-Activated Reversible Imine Isomerization: Towards a Photochromic Protein Switch. *ChemBioChem* **2016**, 17, 407-414.

45. Nani, R.R., Kelley, J.A., Ivanic, J. & Schnermann, M.J. Reactive species involved in the regioselective photooxidation of heptamethine cyanines. *Chem. Sci.* **2015**, 6, 6556-6563.

46. Mosmann, T. Rapid colorimetric assay for cellular growth and survival: Application to proliferation and cytotoxicity assays. *J. Immunol. Methods* **1983**, 65, 55-63.

47. Assar, Z. et al. Domain-Swapped Dimers of Intracellular Lipid-Binding Proteins: Evidence for Ordered Folding Intermediates. *Structure* **2016**, 24, 1590-1598.

48. Uttamapinant, C. et al. A fluorophore ligase for site-specific protein labeling inside living cells. *Proc. Natl. Acad. Sci. U. S. A.* **2010**, 107, 10914-10919.

49. Grimm, J.B. et al. A general method to fine-tune fluorophores for live-cell and in vivo imaging. *Nat. Methods* **2017**, 14, 987-994.

50. Shcherbo, D. et al. Near-infrared fluorescent proteins. *Nat. Methods* **2010**, 7, 827-829.

51. Rafiq, S.M., Sivasakthikumaran, R. & Mohanakrishnan, A.K. Lewis Acid/Brönsted Acid Mediated Benz-Annulation of Thiophenes and Electron-Rich Arenes. *Org. Lett.* **2014**, 16, 2720-2723.

52. Demchenko, A.P. Practical aspects of wavelength ratiometry in the studies of intermolecular interactions. *J. Mol. Struct.* **2014**, 1077, 51-67.

53. Gill, S.C. & von Hippel, P.H. Calculation of protein extinction coefficients from amino acid sequence data. *Anal. Biochem.* **1989**, 182, 319-326.

54. Würth, C., Grabolle, M., Pauli, J., Spieles, M. & Resch-Genger, U. Relative and absolute determination of fluorescence quantum yields of transparent samples. *Nat. Protoc.* **2013**, 8, 1535-1550.

55. Turro, N.J., Ramamurthy, V., Cherry, W. & Farneth, W. The effect of wavelength on organic photoreactions in solution. Reactions from upper excited states. *Chem. Rev.* **1978**, 78, 125-145.

56. Rurack, K. & Spieles, M. Fluorescence Quantum Yields of a Series of Red and Near-Infrared Dyes Emitting at 600–1000 nm. *Anal. Chem.* **2011**, 83, 1232-1242.

57. Wohlfarth, C. in Ch48: Refractive index of ethanol. *Refractive Indices of Pure Liquids and Binary Liquid Mixtures*. Landolt-Börnstein – Group III Condensed Matter. Vol. 47, (ed. Lechner, M. D.), 108-115 (Springer-Verlag Berlin Heidelberg; Springer Materials; **2008**).

58. Schoch, R.L., Kapinos, L.E. & Lim, R.Y.H. Nuclear transport receptor binding avidity triggers a self-healing collapse transition in FG-nucleoporin molecular brushes. *Proc. Natl. Acad. Sci. U. S. A.* **2012**, 109, 16911-16916.

59. Schindelin, J. et al. Fiji: an open-source platform for biological-image analysis. *Nat. Methods* **2012**, 9, 676-682.

60. Barbero, M., Cadamuro, S. & Dughera, S. The efficient o-benzenedisulfonimide catalysed synthesis of benzothiazoles, benzoxazoles and benzimidazoles. *Arkivoc* **2012**, 262-279.

61. Gerowska, M., Hall, L., Richardson, J., Shelbourne, M. & Brown, T. Efficient reverse click labeling of azide oligonucleotides with multiple alkynyl Cy-Dyes applied to the synthesis of HyBeacon probes for genetic analysis. *Tetrahedron* **2012**, 68, 857-864.

62. Joachim, G., Götz, N., Jaedicke, H., Mayer, G. & Rack, M., Process for the Preparation of Pyridine Derivatives. WO/2005/063780, **2005**, DOW Agrosciences LLC.

63. Sovdat, T. et al. Backbone Modification of Retinal Induces Protein-like Excited State Dynamics in Solution. *J. Am. Chem. Soc.* **2012**, 134, 8318-8320.

EXCITED STATE PROTON TRANSFER OF FR PHOTOBASES AND DEVELOPING DYE-HCRBPII COMPLEXES INTO BRIGHT, LONG STOKES SHIFT, FAST-FORMING TAGS VIA EXCITED-STATE HYDROGEN BONDING.

The NIR photoswitch described in **0** solves the fluorescence background issue. Although the molecular brightness of its NIR emission is comparatively high, the absolute fluorescence quantum yield (0.16 of **CF-1**) is still lower than those of the synthetic dyes listed in **Section I.4.2**. The partial reason is that CrimFluors have significantly larger Stokes shifts than those polymethine or polyene dyes with higher quantum yields. Along the charge transfer coordinate, the larger momentum change is usually correlated to a longer timescale that may allow more non-radiative decay pathways to happen and lead to lower QYs.

In particular, the imine-isomerization of **CF-1/2** is highly probable to happen in the excited state after local excitation. This excited-state photochemical transformation should result in more molecular motion prior to the radiative decay and appears to be a trade-off for the NIR fluorescence photoactivation. Even the non-switchable mutant complex (**Section I.12.2**) may undergo transient excited-state isomerization but not end in a stabilized ground-state isomeric form. Thus, a fundamental question arises: can we minimize molecular motions in the excited state to achieve superior quantum yield, not by structural rigidification but preferably via a photochemical event, meanwhile retaining the large Stokes shift?

I.14 Discovery of intermolecular ESPT in the solution study of FR0

While investigating the spectroscopic behavior of **FR-1V** in various organic solvents, its precursor **FR0** was also studied to make a fair comparison and to validate

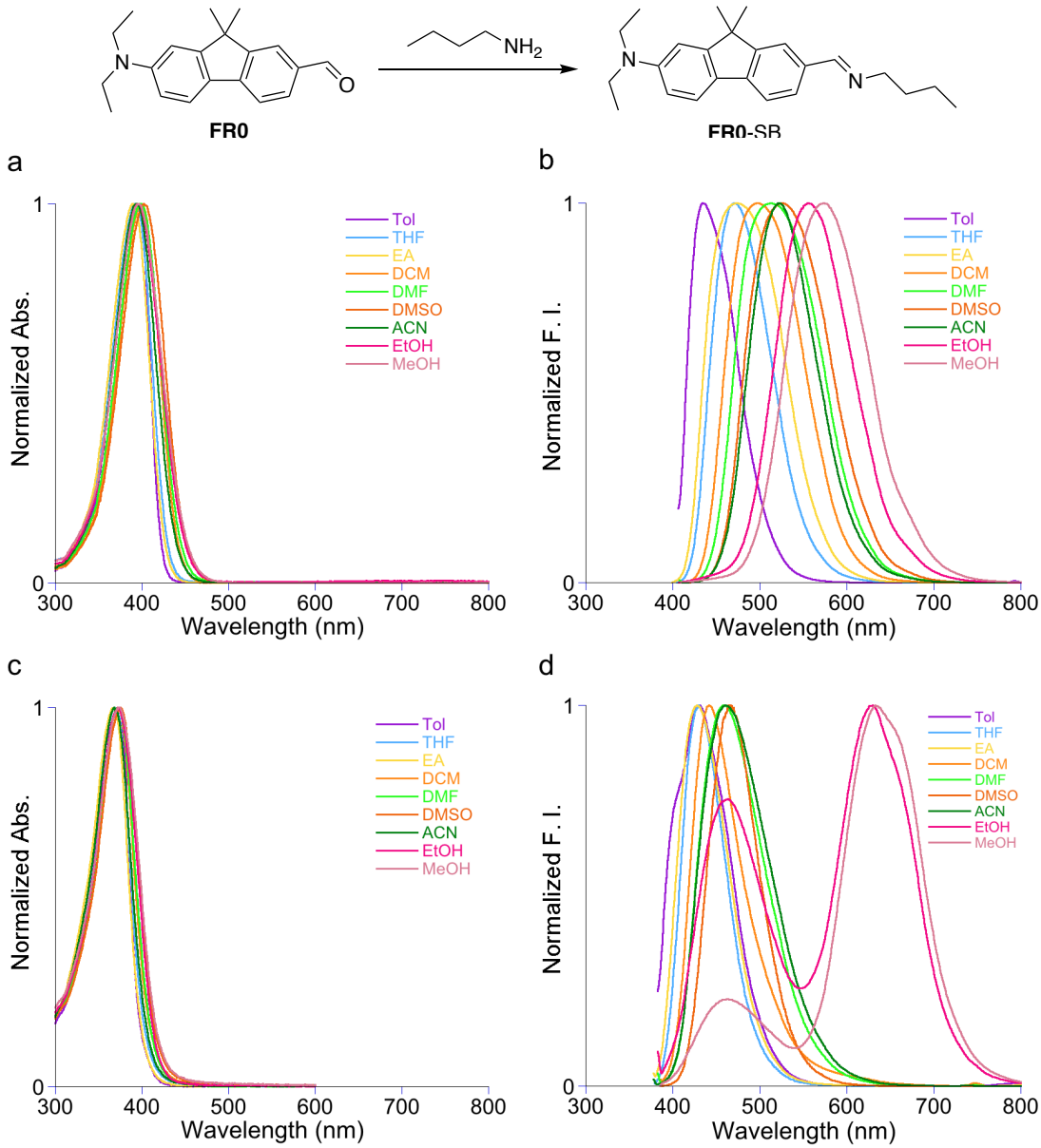


Figure 0-1 Normalized spectra of **FR0** in various solvents: (a) absorbance, (b) emission. Normalized spectra of **FR0**-SB (*n*-butylamine) in various solvents: (c) absorbance, (d) emission. Tol: toluene; THF: tetrahydrofuran; EA: ethyl acetate; DCM: dichloromethane; DMF: *N,N*-dimethyl formamide; DMSO: dimethyl sulfone; ACN: acetonitrile; EtOH: ethanol; MeOH: methanol. Scheme shows the SB formation between **FR0** and *n*-butylamine.

the strong solvatochromism is present along with ICT character. As shown in **Figure III-1**, **FR0** does show the reported strong solvatochromism in its fluorescence when exposed in various solvents. The absorption maximum of **FR0** is centered around 400 nm, and the emission maximum spans a range of 139 nm (from 434 nm in toluene to 573 nm in methanol). **FR-1V** absorption is centered at 420 nm, while its emission spans a wider range from 488 nm (in toluene) to 669 nm (in methanol). This is expected as the bathochromic shifts in **FR-1V** is a result of its conjugation, which also makes the excited state more prone to solvent relaxation, leading to a stronger emission solvatochromism.

Notably, the absorption maxima of both **FR0** and **FR-1V** are blue-shifted accordingly when the *n*-butylimine Schiff bases are formed. However, the emission of **FR0**-SB is remarkably different from that of **FR-1V**-SB (**Figure II-7**). In non-protic solvents, **FR-1V**-SB (*n*-butylimine) displays a normal positive solvatochromism of emission which spans a range of 85 nm from 447 nm in toluene to 532 nm in DMSO, while the emission of **FR0**-SB (*n*-butylimine) spans a much narrower range of 36 nm from 430 nm (in toluene)

Table 0-1 Spectral comparison of **FR0**-SB and **FR-1V**-SB in organic solvents.

	$E_T(30)$	**FR0**-SB[a]			**FR-1V**-SB[a]		
		λ_{abs} (nm)	λ_{em} (nm)	Φ^b	λ_{abs} (nm)	λ_{em} (nm)	Φ
Toluene	33.9	373	429	0.457	386	447	0.662
THF	37.4	368	430	0.699	389	481	0.597
Ethyl acetate	38.1	368	428	0.623	384	476	0.595
Dichloromethane	40.7	373	442	0.758	391	498	0.685
DMF	43.2	373	460	0.748	393	525	0.658
DMSO	45.1	375	466	0.784	396	532	0.749
Acetonitrile	45.6	368	460	0.751	388	524	0.738
Ethanol	51.9	372	463, 630	0.402	394	510	0.049
Methanol	55.4	374	463, 633	0.169	393	557	0.065

[a]*n*-Butylimine Schiff base. [b]Absolute fluorescence quantum yield measurement using Quantaurus-QY at room temperature.

to 466 nm (in DMSO). In protic solvents (e.g., ethanol and methanol), **FR0**-SB not only shows the normal fluorescence centered around 460 nm, it also displays a strong emission band at 630 nm with much greater bathochromic shift (**Figure III-1d**, **Table III-1**).

A closer look at the correlation between the emission maxima and the solvent polarity is presented in **Figure III-2**. As shown, the emission wavelengths are converted to wavenumbers and correlated with Reichardt's $E_T(30)$ solvent polarity scale,[1] which is a measurement of the linear free-energy between the ground- and excited-state of Reichardt's betaine. **FR0** displays a nice linear correlation in the energy terms, proving its characterized wavelength solvatochromism. Similarly, **FR-1V** also shows a nice linear correlation. In the case of their corresponding SBs (*n*-butylimine), **FR-1V**-SB demonstrates a decent correlation. Interestingly, by selecting and plotting the short-wavelength (SW) emission maxima in ethanol and methanol, **FR0**-SB also exhibits the same level of the linear free-energy relationship. This indicates that the origin of the

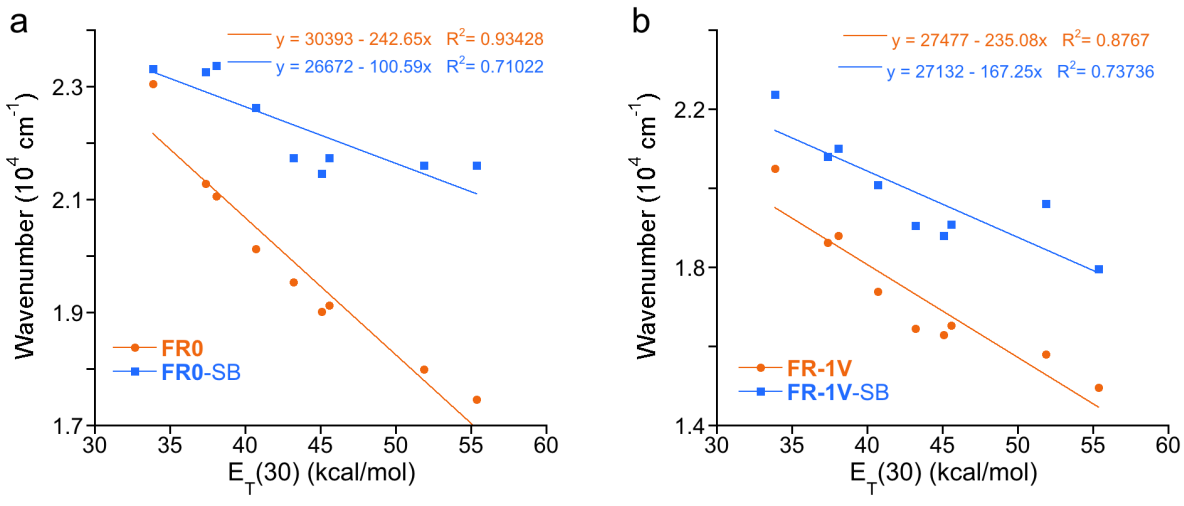


Figure 0-2 Solvatochromism of **FR0**, **FR-1V**, and their SBs as evident by their emission wavelengths in different solvents. Plots illustrate the correlation between wavenumbers and solvent polarities. The short wavelength emission maxima of **FR0**-SB in ethanol and methanol were selected for the plot. Reichardt's $E_T(30)$ scale is applied.

abnormal long-wavelength (LW) emission bands in alcohols is different from the solvent polarity effect. There is no clear correlation between the fluorescence quantum yields and solvent polarity as plotted in **Figure III-3**. However, general trend line should be presented in the aprotic solvents if wavelength solvatochromism is observed in this sub-group of solvents against $E_T(30)$ values. Because the Reichardt's solvent scale takes into account H-bond interactions between the betaine and protic solvents, a clearer evidence of potential H-bond in the ground-state of **FR0**-SB would be the two distinct trend lines with aprotic and protic solvent groups, respectively. The protic solvents examined are limited to ethanol and methanol in **Figure III-2** and **Figure III-3**, and thus more protic solvents need to be evaluated to provide a more concrete conclusion. Nonetheless, in **Figure III-3** we can observe a rough trend among aprotic solvents that shows the increase in QY with increasing solvent polarity (from toluene to acetonitrile), although not quite linear. It will be interesting to know if a linear trend line is apparent with protic solvents. Due to the structural similarity of **FR0**-SB and **FR-1V**-SB, one might expect the same propensity of QY decreasing from methanol to ethanol, however, a large increase in QY of **FR0**-SB is

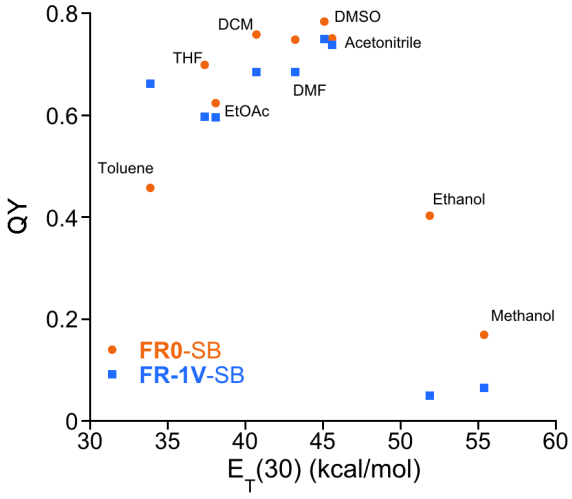


Figure 0-3 QY as a function of solvent polarity of **FR0**-SB and **FR-1V**-SB.

observed. It is not clear if the QY increase is related to the LW emission or simply due to the non-linear effects.

As shown in **Figure III-4b**, the 630-nm LW emission band originates from the 373-nm excitation as does the 463-nm SW emission band. Acidification of **FR0**-SB in ethanol with either hydrochloric acid (aq.) or perchloric acid (EtOH) solutions gives the protonated iminium (**FR0**-PSB) with the absorption maximum at 488 nm (**Figure III-5a**). Further acidification can protonate **FR0**-SB at the diethylamino nitrogen atom instead of the imine and yields an ammonium that shows blue-shifted absorption and emission maxima at 345 nm and 410 nm, respectively, and is quickly hydrolyzed or ethanolyzed. The emission spectrum of the 488-nm absorbing **FR0**-PSB perfectly overlaps with the LW emission band of **FR0**-SB in ethanol solution (**Figure III-5b**), proving that the LW emission band is radiated from the protonated **FR0**-SB in the excited state. Considering the solution environment of **FR0**-SB and the direct excitation of 373 nm that pumps the excited state

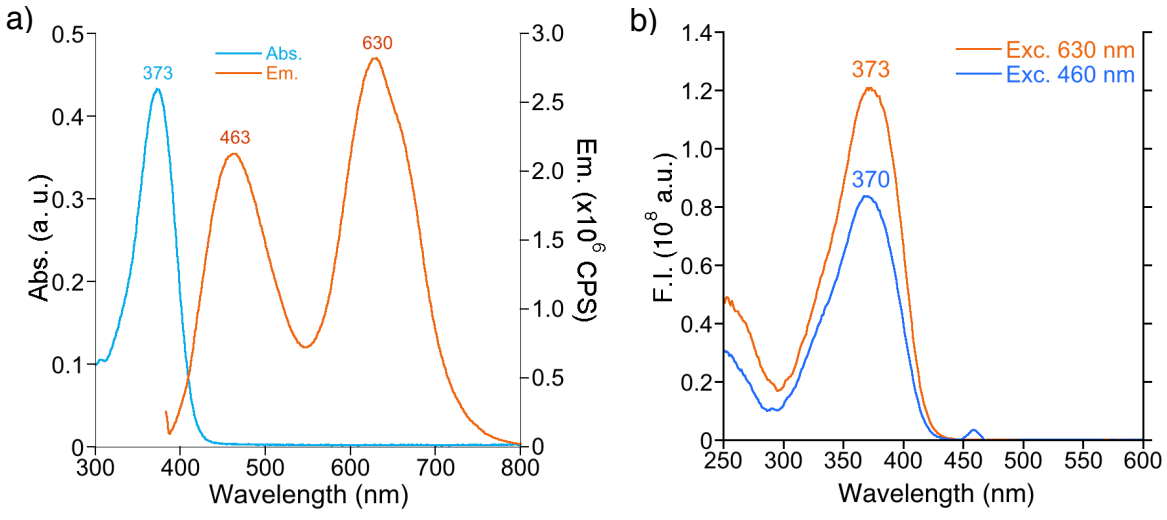


Figure 0-4 (a) Absorption and emission of **FR0**-SB in ethanol. (b) Excitation spectra of **FR0**-SB in ethanol at 460 nm and 630 nm, corrected against Rhodamine-B.

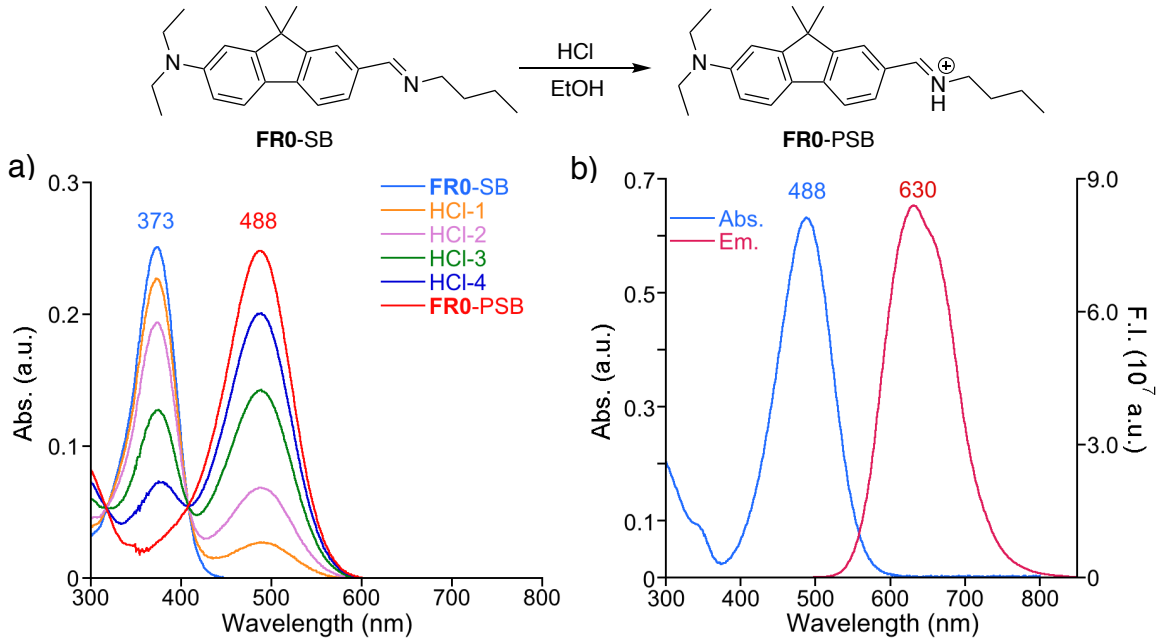


Figure 0-5 (a) Stacked absorption traces of **FR0**-SB acidification with hydrochloric acid. (b) Absorption and emission spectra of acidified **FR0**-SB.

of **FR0**-SB, the abnormal LW emission phenomenon can clearly be described as an *excited-state intermolecular proton transfer* (ESiPT) process.

This ESiPT process is not only observed in ethanol and methanol. In fact, solvents that provide exchangeable protons can all induce this LW emission. Shown in **Figure III-6**, in all 6 mono-/di-alcohols tested, **FR0**-SB exhibits the LW emission, with a varying peak maximum. It is tempting to linearly correlate the observed LW maxima with the $E_T(30)$ values of the solvents, which actually gives an R^2 coefficient of 0.84. However, a closer look at both the SW and LW emission bands reveals more complex structures as featured by shoulders and plateaus. A peak fitting of the experimental spectra performed with a second-derivative analysis gives four Voigtian-type traces in **Figure III-6**. In all cases, the SW and LW emission bands can be deconvoluted into two traces. The envelope spectra of the four traces in each solvent present a perfect fit for the experimental results,

satisfying shoulders and plateau features. Although there is no clear physical insight to

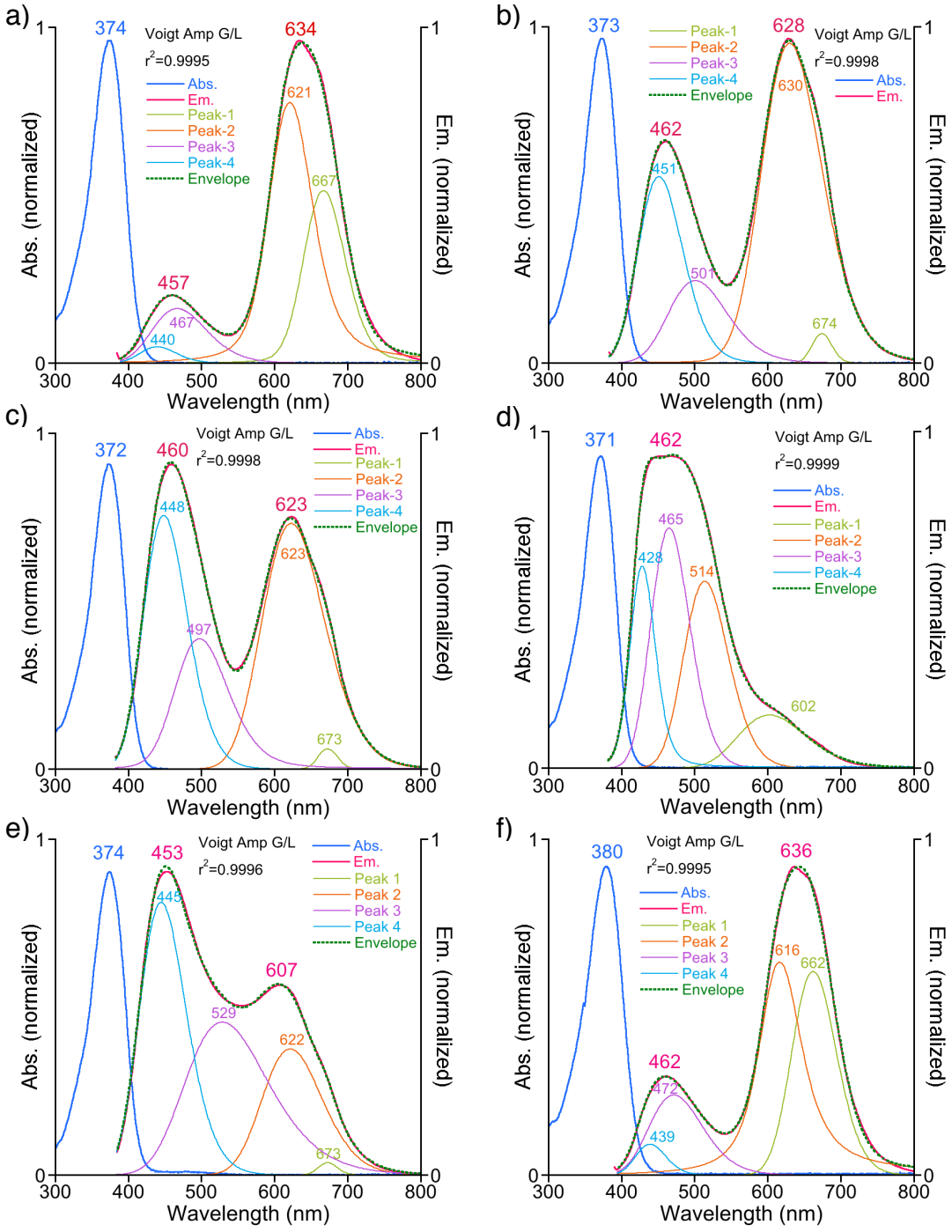


Figure 0-6 Absorption and emission spectra of **FR0**-SB in different alcoholic solvents. (a) methanol, (b) ethanol, (c) 1-propanol, (d) 2-propanol, (e) *n*-amyl alcohol, (f) ethylene glycol. Traces labeled with *Peak-i* (1 ~ 4) are fluorescence spectra simulated by second derivative fitting with a Voigtian amplitude distribution using PeakFit™. The *Envelope* traces are the convolution of multiple *Peak-i*, showing a perfect overlap with the experimental spectra.

support this type of peak fitting, it is reasonable to conclude that the real transitions and/or emissive species should be no less than the 4 traces deciphered here. Tentatively, it might be plausible to accept the two traces for each emission band, given the possibility of imine isomerization in the excited states.

More interestingly, dissolving **FR0**-SB in glacial acetic acid gives the absorption spectrum in **Figure III-7a**. The 342-nm absorption peak corresponds to the protonation of the diethylamino group, with the coexistence of the PSB iminium absorbing at 472 nm. Excitation at 342 nm leads to the ammonium emission at 405 nm and the LW emission centered at 622 nm, which corresponds to the iminium emission as shown in **Figure III-7b** with the excitation at 472 nm. This suggests the ESiPT not only happens on the neutral imine nitrogen atom, but also can have a double proton transfer at the excited state, namely, the deprotonation of the ammonium and the protonation of the imine.

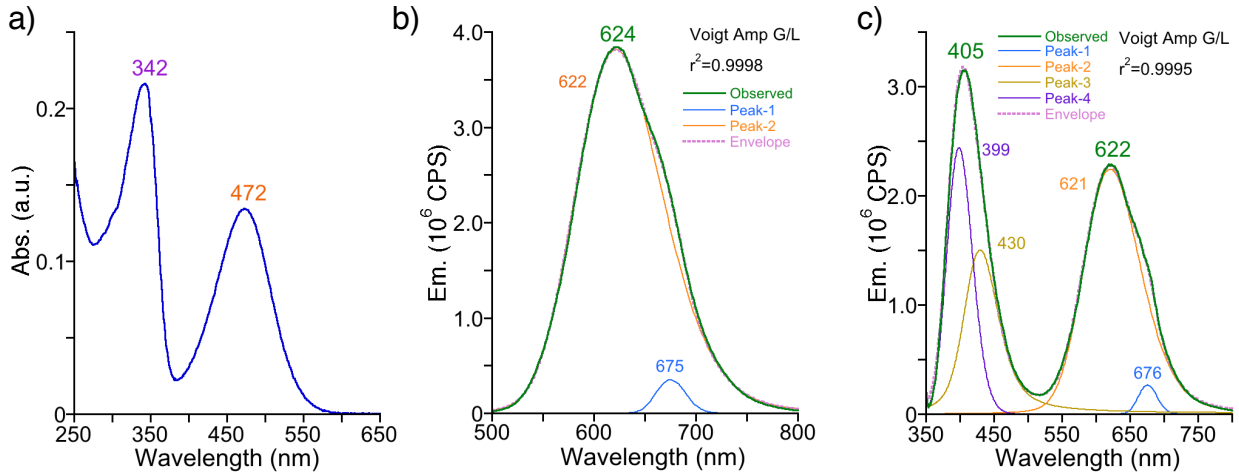
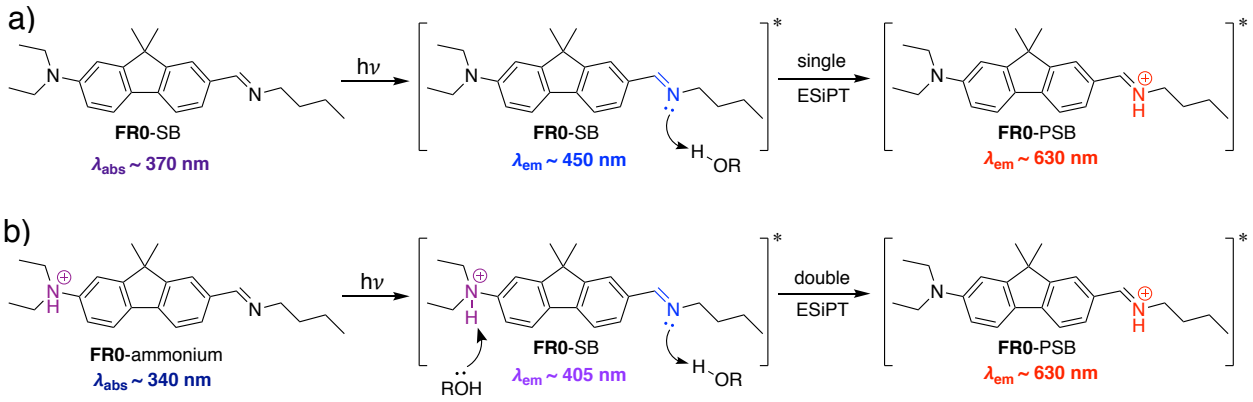


Figure 0-7 Absorption and emission spectra of **FR0**-SB dissolved in acetic acid. (a) Absorption spectrum, showing ammonium peaks at 342 nm and iminium peaks at 472 nm. (b) Emission spectra excited at 472 nm. (c) Emission spectra excited at 342 nm. In (b) and (c), emission traces labeled with *Peak-i* are simulated by second derivative fitting with a Voigtian amplitude distribution using PeakFit™. The *Envelope* traces are the convolution of multiple *Peak-i*.

Thus far, the exceptional LW emission bands of **FR0**-SB observed in protic solvents can be ascribed to two types: 1) a single ESiPT in alcoholic solvents; and 2) a double ESiPT in organic acidic solvents (**Scheme III-1**). In both scenarios, the excited state proton transfer on the imine nitrogen atom is responsible for the LW emission. The emission intensity of the LW band is variable in different alcohols, indicating a possible correlation with the H-bond donor strength instead of the commonly studied solvent polarity. In the case of 2-propanol and *n*-amyl alcohol, the SW and LW emission bands are not well resolved. This may suggest the impact of the steric hindrance projected by the aliphatic side chains. The two traits here further suggest that a preset H-bonding may be already present between the solute and solvent in the ground state.

I.15 Time-resolved study of FR0-SB ESiPT

Time-resolved spectroscopic studies were carried out to provide in-depth understanding of the excited state photodynamics of **FR0**-SB ESiPT. This part of the work results from a strong collaboration with Dr. Muath Nairat from Prof. Marcus Dantus' research group (Michigan State University).



Scheme 0-1 Schematic transformation of (a) single and (b) double ESiPT of **FR0**-SB in protic solvents.

As described in **Section I.14**, the ESiPT behavior of **FR0**-SB denotes the increased basicity in the excited state such that the proton abstraction from the solvent molecule can happen. This type of molecules that show weak basicity in the ground state but elicit an increased basicity upon light excitation is defined as a "photobase" ($pK_a^* > pK_a$). The underlying dynamics and principles of the key excited state proton transfer process have been the long-standing interest ever since Förster and Weller's early work.[2, 3] In this field, photoacids ($pK_a^* < pK_a$) are more commonly reported. Both intra- and inter-molecular ESPT of photoacids have been observed and surveyed.[4-7] The most and earliest studied photoacids are substituted α- and β-naphthols.[8, 9] More recently, it was found that substitution with strong electron withdrawing groups on hydroxyarenes can generate "super" photoacids, which are denoted by drastic pK_a change in the excited state (greater than 6 units) and have a negative pK_a^*. The most investigated is 8-hydroxypyren-1,3,6-trisulfonic acid (HPTS), or pyranine.[10-13]

Conversely, studies on photobases are scarce and limited to heterocyclic nitrogen-containing compounds such as acridine,[14] 3-styrylpyridine,[15] aminoanthraquinone,[16] quinolines,[17] dibenzophenazine,[18] 7-azaindoles,[19, 20] as well as carbonyl compounds such as xanthone,[21] curcumin,[22] or bifunctional naphthol photoacids in which a basic moiety becomes moderately more basic upon photo excitation.[23, 24]

An interesting theoretical investigation is recently reported by Lischka's group. They applied different high-level computational methods to study the excited-state properties and environmental effects of retinal PSBs. It was found that the feasibility of the proton transfer process from the PSB to its surrounding solvent partner is significantly

enhanced in the excited state, meaning that an ESPT step could be initiated already in the early stage of photodynamics of retinal PSB which functions as a photoacid.[25] This, however, is in contrast to our observation for the ESPT in **FR0**-SB.

Acetonitrile and ethanol were selected to represent non-proton transfer and proton-transfer solvents for ultrafast spectroscopic studies, respectively. The steady-state absorption and emission spectra of **FR0**-SB/PSB in these two solvents are aligned in **Figure III-8** for a clearer view. The time-correlated single-photon counting (TCSPC) measurements of **FR0**-SB/PSB in acetonitrile and ethanol are summarized in **Figure III-9**. The emission in ACN is featured by a single exponential decay with a lifetime with 2.11 ns. This SW emission lifetime is sharply decreased to ca. 89 ps in ethanol. The decrease

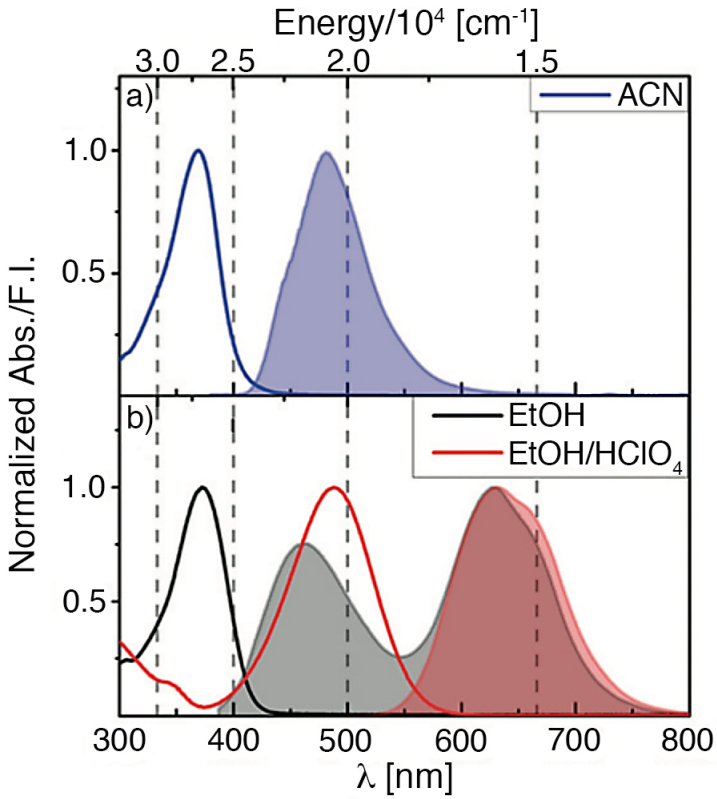


Figure 0-8 Steady-state absorption (solid) and emission (shaded) spectra of **FR0**-SB in (a) acetonitrile (ACN) and (b) ethanol (EtOH). The spectra of **FR0**-PSB (acidified by perchloric acid in ethanol) are also overlaid.

in SW emission lifetime can be explained by the competing intermolecular proton transfer of **FR0**-SB in the excited state. On the other hand, the LW emission of **FR0**-SB in ethanol has a lifetime of 1.31 ns, which is in the same order of magnitude as the SW emission lifetime in ACN. Comparing the **FR0**-PSB TCSPC trace with that of **FR0**-SB LW emission trace, the two have an identical single-exponential decay as plotted in **Figure III-9 inset**, further validating the origin of the **FR0**-SB LW emission from the excited state proton transfer.

An isotope study was carried out with deuterated ethanol (ethanol-d_6, EtOD). The absorption spectra in EtOH and EtOD are identical. The emission spectrum in EtOD has a less prominent LW emission. With a heavier deuterium, more vibrational crossover is expected and correspondingly the SW and LW emission band are less resolved (**Figure**

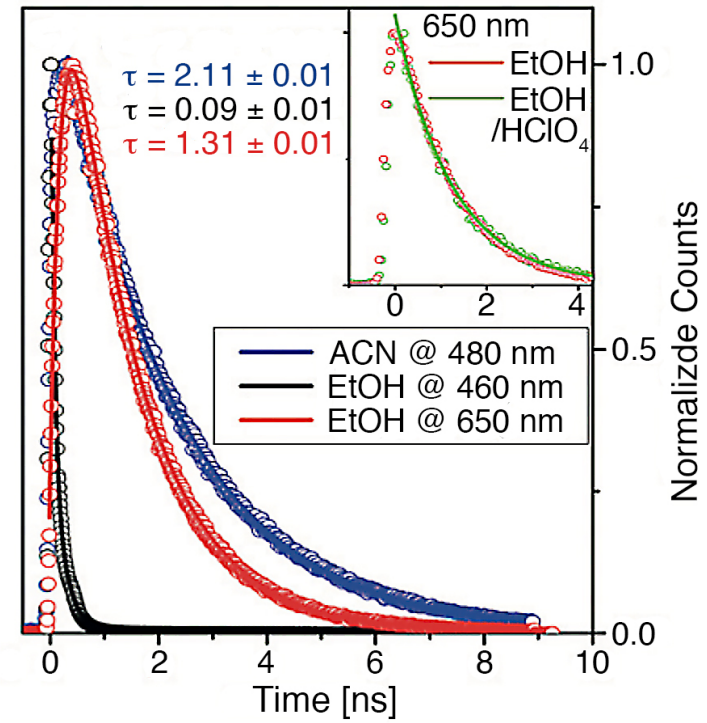


Figure 0-9 TCSPC traces with single exponential fits for **FR0**-SB near the emission maxima when dissolved in ACN and EtOH. Inset shows that the red emission trace at 650 nm of **FR0**-SB is identical to the **FR0**-PSB emission.

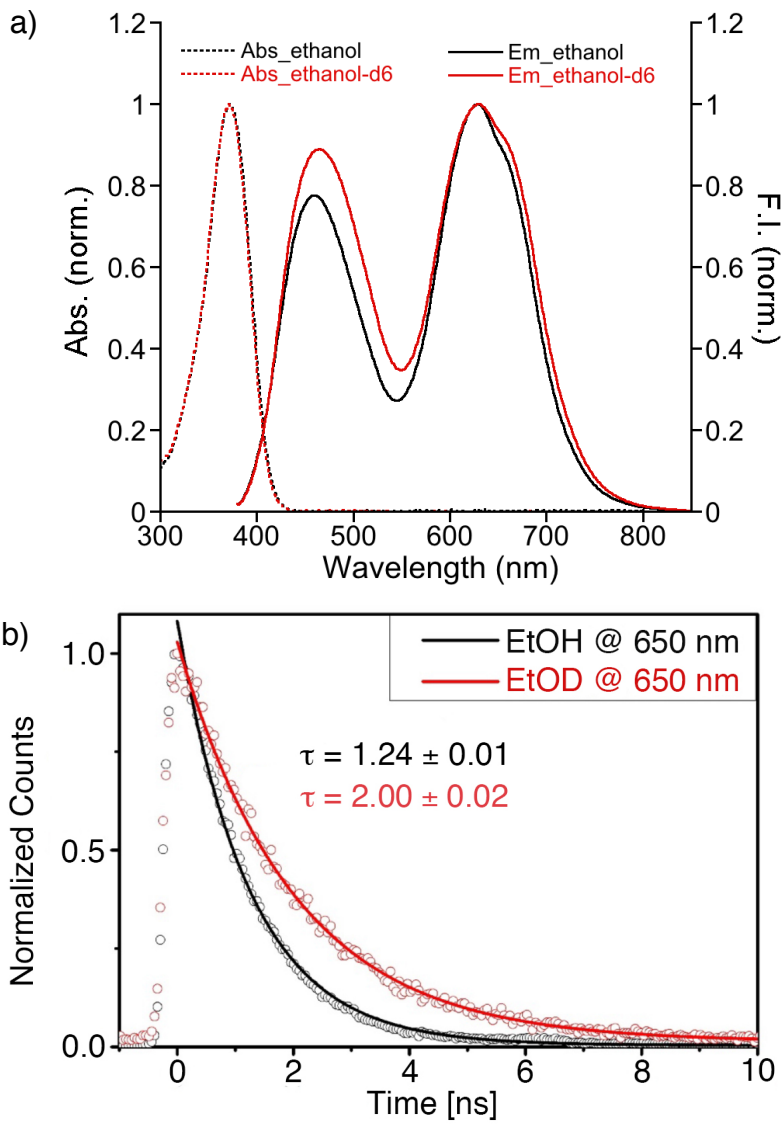


Figure 0-10 Isotopic effect of **FR0**-SB in EtOH and ethanol-d_6 (EtOD). (a) Steady-state absorption and emission spectra of **FR0**-SB in EtOH and EtOD. (b) TCSPC decay curves of **FR0**-SB LW emission along with single exponential decay fits in EtOH and EtOD. An isotope effect of 1.6 is observed in EtOD.

III-10a). Because the fluorescence lifetime is measuring the population decay of the excited state species, the ratio of decay time should directly reflect the ratio of the kinetic rates of the proton transfer reaction. In the deuterated ethanol, the LW emission lifetime increases from 1.24 ns to 2.00 ns, showing a noticeable isotope effect of 1.6 (**Figure III-10b**). Comparing methanol and methanol-d_4, a more prominent primary isotope effect

of 1.9 is observed (**Figure III-11**). Together, these results validate the determining role of the proton transfer in the origin of this LW emission.

It is now clear that **FR0**-SB is acting as a photobase in the excited state in protic solvents. The change in pK_a upon excitation is determined using the Förster equation:[2, 12]

$$pK_a^* - pK_a = \left(h\nu_1 - h\nu_2\right) / 2.3RT$$

Equation 0-1 Förster equation for calculating the excited-state pK_a difference.

where pK_a^* and pK_a are the excited state and ground state logarithmic acidity constants, respectively. *R* is the ideal gas constant, *T* is the temperature in Kelvin, and $h\nu$ is the energy of 0-0 electronic transition of **FR0**-SB and **FR0**-PSB. The 0-0 transition energies are estimated as 24,450 cm^{-1} and 17,890 cm^{-1} from the corresponding crossover points in the absorption and emission spectra of **FR0**-SB and **FR0**-PSB, respectively (**Figure III-8b**). The calculated pK_a increase of **FR0**-SB is 13.8 units. While pK_a changes up to 14 units have been reported for photoacids,[26] to the best of our knowledge the largest pKa change reported for a photobase is 10.8 for 5-aminoquinoline.[17] With the ΔpK_a in hand,

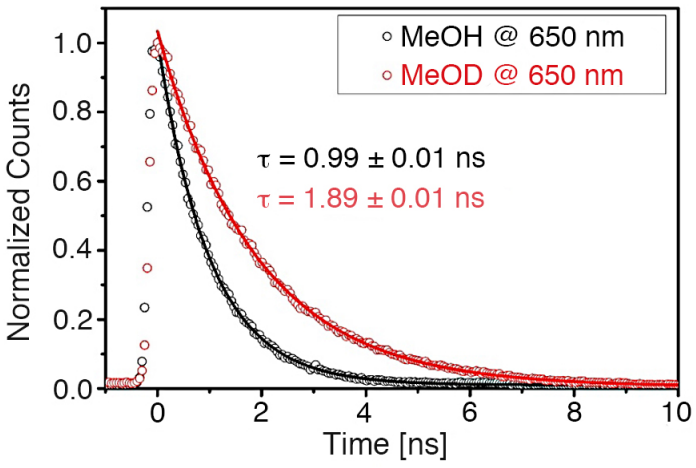


Figure 0-11 TCSPC decay curves of **FR0**-SB LW emission with single exponential decay fits in MeOH and methanol-d_4 (MeOD). An isotope effect of 2.0 is observed in MeOD.

calculation of the excited state pK_a^* requires an estimate for the ground state pK_a of **FR0**-PSB. Although a good estimate for the pK_a in EtOH can be derived from the pK_a of the imine in water, this was hampered by the insoluble nature of FR0-SB in water. Note that the pK_a of ammonium salt is generally elevated by ~3 units when dissolved in ethanol instead of water.[27] Therefore, we resorted to an indirect measurement of the pK_a via quantifying the mole fraction of each species by multi-variant linear regression with known

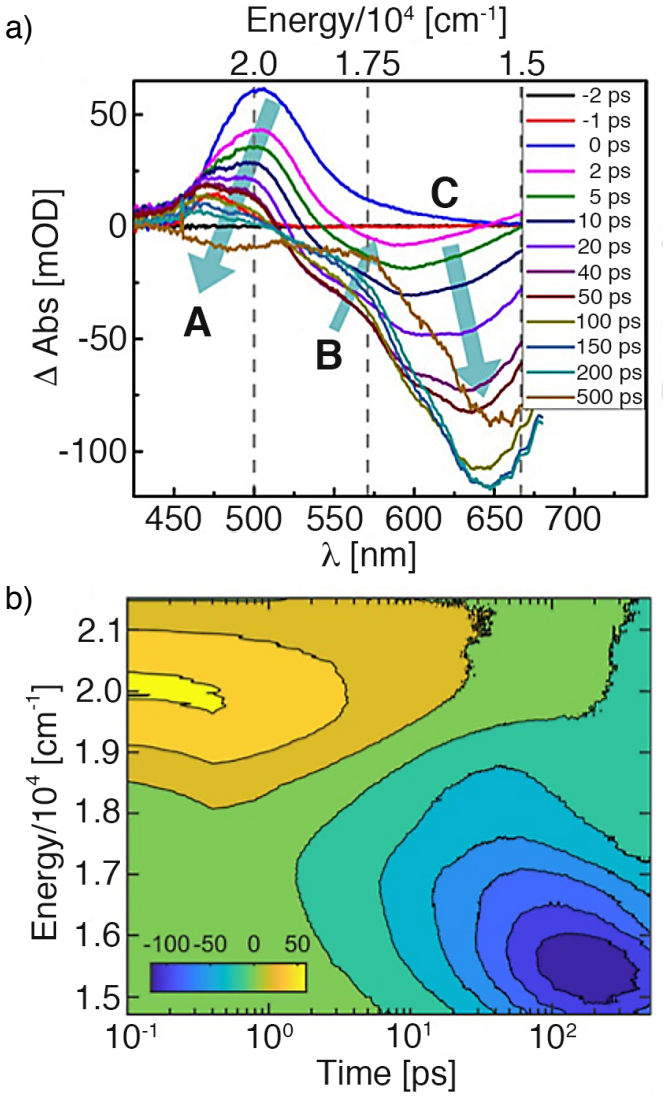


Figure 0-12 (a) Transient absorption spectra of **FR0**-SB at various time intervals after excitation in EtOH. Labeled arrows show the steps during the ESPT process. (b) Energy progression during the proton transfer process.

extinction coefficients as a function of wavelengths (UV/Vis analysis), generated between the acid-base reaction of **FR0**-SB with α-naphthylammonium in EtOH as described in a previously reported procedure.[28] **FR0**-PSB shows a 0.23 unit lower pK_a than that of α-naphthylammonium in EtOH. The pK_a of α-naphthylammonium in water is 3.9, thus, its pK_a in EtOH is estimated at 6.9. Considering the difference in pK_a values for a-naphthylammonium and **FR0**-PSB, the pKa of the latter in EtOH is estimated to be 6.7. This results in an estimated excited state pK_a^* of 21 for **FR0**-SB.

A better understanding of the mechanism and associate dynamics of the **FR0**-SB excited state proton transfer is provided by the transient absorption spectra (TAS). As shown in **Figure III-12**, only a decrease in the absorption (positive signal) around 500 nm (20,000 cm^{-1}) was observed upon excitation. This is ascribed to the excited state absorption (ESA) of **FR0**-SB. The ESA signal decays quickly and is accompanied by a transient negative signal centered at 588 nm (17,000 cm^{-1}). This transient negative signal gives rise to another negative signal that initially centers at 630 nm (15,870 cm^{-1}) and shifts to lower energy over time. The negative signal at 630 nm persists longer than 500 ps and is assigned as the stimulated emission (SE) from **FR0**-PSB. Accordingly, the transient signal at 588 nm is ascribed to the SE from an intermediate species that is formed during the intermolecular proton transfer process. The intermediate can be viewed as a caged complex between **FR0**-SB and the solvent molecule (ethanol) with a partial transfer of the proton (*vide infra*) prior to the full proton transfer process. This feature is commonly observed in the excited state intermolecular proton transfer of photoacids.[26, 29]

In the absence of proton transfer (e.g. in ACN), the transient absorption of **FR0**-SB shows rapid ESA and SE emergence soon after excitation, since both correspond to the non-protonated form (**Figure III-13a**). Moreover, both signals are long lived and can be fit to a biexponential decay. A long component of ca. 1.89 ns corresponding to the lifetime of the excited state is observed, together with a short 24 ~ 30 ps component that can be ascribed to an intramolecular response from the molecule upon excitation (**Figure III-13**, **b** and **c**). The 24 ps decay component is also observed in the SE of **FR0**-PSB

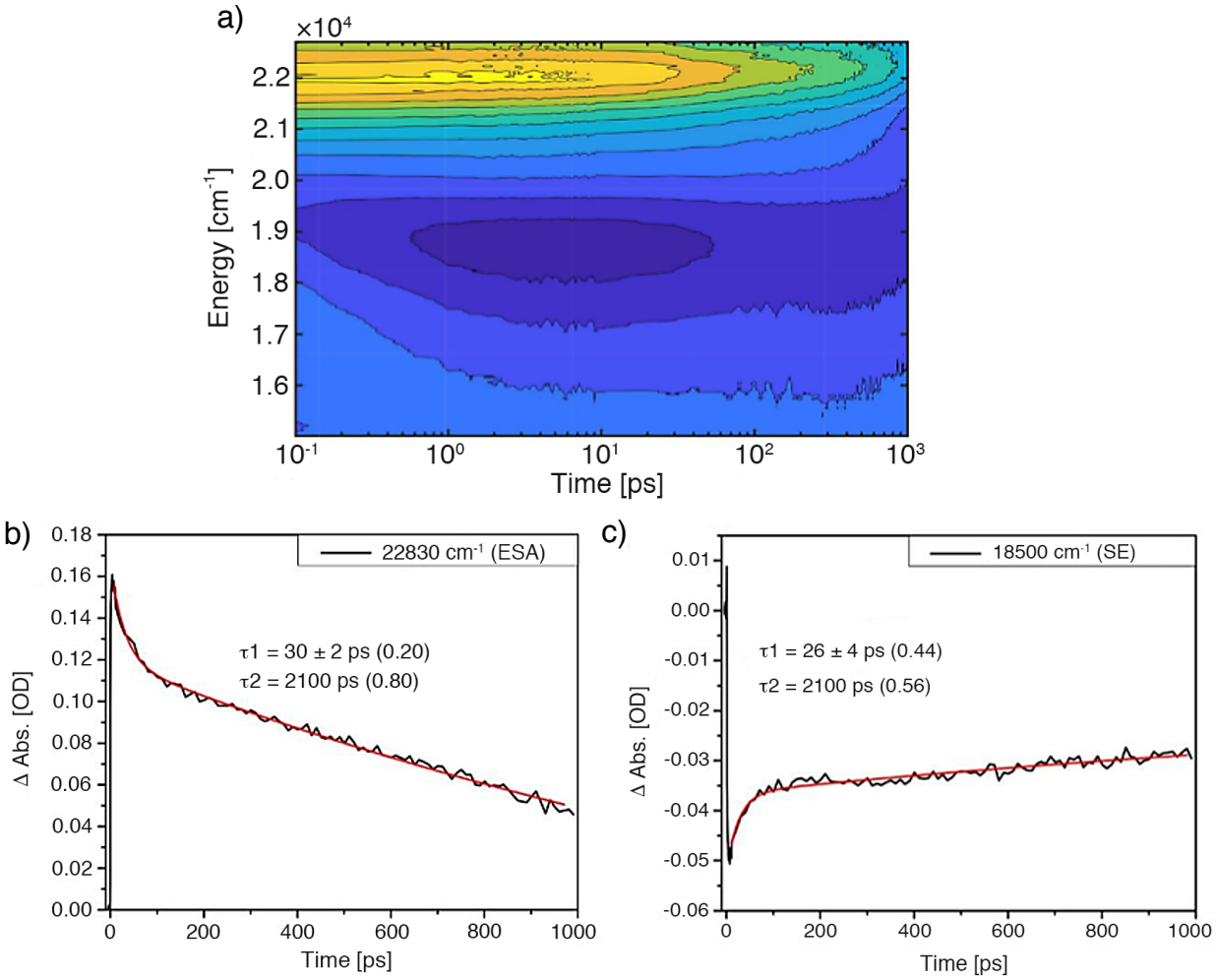


Figure 0-13 (a) Transient absorption of **FR0**-SB in ACN, showing the long-lived excited state absorption and stimulated emission signals from the non-protonated form with biexponential fits at the frequencies of (b) excited state absorption and (c) stimulated emission signals.

(acidified with $HClO_4$/EtOH), confirming its nature as an intramolecular mode from **FR0**-SB regardless of its protonation status (**Figure III-14**).

A four-level sequential global analysis model can be used to provide more complete description of the experimental transient absorption data of **FR0**-SB in EtOH.[30] The resulting evolution associated spectra (EAS) are provided in **Figure III-15**. The model shows that the first component (black trace), which is the ESA of **FR0**-SB centered around 500 nm (20,000 cm^{-1}), decays with a 15.8 ps time constant. This timescale is in agreement with the average dielectric relaxation of EtOH.[31] This decay is accompanied with a rise in the second component (red trace) that features a broad SE signal centered at 588 nm (17,000 cm^{-1}) and decays with a 73.9 ps time constant. Based on these time constants, we infer that the dielectric relaxation of the solvent is coupled with the formation of an intermediate species prior to the full proton transfer step. This intermediate can be viewed as a complex with a partially transferred proton or a highly polarized H-bonding state

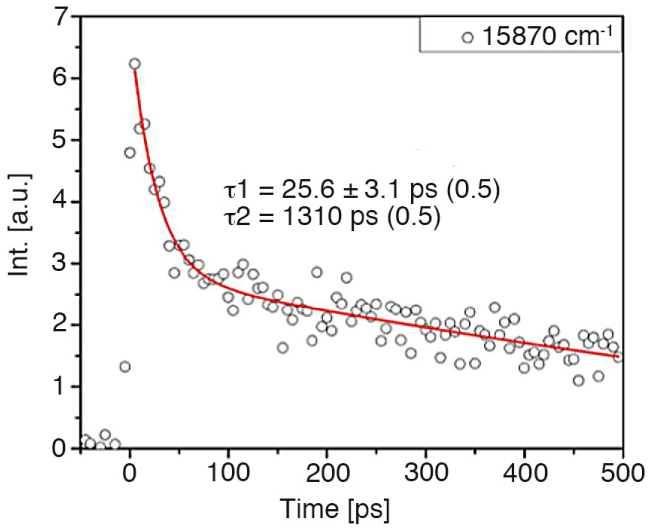


Figure 0-14 Stimulated emission signal from the transient absorption of **FR0**-PSB in acidic EtOH. Two decay components are observed, with a fast one corresponding to an intramolecular response from **FR0**-SB, and a slow one corresponding to the excited state lifetime.

between the base and the solvent. Characterized by the **FR0**-PSB SE feature with maxima around 630-660 nm (15,870 ~ 15,150 cm^{-1}), the final step is best described with two EAS components (blue and purple traces). Considering the similarities between the last two EAS components 3 and 4, we contemplate them as a single step for the formation of the fully protonated **FR0**-PSB. The two exponential components are better fit for the non-exponential decay of the protonated form that can undergo geminate recombination after the proton transfer.[32, 33] The last EAS component is long lived and decays with a

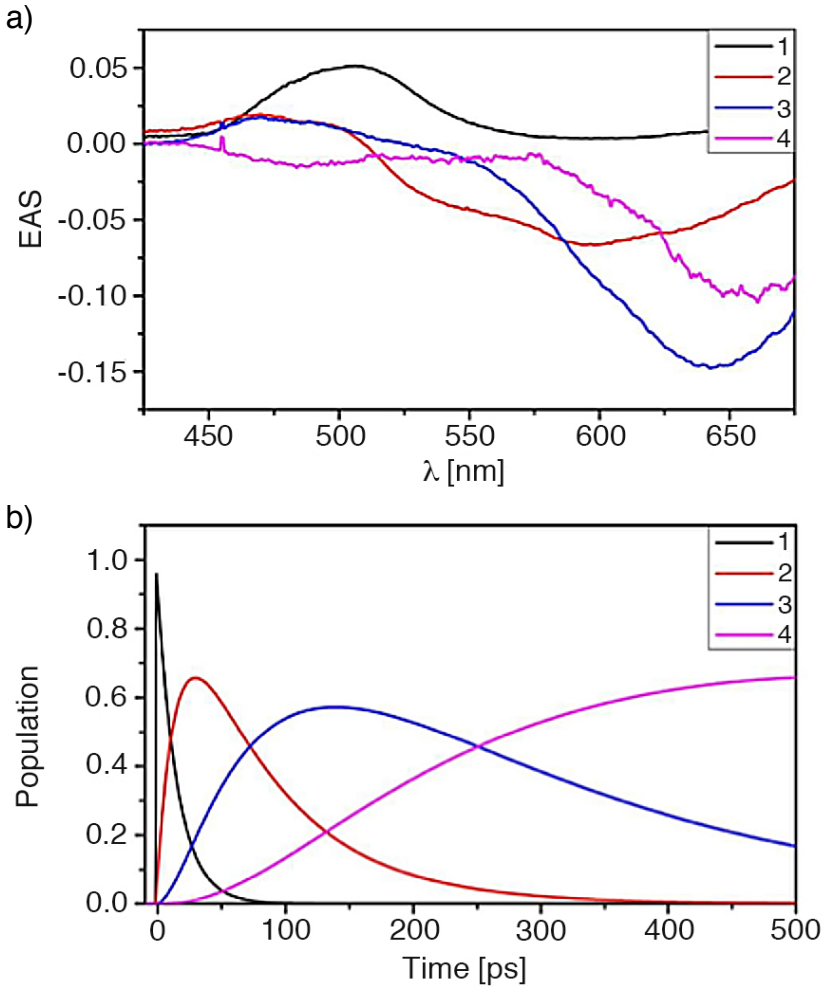


Figure 0-15 (a) Evolution associated spectra (EAS) of the four levels used in the sequential global analysis model to describe the proton transfer dynamics of **FR0**-SB in EtOH. (b) Population kinetics of the four levels used in the global analysis model.

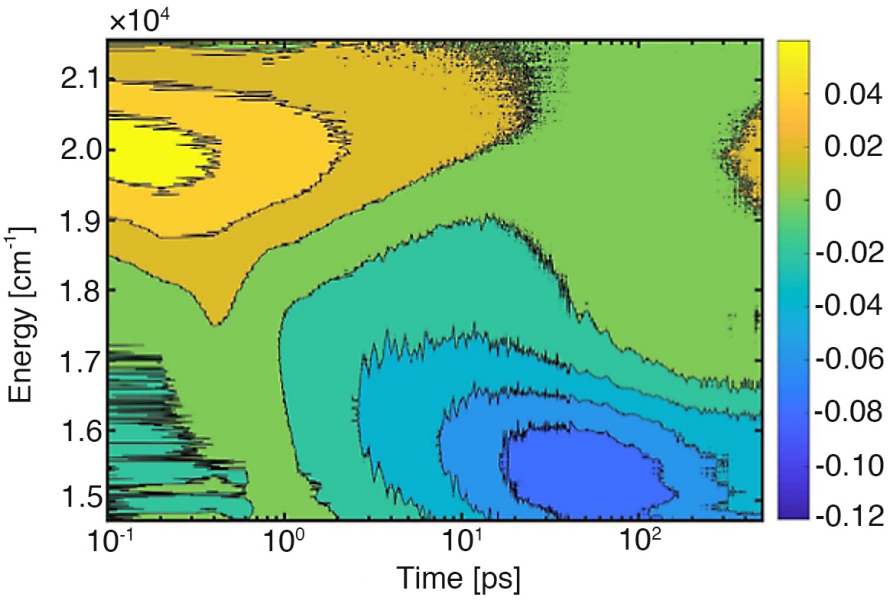


Figure 0-16 Transient absorption trace showing the energy progression during the excited state **FR0**-SB proton transfer process in MeOH.

1.15 ns time constant. This value agrees with the previously determined lifetime of **FR0**-PSB using TCSPC (**Figure III-9**).

Similar photophysical behavior is observed when **FR0**-SB is dissolved in MeOH (**Figure III-16**). The global analysis model shows that the ESA signal from the non-protonated form decays to form the partially proton transferred complex on a 2.9 ps timescale, which also agrees with the average dielectric solvation time of MeOH.[31] The protonated **FR0**-PSB is formed on a 27.1 ps timescale according to the global analysis model.

A further validation study of the global analysis model was done by viewing the transient absorption traces at selected wavelengths of **FR0**-SB in EtOH and ethanol-d_6 (EtOD). Observed through the SE signal at 570 nm, the dielectric solvent relaxation that couples with the intermediate formation is formed with a time constant of 15.2 ps that closely agrees with the intermediate formation time determined by the global analysis

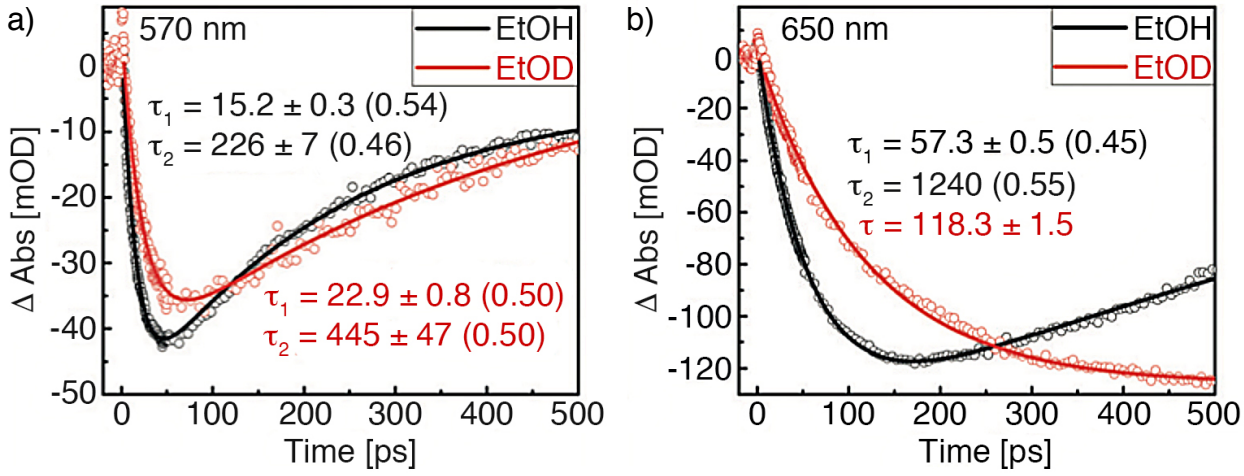


Figure 0-17 Transient absorption traces at (a) 570 nm where stimulated emission from the intermediate formation is observed, and (b) 650 nm where stimulated emission from **FR0**-PSB can be seen while dissolved in EtOH (black) and EtOD (red). Biexponential decay constants are given in the inset along with the pre-exponential factors in parentheses. An isotope effect of 1.5 is observed during the formation of the partially proton transferred intermediate, while an isotope effect of 2.0 is observed during the formation of final protonated **FR0**-PSB.

model (15.8 ps). Nonetheless in EtOD, we notice an isotope effect of 1.5 (*vide supra*), further confirming that the dielectric solvent relaxation is coupled with partial hydrogen bonding formation and dissociation (**Figure III-17a**).

The SE from the fully protonated **FR0**-PSB (i.e., the second trace at 650 nm) shows its formation is associated with a time constant of 57.3 ps. This value is ascribed to the dissociation of the intermediate that leads to **FR0**-PSB formation and is more accurately validated by the global analysis as a time constant of 73.9 ps. A primary isotope effect of 2.0 is observed in the EtOD trace at this wavelength. The two strong isotope effects observed both before and after the proton transfer step clearly elucidate the “contact” or “covalency” feature of the geminate ion complex intermediate,[34] which can be more accurately described as *excited state hydrogen bonding* (ESHB) complex. The isotope effect in methanol-d_4 (MeOD) is more pronounced. In both of the intermediate and the

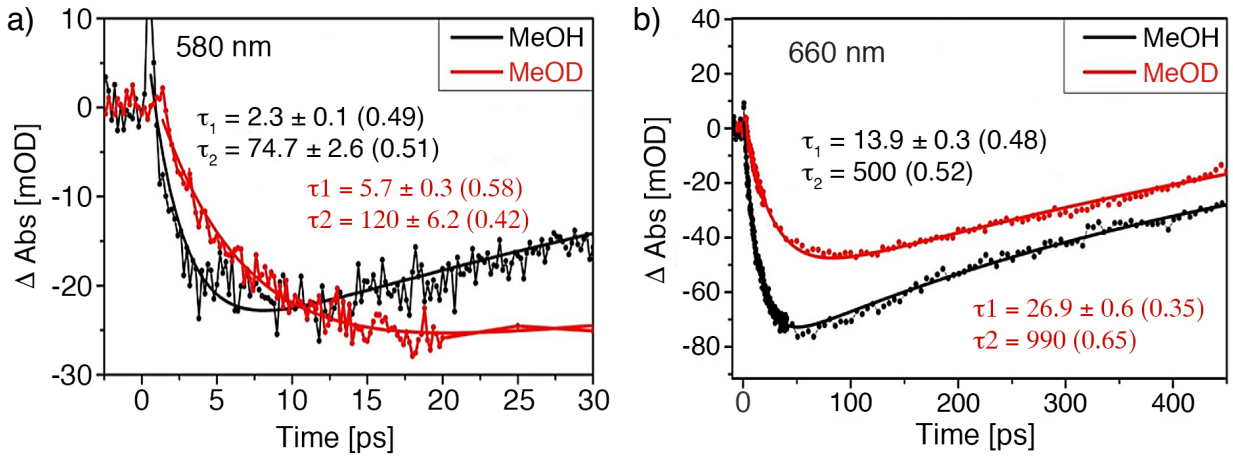


Figure 0-18 Transient absorption traces at (a) 580 nm where stimulated emission from the intermediate formation is observed, and (b) 660 nm where stimulated emission from **FR0**-PSB can be seen while dissolved in MeOH (black) and MeOD (red). Biexponential decay constants are given in the inset along with the pre-exponential factors in parentheses. An isotope effect of 2 is observed during the formation of the intermediate as well as in the final protonated form formation.

protonated FR0-SB formations, a primary isotope effect (greater than 2) is observed (**Figure III-18**).

Overall, the scheme of excited state intermolecular proton transfer (ESiPT) from EtOH to **FR0**-SB is depicted in **Figure III-19** and can be summarized as following: (i) The lifetime of the non-protonated **FR0**-SB in aprotic solvent, where proton transfer is not feasible, can be deduced from the emission lifetime at 480 nm in ACN solution. (ii) In protic solvents, a highly polarized H-bonding complex is formed on a timescale that competes with the solvent dielectric relaxation, with the observation of an isotope effect of 1.5 ~ 2 during the formation of this intermediate. (iii) The final proton transfer step occurs on a 73.9 ps timescale and involves the dissociation of the partially-transferred proton to produce the protonated **FR0**-PSB. An isotope effect of 2 is observed for this step. (iv) The protonated **FR0**-PSB is long lived and emit with a 1.31 ns lifetime.

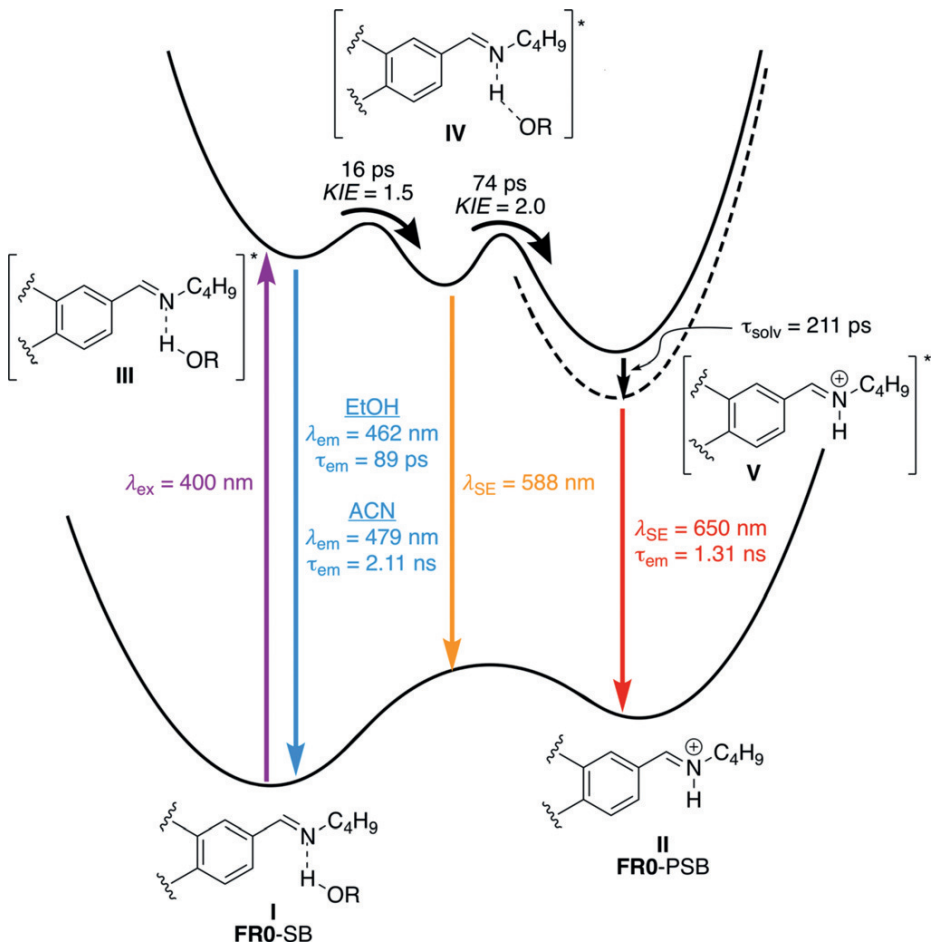


Figure 0-19 The observed intermolecular ESPT dynamics in EtOH along with the associated time constants for the steps as obtained from global analysis (black) and the TCSPC data (colored).

Having established the super photobasicity of **FR0**-SB in protic solvents, we explore the ability of this compound to abstract protons from stronger C-H bonds. We notice that there is no clear sign of proton transfer from C-H bonds, even with low pK_a solvents such as chloroform. On the other hand, N-H compounds such as imidazole were deprotonated in the presence of **FR0**-SB upon excitation (**Figure III-20**). This is not surprising since the bond dissociation energy of chloroform C-H bond is much higher than that of the solvated O-H or N-H bonds. These results may infer the importance of H-bonding between the base and the solvent in the ground state for ESiPT to be feasible.

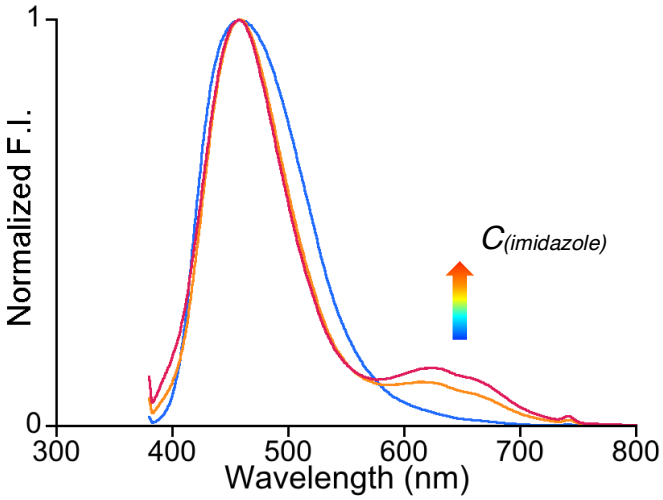


Figure 0-20 Normalized fluorescence spectra of **FR0**-SB in the acetonitrile solution of imidazole. The arrow shows the LW emission band (630-660 nm) emerging with the addition of imidazole (from blue to red), indicating the proton transfer from imidazole to **FR0**-SB.

The ground state H-bond requirement may also be related to the lifetime of the excited state super photobase and diffusion of the proton donor.

I.16 Recapitulate ESHB in hCRBPII complexes to develop bright, long Stokes Shift, and fast-forming imaging tag

I.16.1 ESHB of photoacids and the applications

Both intermolecular and intramolecular excited state proton transfer, or more generally excited state hydrogen bonding, are hot topics in fundamental research as well as application design.[35, 36] The representative molecules showing excited state intramolecular proton transfer (ESIPT) are hydroxyflavones and hydroxychromones.[37-39] These scaffolds commonly have a photoacidic hydroxyl group that can transfer the proton to an adjacent carbonyl group, realizing a light-triggered keto-enol tautomerization in the excited state. Actually, compounds bearing an H-bonding donor (HBD) that can form a five- or six-membered ring transition state with an adjacent H-bonding acceptor (HBA)

can demonstrate this type of ESiPT phenomenon.[40-43] In line with this mechanism, ESiPT essentially features a dual fluorescence of the normal and the tautomer form, respectively. This feature has been applied to probe the environment basicity since the dual emission ratio reflects the strength of the intramolecular proton transfer which is affected by the hydrogen bond accepting ability of the environment.[44] This concept has been further developed to sense anions such as acetate and fluoride that can establish strong ESHB with the hydroxyl group and therefore inhibit the ESiPT process.[45-49] ESiPT has also been used to design materials that can entirely frustrate the energy transfer between a large band-gap donor and a small band-gap acceptor such that a concentration-independent white-light-emitting single molecule is feasible.[50]

On the other hand, ESiPT is the critical step for wildtype GFP to fluoresce. Mentioned in **Section I.1**, the initially matured GFP chromophore *p*-HBI is in a neutral phenol form. Upon a 390-nm photon excitation, the phenol is deprotonated via a water mediated proton wire composing Ser205 and Glu222 and results in a highly fluorescent phenolate emitting green light.[51] This intermolecular ESPT pathway was also studied with conformationally locked model compounds in solution and revealed the important role of ESPT in excited state photoisomerization,[52] which is the key transformation observed for RSFP Dronpa.[53] In another model study with synthetic imidazole fluorophores, it was shown that ESPT-coupled excited state charge transfer (ESCT) may be responsible for the observed emission pH sensitivity in many FPs due to the charge swapping between the two imidazole nitrogen atoms on the excited state.[54]

Intermolecular ESPT has been widely used to increase the Stokes shift of FPs. ESPT is suggested as the mechanism responsible for the large Stokes shifts observed in LSSmKates RFPs based on crystallographic and mutagenesis analyses.[55] In viewing the hydrogen bonding between the DsRed-chromophore hydroxyl group and Glu160 in LSSmKate1, the proton relay involving the hydroxyl, Ser158 and the Asp160 carboxylate in LSSmKate2, and also the proton relay composed of the hydroxyl, Ser143 and Asp158 in mKeima, similar ESPT pathways were engineered for other DsRed RFPs based on these templates. It was successfully shown by Verkhusha's group that the Stokes shifts were all greatly enlarged by over 100 nm in mNeptune, mCherry, mStrawberry, mOrange, and mKO.[56] Similar strategies have been adopted in intramolecular cases with synthetic analogues to develop DNA labels.[57] Recently, a phenylbenzothiazole derivative HABT was designed to bind to a tyrosine kinase to establish a hydrogen bonding network with neighboring T766 and active-site water to facilitate ESPT for probing the protein binding site by the change in Stokes shift.[58]

I.16.2 ESHB in dye/hCRBPII complexes

Described thus far in this section, all of the large Stokes shift strategies are based on photoacidic hydroxyls or N-Hs. In **Section I.14** and **I.15** we described the super photobasic behavior of **FR0**-SB and its apparent larger Stokes shift. Is it possible to recapitulate this photobase initiated ESPT or ESHB in the hCRBPII scaffold? Actually, the phenomenon was already observed in complexes of **DiAI-2V**/Q108K:K40L:T51V: T53S:V62E and **DiAI-2V**/Q108K:K40L:T51A:T53S: V62E (**Table II-1**). However, the key mutations of hCRBPII that facilitate ESHB were not clear at that time.

During the course of engineering hCRBPII mutants for regulating the emission wavelengths of **ThioFluor-1**, Dr. Elizabeth M. Santos found a mutant Q108K:K40E:T53A:R58L:Q38F:Q4F (KEALFF) that emits at around 600 nm with a 390-nm excitation after binding with **ThioFluor-1**. The apparent 200 nm Stokes shift cannot be explained by the direct emission of **ThioFluor-1**/**KEALFF** SB. The emission wavelength is also blue-shifted about 100 nm from the regular **ThioFluor-1**/hCRBPII PSB emission maxima.[59] Contemplating the super photobasicity of **FR0**-SB and its corresponding LW emission, the emission character of **ThioFluor-1**/**KEALFF** presents a similar feature and is ascribed to ESPT, or more accurately ESHB due to the blue-shift in the emission wavelength that is not the signature of protonated complexes. Collaboratively, this was investigated to scope the generality of the ESHB phenomenon in engineered hCRBPII with different fluorophores that could form a neutral imine in the ground state. A more detailed description of the related protein engineering investigation can be found in Dr. Santos' PhD thesis.

The important mutations for ESHB of **FR** dyes can be visualized in the docking simulation of **FR-1V** in a model hCRBPII scaffold (**Figure III-21**). In principle, an H-bonding acceptor located within a proper distance to the **FR-1V** imine nitrogen atom should be able to stabilize the proton on the nitrogen atom via a partial H-bond and hence facilitate the ESHB to proceed. With this consideration and accounting for the average H-bonding length, a radius of 5 ~ 6 Å is scanned from the **FR-1V** imine nitrogen in the docking model. As shown in **Figure III-21**, residues within 5 Å radius are highlighted in green. These include W106 and E117. The former is conservative towards mutagenesis.

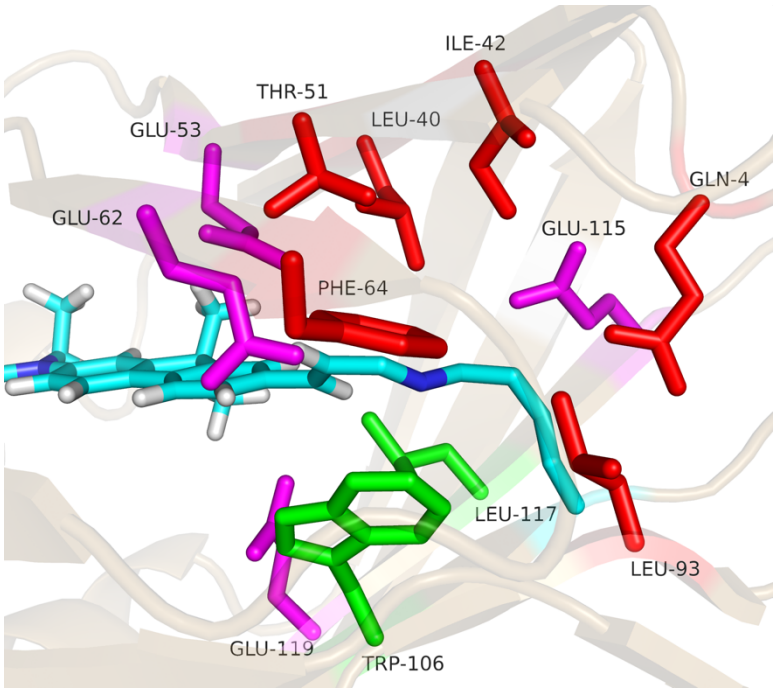


Figure 0-21 Potential residues facilitating excited state hydrogen bonding on **FR-1V** imine nitrogen atom. Residues within 5 Å to the nitrogen atom are shown in green. Residues within 6 Å distance are shown in red and magenta. The pose of **FR-1V** is simulated with a flexible docking method by using AutoDock Vina. The protein matrics is extracted from hCRBPII mutant **KL** (PDB ID: 4EXZ). **FR-1V**:carbon (cyan), nitrogen (blue), hydrogen (grey). Magenta residues are simulated with PyMOL.

The latter shows enhanced ESHB with **ThioFluor-1** but impedes the binding with **FR-1V.** Residues at 6 Å radius are highlighted in red, including L93, Q4, L40, I42, T51, and F64. Considering the elongation of short aliphatic residues to glutamate, four other mutations that can potentially fit in 6 Å radius are also simulated and highlighted in magenta, including V62E, T53E, L115E, and L119E.

Mutagenesis at these positions with HBA residues (i.e., glutamate, aspartate, and histidine) along with other mutations leads to a panel of mutants that are subsequently screened over all of the **FR** dyes. Not surprisingly, the expressible mutants, predominantly as glutamates, show various extent of ESHB emissions with different compounds (**Figure III-22**). It is notable that the LW emission band of ESHB by exciting the SB of the

fluorophores are all blue-shifted as compared to the corresponding PSB emissions. In the case of **FR0**/Q108K:K40E:T53A:R58L:Q38F:Q4F (**psES235**) complex, the SB shows two resolved absorption maxima. The excitation of these two maxima (383 and 413 nm) give slightly different ESHB emission spectra with similar quantum yields (0.75 and 0.80, respectively). Interestingly, the long-wavelength excitation actually leads to the short-wavelength emission (**Figure III-22**). The complex of **FR0**/Q108K:K40D:T53A:R58L:Q38F:Q4F:V62E (dimer) has an ESHB emission with significant bathochromic shift of ~

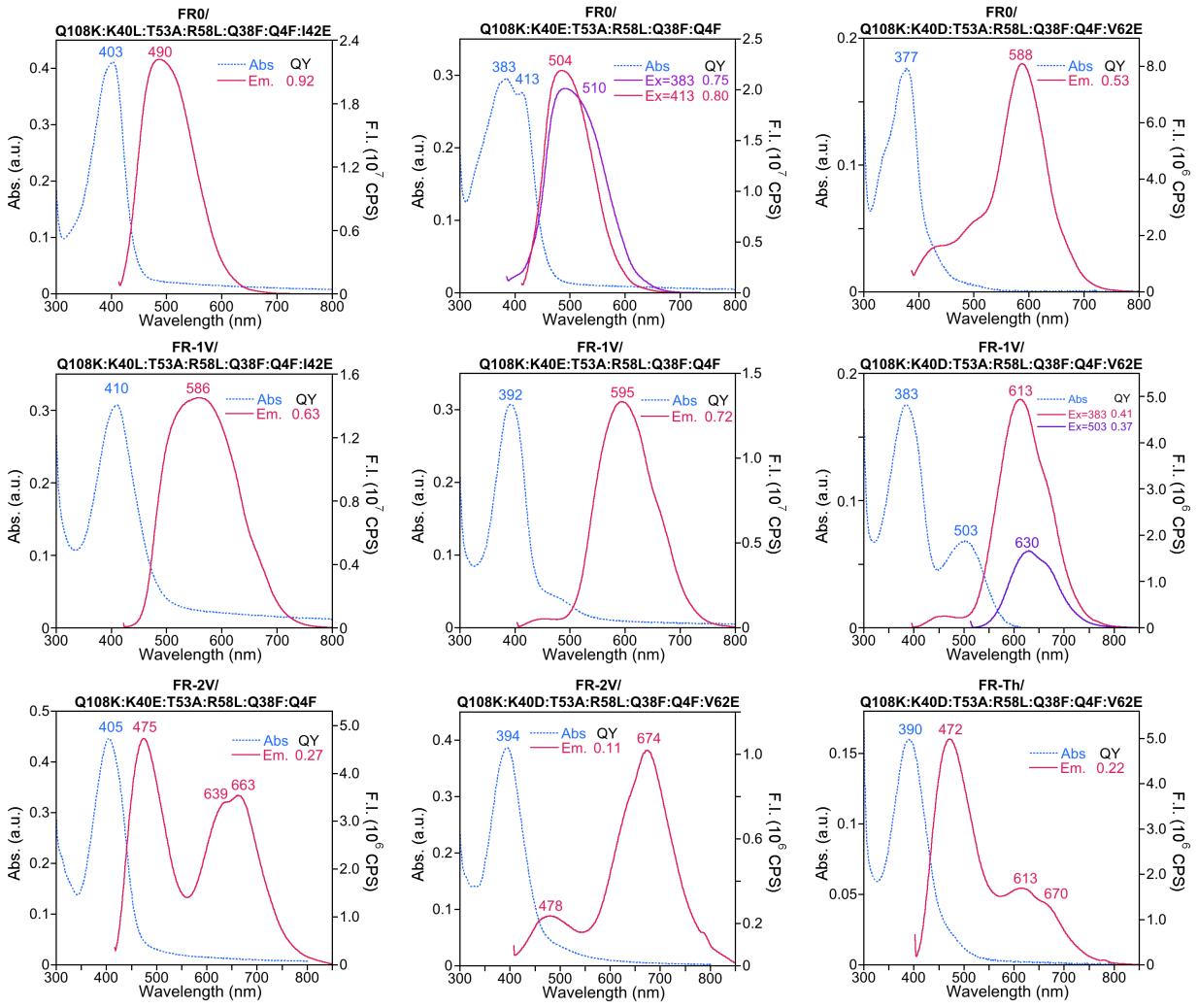


Figure 0-22 Representative **FR**/hCRBPII complexes showing excited state hydrogen bonding long wavelength emissions. Mutant Q108K:K40D:T53A:R58L:Q38F:Q4F:V62E is in the dimeric form.

80 nm. This dimer effect has also been observed elsewhere. The ESHB energy transfer efficiency is determined by both the ligand and the protein host. In some cases, the complexes even show the distinguishable shoulder band in the long-wavelength region. These observations together suggest the existence of a complex proton network in these dye/hCRBPII complexes that may have varying solvent reorganization time constants in the ESHB processes to cause the different ratio of the LW emission components, as discussed in **Section I.15**.

I.16.3 A bright ESHB tag with large Stokes shift and fast-forming kinetics

Considering application for live cell imaging, **FR-1V/psES235** complex was selected for its optimal emission wavelength (λ_{em} = 595 nm) and high fluorescence quantum yield ($\Phi = 0.72$). **FR0/psES235** exhibits a 92% quantum yield with an emission maximum around 510 nm. The excitation spectrum of **FR-1V/psES235** is shown in **Figure**

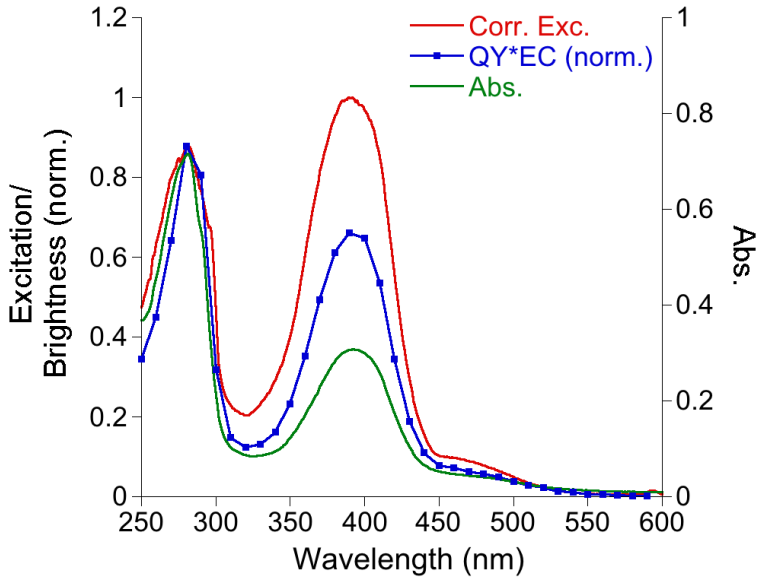


Figure 0-23 Excitation spectrum of **FR-1V/psES235** 600 nm emission. The red trace is the excitation spectrum corrected against Rhodamine-B. The green trace is the absorption spectrum. The blue trace is the normalized brightness curve, plotting the product of $\boldsymbol{\varepsilon}$ and $\boldsymbol{\phi}$ with each square as a data point.

III-23. Interestingly, the ESHB emission is not only observed by 392-nm excitation but also by irradiation at 280 nm, although the energy transfer efficiency from the 280-nm absorbing tryptophans is much lower than the **FR0** SB as demonstrated by the comparison between the absorption spectrum and the normalized brightness curve. This might suggest the near-field energy transfer between W106 and **FR-1V** imine in the excited state.

The binding of **FR-1V** and **psES235** is instantaneous. Under the condition of pseudo-first order measurement (**Figure III-24a**), it only takes 0.18 sec as the binding half-time. In the more accurate second-order rate constant measurement, it is showing the rate at the level of 10^6 $M^{-1}s^{-1}$ (**Figure III-24b**). The ultrafast binding kinetics of **FR-1V/psES235** is critical for live cell imaging. Because of the sub-minute binding, the

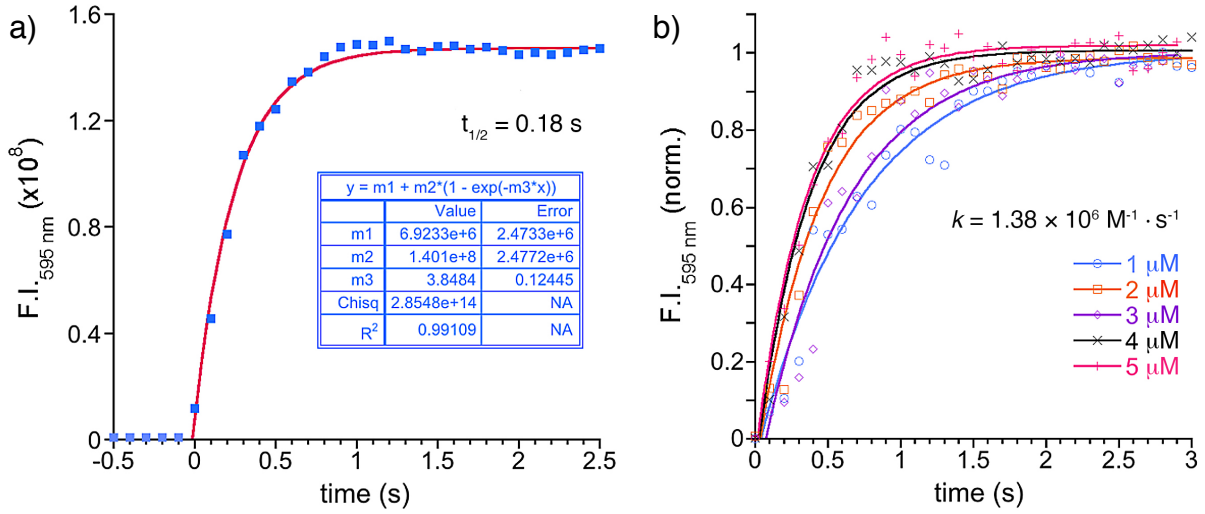


Figure 0-24 Binding kinetics of **FR-1V** with **psES235**. a) Pseudo-first order binding of **FR-1V** (10 μM) with **psES235** (20 μM). The binding was monitored at the 595 nm ESHB emission maximum. An exponential fit gives the binding half-time as 0.18 s. b) Second-order rate constant measurement. Variable concentrations of **FR-1V** were used to bind 100 nM of **psES235**. Observable rate constants were derived from single exponential fits. The second-order rate constant was then derived from the linear regression of observable pseudo first order rate constants as a function of concentration. All measurements were taken in PBS buffer (pH = 7.3).

required cell staining time is only limited by **FR-1V**'s permeation and diffusion into the cells. This fast rate can differentiate the binding of **FR-1V** with **psES235** from other nonspecific cellular proteins, thus providing a feasible mechanism to reduce nonspecific fluorescence background by removing the excess amount of **FR-1V** before its reaction with nonspecific targets.

To test the imaging performance of **FR-1V/psES235** *in cellulo*, the gene of **psES235** is cloned into pFlag-CMV2 vectors with a N-terminal EGFP sequence and C-terminal localization peptides (i.e., NLS, NES, and CAAX) as described in **0**. The high brightness of **FR-1V/psES235** allows a final staining concentration of 500 nM of **FR-1V**,

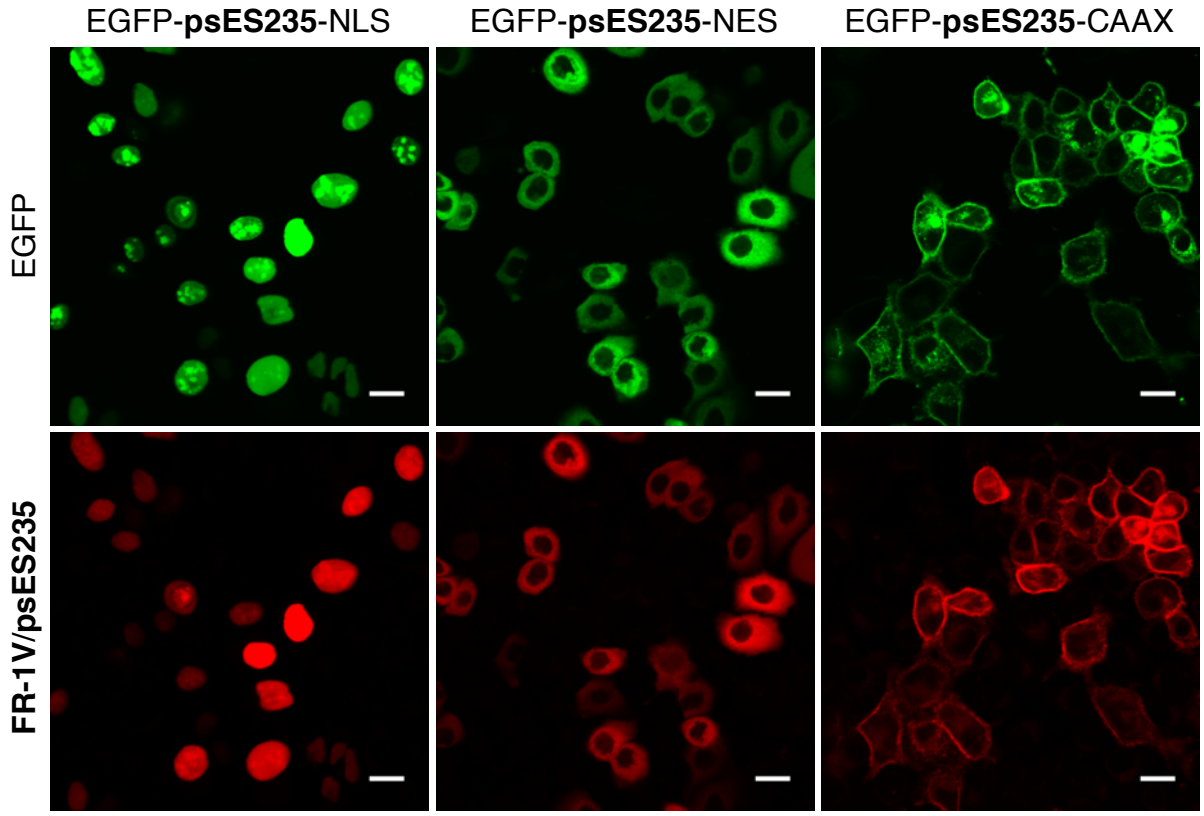


Figure 0-25 Compartmentalized **FR-1V/psES235** imaging in live HeLa cells. NLS = nuclear localization sequence. NES = nuclear export sequence. CAAX = prenylation tag. Cells were stained with 500 nM **FR-1V** and incubated at 37 °C for 1 min. Cells were washed 3 times with DPBS before imaging. Scale bar, 10 μm.

which is much lower than the amount required for the photoswitching mutants. The fast binding enables a quick labeling protocol with 1 min staining at 37 °C followed by 3 wash steps (**Figure III-25**). In all sub-cellular images, the confocal red channel (LP615) shows bright emission from the long-wavelength ESHB fluorescence of the complex. The line profile analysis demonstrates high signal specificity of the red fluorescence that is colocalizing with the reference EGFP signal (**Figure III-26**). To this end, an imaging tag featuring high brightness, large Stokes shift, and fast labeling kinetics has been established.

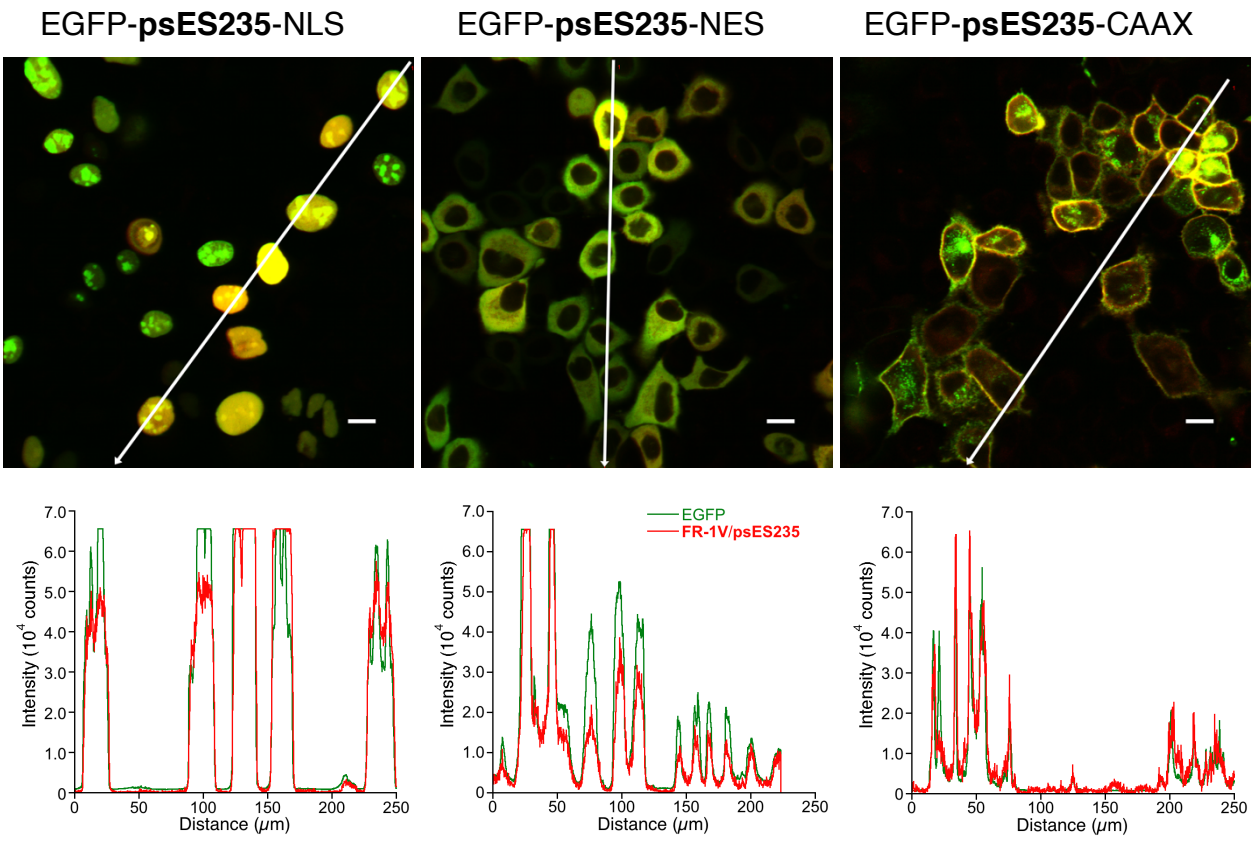


Figure 0-26 ESHB fluorescence specificity of **FR-1V/psES235**. Top row shows the merged EGFP and LP615 channels in cell nuclei, cytosol, and plasma membrane-localized HeLa cells. Bottom row shows the line profile of colocalized EGFP and ESHB signal along the white arrows in the top images. Scale bar, 10 μm.

I.17 Dual-color live cell imaging enabled by a single dye

Current multicolor live cell imaging is enabled by combining multiple FPs or synthetic dyes that have separate excitation or emission channels in the confocal microscope. A good example of spontaneously labeling six FPs is given in the beginning of **Section I.2**. However, multicolor labeling with synthetic dyes require the choice of different dye scaffolds and necessitates multiple rounds of staining and washing.

On the other hand, the 200 nm difference in the excitation wavelengths (405-nm Diode vs 594-nm HeNe) and 100-nm difference in emission maxima (595 nm vs 704 nm) of the ESHB **FR-1V/psES235** and the photoswitching **FR-1V/ps4** tags provide the opportunity to achieve dual-color imaging by using just a single dye (**FR-1V**) with conventional dichroic settings. Or more generally, the dual-color imaging is achievable if two hCRBPII mutants can be properly expressed in the target cell and give the desired ESHB and PSB excitation/emission, respectively, without any interfering nonspecific background.

The initial attempts to co-express **ps4** and **psES235** in HeLa cells for dual-color imaging was not successful. For unknown reasons, the expression of the two mutants was problematic. Besides, the binding rates of **FR-1V** with the two mutants are different (1.9 min vs 0.18 s), which results either in insufficient labeling time for **ps4** or in increasing the nonspecific background for **psES235**. Moreover, the absolute fluorescence quantum yields also have 4-fold difference, resulting in incomparable sensitivity of the two imaging channels. In this context, it is necessary to find a mutant with comparable binding kinetics and quantum yield to **psES235** that can form a stable **FR-1V** PSB after thermal binding.

Mutant **psST61** (Q108K:K40H:T53A:R58L:Q38F:Q4F) was identified after mutagenesis and screening. As shown in **Figure III-27**, the complex of **FR-1V/psST61** has a predominant PSB absorption at 516 nm, with a small portion of SB absorption at 398 nm. Excitation at 516-nm leads to the signature PSB emission centered at 630 nm with a shoulder at 650 nm. Interestingly, this spectrum is almost identical to the emission spectrum of **FR0**-PSB in $HClO_4$/EtOH (**Figure III-8b**). The excitation at 398-nm emits a typical SB fluorescence at 450 nm, however, with a small fraction at 630 nm as the ESHB emission. Nonetheless, the quantum yield of the PSB emission is 39%. Together with a 2-fold stronger absorption, the brightness of the PSB emission is estimated as 14-fold higher than that of the unwanted ESHB emission.

The binding of **FR-1V** with **psST61** is also fast (**Figure III-28**). The binding assay displays a half-time of 6.8 sec, not as fast as the 0.18 s of **psES235**, but closer in the magnitude than the 1.9 min observed with **ps4**. The second-order rate constant is determined as 2.5×10^4 $M^{-1} \cdot s^{-1}$, only about 50-fold smaller than that of **psES235**.

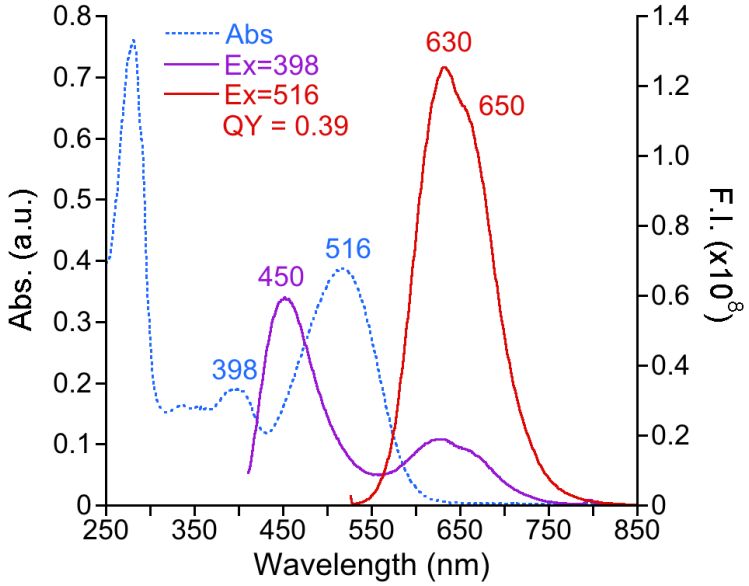


Figure 0-27 Absorption and emission spectra of **FR-1V/psST61**.

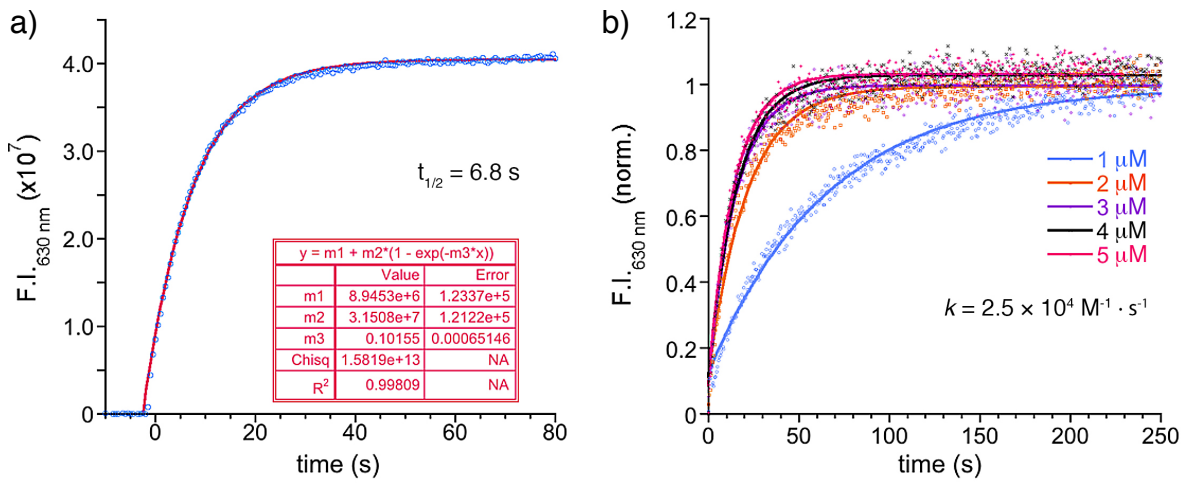


Figure 0-28 Binding kinetics of **FR-1V/psST61**. a) Binding of **FR-1V** (10 μM) and **psST61** (10 μM) monitored at the 630 nm fluorescence maximum. The intensity curve is fit with a single exponential function. b) Second-order rate constant measurement. Variable concentrations of **FR-1V** were used to bind 100 nM of **psST61**. Observable rate constants were derived from single exponential fits. The second-order rate constant was then derived from the linear regression of observable pseudo first order rate constants as a function of concentration. All measurements were taken in PBS buffer (pH = 7.3).

To test dual-color imaging, HeLa cells are co-transfected with pFlag-CMV2 vectors encoding EGFP-**psES235**-NES and EGFP-**psST61**-NLS, respectively. Ideally, the ESHB emission of **FR-1V/psES235** should be localized in the cytosol and the PSB emission of **FR-1V/psST61** should be observed only inside cell nuclei. Shown in **Figure III-29b**, the PSB emission is colored red and delineated inside the cell nuclei as expected. However, in the cyan-colored ESHB channel, the fluorescence is not only observed in cell cytosol but also in the nuclei (**Figure III-29a**). In fact, the latter signal is colocalized with signals from the PSB emission channel, indicating that it originates from the ESHB emission of **FR-1V/psST61**. Although this “leaky” fluorescence of **FR-1V/psST61** is observed in the ESHB channel, it should be noted that the ESHB emission from the two constructs are clearly delineated rather than mingled, as well as in the reference EGFP channel. As a proof of concept, this imaging assay successfully demonstrated the feasibility to label two

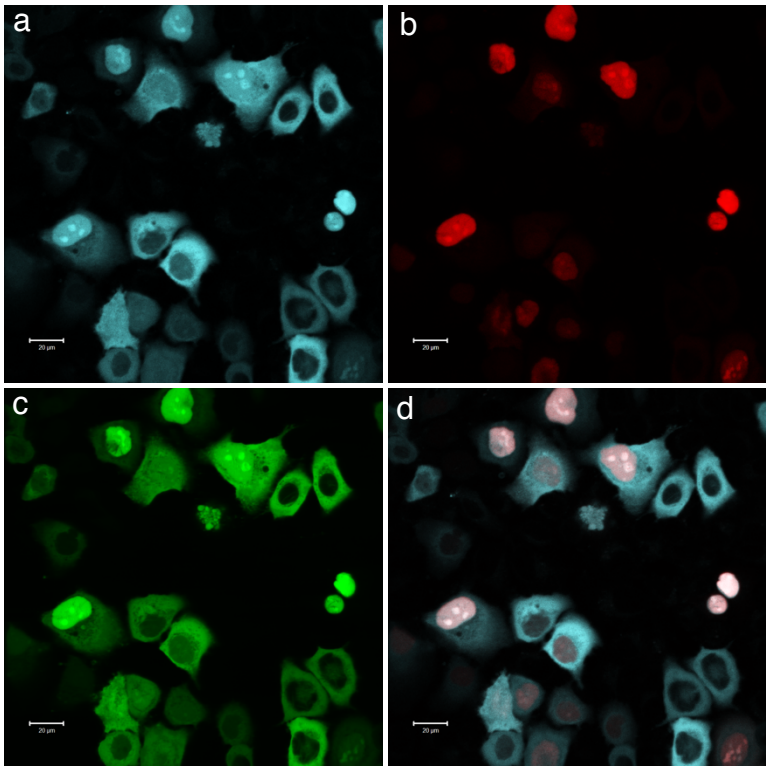


Figure 0-29 Dual-color live cell imaging with **FR-1V** in HeLa cells co-transfected with pFlag-CMV2 vectors encoding EGFP-**psES235**-NES and EGFP-**psST61**-3xNLS. a) ESHB channel: λ_{ex} = 405 nm, LP615. b) PSB channel: λ_{ex} = 514 nm, LP650. c) Reference EGFP channel: λ_{ex} = 488 nm, BP505-530. d) Merged image of a) and b), showing well-defined edges of cell nuclei and surrounding cytosol. Cells were stained with 500 nM of **FR-1V** and incubated at 37 °C for 1 min, then washed with DPBS for 3 times before imaging. Scale bars, 20 μm.

sub-cellular compartments with **FR-1V** and different hCRBPII tags. Clearly resolved fluorescence signals have been acquired (**Figure III-29d**).

The high intensity of the "leaky" ESHB emission of **FR-1V**/**psST61** is somewhat unexpected since it does not show this level of ESHB *in vitro*. This might be caused by the pH difference or expression variability between *E. coli* and mammalian cancer cells. Nonetheless, the crystal structure of **FR-1V**/**psST61** provides some understanding of the unwanted spectral behavior. It shows two orientations of the key K40H mutation with a 50:50 ratio (**Figure III-30**). The population with a short distance (2.9 Å) between the

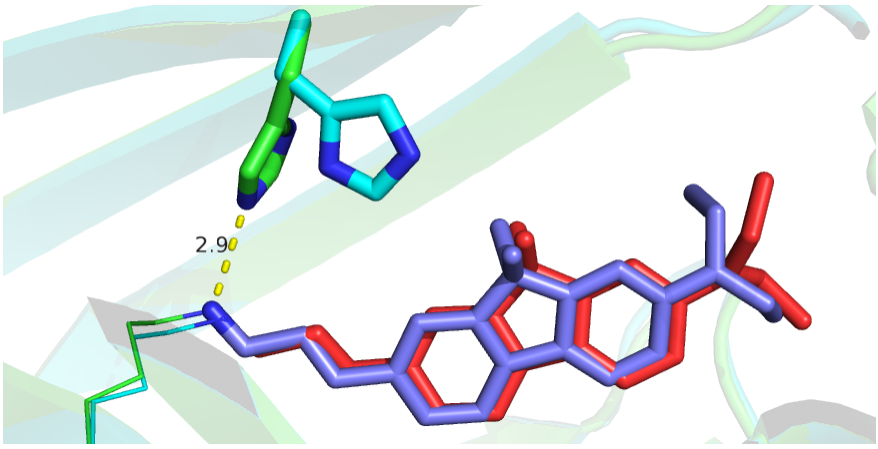


Figure 0-30 Crystal structure of **FR-1V/psST61** complex, showing two trajectories of the 40H residue in a 50:50 population ratio. The closer conformer has a 2.9 Å distance between the histidine and the imine nitrogen atom. Protein crystallized by Dr. Alireza Ghanbarpour.

imidazole and the imine nitrogen atoms is susceptible to ESHB. Therefore, a logical approach to suppress this unwanted ESHB is to force His40 to adopt the flipped conformation. As shown in **Figure III-31**, Phe130 and Gln128 are in close distance to the cyan conformer of His40. These two positions can be mutated to polar or anionic residues to facilitate H-bonding with His40 and lock its geometry. On the other side, Ile42 is close

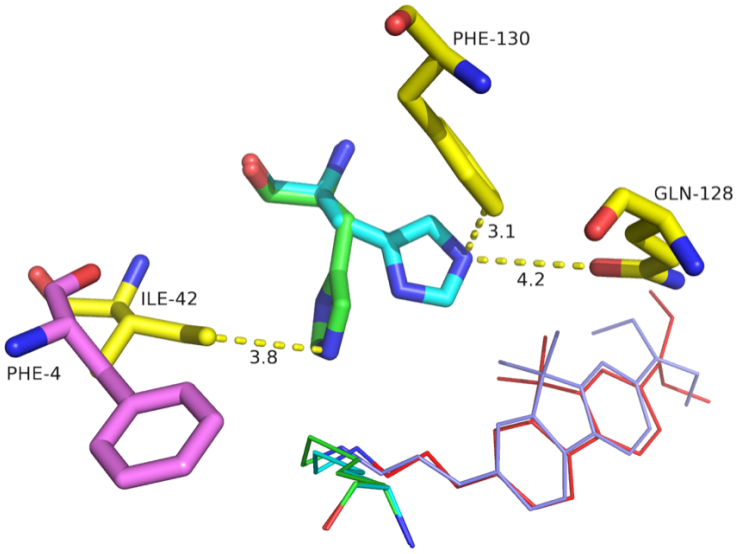


Figure 0-31 Proposed key residues for mutagenesis to suppress K40H ESHB. Distances are measured from the **FR-1V/psST61** crystal structure.

to the green conformer of His40. It can be mutated to bulky aromatic residues so that the green His40 can be pushed away to the cyan pose. Mutagenesis work is currently in progress and followed up by Rahele Esmatpoursalmani.

I.18 Conclusion and significance

A donor-acceptor ICT-type fluorenyl imine is identified as a super photobase in protic solvents, featuring a rare and strong dual-emission phenomenon originating from the intermolecular excited state proton transfer process between the solute and surrounding solvent molecules. Steady-state and ultrafast spectroscopic techniques show a partially transferred H-bonding complex formation on a picosecond timescale as an intermediate step during the ESPT process. Investigations with other carbon and nitrogen based solvents suggest a ground-state H-bonding complex as the prerequisite.

A more general excited state hydrogen bonding process is realized in dye/hCRBPII complexes, featuring large Stokes shifts and high fluorescence quantum yields. The optimal complex is engineered into a fast-forming tag for live cell imaging. The emitting process can be contemplated as the counterpart of the ESPT pathway in GFP-like FPs such that the ESHB is initiated by a photobase instead of a photoacid.

A variant of the ESHB mutants is identified to feature a stable PSB absorption and emission. Combining the ESHB and PSB mutants, a proof-of-concept dual-color imaging system is established with the single dye **FR-1V** and demonstrated feasible. Further engineering effort is in progress to optimize the dual-color labeling system.

I.19 Experimental section

General procedures for protein mutagenesis, cell-based assays, and steady-state spectroscopic measurement are as described in **Section I.13**. The transient absorption experiments were performed by Dr. Muath Nairat and are described briefly as followed.

General procedure of transient absorption experiment

The transient absorption setup consists of a regeneratively amplified Ti:Sapphire laser (Legend, Coherent, Santa Clara, CA) producing femtosecond pulses at a repetition rate of 1 kHz. The pulses were compressed to their transform-limit duration with a pulse shaper utilizing the Multiphoton Intrapulse Interference Phase Scan (MIIPS) approach. The output was centered at 800 nm with a duration of 40 fs. The pulses were split using a beam splitter into an arm that was used to generate the second harmonic signal centered at 400 nm using a β-BBO crystal which served as the pump. The probe arm was sent into an optical delay line and was focused on a 2 mm YAG crystal to generate a white light continuum that extends from 450 to 900 nm. A 680 nm short pass filter was used to filter the continuum probe pulses. The two arms were non-collinearly combined and focused using a 25.0 cm lens into a 1 mm quartz cuvette. The probe signal was collected using a compact CCD (QE65000, Ocean Optics). Temporal dispersion of the probe pulse was measured by cross correlation and the observed chirp was used to correct the transient absorption data during global analysis**.** Global analysis of the results was carried out using Glotaran software. The synthetic procedure for **FR0**-SB is detailed in the supporting information along with NMR data.

General procedure of pK_a measurement by UV/Vis spectrophotometry

It is feasible to use an acid with known pK_a value to titrate the pK_a of an unknown acid. This can be generalized to the base case as well. The general acid case is used to derive the method as followed.

Considering two partially ionized acids in the same solution with a given volume of *V*, the equilibria of the two acids are in the forms:

$$HA_1 \overset{K_{a1}}{\rightleftharpoons} H^+ + A_1^-$$
$$HA_2 \overset{K_{a2}}{\rightleftharpoons} H^+ + A_2^-$$

where the footnotes of *1* and *2* denote the known acid and the unknown sample, and HA is the acid and A^- is the conjugate base. K_a is the ionization constant. Therefore, at any pH in the equilibria, it has the overall equilibrium:

$$\frac{K_{a1}}{K_{a2}} = \frac{[A_1^-]}{[A_2^-]} \cdot \frac{[HA_2]}{[HA_1]}$$
$$\therefore \Delta pK_a = pK_{a2} - pK_{a1} = \log\left(\frac{[A_1^-]}{[HA_1]} \cdot \frac{[HA_2]}{[A_2^-]} \right)$$

With the given *V*, it can be rewritten as:

$$\Delta pK_a = pK_{a2} - pK_{a1} = \log\left(\frac{n_{A_1^-}}{n_{HA_1}} \cdot \frac{n_{HA_2}}{n_{A_2^-}} \right)$$

and for a given solution, it has:

$$n_{A_i} = n_{A_i^-} + n_{HA_i} \quad (i = 1,2)$$

If define:

$$\alpha_i = \frac{n_{HA_i}}{n_{HA_i} + n_{A_i^-}}$$

there is:

$$\Delta pK_a = \log \frac{(1-\alpha_1)\cdot\alpha_2}{\alpha_1\cdot(1-\alpha_2)}$$

For a binary acidic solution with a certain pH, there is always:

$$\frac{A^\lambda}{l} = [A_1^-]\cdot\varepsilon^\lambda_{A_1^-} + [HA_1]\cdot\varepsilon^\lambda_{HA_1} + [A_2^-]\cdot\varepsilon^\lambda_{A_2^-} + [HA_2]\cdot\varepsilon^\lambda_{HA_2}$$

that is,

$$\left(\frac{V}{l}\right)A^\lambda = n_{A_1^-}\cdot\varepsilon^\lambda_{A_1^-} + n_{HA_1}\cdot\varepsilon^\lambda_{HA_1} + n_{A_2^-}\cdot\varepsilon^\lambda_{A_2^-} + n_{HA_2}\cdot\varepsilon^\lambda_{HA_2}$$

and can be rewritten as:

$$\left(\frac{V}{l}\right)A^\lambda = n_{A_1}\cdot\varepsilon^\lambda_{A_1^-} + \alpha_1\cdot n_{A_1}\left(\varepsilon^\lambda_{HA_1} - \varepsilon^\lambda_{A_1^-}\right) + n_{A_2}\cdot\varepsilon^\lambda_{A_2^-} + \alpha_2\cdot n_{A_2}\left(\varepsilon^\lambda_{HA_2} - \varepsilon^\lambda_{A_2^-}\right)$$

where ε is the extinction coefficient as a function of wavelength and A is the absorption as a function of wavelength that can be determined by spectroscopic measurements. Specifically, $\varepsilon^\lambda_{HA_i}$ and $\varepsilon^\lambda_{A_i^-}$ can be determined with the pure solutions of the acids and their conjugate bases. And with known n_{A_i} values, α_i can be determined by multi-variant linear regression analysis.

Similarly, if the binary solution is basified to completely form conjugate bases, there is:

$$\left(\frac{V}{l}\right)A^\lambda = n_{A_1}\cdot\varepsilon^\lambda_{A_1^-} + n_{A_2}\cdot\varepsilon^\lambda_{A_2^-}$$

and the two-variant linear regression with the following model can simply give n_{A_i}

$$S = \sum_i^\lambda [A^\lambda - f\left(\varepsilon^\lambda_{A_i^-}\right)]^2$$

Synthesis and characterization of FR0-SB

To a solution of **FR0** (10.5 mg, 35.8 μmol) in ethanol (3.0 mL) was added *n*-butylamine (100 μL, 28.2 equiv.). The resulting solution was stirred at room temperature for 4 h to complete the reaction. The solvent and the excess amount of *n*-butylamine was removed *in vacuo* to afford 12.5 mg light yellow solid (yield = quant.).

^{1}H NMR ($CDCl_3$, 500 MHz), δ (ppm): 8.30 (s, 1H), 7.83 (d, J = 1.3 Hz, 1H), 7.61 – 7.51 (m, 3H), 6.74 – 6.65 (m, 2H), 3.67 – 3.60 (m, 2H), 3.45 (q, J = 7.1 Hz, 4H), 1.72 (p, J = 7.2 Hz, 2H), 1.50 (s, 6H), 1.47 – 1.39 (m, 2H), 1.23 (t, J = 7.0 Hz, 6H), 0.98 (t, J = 7.4 Hz, 3H). ^{13}C NMR ($CDCl_3$, 125 MHz), δ (ppm): 161.52, 156.42, 153.14, 148.22, 142.73, 133.14, 128.59, 126.33, 121.49, 120.85, 118.09, 110.74, 105.49, 61.64, 46.70, 44.70, 33.22, 27.43, 20.52, 13.97, 12.64. ESI-MS: (calc.) (m/z) calcd for $C_{24}H_{33}N_2$ $[M+H]^+$ 349.2644, found 349.2643.

REFERENCES

REFERENCES

1. Reichardt, C. Solvatochromic Dyes as Solvent Polarity Indicators. *Chem. Rev.* **1994**, 94, 2319-2358.

2. Weller, A. Quantitative Untersuchungen der Fluoreszenzumwandlung bei Naphtholen. *Zeitschrift für Elektrochemie, Berichte der Bunsengesellschaft für physikalische Chemie* **1952**, 56, 662-668.

3. Förster, T. Die pH - Abhängigkeit der Fluoreszenz von Naphthalinderivaten. *Zeitschrift für Elektrochemie und angewandte physikalische Chemie* **1950**, 54, 531-535.

4. Pines, E. & Pines, D. in Ch7: Proton Dissociation and Solute-Solvent Interactions Following Electronic Excitation of Photoacids. *Ultrafast Hydrogen Bonding Dynamics and Proton Transfer Prosesses in the Condensed Phase*. (eds. Elsaesser, T. & Bakker, H. J.), 155-184 (Springer Netherlands; Dordrecht; **2002**).

5. Douhal, A., Lahmani, F. & Zewail, A.H. Proton-transfer reaction dynamics. *Chem. Phys.* **1996**, 207, 477-498.

6. Arnaut, L.G. & Formosinho, S.J. Excited-state proton transfer reactions I. Fundamentals and intermolecular reactions. *J. Photochem. Photobiol. A* **1993**, 75, 1-20.

7. Ireland, J.F. & Wyatt, P.A.H. in Acid-Base Properties of Electronically Excited States of Organic Molecules. *Advances in Physical Organic Chemistry*. Vol. 12, (ed. Gold, V.), 131-221 (Academic Press; **1976**).

8. Agmon, N. Elementary Steps in Excited-State Proton Transfer. *J. Phys. Chem. A* **2005**, 109, 13-35.

9. Jankowski, A., Dobryszycki, P., Lipiński, J. & Stefanowicz, P. Excited-State Proton Transfer in Hydroxynaphthaldehydes Covalently Bound to Proteins. *J. Fluoresc.* **1998**, 8, 103-113.

10. Heo, W. et al. Coherent intermolecular proton transfer in the acid-base reaction of excited state pyranine. *Phys. Chem. Chem. Phys.* **2017**, 19, 18243-18251.

11. Finkler, B. et al. Highly photostable "super"-photoacids for ultrasensitive fluorescence spectroscopy. *Photochem. Photobiol. Sci.* **2014**, 13, 548-562.

12. Tolbert, L.M. & Solntsev, K.M. Excited-State Proton Transfer: From Constrained Systems to “Super” Photoacids to Superfast Proton Transfer. *Acc. Chem. Res.* **2002**, 35, 19-27.

13. Clower, C., Solntsev, K.M., Kowalik, J., Tolbert, L.M. & Huppert, D. Photochemistry of “Super” Photoacids. 3. Excited-State Proton Transfer from Perfluoroalkylsulfonyl-Substituted 2-Naphthols. *J. Phys. Chem. A* **2002**, 106, 3114-3122.

14. Ryan, E.T., Xiang, T., Johnston, K.P. & Fox, M.A. Absorption and Fluorescence Studies of Acridine in Subcritical and Supercritical Water. *J. Phys. Chem. A* **1997**, 101, 1827-1835.

15. Favaro, G., Mazzucato, U. & Masetti, F. Excited state reactivity of aza aromatics. I. Basicity of 3-styrylpyridines in the first excited singlet state. *J. Phys. Chem.* **1973**, 77, 601-604.

16. Yatsuhashi, T. & Inoue, H. Molecular Mechanism of Radiationless Deactivation of Aminoanthraquinones through Intermolecular Hydrogen-Bonding Interaction with Alcohols and Hydroperoxides. *J. Phys. Chem. A* **1997**, 101, 8166-8173.

17. Driscoll, E.W., Hunt, J.R. & Dawlaty, J.M. Photobasicity in Quinolines: Origin and Tunability via the Substituents’ Hammett Parameters. *J. Phys. Chem. Lett.* **2016**, 7, 2093-2099.

18. Dey, D., Sarangi, M.K., Ray, A., Bhattacharyya, D. & Maity, D.K. Excited state hydrogen bonding fluorescent probe: Role of structure and environment. *J. Lumin.* **2016**, 173, 105-112.

19. Wu, Y.-S. et al. Water-Catalyzed Excited-State Proton-Transfer Reactions in 7-Azaindole and Its Analogues. *J. Phys. Chem. B* **2015**, 119, 2302-2309.

20. Shen, J. Y. et al. Probing water micro-solvation in proteins by water catalysed proton-transfer tautomerism. *Nat. Commun.* **2013**, 4, 2611.

21. Vogt, B.S. & Schulman, S.G. Reversible proton transfer in photoexcited xanthone. *Chem. Phys. Lett.* **1983**, 97, 450-453.

22. Akulov, K. et al. Acid Effect on Photobase Properties of Curcumin. *J. Phys. Chem. A* **2014**, 118, 2470-2479.

23. Ditkovich, J., Pines, D. & Pines, E. Controlling reactivity by remote protonation of a basic side group in a bifunctional photoacid. *Phys. Chem. Chem. Phys.* **2016**, 18, 16106-16115.

24. Ditkovich, J., Mukra, T., Pines, D., Huppert, D. & Pines, E. Bifunctional Photoacids: Remote Protonation Affecting Chemical Reactivity. *J. Phys. Chem. B* **2015**, 119, 2690-2701.

25. Aquino, A.J.A., Barbatti, M. & Lischka, H. Excited-State Properties and Environmental Effects for Protonated Schiff Bases: A Theoretical Study. *ChemPhysChem* **2006**, 7, 2089-2096.

26. Kütt, A. et al. A Comprehensive Self-Consistent Spectrophotometric Acidity Scale of Neutral Brønsted Acids in Acetonitrile. *J. Org. Chem.* **2006**, 71, 2829-2838.

27. Goodhue, L.D. & Hixon, R.M. Electron-Sharing Ability of Organic Radicals. VII. Dissociation Constants of a Series of Organic Acids and Amines in Water, Methanol and Ethanol. *J. Am. Chem. Soc.* **1934**, 56, 1329-1333.

28. Kumpulainen, T., Lang, B., Rosspeintner, A. & Vauthey, E. Ultrafast Elementary Photochemical Processes of Organic Molecules in Liquid Solution. *Chem. Rev.* **2017**, 117, 10826-10939.

29. Simkovitch, R. et al. Comprehensive Study of Ultrafast Excited-State Proton Transfer in Water and D_2O Providing the Missing $RO^{-}\cdots H^{+}$ Ion-Pair Fingerprint. *J. Phys. Chem. A* **2014**, 118, 4425-4443.

30. Snellenburg, J.J., Laptenok, S.P., Seger, R., Mullen, K.M. & van Stokkum, I.H.M. Glotaran: A Java-Based Graphical User Interface for the R Package TIMP. *J. Stat. Softw.* **2012**, 49, 1-22.

31. Horng, M.L., Gardecki, J.A., Papazyan, A. & Maroncelli, M. Subpicosecond Measurements of Polar Solvation Dynamics: Coumarin 153 Revisited. *J. Phys. Chem.***1995**, 99, 17311-17337.

32. Agmon, N., Pines, E. & Huppert, D. Geminate recombination in proton-transfer reactions. II. Comparison of diffusional and kinetic schemes. *J. Chem. Phys.* **1988**, 88, 5631-5638.

33. Pines, E. & Huppert, D. Observation of geminate recombination in excited state proton transfer. *J. Chem. Phys.* **1986**, 84, 3576-3577.

34. Paul, B.K., Ganguly, A. & Guchhait, N. Quantum chemical exploration of the intramolecular hydrogen bond interaction in 2-thiazol-2-yl-phenol and 2-benzothiazol-2-yl-phenol in the context of excited-state intramolecular proton transfer: A focus on the covalency in hydrogen bond. *Spectrochim. Acta, Part A* **2014**, 131, 72-81.

35. Zhao, G. J. & Han, K. L. Hydrogen Bonding in the Electronic Excited State. *Acc. Chem. Res.* **2012**, 45, 404-413.

36. Han, K. L. & Zhao, G. J. (eds.) *Hydrogen Bonding and Transfer in the Excited State*. Vol. I & II, (John Wiley & Sons, Ltd.; **2010**).

37. Dziuba, D. et al. Rational Design of a Solvatochromic Fluorescent Uracil Analogue with a Dual-Band Ratiometric Response Based on 3-Hydroxychromone. *Chem. Eur. J.* **2014**, 20, 1998-2009.

38. Klymchenko, A.S. & Demchenko, A.P. Multiparametric probing of intermolecular interactions with fluorescent dye exhibiting excited state intramolecular proton transfer. *Phys. Chem. Chem. Phys.* **2003**, 5, 461-468.

39. Sengupta, P.K. & Kasha, M. Excited state proton-transfer spectroscopy of 3-hydroxyflavone and quercetin. *Chem. Phys. Lett.* **1979**, 68, 382-385.

40. Hubin, P.O., Laurent, A.D., Vercauteren, D.P. & Jacquemin, D. Investigation of ESIPT in a panel of chromophores presenting N-H[three dots, centered]N intramolecular hydrogen bonds. *Phys. Chem. Chem. Phys.* **2014**, 16, 25288-25295.

41. Fang, X. et al. Synthesized Blue Fluorescent Protein Analogue with Tunable Colors from Excited-State Intramolecular Proton Transfer through an N–H···N Hydrogen Bond. *J. Phys. Chem. Lett.* **2014**, 5, 92-98.

42. Zhao, J., Ji, S., Chen, Y., Guo, H. & Yang, P. Excited state intramolecular proton transfer (ESIPT): from principal photophysics to the development of new chromophores and applications in fluorescent molecular probes and luminescent materials. *Phys. Chem. Chem. Phys.* **2012**, 14, 8803-8817.

43. Formosinho, S.J. & Arnaut, L.G. Excited-state proton transfer reactions II. Intramolecular reactions. *J. Photochem. Photobiol., A* **1993**, 75, 21-48.

44. Bilokin', M.D. et al. Dual-Fluorescence Probe of Environment Basicity (Hydrogen Bond Accepting Ability) Displaying no Sensitivity to Polarity. *J. Fluoresc.* **2008**, 19, 545-553.

45. Wu, J., Liu, W., Ge, J., Zhang, H. & Wang, P. New sensing mechanisms for design of fluorescent chemosensors emerging in recent years. *Chem. Soc. Rev.* **2011**, 40, 3483-3495.

46. Wu, Y. et al. Fluorescence Sensing of Anions Based on Inhibition of Excited-State Intramolecular Proton Transfer. *J. Org. Chem.* **2007**, 72, 62-70.

47. Peng, X., Wu, Y., Fan, J., Tian, M. & Han, K. Colorimetric and Ratiometric Fluorescence Sensing of Fluoride: Tuning Selectivity in Proton Transfer. *J. Org. Chem.* **2005**, 70, 10524-10531.

48. Zhang, X., Guo, L., Wu, F.-Y. & Jiang, Y.-B. Development of Fluorescent Sensing of Anions under Excited-State Intermolecular Proton Transfer Signaling Mechanism. *Org. Lett.* **2003**, 5, 2667-2670.

49. Choi, K. & Hamilton, A.D. A Dual Channel Fluorescence Chemosensor for Anions Involving Intermolecular Excited State Proton Transfer. *Angew. Chem. Int. Ed.* **2001**, 40, 3912-3915.

50. Park, S. et al. A White-Light-Emitting Molecule: Frustrated Energy Transfer between Constituent Emitting Centers. *J. Am. Chem. Soc.* **2009**, 131, 14043-14049.

51. Acharya, A. et al. Photoinduced Chemistry in Fluorescent Proteins: Curse or Blessing? *Chem. Rev.* **2017**, 117, 758-795.

52. Baranov, M.S. et al. Conformationally Locked Chromophores as Models of Excited-State Proton Transfer in Fluorescent Proteins. *J. Am. Chem. Soc.* **2012**, 134, 6025-6032.

53. Fron, E. et al. Ultrafast Excited-State Dynamics of the Photoswitchable Protein Dronpa. *J. Am. Chem. Soc.* **2007**, 129, 4870-4871.

54. Berezin, M.Y., Kao, J. & Achilefu, S. pH-Dependent Optical Properties of Synthetic Fluorescent Imidazoles. *Chem. Eur. J.* **2009**, 15, 3560-3566.

55. Piatkevich, K.D. et al. Monomeric red fluorescent proteins with a large Stokes shift. *Proc. Natl. Acad. Sci. U. S. A.* **2010**, 107, 5369-5374.

56. Piatkevich, K.D., Malashkevich, V.N., Almo, S.C. & Verkhusha, V.V. Engineering ESPT Pathways Based on Structural Analysis of LSSmKate Red Fluorescent Proteins with Large Stokes Shift. *J. Am. Chem. Soc.* **2010**, 132, 10762-10770.

57. Wenge, U. & Wagenknecht, H. A. Synthetic GFP Chromophore and Control of Excited-State Proton Transfer in DNA: An Alternative Concept for Fluorescent DNA Labels with Large Apparent Stokes' Shifts. *Synthesis* **2011**, 502-508.

58. Mancini, D.T., Sen, K., Barbatti, M., Thiel, W. & Ramalho, T.C. Excited-State Proton Transfer Can Tune the Color of Protein Fluorescent Markers. *ChemPhysChem* **2015**, 16, 3444-3449.

59. Santos, Elizabeth M. in PhD thesis. *Michigan State University* **2017**.

MINIMIZING IMAGING BACKGROUND OF DYE-HCRBPII TAGS VIA PHOTOINDUCED ELECTRON TRANSFER QUENCHING.

In the previous two chapters, we have shown two different strategies to diminish the nonspecific fluorescence background, namely, ICT-promoted NIR emission with photoisomerization and ultrafast binding featured in ESHB mutants. The former requires specific mutants to keep the **FR-1V**/hCRBPII complexes in the imine state to prevent NIR emission from nonspecifically formed iminiums. The latter takes advantage of the unique sub-second binding kinetics facilitated by special ESHB mutants. Both systems rely on specific photochemical transformations of their excited states to mitigate nonspecific background. On the other hand, a broad range of dye/hCRBPII complexes will find use in: 1) utilizing the ICT character of **FR-1V** to make triple- or multi-color imaging tag (see **Section I.17**); 2) developing **FR-1V**/hCRBPII into a dual-channel ratiometric pH probe (see **Section I.12.2**). However, the two applications cannot be realized with merely the two aforementioned photochemical systems, since none of the two strategies will be suitable for the removal of unwanted fluorescence in the two scenarios that require the incorporation of other dye/hCRBPII complexes. In this context, a more general approach is needed to control the nonspecific background while allowing a no-wash protocol.

I.20 Current strategies to enable no-wash live cell imaging

Fluorogenicity, i.e., the ability to keep the fluorophore in dark (or a spectrally resolved emission state other than that for imaging) before a specifically designed event to turn on the fluorescence, can be achieved by either physical or chemical mechanisms.

I.20.1 Fluorogenicity based on physical interaction with environments

The photophysical approach usually relies on the environmental change of the fluorophores to restore the fluorescence that is initially quenched by various non-chemical mechanisms.[1] As a mimicry of GFP fluorophore, which shows strong emission inside the restricted protein scaffold but completely non-emissive in free environments,[2] molecular rotors that become fluorescent as a result of the restriction of internal conversion (RIR) have been used in the design of fluorogens. The classical examples are DCVJ and its derivatives. These compounds show strong viscosity-dependent fluorescence and have been used to visualize the fluid shear stress on the membrane of endothelial cell layers.[3] The most representative RIR dyes for no-wash imaging are the ligands of RNA aptamer, PYP- and FAP-tags (**Section I.2.2.2**).[4-6] Examples of coupling cyanines as fluorescent antennae to malachite green of which the fluorescence can be activated by FAP has also been reported.[7, 8] Very recently, a new family of synthetic 1,3,4-oxadiazole aryl fluorosulfates has been designed to specifically bind to intraorganellar transthyretins and realize no-wash imaging in living cells and *Caenorhabditis elegans.*[9]

Besides the fluorescence restoration by RIR, dyes featuring fluorescence quenching by polarity-dependent TICT and PLICT, which is generally termed as “solvatochromism”, have also been used to develop no-wash imaging tags.[10, 11] One example is the push-pull type fluorene derivatives with excitation/emission wavelengths more red-shifted than Laurdan. These dyes show largely increased fluorescence quantum yields after moving from hydrophilic to lipophilic environments, thus being used as imaging tags for lipid domains and plasma membranes.[12] The red-region

solvatochromic dye Nile Red has also been developed into fluorogenic tags for plasma membrane imaging. It has negligible fluorescence in polar aqueous environments but is highly fluorescent after being located to apolar lipid membranes by either SNAP tagging or ligand-receptor binding.[13, 14] Application of other known solvatochromic dyes with the same strategy are also widely reported.[1, 15] Strictly speaking, this approach is not truly fluorogenic because these fluorophores are not completely dark in polar environments.

Another non-chemical strategy for no-wash labeling is to make use of aggregation-caused quenching (ACQ). Basically, the fluorophores can stack into H-aggregates or self-assemble to nanoparticles at high concentration and quench fluorescence. Yoshii *et al*. reported that by tethering TMR and an eDHFR inhibitor with a 15-carbon alkyl phenylalanine sulfonamide linker, the rhodamine-based tag can self-template into nanoparticles and have a dynamic assembly-disassembly equilibrium inside living cells. When disassembled, this tag can bind to the dihyrofolate reductase and emit green fluorescence originating from TMR.[16] Similar strategy has been applied to a Cy5 derivative.[17] Ajayaghosh's group reported an asymmetric NIR squaraine dye assembly that does not need a binding ligand. In *in vitro* studies, the NIR fluorescence is quenched due to the self-assembly and consequent ACQ. After disassembly, this squaraine dye can undergo a Michael addition with cysteine-rich proteins to trigger a green fluorescence.[18] Further progress was reported by Klymchenko and co-workers. A 3,3-dimethyl indoline-based symmetric squaraine was synthesized and made into a series of dimers with PEG linkers of different lengths that form H-aggregates in aqueous surroundings and have their fluorescence quenched. The PEGylated squaraine dimers

were tethered to carbetocin and able to bind to the oxytocin receptor overexpressed on the surface of HEK cells. After binding, the dimers were inserted into lipid layers and subsequently de-aggregate to turn on squaraine fluorescence.[19]

Alternatively, aggregation-induced emission (AIE) has been used for no-wash imaging. The non-fluorescent AIEgen TPE has been tethered to target-recognition ligands or bioorthogonal click moieties and delivered to mammalian cell membrane or inside bacteria. The AIEgen is brought to close vicinity by elevated local concentration and hence emits light.[20, 21] An interesting type of AIEgens is reported by Liu's group. In their design, ESIPT has been incorporated with AIE.[22] An acetyl group can be hydrolyzed by esterase to reveal a phenolic hydroxyl group that facilitates ESIPT to the imine of an AIE moiety at the ortho position, turning on bright and red-shifted emission. Interestingly, only the diethyl amino variant demonstrates this AIE effect because steric hindrance of the ethyl groups prevents the close stacking of the molecules that can cause π-π stacking. Accordingly, dimethyl amino variant lost this AIE.[22]

I.20.2 Fluorogenicity based on chemical modification of fluorophores

The fluorescence restoration mechanisms described in **Section I.20.1** do not involve any chemical transformation of the fluorophores. Chemical modifications of these fluorogens are solely for targeting purpose or improvement of physical properties. However, as discussed, these approaches usually cannot afford complete fluorescence quenching of the fluorogens because of the inability of a clearly differentiated local environment in living organisms. In this context, various chemical modifications are

introduced onto the fluorophore scaffolds so that the fluorescence can be quenched and reactivated in a controllable manner.

Often these modifications incorporate different photophysical mechanisms to suppress the fluorophore's emission, such as TICT for biarsenical probes like FlAsH and ReAsH.[23] A recent report by Wang *et al.* also incorporated RIR with this trivalent arsenical EDT moiety, showing that the emission of the D-A-D type benzopyrylium dye could be restored due to the high viscosity elicited in the local environment after binding of the arsenic with a vicinal dithiol peptide (VDP).[24] Spirolactonization is another commonly adopted chemical transformation on xanthene-type dyes to afford switchable fluorophore. An *ortho*-carboxyl substituted on the phenyl ring at the meso position cyclizes with the meso carbon under apolar conditions and forms a non-emissive spirolactone. In polar or low pH environment, the spirolactonization is reversed and a fully conjugated xanthene core is restored, bringing back the emission. This strategy has been applied to fluorescein, rhodamine, and silicon-rhodamine derivatives.[25, 26]

No matter how intricate the fluorogens are designed, targeting specificity is always desired but difficult. Aforementioned mechanisms incorporated for fluorogenicity are not for this purpose. In this context, fluorophores are now commonly coupled to target-recognition ligands that can quench the fluorescence and undergo designed reactions to restore their emission properties. These fluorogens are termed quenched activity-based probes (qABPs).[27, 28] The strategies being used to stop fluorescence quenching are normally enzyme-based reactions. For example, acetyl ester groups have been installed on the position 2 and 7 of fluorescein or the meso position of BODIPYs to invert the

electron-donating ability and stop emission. An esterase is able to hydrolyze the esters and correct the electron flow to restore emission.[29] A similar approach is reported to amidate rhodamine and rhodol amine groups with amino acids and later on to activate the fluorescence by carboxypeptidases.[30]

Although utilizing an enzymatic reaction to deprotect the enzyme substrate from the fluorophore scaffold is a feasible way, this approach limits the choice of dye scaffolds since a chemical modifiable functional group is necessary with the requirement that its presence can quench fluorescence. Therefore, a more general strategy to develop fluorogens is to append a quencher group onto the fluorophore. Consequently, a variety of quenching mechanisms have been applied to design the quencher part.

FRET has been applied in the early designs as quencher groups. In many qABPs, a second dye or a black-hole quencher that has spectral overlap with the observing dye is tethered with the reporter by a lengthy linker, which also contains an enzyme reactive motif. Numerous FRET-based fluorogens have been published to probe the activities of different enzymes.[31] For a broad application scope, SNAP-tag has been developed into FRET-based qABPs.[32] Recently, AIEgen has also been successfully incorporated to FRET-qABPs to image caspase activity.[33]

FRET is a long-range energy transfer process. From a fundamental point of view, Förster resonance energy transfer is facilitated by dipole-dipole interaction, or a Coulombic interaction. Basically, the excited donor *D with an excited electron can undergo periodic harmonic oscillations along the molecular framework, creating an oscillating electric dipole. In turn it produces an oscillating electric field in the space

around *D, which in classical theory can drive a nearby acceptor A into resonance with matched oscillating frequency in its natural excited state. This frequency matching prerequisite is described by spectral overlap and sufficient oscillating strength. Because the energy transfer efficiency decrease is inversely proportional to the sixth power of the distance between donor (D) and acceptor (A), it usually requires this distance to be within 1-10 nm, which makes the linker lengthy. Besides, the requirement for spectral-overlapped donor-acceptor pair also limits the choice of reporters.

On the other hand, in contrast to the long-range Förster-type energy transfer, Dexter energy transfer (DET) features a short-range energy transfer process between donor and acceptor. Different from the transition allowed Förster process, for forbidden transition the Coulombic interaction is negligible and energy transfer is due to the electron

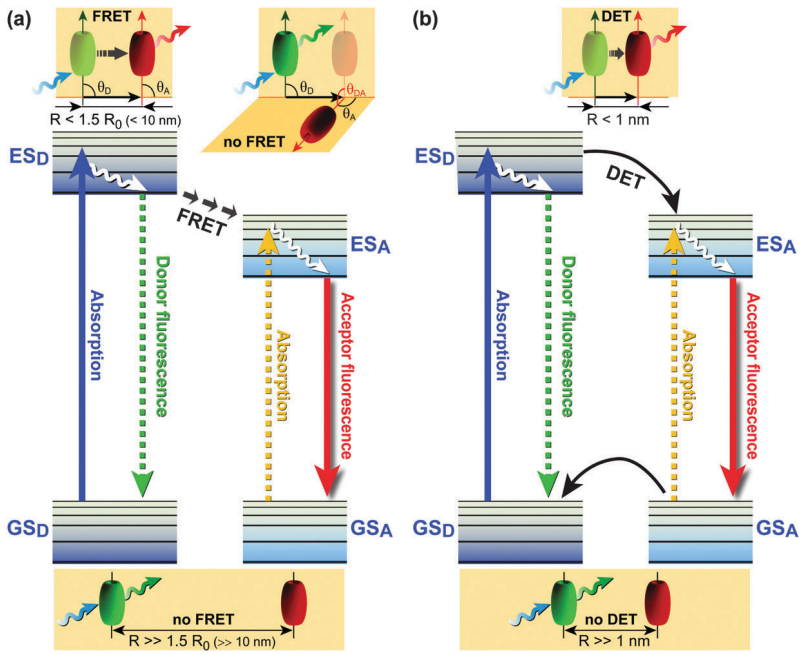


Figure 0-1 Jabloński diagrams of various energy/electron donor-acceptor (D-A) systems. a) Förster Resonance Energy Transfer (FRET). θ: angle between donor emission and acceptor absorption. b) Dexter Energy Transfer (DET). Artwork copied from ref [10].

energy transfer through orbital wavefunction overlap, of which the rate decreases exponentially to the distance between donor and acceptor. Thus, the effective energy transfer distance is smaller than 1 nm, making the design of the fluorogen more compact (**Figure IV-1**). Weissleder and co-workers have attached a clickable tetrazine to coumarins for standard bioorthogonal *trans*-cyclooctene labeling. The emission of coumarins is quenched by this tetrazine moiety and can be restored after click reaction. Mechanistically, the fluorescence intensity of these native fluorogens is independent of solvent polarity, indicating the pivotal role of Dexter-type through-bond energy transfer (TBET).[34]

It should be noted that, both Förster and Dexter theories predict a direct dependence on spectral overlap integral and require orbital orientation. However, in the recent decade, modifications of Dexter theory for short-range intramolecular electron energy transfer have been derived and manifested experimentally. These include orientational-dependent exchange interaction, super exchange, and more generally through-bond interaction (a.k.a. TBET), where energy transfer happens with D and A separation much larger than the sum of their van der Waals radii while selection rule exclude the possibility of dipole-dipole interaction. This type of intramolecular electron energy transfer is especially efficient in rigidly linked Donor-bridge-Acceptor molecules whereas the D-A distance is greater than 1 nm for dipole-dipole forbidden processes. Detailed discussion and description of these physical processes is beyond the scope of this research. Interested readers are referred to Speiser's review article and Turro's book of photochemistry.[35, 36] Pioneered by Kevin Burgess' research group, this type of through

bond interaction has been utilized to develop various through bond energy transfer cassette for fluorescent molecules with large pseudo-Stokes shift, as well as different analytes sensing systems.[37] This TBET process has also been applied as quenching mechanism and expanded to tetrazoles and different dye scaffolds, including BODIPY, Acedan and xanthenes.[38, 39]

Different from excited state energy transfer, static quenching involves ground-state complexation of the emitter and an absorber, which is usually substituted aryls or amines. This particular quenching mechanism has been applied to the development of second and third generation no-wash PYP-tags. The PYP ligand-tethered emitter can form a ground-state complex with the cinnamic acid ligand or a nitrobenzene moiety to have its emission diminished. After binding with PYP-tag, the complex is dissociated, and the emission is restored.[40, 41] A similar design was reported for a Golgi-targeting “on-off” COX-2 probe based on folding and unfolding between ANQ and indomethacin.[42]

Without either the need for spectral or wave function overlap, or ground state complexation, photoinduced electron transfer (PeT) is the most widely adopted quenching mechanism for the design of fluorogens.[43-45] Basically, the emitter is tethered to a quencher moiety via a covalent and non-conjugated spacer. An enzymatic ligand can be incorporated to the spacer so that the quencher is removed after enzymatic digestion, hence the emission is restored. The quencher can also be designed as part of the recognition unit of the peptidic or proteic labeling tag. Upon binding, a specifically placed nucleophile inside the peptidic/proteic tag can react with the quencher and stop the quenching process (for example see **Figure I-19**).

There are two related mechanisms of PeT. The first one involves the participation of an empty low-lying orbital of the quencher (**Figure IV-2a**). Briefly, after the HOMO electron of the fluorophore is excited into the corresponding LUMO, instead of the radiative decay back to the HOMO that gives fluorescence, the excited electron is transferred to the empty orbital of the quencher moiety, thereby leading to the fluorescence quenching. The electron can later on be transferred back to the HOMO of fluorophore following a nonradiative path to restore the stable ground state. Alternatively, a high-lying filled quencher orbital can also participate in a PeT mechanism. As shown in **Figure IV-2b**, the filled high-lying quencher orbital can transfer one electron to the excited HOMO of fluorophore, therefore stopping the radiative decay pathway. The excited electron in the LUMO of the fluorophore can transfer back to the emptied quencher orbital nonradiatively to form the stable ground state.

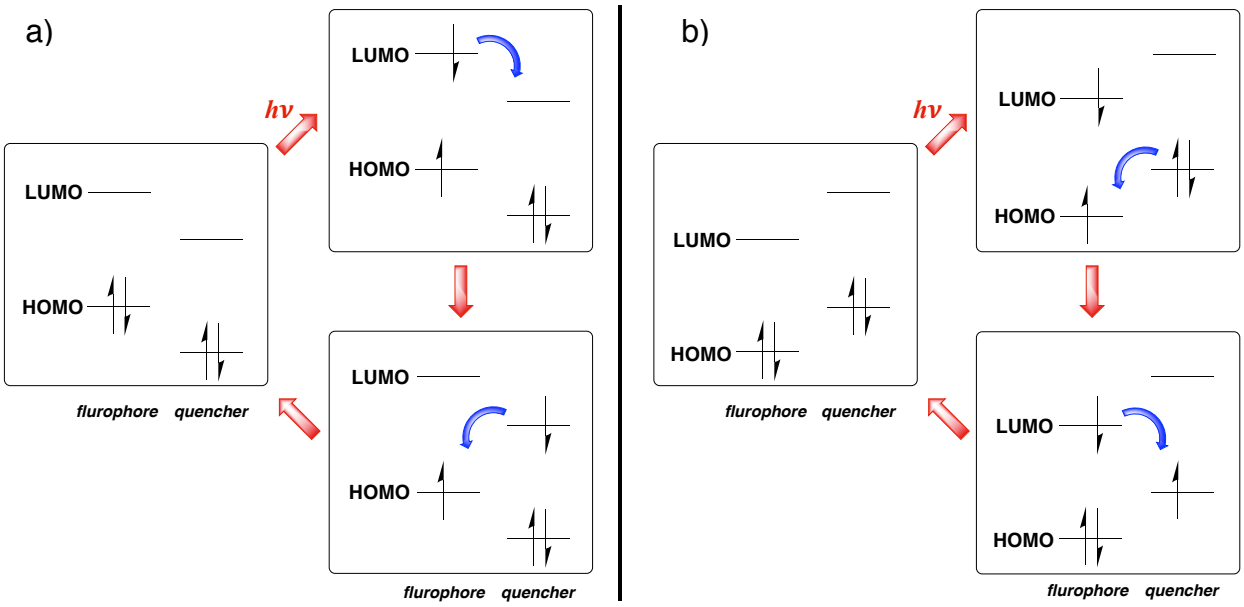


Figure 0-2 PeT mechanisms. a) Participation of fluorophore HOMO-LUMO and an empty quencher orbital. b) Participation of fluorophore HOMO-LUMO and a filled quencher orbital.

Because the fluorophore and the quencher are electronically coupled to each other weakly, PeT provides freedom to select the proper fluorophore and quencher pairs. During recent decades, numerous reports of utilizing PeT have emerged for the development of fluorescent “on-off” tags and probes.[46] PeT has also been incorporated with other photophysical/photochemical mechanisms to develop probes, such as ESIPT, spirocyclization, and ICT, etc.[47-49] There is a wide scope of PeT quencher parts, depending on the match of redox potential with the fluorophores. The common ones include nitrophenyl, trifluoroacyl, anisole,[50] aryl aldehydes,[51] aryl amines,[52] quinone,[53] indanedione,[54] and maleimide,[55] piperidine,[56-58] to name a few. Even β-Gal has been used as a PeT quencher for fluorescein.[59]

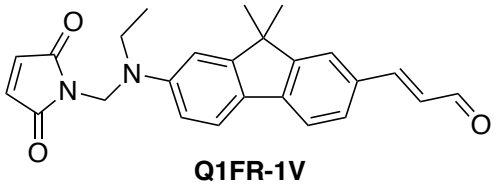
From a publication view, the most important and prevailing quencher is the maleimide. Besides, the maleimide group has been widely used in bioconjugation reactions of various functional molecules with targeting peptides or proteins via a thiol-initiated Michael reaction. An impressive design is reported by Keillor’s group, where a coumarin is attached with two substituted maleimide quenchers to yield PeT fluorescence quenching. Taking a strategy similar to biarsenical FlAsH, the two maleimides bind with the adjacent cysteines of the VDP and have their LUMO elevated, capable of stopping PeT quenching and regenerating coumarin fluorescence (see **Section I.3.4** and **Scheme I-8c**).[60] Maleimide’s quenching mechanism has been substantially investigated.[61, 62] Two maleimide moieties were attached on a dansyl fluorophore. A laser flash photolysis study showed that there was no triplet-state deactivation of the excited dansyl, excluding the possibility of intersystem crossing (ISC). A low-temperature fluorescence intensity study

at 77K further excluded the possible quenching by internal conversion (IC). Both steady-state and time-resolved Stern-Volmer analysis proved the dynamic quenching nature of this maleimide quenching and validated its electron-transfer nature. A further validation was performed by the quenching efficiency change of *meso*-aryl substituted tetramethyl BODIPYs with maleimide installed on the *ortho*-, *meta*-, and *para*-positions of the aryl group. As expected, a distance-dependent fluorescence quenching of the BODIPY was observed, with the *ortho*-substitution as the most quenched variant, further manifesting the electron-transfer nature of the maleimide quenching.[63]

I.21 Designing a PeT-quencher tethered FR0 as a dark stain

Since **FR-1V** demonstrates outstanding properties as a fluorescent lead in many aspects, a maleimide PeT quencher tethered with **FR-1V** is directly proposed following the discussion in **Section 0** as a starting point (**Figure IV-3**). As shown, a maleimide is covalently tethered to the donor amine group of **FR-1V** through a methylene unit. Hence, the PeT quencher part is kept close to the fluorophore and has the flexibility to facilitate the desired energy transfer process.

A DFT calculation was performed with **Q1FR-1V** in vacuum with the basis set 6-31+G to roughly estimate the feasibility of PeT quenching with this scaffold. A further TD-DFT calculation will be necessary to more accurately gauge the orbital distribution in different solvents. The *n*-butylimine and *n*-butyliminium derivatives of **Q1FR-1V** were also



Q1FR-1V

Figure 0-3 Structure of model PeT-quenched **FR** fluorophore.

calculated for their energy diagrams to check the feasibility of PeT quenching. The results are plotted in **Figure IV-4**. For the free aldehyde **Q1FR-1V**, the HOMO and LUMO+1 orbitals reside on the fluorophore framework while the LUMO localizes on the maleimide moiety. This indicates the potential donor-type PeT mechanism (**Figure IV-2a**) as the HOMO electron will populate the LUMO+1 orbital after local excitation and subsequently relaxes into the LUMO on the maleimide. DFT calculation of the *n*-butylimine analog (denoted as **Q1FR-1V_SB**) showed that the relative positions of the HOMO, LUMO, and LUMO+1 remain the same. This is exciting because it indicates the feasibility of PeT

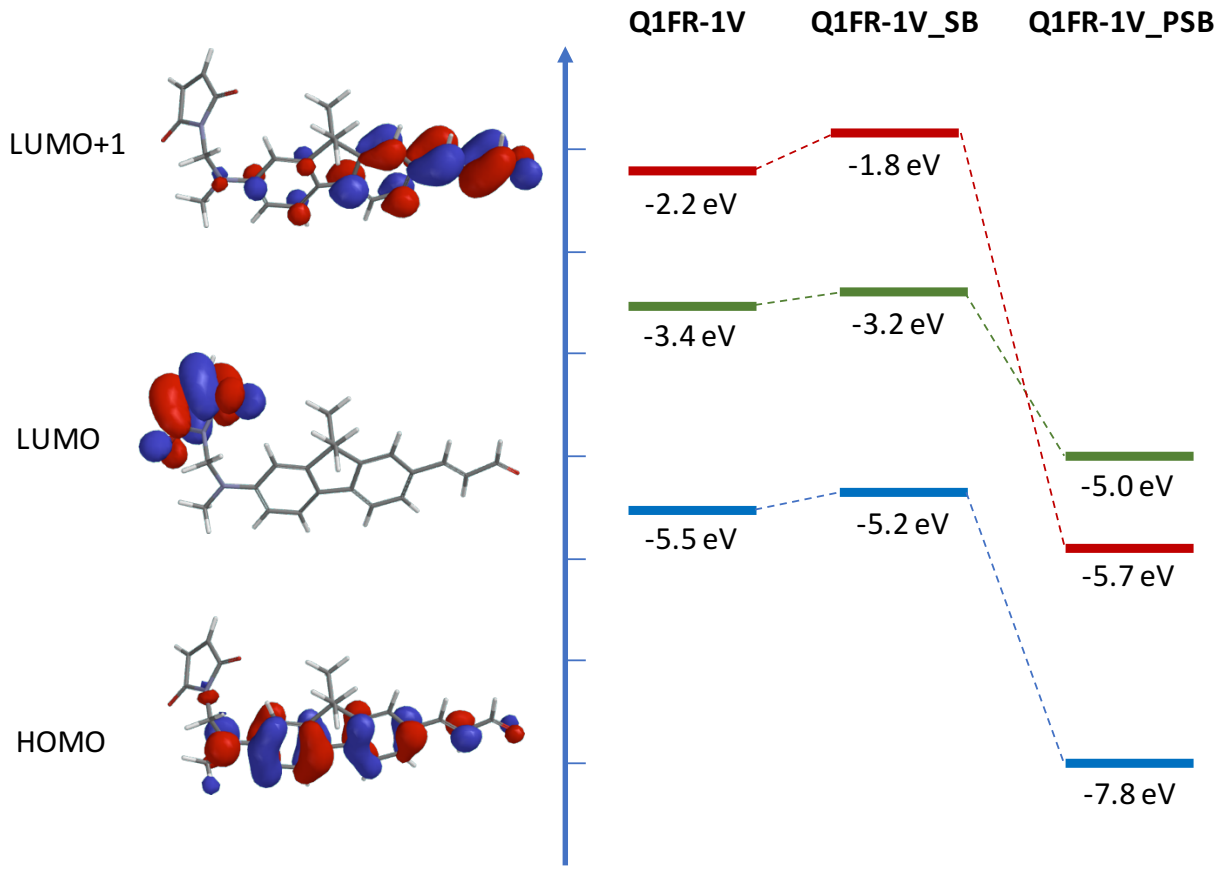


Figure 0-4 Orbital diagram of **Q1FR-1V** and the corresponding *n*-butylimine (**Q1FR-1V_SB**), *n*-butyliminium (**Q1FR-1V_PSB**), calculated with DFT/B3LYP/6-31+G in vacuum. The orbital views on the left side are of **Q1FR-1V**. The color code of the right-side energy diagram is: blue (HOMO of **FR-1V/SB/PSB**), green (LUMO of maleimide), and red (LUMO of **FR-1V/SB/PSB**).

quenching of any protein-bound fluorophore in the SB form, regardless of specific or non-specific binding, if the environmental effects are ignored. Therefore, this simple maleimide quencher can potentially eliminate the non-specific fluorescence background from both the residing free aldehyde after staining and the non-specific imines formed with other proteins *in vivo*. The energy diagram of the *n*-butyliminium analog (denoted as **Q1FR-1V_PSB**) was further calculated to examine the PeT quenching ability of the NIR emission of **FR-1V** if any non-specific PSB were to be formed. The DFT results show that under protonation the LUMO and LUMO+1 change order, therefore none of the donor-PeT or the acceptor-PeT would be operational.

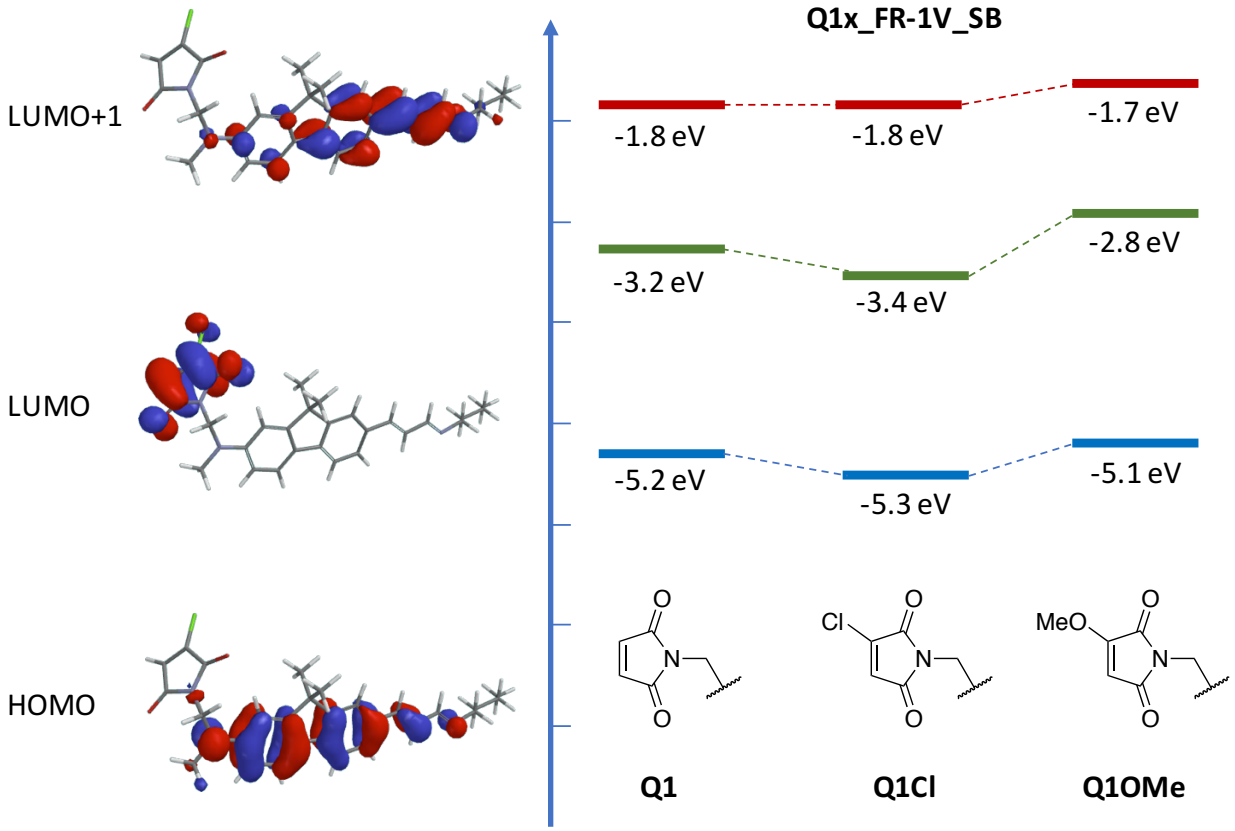


Figure 0-5 Orbital diagram of the *n*-butylimine of **FR-1V** tethered with maleimides bearing different substituents. Left-side orbital views are shown with non-substituted maleimide. The color code on the right-side diagram is: blue (HOMO of **FR-1V_SB**), green (LUMO of maleimides), and red (LUMO of **FR-1V_SB**).

The quenched fluorophore **Q1FR-1V** is supposed to react with a specifically engineered cysteine residue inside the binding cavity of hCRBPII to achieve fluorescence recovery, and hence labeling specificity. Non-substituted maleimide is quite reactive towards different nucleophiles in biological settings and lacks chemoselectivity. In view of this, substitution on the maleimide will be necessary to temper its reactivity. As such, chlorine- and methoxy-substituted maleimides are calculated to roughly represent the EWG- and EDG-modified maleimides. Shown in **Figure IV-5**, there is no change in the relative order of LUMO and LUMO+1 of quencher-tethered **FR-1V** *n*-butylimine. Further calculation was performed to screen a broader scope of substituents for one that

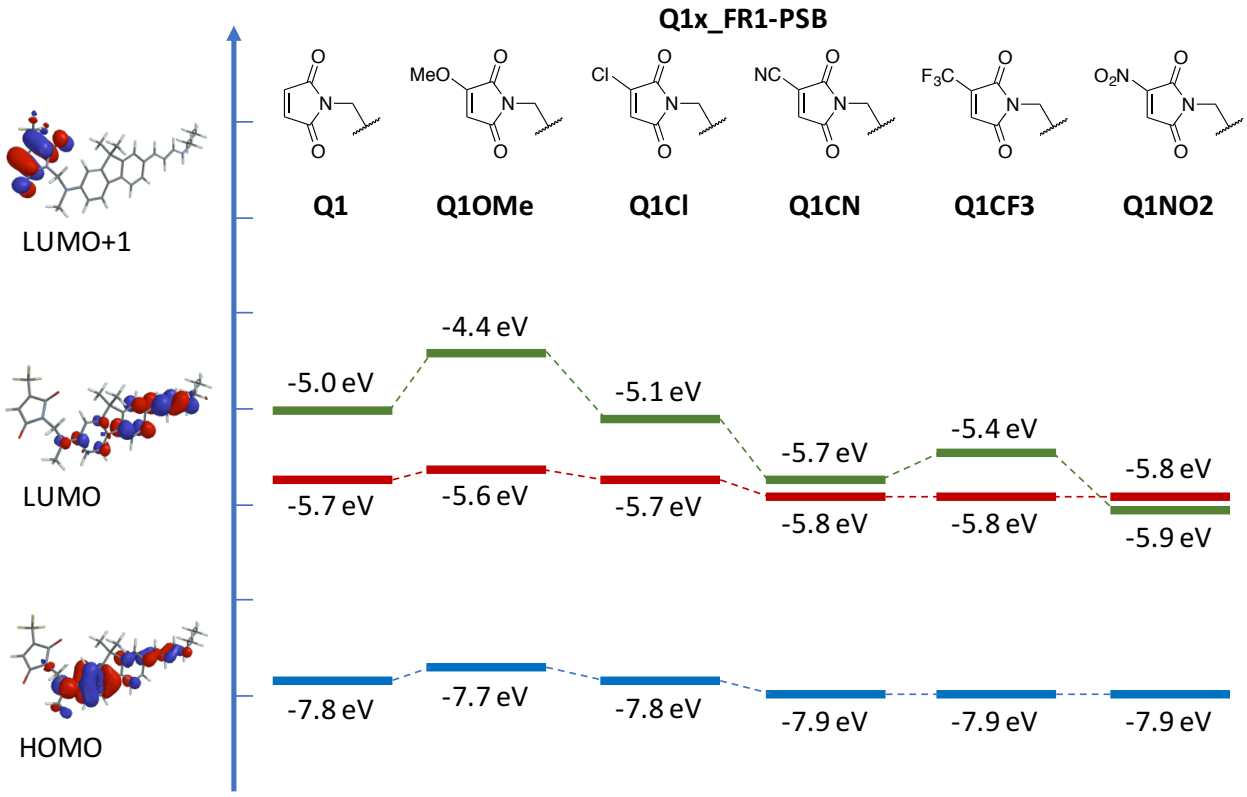
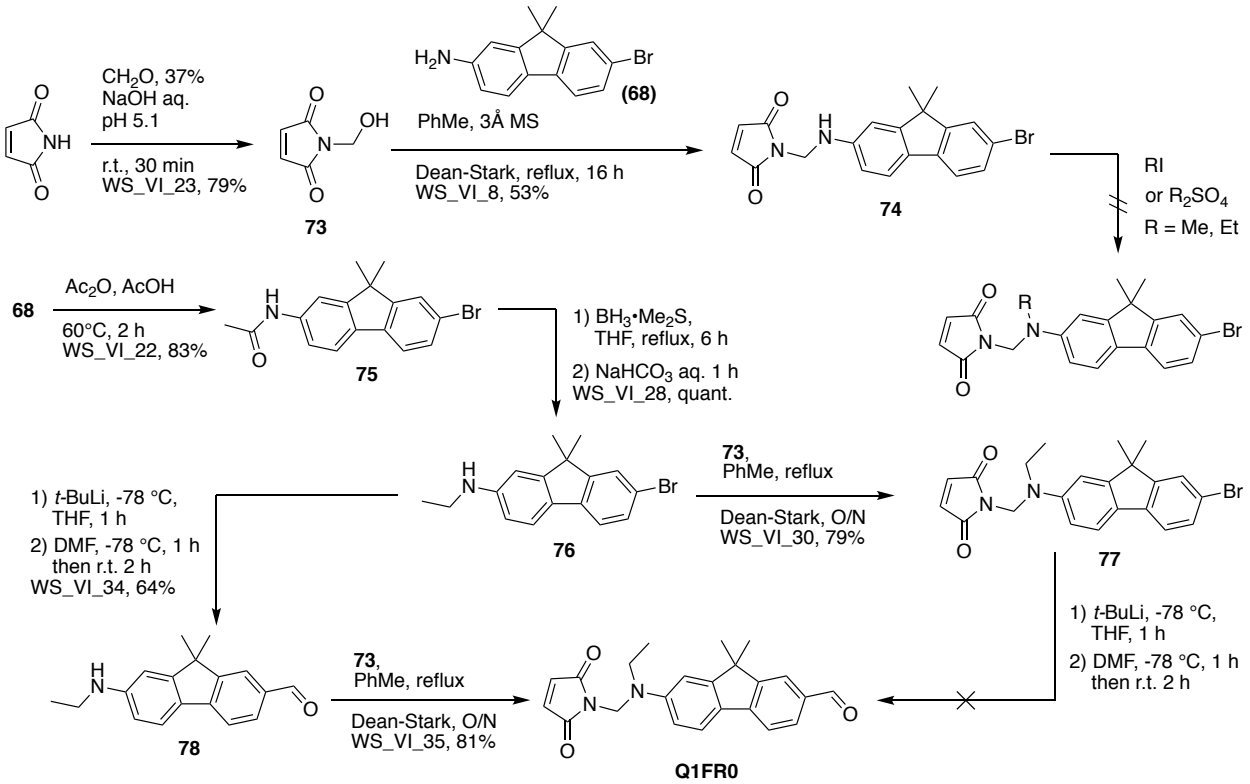


Figure 0-6 Orbital diagram of the *n*-butyliminium of **FR-1V** tethered with maleimides bearing different substituents. Left-side orbital views are shown with non-substituted maleimide. The color code on the right-side diagram is: blue (HOMO of **FR-1V_PSB**), green (LUMO of maleimides), and red (LUMO of **FR-1V_PSB**).

potentially quenches the PSB emission. As shown in **Figure IV-6**, when protonated as iminium, the order of LUMO orbitals of **FR-1V_PSB** and maleimides are inverted except for the maleimide substituted with strongly electron withdrawing nitro group. In another word, except for the nitro-substituted maleimide, all the other maleimides cannot quench the fluorescence of **FR-1V_PSB** through the PeT process. However, the nitro substituent on the maleimide will greatly increase its electrophilicity and thus decrease chemoselectivity.

To test the feasibility of PeT quenching, **Q1FR0** was synthesized to tether a non-substituted maleimide to the amine group of **FR0** via a methylene unit (**Scheme IV-1**). DFT calculation showed that even with a higher HOMO of **FR0** and its corresponding *n*-butylimine SB, the relative order of the maleimide HOMO did not change (data not shown).



Scheme 0-1 Synthesis of **Q1FR0**.

To synthesize **Q1FR0**, initially *N*-hydroxymethyl maleimide **73** was coupled with **68** through an S_N2 reaction using a Dean-Stark apparatus. Nonetheless, the subsequent alkylation of the secondary amine **74** was not successful with either methyl iodide, ethyl iodide, or dimethyl sulfate, only yielding over alkylated byproducts. Arylamine **68** was subjected to acylation and borane reduction to afford **76**. The monoethyl amine was then coupled with **73** to install the *N*-methylmaleimide. After obtaining **77**, a metal-halogen exchange and subsequent formylation were attempted to furnish **Q1FR0,** but met with no success. The maleimide group could not tolerate the strong alkali condition. Instead, **76** was first formylated, and then coupled with **73** to afford **Q1FR0**.

Compared to the original **FR0**, the absorption and emission spectra of **Q1FR0** are slightly blue shifted as recorded in ethanol (**Figure IV-7**). The absorption maximum is at 375 nm, 20 nm blue-shifted as compared to **FR0**. The emission maximum is at 535 nm when excited at 375 nm, also 20 nm more blue. The extinction coefficient of **Q1FR0** is 31,600 $M^{-1}\cdot cm^{-1}$, which is smaller than the 43,000 $M^{-1}\cdot cm^{-1}$ calculated for **FR0**.

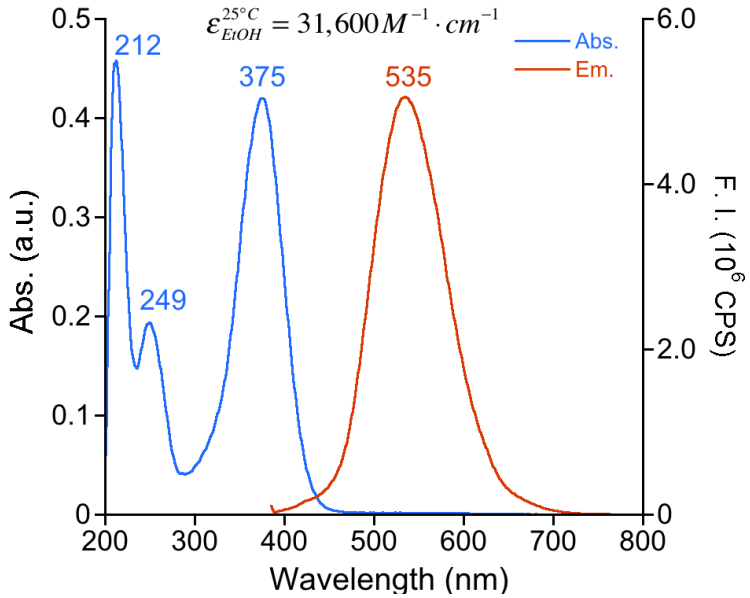


Figure 0-7 Extinction coefficient, absorption and emission spectra of **Q1FR0** in ethanol.

Shown in **Figure IV-8**, *n*-propane thiol was used as the surrogate of cysteine to react with **Q1FR0** and check the propensity of fluorescence recovery after stopping the PeT quenching. Excess equivalent of *n*-propane thiol was added to a solution of **Q1FR0** in ethanol at ambient temperature. As expected, a more than 4-fold increase in the fluorescence intensity was observed. The reaction with *n*-propane thiol was rapid and the aldehyde group remained intact.

Next, the fluorescence recovery was recorded with two sequential additions of *n*-butylamine and *n*-propane thiol. Shown in **Figure IV-9a**, **Q1FR0** was first subjected to the Michael addition with *n*-propane thiol. After the maximal fluorescence recovery of the aldehyde was obtained, excess amount of *n*-butylamine was added to probe the fluorescing ability of **Q1FR0** upon imine formation. A gradual formation of the *n*-butylimine was observed over 1 h and was similar to the binding mode of **Q1FR0** with just *n*-butylamine, indicating the least interference of the maleimide moiety on the imine condensation (**Figure IV-9b, c**). Not surprisingly, excitation at 357 nm resulted in the signature dual emission featuring the regular short-wavelength SB emission at 443 nm

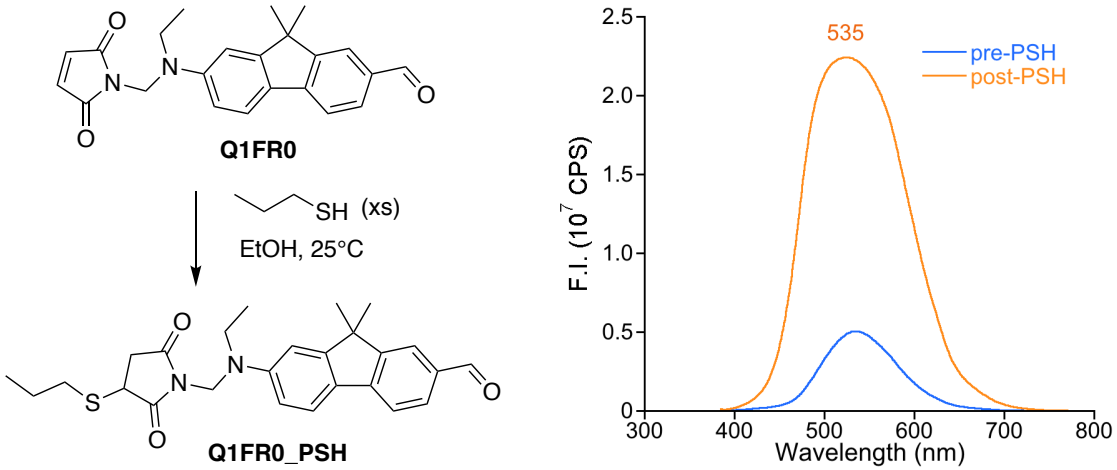


Figure 0-8 Fluorescence recovery of **Q1FR0** after addition of *n*-propane thiol (PSH).

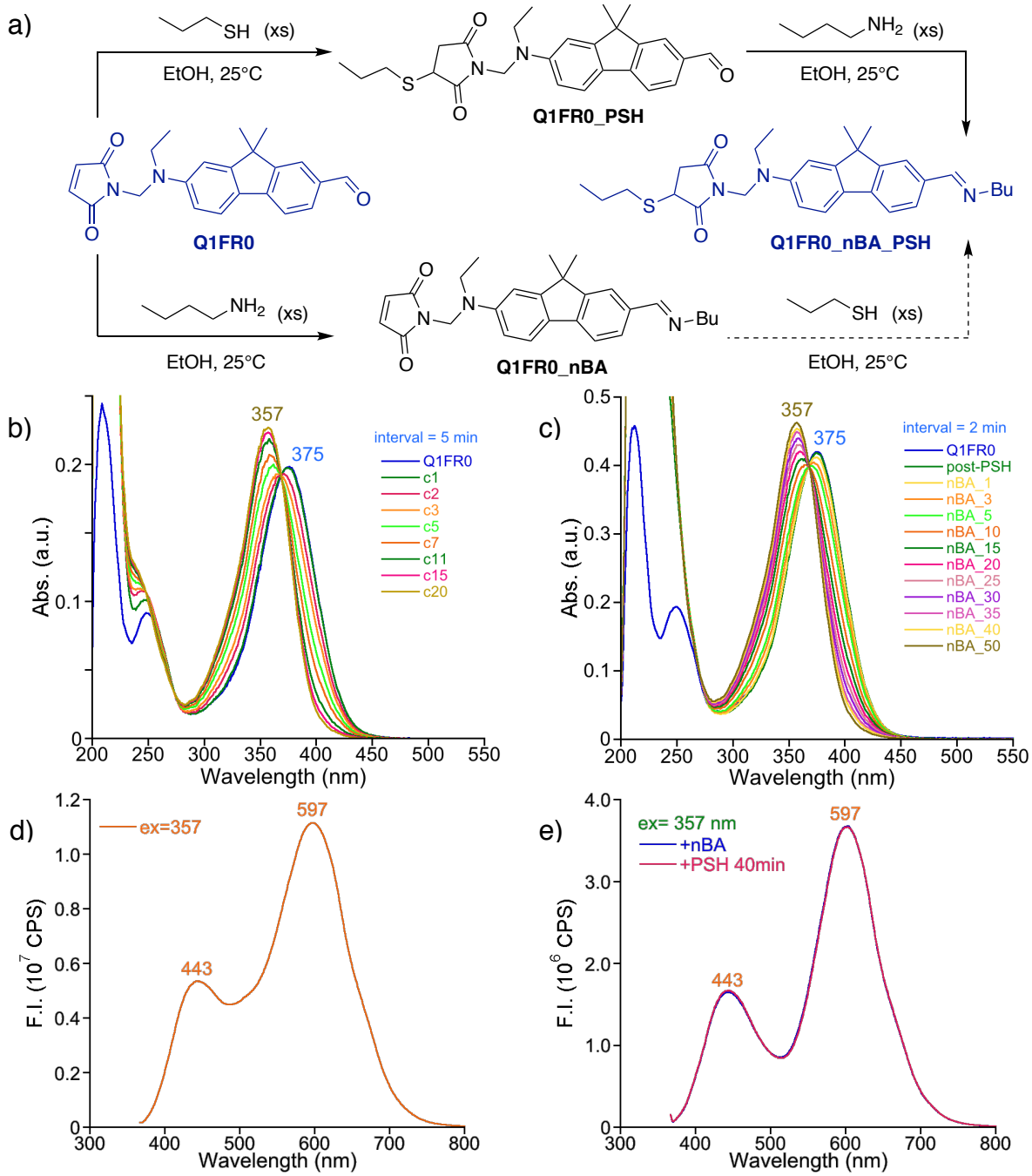


Figure 0-9 Fluorescence recovery of **Q1FR0** tested by sequential addition of *n*-butylamine (nBA) and *n*-propane thiol (PSH) in different order. a) Reaction scheme of two sequential addition orders. b) Stacked traces of time-dependent absorption of **Q1FR0** after addition of excess nBA. c) Stacked traces of time-dependent absorption of **Q1FR0_PSH** adduct after addition of excess nBA. b) and c) showed the same timescale of imine condensation of nBA with **Q1FR0** and **Q1FR0_PSH**. d) Emission spectrum of **Q1FR0** after the sequential addition of PSH then nBA. e) Emission spectrum of **Q1FR0** after the sequential addition of nBA then PSH. d) and e) were recorded with the same concentrations of **Q1FR0**, PSH, and nBA.

and the long-wavelength ESPT emission at 597 nm (**Figure IV-9d**). However, when the

addition order of *n*-propane thiol and *n*-butylamine was reversed (**Figure IV-9a**), the addition of *n*-propane thiol no longer elicited any fluorescence enhancement even after 40 min (**Figure IV-9e**). The results suggested that when excess amount of *n*-butylamine was initially added, both the maleimide and the aldehyde were reacted. Because the two experiments were carried out with the same concentrations of **Q1FR0**, *n*-propane thiol, and *n*-butylamine, the ESPT emission intensity at 597 nm lead us to speculate that the maleimide reacted with *n*-butylamine. In **Figure IV-9d**, the fluorescence intensity was ca. 10^7 CPS and should be considered as the maximal intensity of the non-quenched imine fluorescence. While in **Figure IV-9e**, the corresponding fluorescence intensity was 3 times less. It is clear that *n*-propane thiol could not react with the maleimide, since *n*-butylamine had already reacted, and the Michael product with *n*-butylamine could also partially stop the PeT quenching but not to the full extent.

The reason for the poor resolution of the 443-nm and 597-nm peaks in **Figure IV-9d** was not clear. **Q1FR0** has low stability in protic solvents. Shown in **Figure IV-10a**, equal amount of **Q1FR0** was dissolved in ethanol and DMSO and samples were kept

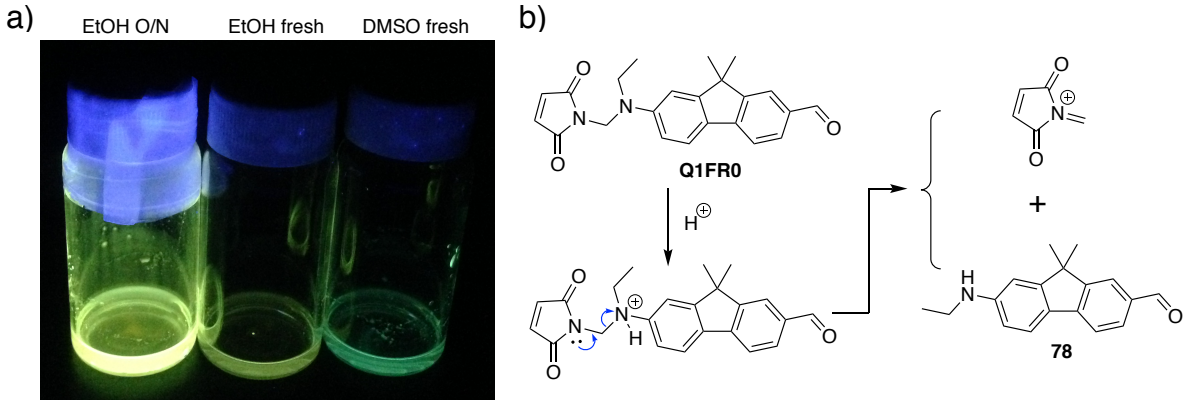


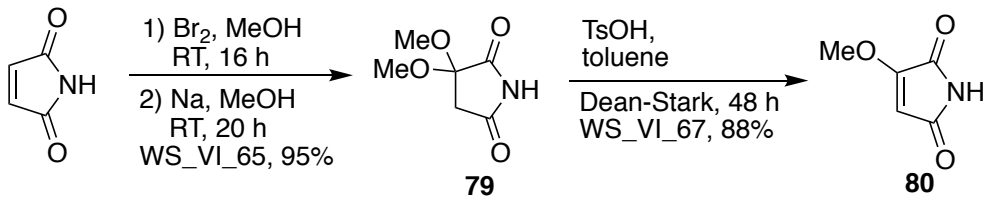
Figure 0-10 Low stability of **Q1FR0**. a) Picture shows the fluorescence of **Q1FR0** samples stored in ethanol at 4 °C overnight (O/N), freshly prepared in ethanol and DMSO. Samples are excited with UV handset. b) Possible degradation pathway.

under different conditions. When excited with a 365-nm UV-light handset, the freshly-made samples showed dim green fluorescence (peak at 535 nm). However, an overnight sample stored in ethanol, even at 4 °C, led to significant increase in fluorescence intensity. A degradation pathway similar to Hofmann elimination is plausible (**Figure IV-10b**).

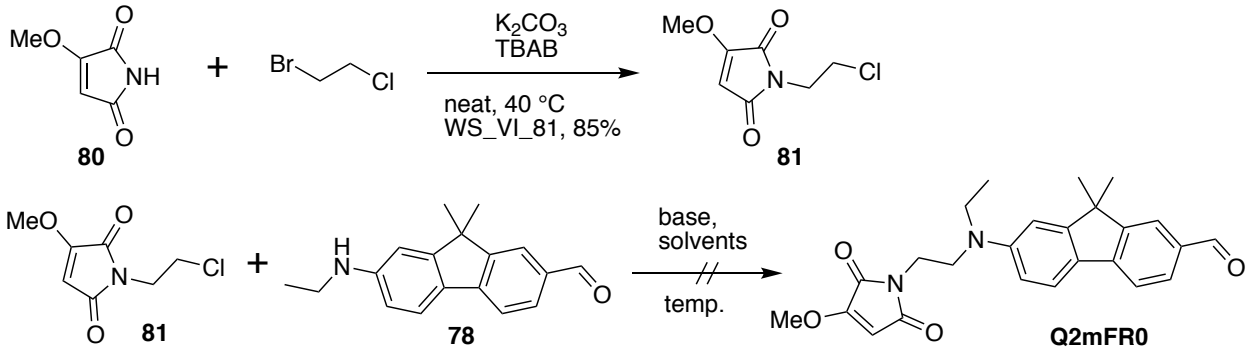
I.22 Modification of the maleimide quencher and *in vitro, in vivo* studies

A second version of donor-PeT quenched fluorophore **Q2mFR0** was synthesized. The maleimide moiety was substituted with a methoxy group to decrease the reactivity towards amines, and the methylene linker connecting the maleimide and **FR0** was extended to an ethylene unit to prevent Hofmann-type elimination. The synthesis started with methoxybromination of maleimide, followed by alkaline elimination in methanol. Concomitantly, methoxide addition to the target molecule **80** happened in the strongly basic condition. Separate acidic elimination was carried out to re-introduce the double bond (**Scheme IV-2**).

3-Methoxy maleimide **80** was then chloroethylated on the nitrogen with 1-bromo-2-chloroethane to give **81**, which was then subjected to an S_N2 reaction with **78** for obtaining **Q2mFR0**. However, use of various bases and solvents under different temperatures failed to deliver the product, returning the starting material **78** (**Scheme IV-3**). The more reactive *N*-bromoethyl maleimide **82** was prepared in a similar manner

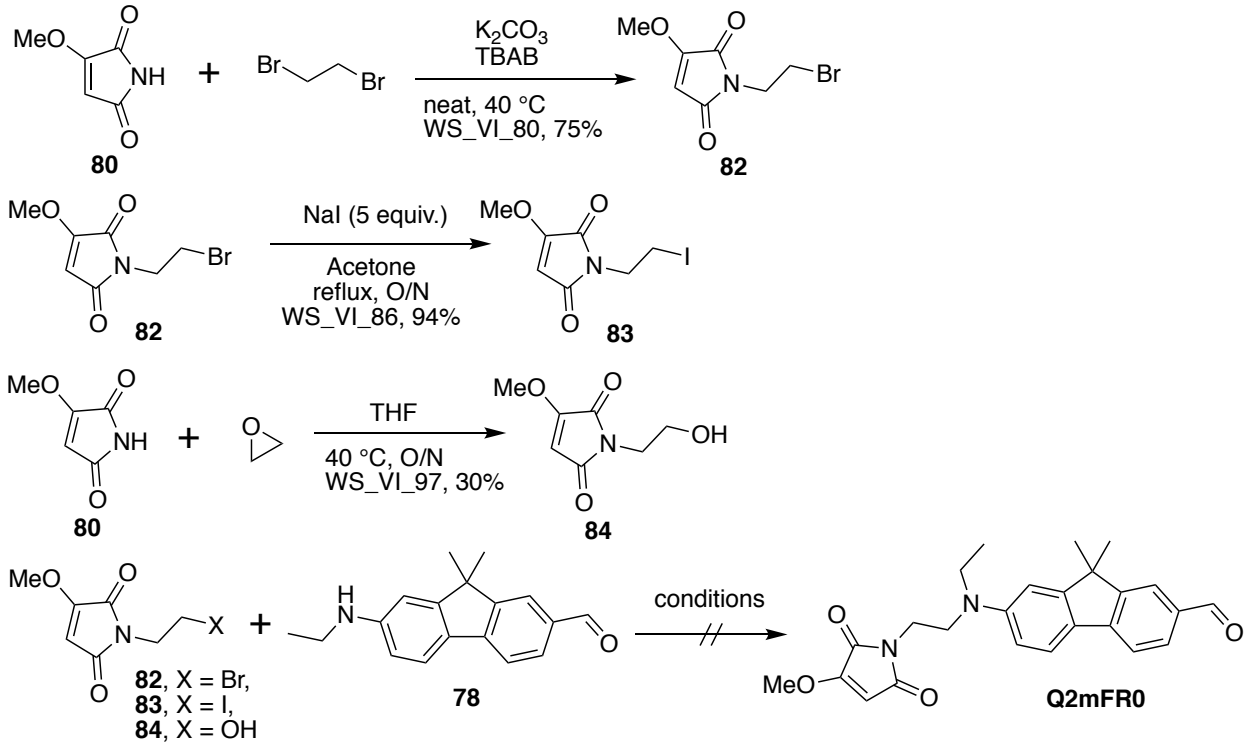


Scheme 0-2 Synthesis of 3-methoxy maleimide.

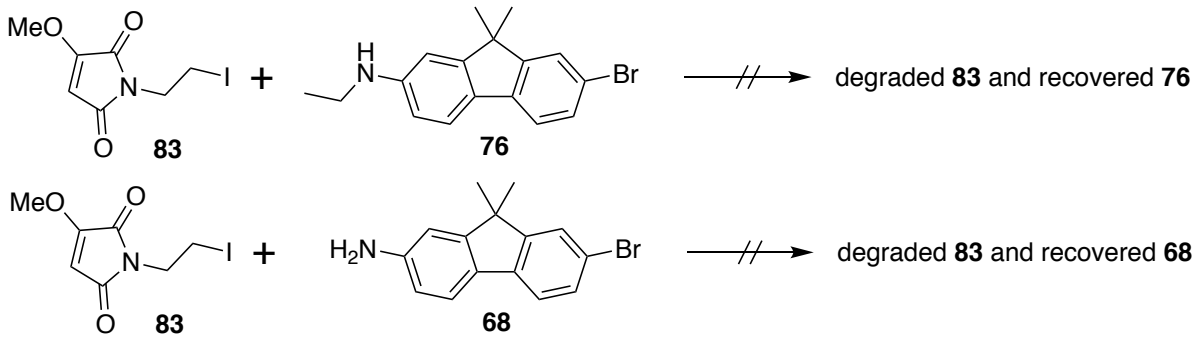


Scheme 0-3 First attempt to synthesize **Q2mFR0**.

and was used to couple with **78**. The *N*-bromoethyl maleimide **82** was also subjected to the Finkelstein halogen exchange reaction to yield *N*-iodomethyl maleimide **83**. *N*-hydroxyethyl maleimide was prepared via the reaction of maleimide with ethylene oxide. Nonetheless, none of these functionalized *N*-ethyl maleimides found success in coupling with **78**, results in degraded maleimides and recovered **78** (**Scheme IV-4**). To trouble-



Scheme 0-4 Attempts to synthesize **Q2mFR0** with different functionalized *N*-ethyl maleimides.

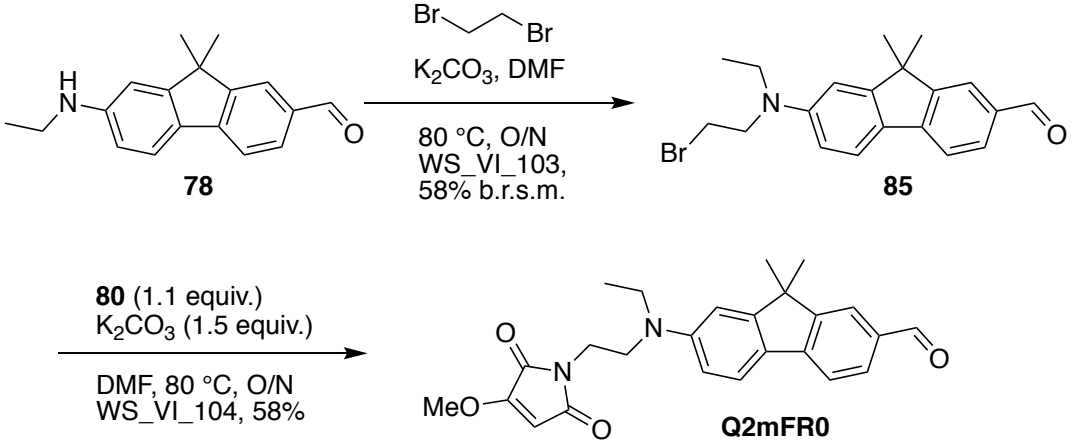


Scheme 0-5 Testing S_N2 reactions of maleimide **83**.

shoot the reactivity problem, precursors of **78**, **76** and **68**, were reacted with **83**, respectively (**Scheme IV-5**). Surprisingly, even with the least sterically hindered **68** did not succumb to the reaction. Possibly, these functionalized *N*-ethyl maleimides are not stable enough to allow the nucleophilic attack of fluorenyl amines.

Knowing this, the synthesis of **Q2mFR0** was redesigned via the stepwise modifications of the fluorene part. Bromoethylation of **78** proceeded with low conversion rate and yielded with the alkyl bromide **85**. The S_N2 reaction of **85** with maleimide **80** furnished **Q2mFR0** with a moderate yield (**Scheme IV-6**).

Compared to **Q1FR0**, **Q2mFR0** has a slightly higher extinction coefficient (32,000 $M^{-1} \cdot cm^{-1}$). The absorption centers at 388 nm and is 13 nm red-shifted as compared to



Scheme 0-6 Final synthesis of **Q2mFR0**.

Q1FR0. Correspondingly, the emission maximum is at 543 nm and is 8 nm red-shifted (**Figure IV-11a**). When different amounts of *n*-propane thiol were added, no change was observed over time in the absorption spectra (**Figure IV-11b**). Contrarily, the emission intensity displayed a significant increase after the addition of thiol, validating the feasibility of the same donor-PeT quenching (**Figure IV-11c**). The fluorescence recovery ratio was quantified with two metrics. Shown in **Figure IV-11d**, the recovery ratio was measured in the absolute height of the emission maximum at 543 nm, giving a 9.3-fold increase after thiol addition. Alternatively, a more accurate measurement was done with the integration

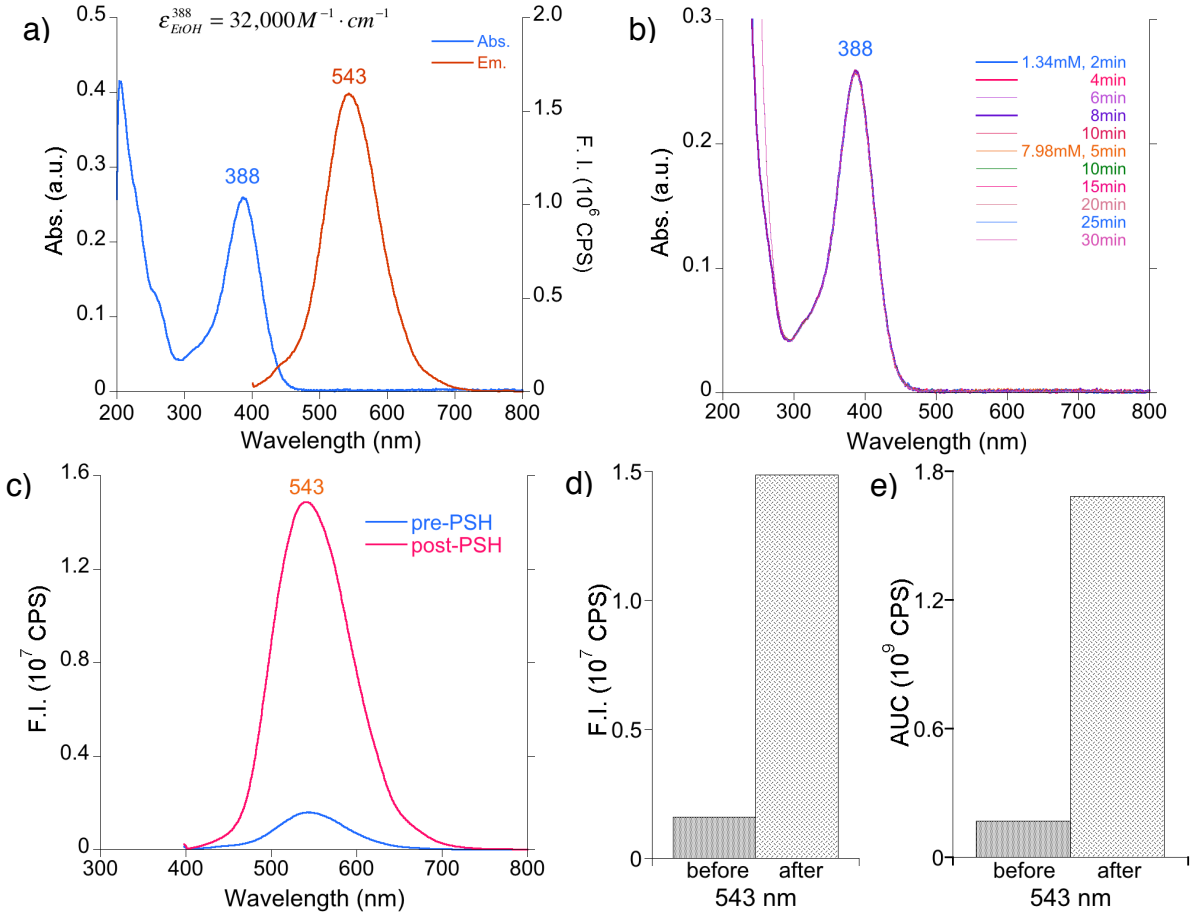
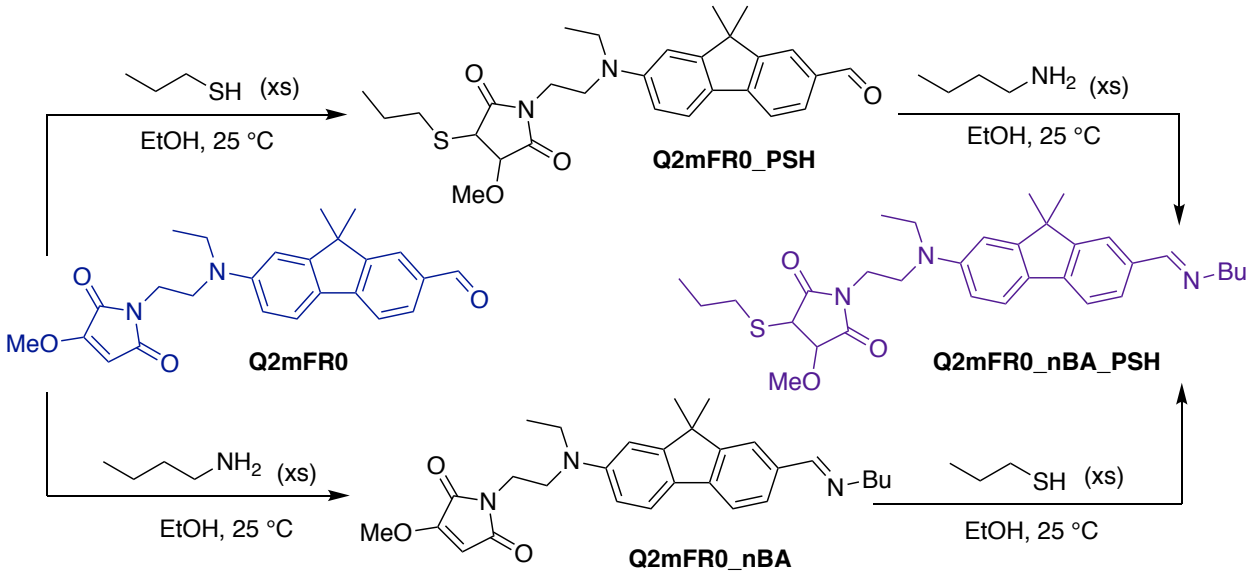


Figure 0-11 a) Absorption and emission spectra of **Q2mFR0** in ethanol. b) Stacked absorption traces of **Q2mFR0** added with *n*-propane thiol (PSH) over time. c) Emission spectra of **Q2mFR0** before and after addition of *n*-propane thiol. d) Fluorescence recovery measured peak intensity. e) Fluorescence recovery measured by whole spectra integration.

of overall fluorescence spectra, resulting in a 9.9-fold increase after thiol addition (**Figure IV-11e**). With either measurement, greater than 90% PeT quenching efficiency was validated.

The chemoselectivity was again tested via different addition sequences of *n*-butylamine and *n*-propane thiol (**Scheme IV-7**). The *n*-butylimine formations of **Q2mFR0** before and after reaction with *n*-propane thiol effectively have the same binding kinetics. The thiol adduct of **Q2mFR0** did not change the absorption spectrum of the *n*-butylimine as evidenced by the same absorption maximum (**Figure IV-12a**, **b**). Two samples of **Q2mFR0** in ethanol were used to react with *n*-butylamine, or first with *n*-propane thiol then *n*-butylamine, respectively. Both exhibited the signature ESPT emission of **FR0** at 620 nm along with the regular imine emission at 450 nm (**Figure IV-12c**, **d**). It should be noted that equal amount and concentration of **Q2mFR0** were used in the two samples, therefore a direct comparison of fluorescence intensity at the peak maxima should reveal



Scheme 0-7 Chemoselectivity and fluorescence recovery of **Q2mFR0** with sequential addition of *n*-butylamine (nBA) and *n*-propane thiol (PSH). a) PSH then nBA. b) nBA then PSH.

the PeT quenching efficiency for both imine and iminium fluorescence. With the addition of only *n*-butylamine, the 620-nm fluorescence intensity was 1.9 million CPS. However, if the thiol adduct was first formed and then followed by addition of *n*-butylamine, the fluorescence intensity at 620 nm was over 7.6 million CPS, giving a 4-fold recovery ratio. Hence, the PeT quenching efficiency of the imine and iminium is about 75%. The

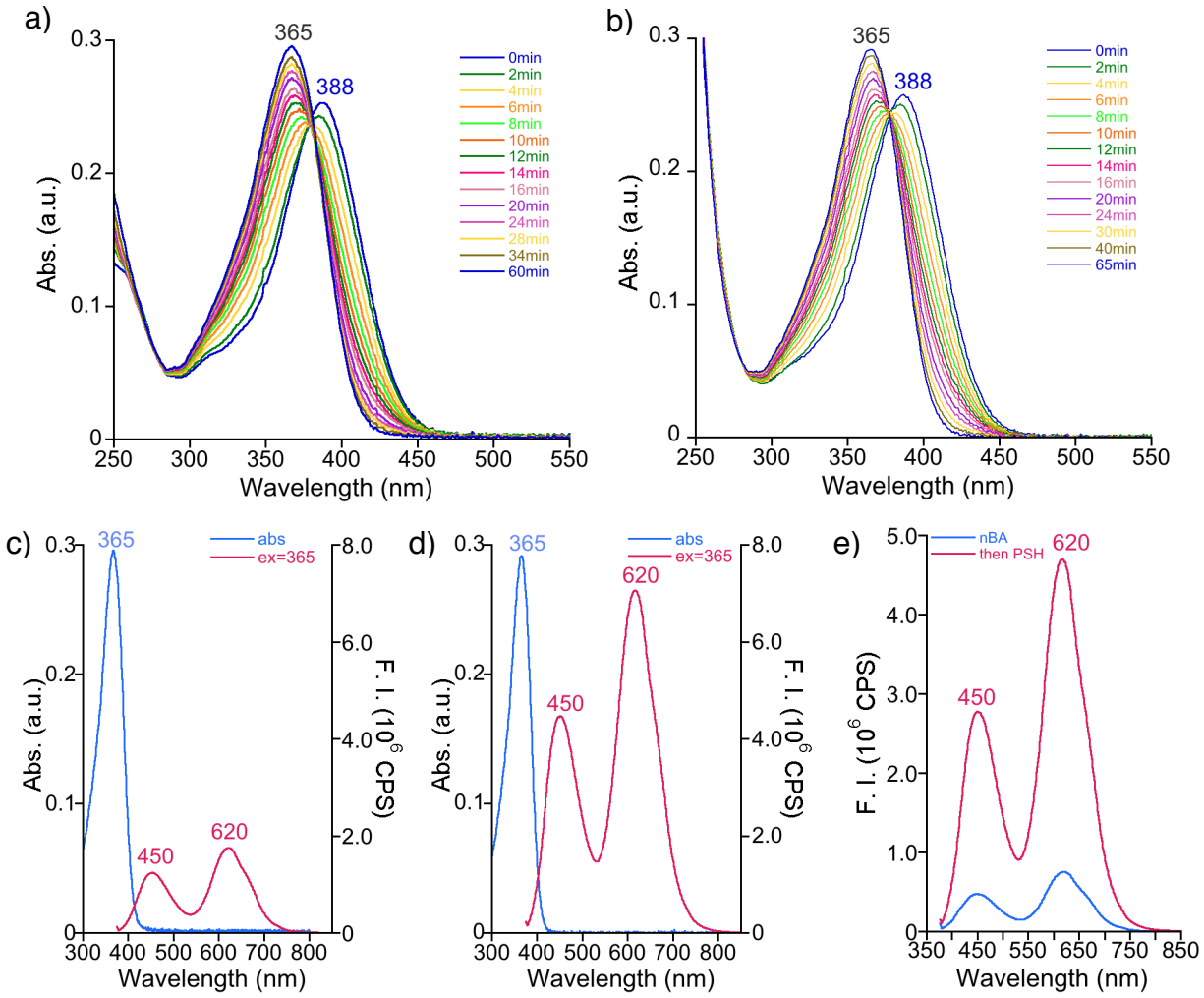


Figure 0-12 Chemoselectivity and fluorescence recovery of **Q2mFR0** with sequential addition of *n*-butylamine (nBA) and *n*-propane thiol (PSH). a) Stacked absorption traces of **Q2mFR0** with excess nBA over time. b) Stacked absorption traces of **Q2mFR0_PSH** adduct with excess nBA over time. a) and b) were recorded in ethanol with same amount of **Q2mFR0**, nBA, and PSH. c) Absorption and emission spectra of **Q2mFR0_nBA**. d) Absorption and emission spectra of the final solution of **Q2mFR0_PSH** added with nBA. c) and d) were recorded in ethanol with same starting concentration of **Q2mFR0**. e) Emission spectra of **Q2mFR0** in ethanol with sequential addition of nBA then PSH.

chemoselectivity of the aldehyde towards thiol over amine was tested by the sequential addition of *n*-butylamine then followed by addition of *n*-propane thiol. Evidenced in **Figure IV-12e**, a greater than 5-fold increase in the fluorescence intensity was observed after thiol addition. This also confirmed that the PeT quenching efficiency was over 80% since all the measurements were carried out in the same cuvette.

Next, flexible docking of **Q2mFR0** was used to propose positions inside hCRBPII for introduction of cysteines that can react with the 3-methoxymaleimide after imine formation. The top 9 poses are displayed in **Figure IV-13**. As shown, all residues within 5 Å distance to the maleimide double bond are highlighted. Among these, L36, R58, S55, A33, and T53 were selected for mutation to cysteine. To demonstrate PeT quenching efficiency *in vitro*, the ESPT mutant **psES235** was selected as the template for

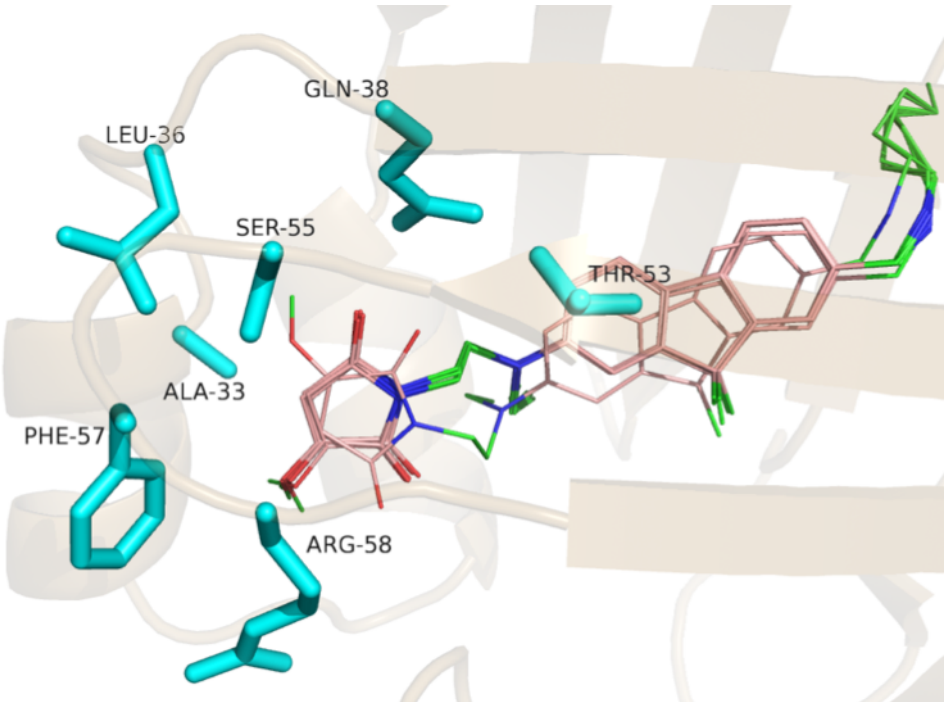


Figure 0-13 Flexible docking results of **Q2mFR0** in hCRBPII KL mutant (PDB ID: 4EXZ). Residues within 5 Å distance to the maleimide double bond carbon atoms are highlighted in cyan and stick form. **Q2mFR0** is covalently attached to the Q108K residue. The top 9 poses are stacked in and displayed line form.

mutagenesis as it featured both long-wavelength emission and ultrafast imine formation kinetics. Before cysteine mutations on the listed positions, residues C95, C121, and C126 of **psES235** were mutated to alanines to avoid any possible reactions with **Q2mFR0** outside the binding cavity. Nonetheless, the resulting triple mutant and its derivatives (i.e., A33C, S55C, L36C, R58C, and Q108L) were not expressed solubly. Hence, cysteine mutations were directly carried out on **psES235**. Summarized in **Table IV-1**, A33C, S55C, and R58C mutations showed protein expressions with different ratio of hCRBPII monomer over domain-swapped dimer. T29C mutant of **psES235** completely altered the expression pattern with only dimer harvested. For a consistent comparison of the spectral features with **psES235**, only monomers were used in the following experiments.

Table 0-1 Oligomeric nature of **psES235** cysteine mutations.

MUTANT		Soluble expression	
		monomer	dimer
psES235	Q108K:K40E:T53A:R58L:Q38F:Q4F	100%	-
psWS44	Q108K:K40E:T53A:R58L:Q38F:Q4F:C95A:C121A:C126A	no expression	
psWS45	Q108K:K40E:T53A:R58L:Q38F:Q4F:C95A:C121A:C126A:A33C	no expression	
psWS47	Q108K:K40E:T53A:R58L:Q38F:Q4F:C95A:C121A:C126A:S55C	no expression	
psWS48	Q108K:K40E:T53A:R58L:Q38F:Q4F:C95A:C121A:C126A:L36C	no expression	
psWS50	Q108K:K40E:T53A:R58C:Q38F:Q4F:C95A:C121A:C126A	no expression	
psWS49	Q108L:K40E:T53A:R58L:Q38F:Q4F:C95A:C121A:C126A	no expression	
psWS51	Q108K:K40E:T53A:R58L:Q38F:Q4F:A33C	68%	32%
psWS52	Q108K:K40E:T53A:R58L:Q38F:Q4F:S55C	54%	46%
psWS53	Q108K:K40E:T53A:R58C:Q38F:Q4F	91%	9%
psWS54	Q108K:K40E:T53A:R58L:Q38F:Q4F:L36C	> 99%	-
psWS55	Q108K:K40E:T53A:R58L:Q38F:Q4F:T29C	-	> 95%

Monomers and dimers were separated by size exclusion chromatography. The isolated yields of oligomers were determined by NanoDrop microvolume spectrophotometer with default protocol. The template mutant **psES235** is shaded blue. Mutants that cannot express are shaded grey. Soluble proteins are shaded green.

The imine formation of **Q2mFR0** with **psES235** and its expressible mutants (i.e., **psWS54** and monomers of **psWS51**, **psWS52**, and **psWS53**) share the same observable pattern. The absorption and emission spectra of **psWS54** are shown in **Figure IV-14** as an example. It should be noted that the imine formation with **psES235**, **psWS51**, **psWS52**, and **psWS53** is fast and takes less than 2 min. With **psWS54**, the imine also forms quickly with ~ 70% conversion upon addition of **Q2mFR0**, although the maximal intensity at 374 nm is observed over 1.5 h. The excitation at 374 nm gives an exclusive long-wavelength

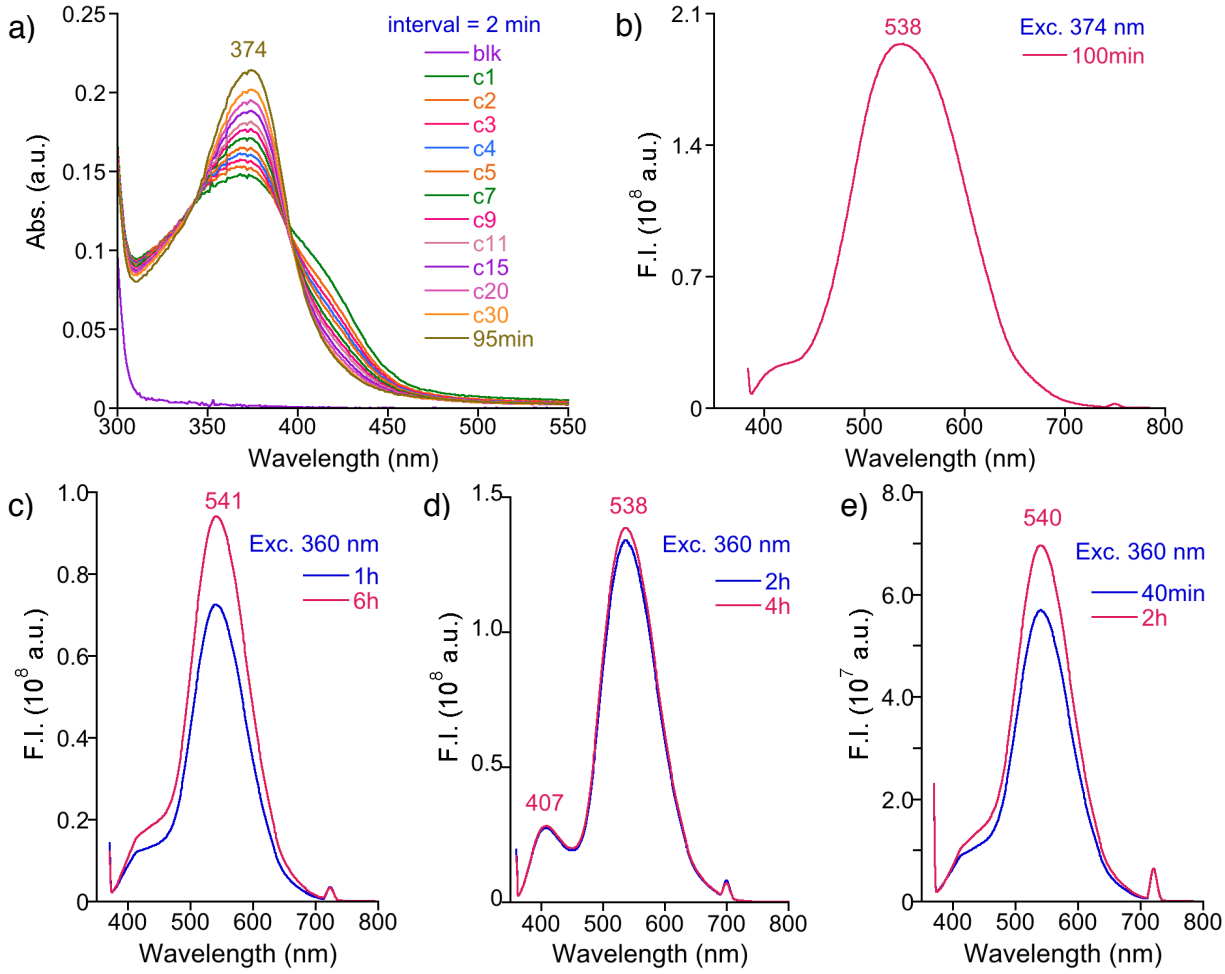


Figure 0-14 Absorption and emission spectra of **Q2mFR0** and **psES235** cysteine mutants. a) Stacked absorption traces of **Q2mFR0** and **psWS54** over time. b) Emission spectrum of **Q2mFR0**/**psWS54** with 374 nm excitation. Emission spectra with excitation at corresponding absorption maxima at different time points after **Q2mFR0** addition to c) **psWS51** monomer, d) **psWS52** monomer, e) **psWS53** monomer.

ESPT emission centered at 538 nm. In contrast, the complex of **Q2mFR0**/**psES235** is essentially non-fluorescent. Shown in **Figure IV-14c-d**, different ratio of regular imine emission and ESPT emission is observed in different mutant complexes, with a more obvious imine emission presented in **psWS53**. The fluorescence recovery checked at different time points post **Q2mFR0** addition shows a gradual increase, validating the effective inhibition of the maleimide PeT quenching by cysteine addition.

A closer look at the fluorescence recovery kinetics is provided in **Figure IV-15**. **Q2mFR0**/**psES235** was used as the control of baseline fluorescence before recovery. As seen, its emission intensity was consistently small over 4 h. Among the four cysteine mutants, **psWS54** showed the fastest recovery kinetics and the highest recovery ratio. The bar graph plotted in **Figure IV-15b** shows that even after 30 min, **psWS54** can recover over 80% of the ESPT fluorescence. The pseudo-first order fluorescence recovery rates can be derived from **Figure IV-15a** by fitting the curves to an exponential function. As shown in **Table IV-2**, **psWS54** also possesses the highest quantum yield.

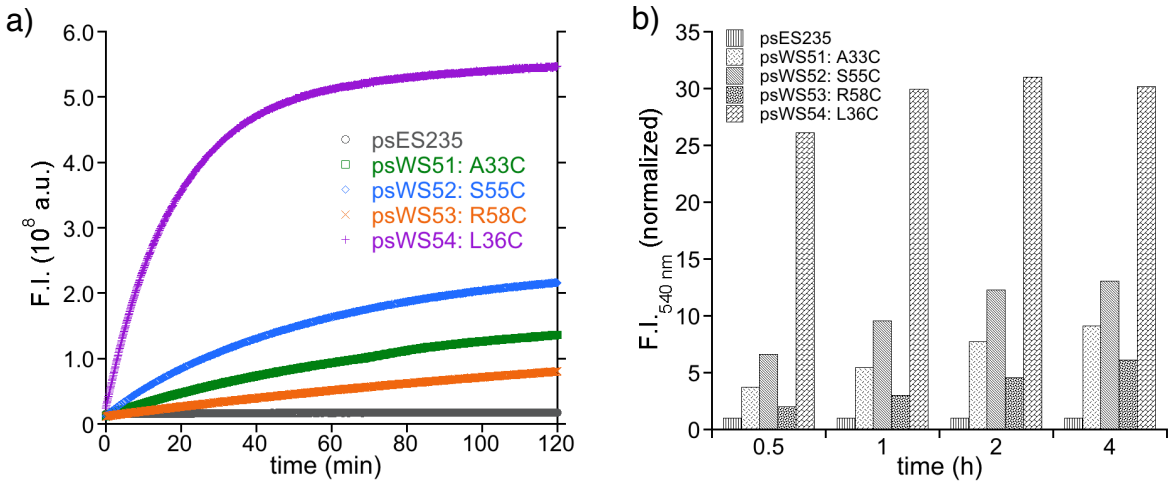


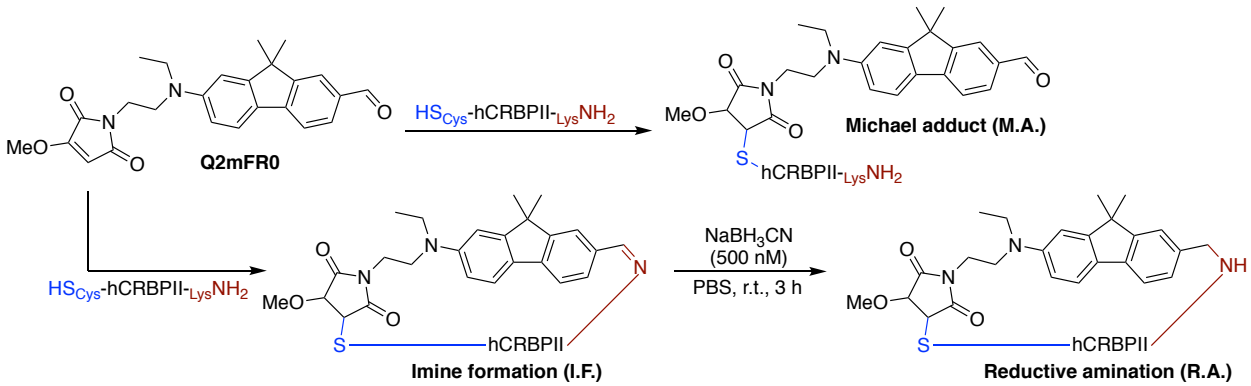
Figure 0-15 Fluorescence recovery of **Q2mFR0**/**psWS51-54**. a) Fluorescence recovery kinetics monitored at 540 nm. b) Fluorescence recovery ratio of different cysteine mutants over **psES235** monitored at 540 nm at different time points.

Table 0-2 QY and fluorescence recovery kinetics of **psES325** and **psWS51-54**.

Mutant	QY[a]	Fluorescence recovery half-time $t_{1/2}$ (min)[b]
psES235	0.05	-
psWS51	0.40	88.7
psWS52	0.31	45.2
psWS53	0.49	154.5
psWS54	0.67	15.0

Fluorescence quantum yields are determined by absolute measurement. The emission recovery half-time is determined by fitting the fluorescence recovery kinetic curves to an exponential rise function.

High-resolution mass spectrometry (HRMS) was used to investigate the stoichiometry of the reactions between **Q2mFR0** and hCRBPII mutants. There are several possibilities after the addition of **Q2mFR0** to a solution of hCRBPII mutants: i) non-covalent residence of **Q2mFR0** in the binding cavity; ii) Michael addition inside the cavity without imine formation; iii) both the aldehyde and maleimide moieties react as desired; iv) multiple Michael additions with cysteines on the exterior of hCRBPII (i.e., C95,



Scheme 0-8 Detectable adducts of **Q2mFR0**/hCRBPII in HRMS. A sequential step of reductive amination after both imine formation and Michael addition was used to derivatize the complex into a more stable form for mass detection.

C121, and C126). There is no difference in HRMS for i) and ii), but one can tell from the aldehyde fluorescence recovery if the Michael addition happens or not. Scenario iii) and iv) can be differentiate by HRMS data and the spectral change in the ESPT emission as well. A brief description of the possibilities is presented in **Scheme IV-8**.

The imine or iminium formed from **Q2mFR0** and hCRBPII complexation was easily hydrolyzed under ESI analysis condition. Hence, reductive amination was carried out with $NaCNBH_3$ in aqueous solution to reduce the imine double bond and furnish more stable derivatives for mass detection (**Scheme IV-8**). As shown in **Table IV-3**, no adduct m/z peak was observed with samples under native condition (indicated by I.F., imine formation). Instead, after reductive amination, correct m/z peaks were found with the corresponding mutants. Importantly, there was no detection of any mutant adducted with

Table 0-3 HRMS of **Q2mFR0**/hCRBPII adducts.

		Apo protein $[M]^+$	+ Q2mFR0 (free/M.A.) $[M+1]^+$	+ Q2mFR0 (I.F.) $[M]^+$	+ Q2mFR0 (R.A.) $[M+1]^+$
psES235	*calc.*	15671.7	16089.9	16071.9	16073.9
	exp.	15671.5	N.O.	N.O.	N.D.
psWS51	*calc.*	15703.8	16123.0	16104.0	16107.0
	exp.	15704.0	16123.0	N.O.	16107.0
psWS52	*calc.*	15687.8	16107.0	16088.0	16091.0
	exp.	N.D.	N.D.	N.D.	N.D.
psWS53	*calc.*	15661.7	16079.9	16061.9	16064.9
	exp.	15662.0	16081.0	N.O.	16065.0
psWS54	*calc.*	15661.7	16079.9	16061.9	16064.9
	exp.	15662.0	16081.0	N.O.	N.D.

Data collected with ESI^+ mode on a Waters Xevo G2-XS QTOF mass spectrometer (Agilent). All samples were run through a BetaBasic column (CN, 10 × 1 mm, 5 μM) with acetonitrile and 0.1% formic acid in H_2O as the mobile phase. N.O.: not observed. N.D.: not determined.

multiple **Q2mFR0**, ensuring the 1:1 stoichiometry of the maleimide adduction. Further evidence of the regio-selectivity with the interior cysteine was provided with **Q2mFR0**/**psES235** as no Michael adduct was observed under native condition.

Based on these HRMS observations, we can conclude that as a proof of principle, **Q2mFR0** successfully bound cysteine variants of **psES235** (**psWS51** to **psWS54**) via the Michael addition of the thiol group on to the maleimide ring, subsequently with the imine formation between Q108K and the aldehyde moiety. As validated with spectroscopic measurement, the unbound **Q2mFR0** is in the "dark" state. Its complex with the above

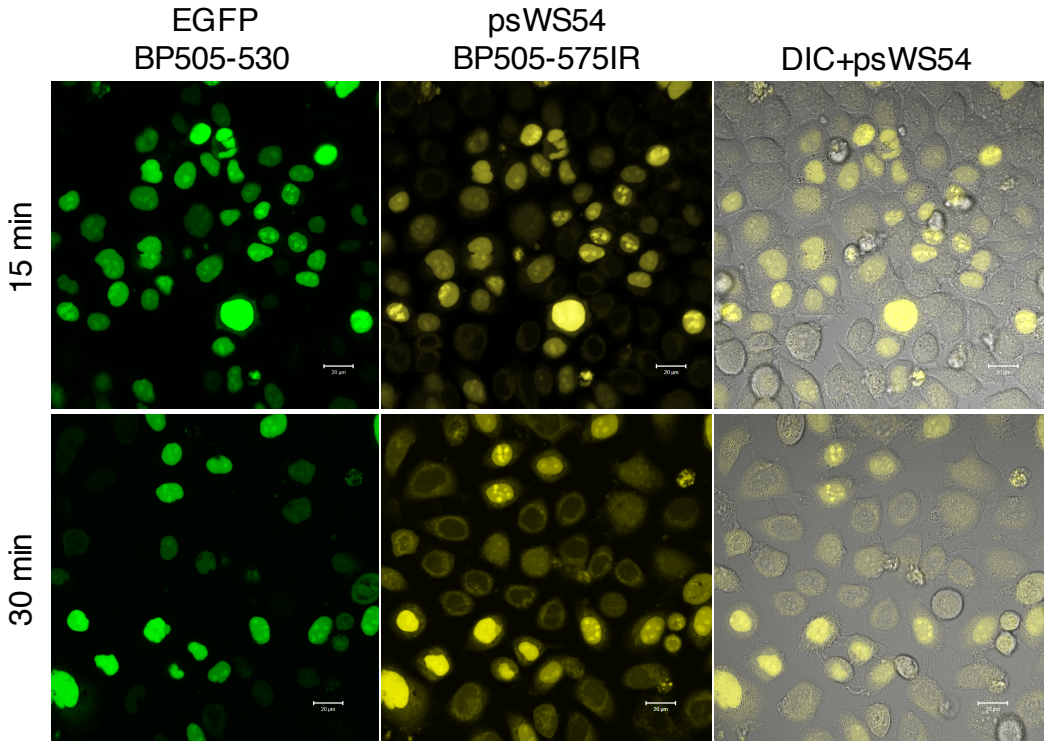


Figure 0-16 Confocal imaging of HeLa cells expressing pFlag-CMV2 construct: EGFP-**psWS54**-3xNLS. Kalman averaging 4 was applied. The reference EGFP channel was excited with a 488 nm laser and collected with a BP505-530 bandpass filter. The **psWS54** channel was excited with a 405 nm laser and collected with a BP505-575IR bandpass filter. Same excitation power, gain and offset levels were applied. Cells were stained with 2 μM **Q2mFR0** and incubated at 37 °C for indicated time. No washing steps were applied before imaging. Scale bar: 20 μm.

psES235 variants successfully restores ESPT emission of the resultant imines after quencher deactivation by the cysteines. These *in vitro* analyses have paved the way for testing PeT-based no-wash *in cellulo* imaging.

psWS54 was cloned into the pFlag2-CMV vectors encoding N-terminal EGFP as a reference reporter and C-terminal signaling peptides as described in **0**. The nuclei-localizing construct was expressed in the living HeLa cells and a no-wash imaging protocol was tested. As shown in **Figure IV-16**, cells were stained with **Q2mFR0** at a final concentration of 2 μM. Samples were directly subjected to imaging at different time duration. After 15 min of **Q2mFR0** incubation, the fluorescence of the dye/hCRBPII complex was observed. A dim but obvious fluorescence background was presented in the non-transfected cells, as more clearly observed in the overlay of DIC and hCRBPII channels. This non-specific background became more profound with extended incubation time, and was directly observable in the hCRBPII channel. Considering the *in vitro*

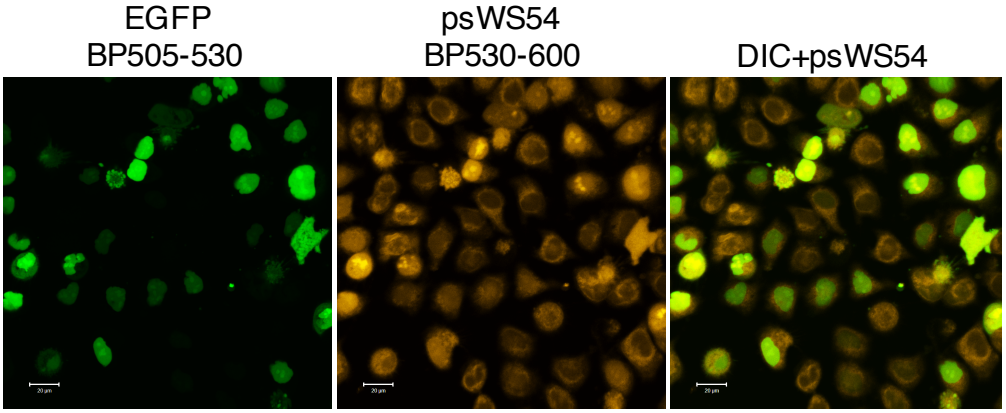


Figure 0-17 Confocal imaging of HeLa cells expressing pFlag-CMV2 construct: EGFP-**psWS54**-3xNLS. The reference EGFP channel was excited with a 488 nm laser and collected with a BP505-530 bandpass filter. The **psWS54** channel was excited with a 405 nm laser and collected with a BP530-600 instead of a BP505-575IR bandpass filter. Cells were stained with 2 μM **Q2mFR0** at room temperature for 35 min. No washing steps were applied before imaging. Scale bar: 20 μm.

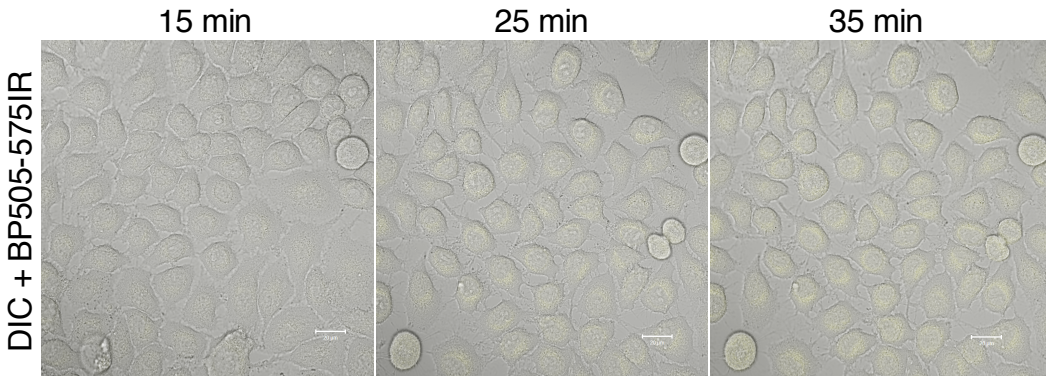


Figure 0-18 Non-specific fluorescence background of **Q2mFR0** at different time points. **Q2mFR0** (2 μM) was used to stain HeLa cells at room temperature. The field of view was excited with a 405 nm laser and images were acquired with a BP505-575IR bandpass filter. No washing steps were applied. Scale bar: 20 μm.

emission spectrum of **Q2mFR0**/**psWS54** (**Figure IV-14b**), the emission dichroic was set to BP530-600 to avoid the crosstalk of EGFP channel. The temperature for dye-staining was lowered to 23 °C to decrease non-specific binding of the maleimide quencher. Nevertheless, severe non-specific background was observed without washing (**Figure IV-17**). The non-specicific fluorescence background caused by unwanted reactions of the maleimide quencher was further estimated with non-transfected HeLa cells. Cells were stained with **Q2mFR0** and kept at room temperature. It was observed that with extended time of incubation, the non-specific background gradually increased (**Figure IV-18**). This non-specific background is probably caused by the restoration of quenched fluorescence due to side reactions of the maleimide with biological thiols, such as GSH. Different reductive sulfur species that are common in biological settings need to be examined along with **Q2mFR0** *in vitro* to identify the origin of the background fluorescence.

I.23 Conclusion and future directions

A fluorogenic dye **Q2mFR0** has been designed based on the PeT quenching by a tethered substituted maleimide moiety for no-wash live cell imaging. The fluorescence

recovery is facilitated by the nucleophilic addition of the maleimide with specifically positioned cysteine resides inside the hCRBPII binding cavity. More importantly, the recovered fluorescence signal for microscopic imaging is the emission from the ESPT process. Hence, three triggering mechanisms have been incorporated to obtain fluorogenicity for this system, namely, i) donor-type PeT quenching, ii) imine formation of the active lysine and the fluorophore's aldehyde, and subsequent iii) long-wavelength emission from the ESPT process.

Modification of **Q2mFR0** is needed to increase its fluorogenicity, i.e., the reaction specificity towards engineered cysteine of hCRBPII. It is hypothesized that non-specific reaction of the maleimide is caused by GSH. Therefore, two strategies are currently adapted for the optimization. The first involves the installment of two substituted maleimide moieties on the scaffold of **FR0**. Presumably, the first non-specific GSH adduct will sterically hinder further addition of GSH to the second maleimide, thus keeping the fluorophore quenched before its specific reaction inside hCRBPII cavity. In turn, two cysteines are needed to be engineered inside the cavity to accommodate the two maleimides.

The second strategy is to further increase the PeT quenching efficiency of the substituted maleimide while introducing more steric bulk to reduce its reactivity towards non-specific thiols. It is evident that the introduction of methoxy effectively decreases the electrophilicity of the maleimide and keeps the quenching at the same time. It can be reasoned that with different alkoxy substitutions, the reactivity and quenching efficiency of the maleimide will be affected both electronically and sterically. A quick method for

$$\frac{1}{\tau_x} = \frac{1}{\tau_0} + k_q[Q] \quad \cdots\cdots\cdots\cdots\cdots\cdots\cdots\cdots\cdots\cdots\cdots\cdots\cdots\cdots \text{(1)}$$

$$\frac{\Phi_e^0}{\Phi_e^x} = 1 + k_q\tau_0[Q] \quad \cdots\cdots\cdots\cdots\cdots\cdots\cdots\cdots\cdots\cdots\cdots\cdots\cdots\cdots \text{(2)}$$

Equation 0-1 Stern-Volmer equations. τ is the fluorescence life-time. k_q is dynamic quenching rate. [Q] is the concentration of maleimides. Φ is the fluorescence quantum yield. Footnote "0" denotes the solution with only **FR0**. Footnote "x" denotes the mixed solutions.

screening the proper alkoxy substituent can be proposed based on Stern-Volmer dynamic quenching analysis (**Equation IV-1**). Briefly, different alkoxy-substituted maleimides can be mixed with **FR0** at various concentrations. For a given maleimide, the PeT quenching rate k_q can simply be derived by plotting the ratio of $QY_{mixture}$ over QY_{FR0l} against the variable concentrations of the maleimide. The lead maleimide can then be tethered to **85** for *in vivo* testing. Apparently, the two strategies can be combined.

I.24 Experimental section

Materials and general methods

All chemicals and solvents were purchased from Sigma-Aldrich and used without further purification. NMR (^{1}H, ^{13}C) spectra were recorded with Agilent DirectDrive2 500 MHz spectrometer and referenced with the residual ^{1}H peak from the deuterated solvents. HRMS (ESI) analysis was done by using a Waters Xevo G2-XS QTOF mass spectrometer (Agilent) and referenced against Polyethylene Glycol (PEG-400-600).

General protocols of site-directed mutagenesis, cloning, protein expression and purification, mammalian cell culture and transfection, UV/Vis and fluorescence spectroscopies, dye-hCRBPII binding kinetics, absolute quantum yield measurement,

and live cell confocal imaging can be referred to the description of general methods in **Section I.13**.

***N*-methyloylmaleimide (73)**[64]

To a suspension of maleimide (1.0 g, 0.010 mmol) in an aqueous solution of NaOH (pH 5.1, 1.0 mL) was added 37% formalin (0.33 g, 0.011 mmol). The mixture was stirred at room temperature for 30 min. A white crystalline solid precipitated from the mixture. The solid was filtered and recrystallized from ethyl acetate to afford white crystal (1.03 g, 79% yield).

^{1}H NMR (500 MHz, DMSO-d_6), δ (ppm): 7.06 (s, 2H), 6.27 (t, J = 7.0 Hz, 1H), 4.76 (d, J = 7.0 Hz, 2H). ^{13}C NMR (126 MHz, DMSO-d_6) δ (ppm): 171.05, 135.37, 60.06. ESI-MS: (calc.) (m/z) calcd for $C_5H_5NO_3$ $[M+H]^+$ 128.03, found 128.10.

7-Bromo-*N*-maleimidomethyl-9,9-dimethyl-9*H*-fluoren-2-amine (74)

To a solution of **68** (1.00 g, 3.46 mmol) in anhydrous toluene (30 mL) was added **73** (530 mg, 4.16 mmol) and 3 Å MS. The reaction was performed in a Dean-Stark apparatus and was refluxed overnight. After full conversion, the reaction mixture was concentrated *in vacuo* and the raw product was purified by gradient chromatography with 15 ~ 20% ethyl acetate in hexane to afford a light yellow solid (733 mg, 53% yield).

^{1}H NMR (500 MHz, DMSO-d_6) δ (ppm): 7.64 (d, J = 1.9 Hz, 1H), 7.52 (dd, J_1 = 8.2 Hz, J_2 = 2.5 Hz, 2H), 7.39 (dd, J_1 = 8.1 Hz, J_2 = 1.9 Hz, 1H), 7.03 (s, 2H), 6.94 (d, J = 2.1 Hz, 1H), 6.79 (t, J = 7.1 Hz, 1H), 6.73 (dd, J_1 = 8.3 Hz, J_2 = 2.2 Hz, 1H), 4.86 (d, J = 7.0

Hz, 2H), 1.34 (s, 6H). ^{13}C NMR (126 MHz, DMSO-d_6) δ (ppm): 171.73, 155.20, 155.14, 146.98, 139.16, 135.71, 135.18, 130.09, 127.40, 126.11, 121.61, 120.72, 118.42, 112.41, 106.63, 46.98, 46.92, 27.32, 14.55. ESI-MS: (calc.) (m/z) calcd for $C_{20}H_{17}BrN_2O_2$ $[M+H]^+$ 397.05, found 397.13.

***N*-(7-bromo-9,9-dimethyl-9*H*-fluoren-2-yl)acetamide (75)**

To a solution of **68** (300 mg, 1.04 mmol) in glacial acetic acid (3 mL) was added acetic anhydride (531 mg, 5.20 mmol). The solution was stirred at 60 °C for 2 h. The resulting mixture was then neutralized with aqueous sodium carbonate solution and extracted with ethyl acetate. The combined organic phase was concentrated *in vacuo*. The crude was purified by flash column with 30% ethyl acetate in hexane to afford a white solid (285 mg, 83% yield).

^{1}H NMR (500 MHz, Chloroform-*d*) δ (ppm): 7.73 (d, J = 2.0 Hz, 1H), 7.62 (d, J = 8.2 Hz, 1H), 7.56 – 7.50 (m, 2H), 7.44 (dd, J_1 = 8.1 Hz, J_2 = 1.9 Hz, 1H), 7.36 (dd, J_1 = 8.1 Hz, J_2 = 2.0 Hz, 1H), 2.22 (s, 3H), 1.47 (s, 6H). ^{13}C NMR (126 MHz, Chloroform-*d*) δ (ppm): 193.48, 155.62, 154.39, 137.77, 137.55, 134.35, 130.08, 126.08, 120.98, 120.46, 118.78, 114.40, 109.99, 47.25, 26.99, 24.82. ESI-MS: (calc.) (m/z) calcd for $C_{17}H_{16}BrNO$ $[M+H]^+$ 330.05, found 330.09.

7-Bromo-*N*-ethyl-9,9-dimethyl-9*H*-fluoren-2-amine (76)

To a solution of **75** (440 mg, 1.33 mmol) in anhydrous THF (25 mL) was added borane-dimethyl sulfide (152 mg, 190 μL, 2.00 mmol). The reaction mixture was refluxed

for 6 h. Saturated sodium bicarbonate (10 mL) was then added and the mixture was refluxed for another 1 h. The final mixture was diluted with water and extracted with ethyl acetate. The organic phase was combined and dried with anhydrous sodium sulfate. The solvent was removed under reduced pressure to afford a white solid (420 mg, yield = quant.)

^{1}H NMR (500 MHz, Chloroform-*d*) δ (ppm): 7.54 (d, *J* = 8.1 Hz, 1H), 7.49 (d, *J* = 1.7 Hz, 1H), 7.45 (d, *J* = 8.0 Hz, 1H), 7.40 (dd, *J* = 8.0, 1.8 Hz, 1H), 6.89 (s, 1H), 6.83 (s, 1H), 3.29 (q, *J* = 7.1 Hz, 2H), 1.44 (s, 6H), 1.34 (t, *J* = 7.2 Hz, 3H). ^{13}C NMR (126 MHz, Chloroform-*d*) δ (ppm): 155.18, 154.79, 148.42, 138.89, 129.81, 128.00, 125.74, 121.02, 119.82, 118.68, 111.94, 106.82, 46.85, 38.85, 27.26, 14.81. ESI-MS: (calc.) (m/z) calcd for $C_{17}H_{18}BrN$ $[M+H]^+$ 316.07, found 316.12.

7-Bromo-*N*-ethyl-*N*-maleimidomethyl-9,9-dimethyl-9*H*-fluoren-2-amine (77)

To a solution of **76** (160 mg, 0.506 mmol) in anhydrous toluene (20 mL) was added **73** (130 mg, 1.01 mmol). The reaction was refluxed at 130 °C overnight with a Dean-Stark apparatus. The reaction mixture was then purified by flash chromatography with 10% ethyl acetate in hexane to afford a bright red solid (170 mg, 79% yield).

^{1}H NMR (500 MHz, DMSO-d_6) δ (ppm): 7.65 (d, *J* = 2.0 Hz, 1H), 7.58 (d, *J* = 8.4 Hz, 1H), 7.54 (d, *J* = 8.0 Hz, 1H), 7.39 (dd, J_1 = 8.1 Hz, J_2 = 1.9 Hz, 1H), 7.18 (d, *J* = 2.4 Hz, 1H), 7.05 (s, 2H), 6.90 – 6.83 (m, 1H), 5.03 (s, 2H), 3.59 (q, *J* = 7.0 Hz, 2H), 1.38 (s, 6H), 1.11 (t, *J* = 7.0 Hz, 3H). ESI-MS: (calc.) (m/z) calcd for $C_{22}H_{21}BrN_2O_2$ $[M+H]^+$ 425.08, found 425.17.

7-(Ethylamino)-9,9-dimethyl-9*H*-fluorene-2-carbaldehyde (78)

To a solution of **76** (30 mg, 0.095 mmol) in anhydrous THF (3 mL) was added *tert*-butyllithium (0.14 mL, 1.7 M in pentane, 0.24 mmol) at -78 °C under argon. The reaction mixture was stirred at -78 °C for 1 h. A solution of DMF (17 mg, 0.24 mmol) in anhydrous THF was added and the mixture was stirred for another 1 h. The mixture was then gradually warmed to room temperature and kept for another 2 h. The reaction was quenched with chilled methanol and extracted with ethyl acetate. The organic phase was combined, dried over anhydrous sodium sulfate, and concentrated *in vacuo*. The crude was purified by flash chromatography with 15% ethyl acetate in hexane to afford a yellow solid (16 mg, 64% yield).

^{1}H NMR (500 MHz, Chloroform-*d*) δ (ppm): 9.99 (s, 1H), 7.88 (d, J = 1.4 Hz, 1H), 7.78 (dd, J_1 = 7.8 Hz, J_2 = 1.4 Hz, 1H), 7.66 (d, J = 7.8 Hz, 1H), 7.60 (d, J = 8.2 Hz, 1H), 6.68 (d, J = 2.1 Hz, 1H), 6.63 (dd, J_1 = 8.3 Hz, J_2 = 2.2 Hz, 1H), 3.26 (q, J = 7.1 Hz, 2H), 1.48 (s, 6H), 1.32 (t, J = 7.2 Hz, 3H). ^{13}C NMR (126 MHz, Chloroform-*d*) δ (ppm): 192.09, 157.32, 153.26, 149.46, 146.70, 133.73, 131.16, 127.31, 122.47, 122.44, 118.41, 112.32, 106.52, 46.61, 38.70, 27.13, 14.70. ESI-MS: (calc.) (m/z) calcd for $C_{18}H_{19}NO$ $[M+H]^+$ 266.15, found 266.24.

7-((Maleimidomethyl)(ethyl)amino)-9,9-dimethyl-9*H*-fluorene-2-carbaldehyde (Q1FR0)

The procedure is similar to the preparation of **77**. To a solution of **78** (15 mg, 0.057 mmol) in dry toluene (5 mL) was added **73** (14 mg, 0.11 mmol). The reaction was carried

out with a Dean-Stark apparatus overnight. The crude product was purified with 20% ethyl acetate in hexane to afford an orange solid (17 mg, 81% yield).

^{1}H NMR (500 MHz, Chloroform-*d*) δ (ppm): 10.00 (s, 1H), 7.93 – 7.88 (m, 1H), 7.80 (dd, J_1 = 7.8 Hz, J_2 = 1.5 Hz, 1H), 7.68 (dd, J_1 = 12.7 Hz, J_2 = 8.1 Hz, 2H), 7.23 (d, J = 2.4 Hz, 1H), 6.99 (dd, J_1 = 8.5 Hz, J_2 = 2.5 Hz, 1H), 6.74 (s, 2H), 5.18 (s, 2H), 3.75 (q, J = 7.1 Hz, 2H), 1.52 (s, 6H), 1.27 (t, J = 7.0 Hz, 3H). ^{13}C NMR (126 MHz, Chloroform-*d*) δ (ppm): 192.10, 171.13, 157.14, 153.62, 147.19, 146.33, 134.45, 134.01, 131.01, 127.75, 122.61, 122.29, 118.77, 112.45, 107.59, 54.61, 46.87, 45.38, 27.10, 12.63. ESI-MS: (calc.) (m/z) calcd for $C_{23}H_{22}N_2O_3$ $[M+H]^+$ 375.17, found 375.25.

3,3-Dimethoxypyrrolidine-2,5-dione (79)[65]

Bromine (12.4 g, 4.00 ml, 77.3 mmol) was added dropwise to a solution of maleimide (5.00 g, 51.5 mmol) in methanol (200 mL) at 0 °C. The reaction mixture was stirred for 16 h at RT, then concentrated in vacuo. The crude was dissolved in methanol (75 mL) and added dropwise to a solution of metal sodium (4.74 g, 206 mmol) in methanol (200 mL). After 20 h the reaction mixture was concentrated *in vacuo* and diluted with EtOAc (100 mL). The mixture was neutralized by slow addition of HCl aq. (6 M), then diluted into water and extracted with EtOAc. The combined organic phase was washed with brine and dried over anhydrous $NaSO_4$. Concentration *in vacuo* afforded a white solid (7.8 g, 95% yield).

^{1}H NMR (500 MHz, Chloroform-*d*) δ (ppm): 8.18 (s, 1H), 3.44 (s, 6H), 2.86 (s, 2H). ESI-MS: (calc.) (m/z) calcd for $C_6H_9NO_4$ $[M+H]^+$ 160.06, found 160.15.

3-Methoxy maleimide (80)[65]

To a solution of **79** (7.8 g, 44 mmol) in toluene (200 mL) was added $TsOH \cdot H_2O$ (0.84 g, 4.4 mmol). The reaction was refluxed with a Dean-Stark apparatus for 24 h. Toluene (80 mL) was removed and the flask was replenished with fresh toluene. The reaction mixture was refluxed for another 24 h before being concentrated *in vacuo*. The crude was purified by flash chromatography with 40 ~ 60% EtOAc in Hexane to afford a white flak7 solid (5.5 g, 88% yield).

^{1}H NMR (500 MHz, Chloroform-*d*) δ (ppm): 7.28 (s, 1H), 5.44 (d, J = 1.5 Hz, 1H), 3.94 (s, 3H). ^{13}C NMR (126 MHz, Chloroform-*d*) δ (ppm): 169.46, 165.27, 161.08, 97.45, 59.07. ESI-MS: (calc.) (m/z) calcd for $C_5H_5NO_3$ $[M+H]^+$ 128.03, found 128.10.

***N*-chloroethyl-3-methoxy maleimide (81)**

Powdered solid of **80** (50 mg, 0.39 mmol) was mixed with anhydrous potassium carbonate (163 mg, 1.2 mmol) and tetrabutylammonium bromide (TBAB, 13 mg, 0.039 mmol). To the mixture was added 1-bromo-2-chloroethane (680 mg, 4.7 mmol) and the suspension was stirred at 40 °C for 3 h. The crude was purified by flash chromatography with 30% EtOAc in hexane to afford a yellow solid (64 mg, 85% yield).

^{1}H NMR (500 MHz, Chloroform-*d*) δ (ppm): 5.44 (s, 1H), 3.94 (s, 3H), 3.85 (t, J = 6.3 Hz, 2H), 3.66 (t, J = 6.3 Hz, 2H). ^{13}C NMR (126 MHz, Chloroform-*d*) δ (ppm): 169.56, 165.18, 160.86, 96.39, 59.03, 40.85, 39.04. ESI-MS: (calc.) (m/z) calcd for $C_7H_8ClNO_3$ $[M+H]^+$ 190.03, found 190.13.

***N*-bromoethyl-3-methoxy maleimide (82)**

The procedure is similar to the preparation of **81**. Powdered solid **80** (50 mg, 0.39 mmol) was mixed with anhydrous K_2CO_3 (163 mg, 1.2 mmol), TBAB (13 mg, 0.039 mmol), and 1,2-dibromoethane (890 mg, 4.7 mmol). Flash chromatography afforded an off-white solid (69 mg, 75% yield).

^{1}H NMR (500 MHz, Chloroform-*d*) δ (ppm): 5.44 (s, 1H), 3.95 (s, 3H), 3.92 (t, *J* = 6.6 Hz, 2H), 3.51 (t, *J* = 6.7 Hz, 2H). ^{13}C NMR (126 MHz, Chloroform-*d*) δ (ppm): 169.46, 165.06, 160.87, 96.39, 59.04, 38.93, 28.28. ESI-MS: (calc.) (m/z) calcd for $C_7H_8BrNO_3$ $[M+H]^+$ 233.98, found 234.10.

***N*-iodoethyl-3-methoxy maleimide (83)**

To a solution of **82** (100 mg, 0.427 mmol) in anhydrous acetone (5 mL) was added sodium iodide (320 mg, 2.14 mmol). The reaction mixture was refluxed overnight and then concentrated *in vacuo*. The crude was purified by flash chromatography with 30% EtOAc in hexane to afford an off-white solid (113 mg, 94% yield).

^{1}H NMR (500 MHz, Chloroform-*d*) δ (ppm): 5.44 (s, 1H), 3.95 (s, 3H), 3.89 (t, *J* = 7.2 Hz, 2H), 3.30 (t, *J* = 7.2 Hz, 2H). ^{13}C NMR (126 MHz, Chloroform-*d*) δ (ppm): 169.32, 164.89, 160.89, 96.38, 59.04, 39.67, 0.18. ESI-MS: (calc.) (m/z) calcd for $C_7H_8INO_3$ $[M+H]^+$ 281.96, found 282.05.

***N*-hydroxyethyl-3-methoxy maleimide (84)**

A solid of **80** (50 mg, 0.39 mmol) and a solution of ethylene oxide (0.20 mL, 2.5 M, 0.41 mmol) in THF (2.5 mL) was mixed and heated to 40 °C in a sealed tube overnight. A light orange solid was filtered and purified by flash chromatography with 50% EtOAc in hexane, affording 20 mg (30% yield).

^{1}H NMR (500 MHz, Chloroform-*d*) δ (ppm): 5.44 (s, 1H), 3.94 (s, 3H), 3.77 (m, 2H), 3.73 – 3.66 (m, 2H), 2.16 (s, 1H). ^{13}C NMR (126 MHz, Chloroform-*d*) δ (ppm): 170.63, 165.93, 160.98, 96.31, 60.96, 59.02, 40.53. ESI-MS: (calc.) (m/z) calcd for $C_7H_9NO_4$ $[M+H]^+$ 172.06, found 172.15.

7-((2-Bromoethyl)(ethyl)amino)-9,9-dimethyl-9*H*-fluorene-2-carbaldehyde (85)

To a solution of **78** (130 mg, 0.490 mmol) in dry DMF (5 mL) was added 1,2-dibromoethane (460 mg, 2.45 mmol). The mixture was stirred and heated at 80 °C overnight. The crude was washed with water and extracted with EtOAc. The combined organic phase was dried over anhydrous sodium sulfate and concentrated *in vacuo*. The title product was purified by flash chromatography with 10% EtOAc in hexane to afford an orange solid (68 mg, 61% yield b.r.s.m.).

^{1}H NMR (500 MHz, Chloroform-*d*) δ (ppm): 10.00 (s, 1H), 7.90 (d, J = 1.4 Hz, 1H), 7.81 (m, 1H), 7.67 (m, 2H), 6.73 (s, 2H), 3.80 (t, J = 7.9 Hz, 2H), 3.59 – 3.45 (m, 4H), 1.51 (s, 6H), 1.27 (t, J = 7.1 Hz, 4H). ^{13}C NMR (126 MHz, Chloroform-*d*) δ (ppm): 192.06, 157.42, 153.34, 146.36, 133.86, 131.17, 130.90, 122.79, 122.65, 122.53, 118.55, 111.06, 105.46, 52.69, 46.80, 45.63, 28.24, 27.20, 12.56. ESI-MS: (calc.) (m/z) calcd for $C_{20}H_{22}BrNO$ $[M+H]^+$ 372.09, found 372.17.

7-((3-Methoxy-maleimidoethyl)(ethyl)amino)-9,9-dimethyl-9*H*-fluorene-2-carbaldehyde (Q2mFR0)

To a solution of **85** (4.0 mg, 0.011 mmol) in dry DMF (1 mL) was added **80** (2.7 mg, 0.022 mmol) and potassium carbonate (7.4 mg, 0.54 mmol). The mixture was stirred and heated at 80 °C overnight. The resulting mixture was washed with water and extracted with ethyl acetate. The combined organic phase was dried and concentrated *in vacuo*. The title compound was purified by prep-TLC with 40% EtOAc in hexane to afford a light yellow solid (2.6 mg, 58% yield).

^{1}H NMR (500 MHz, Chloroform-*d*) δ (ppm): 9.98 (s, 1H), 7.89 (d, J = 1.3 Hz, 1H), 7.78 (dd, J_1 = 7.8 Hz, J_2 = 1.5 Hz, 1H), 7.64 (m, 2H), 6.94 – 6.88 (m, 1H), 6.77 (d, J = 8.3 Hz, 1H), 5.36 (s, 1H), 3.87 (s, 3H), 3.74 (dd, J_1 = 8.6 Hz, J_2 = 6.1 Hz, 2H), 3.57 (dd, J_1 = 8.6 Hz, J_2 = 6.1 Hz, 2H), 3.48 (q, J = 7.1 Hz, 2H), 1.51 (s, 7H), 1.23 (t, J = 7.1 Hz, 3H). ^{13}C NMR (126 MHz, Chloroform-*d*) δ (ppm): 192.08, 169.97, 165.53, 160.94, 157.47, 153.46, 146.57, 133.69, 131.11, 122.52, 122.49, 118.40, 111.40, 106.02, 97.49, 96.28, 59.06, 58.95, 46.79, 34.54, 29.70, 27.14, 12.40. ESI-MS: (calc.) (m/z) calcd for $C_{25}H_{26}N_2O_4$ $[M+H]^+$ 419.1971, found 419.1973.

REFERENCES

REFERENCES

1. Klymchenko, A.S. Solvatochromic and Fluorogenic Dyes as Environment-Sensitive Probes: Design and Biological Applications. *Acc. Chem. Res.* **2017**, 50, 366-375.

2. Walker, C.L. et al. Fluorescence imaging using synthetic GFP chromophores. *Curr. Opin. Chem. Biol.* **2015**, 27, 64-74.

3. Haidekker, M.A. & Theodorakis, E.A. Molecular rotors-fluorescent biosensors for viscosity and flow. *Org. Biomol. Chem.* **2007**, 5, 1669-1678.

4. Ludovic, J. & Arnaud, G. Fluorogen-based reporters for fluorescence imaging: a review. *Methods Appl. Fluoresc.* **2015**, 3, 042007.

5. Hövelmann, F., Gaspar, I., Ephrussi, A. & Seitz, O. Brightness Enhanced DNA FIT-Probes for Wash-Free RNA Imaging in Tissue. *J. Am. Chem. Soc.* **2013**, 135, 19025-19032.

6. Hori, Y. & Kikuchi, K. Protein labeling with fluorogenic probes for no-wash live-cell imaging of proteins. *Curr. Opin. Chem. Biol.* **2013**, 17, 644-650.

7. Bruchez, M.P. Dark dyes–bright complexes: fluorogenic protein labeling. *Curr. Opin. Chem. Biol.* **2015**, 27, 18-23.

8. Szent-Gyorgyi, C., Schmidt, B.F., Fitzpatrick, J.A.J. & Bruchez, M.P. Fluorogenic Dendrons with Multiple Donor Chromophores as Bright Genetically Targeted and Activated Probes. *J. Am. Chem. Soc.* **2010**, 132, 11103-11109.

9. Baranczak, A. et al. A Fluorogenic Aryl Fluorosulfate for Intraorganellar Transthyretin Imaging in Living Cells and in Caenorhabditis elegans. *J. Am. Chem. Soc.* **2015**, 137, 7404-7414.

10. Sasaki, S., Drummen, G.P.C. & Konishi, G.-i. Recent advances in twisted intramolecular charge transfer (TICT) fluorescence and related phenomena in materials chemistry. *J. Mater. Chem. C* **2016**, 4, 2731-2743.

11. Haberhauer, G., Gleiter, R. & Burkhart, C. Planarized Intramolecular Charge Transfer: A Concept for Fluorophores with both Large Stokes Shifts and High Fluorescence Quantum Yields. *Chem. Eur. J.* **2016**, 22, 971-978.

12. Shaya, J. et al. Turn-on Fluorene Push–Pull Probes with High Brightness and Photostability for Visualizing Lipid Order in Biomembranes. *ACS Chem. Biol.* **2017**, 12, 3022-3030.

13. Prifti, E. et al. A Fluorogenic Probe for SNAP-Tagged Plasma Membrane Proteins Based on the Solvatochromic Molecule Nile Red. *ACS Chem. Biol.* **2014**, 9, 606-612.

14. Karpenko, I.A. et al. Red Fluorescent Turn-On Ligands for Imaging and Quantifying G Protein-Coupled Receptors in Living Cells. *ChemBioChem* **2014**, 15, 359-363.

15. Liu, T.-K. et al. A Rapid SNAP-Tag Fluorogenic Probe Based on an Environment-Sensitive Fluorophore for No-Wash Live Cell Imaging. *ACS Chem. Biol.* **2014**, 9, 2359-2365.

16. Yoshii, T., Mizusawa, K., Takaoka, Y. & Hamachi, I. Intracellular Protein-Responsive Supramolecules: Protein Sensing and In-Cell Construction of Inhibitor Assay System. *J. Am. Chem. Soc.* **2014**, 136, 16635-16642.

17. Hou, T. C., Wu, Y.-Y., Chiang, P. Y. & Tan, K. T. Near-infrared fluorescence activation probes based on disassembly-induced emission cyanine dye. *Chem. Sci.* **2015**, 6, 4643-4649.

18. Anees, P., Sreejith, S. & Ajayaghosh, A. Self-Assembled Near-Infrared Dye Nanoparticles as a Selective Protein Sensor by Activation of a Dormant Fluorophore. *J. Am. Chem. Soc.* **2014**, 136, 13233-13239.

19. Karpenko, I.A. et al. Fluorogenic Squaraine Dimers with Polarity-Sensitive Folding As Bright Far-Red Probes for Background-Free Bioimaging. *J. Am. Chem. Soc.* **2015**, 137, 405-412.

20. Yuan, Y., Xu, S., Cheng, X., Cai, X. & Liu, B. Bioorthogonal Turn-On Probe Based on Aggregation-Induced Emission Characteristics for Cancer Cell Imaging and Ablation. *Angew. Chem. Int. Ed.* **2016**, 55, 6457-6461.

21. Zhao, E. et al. Light-Enhanced Bacterial Killing and Wash-Free Imaging Based on AIE Fluorogen. *ACS Appl. Mater. Interfaces* **2015**, 7, 7180-7188.

22. Peng, L. et al. Rational Design of a Red-Emissive Fluorophore with AIE and ESIPT Characteristics and Its Application in Light-Up Sensing of Esterase. *Anal. Chem.* **2017**, 89, 3162-3168.

23. Schneider, A.F.L. & Hackenberger, C.P.R. Fluorescent labelling in living cells. *Curr. Opin. Biotechnol.* **2017**, 48, 61-68.

24. Wang, Y. et al. Development of a red fluorescent light-up probe for highly selective and sensitive detection of vicinal dithiol-containing proteins in living cells. *Chem. Sci.* **2016**, 7, 518-524.

25. Lukinavičius, G. et al. Fluorogenic Probes for Multicolor Imaging in Living Cells. *J. Am. Chem. Soc.* **2016**, 138, 9365-9368.

26. Lukinavičius, G. et al. A near-infrared fluorophore for live-cell super-resolution microscopy of cellular proteins. *Nat. Chem.* **2013**, 5, 132-139.

27. Zhang, Q., Liu, H. & Pan, Z. A general approach for the development of fluorogenic probes suitable for no-wash imaging of kinases in live cells. *Chem. Commun.* **2014**, 50, 15319-15322.

28. Blum, G. et al. Dynamic imaging of protease activity with fluorescently quenched activity-based probes. *Nat. Chem. Biol.* **2005**, 1, 203-209.

29. Kim, S., Kim, H., Choi, Y. & Kim, Y. A New Strategy for Fluorogenic Esterase Probes Displaying Low Levels of Non-specific Hydrolysis. *Chem. Eur. J.* **2015**, 21, 9645-9649.

30. Kuriki, Y. et al. Establishment of Molecular Design Strategy To Obtain Activatable Fluorescent Probes for Carboxypeptidases. *J. Am. Chem. Soc.* **2018**, 140, 1767-1773.

31. Mizukami, S., Watanabe, S., Akimoto, Y. & Kikuchi, K. No-Wash Protein Labeling with Designed Fluorogenic Probes and Application to Real-Time Pulse-Chase Analysis. *J. Am. Chem. Soc.* **2012**, 134, 1623-1629.

32. Sun, X. et al. Development of SNAP-Tag Fluorogenic Probes for Wash-Free Fluorescence Imaging. *ChemBioChem* **2011**, 12, 2217-2226.

33. Yuan, Y., Zhang, R., Cheng, X., Xu, S. & Liu, B. A FRET probe with AIEgen as the energy quencher: dual signal turn-on for self-validated caspase detection. *Chem. Sci.* **2016**, 7, 4245-4250.

34. Meimetis, L.G., Carlson, J.C.T., Giedt, R.J., Kohler, R.H. & Weissleder, R. Ultrafluorogenic Coumarin-Tetrazine Probes for Real-Time Biological Imaging. *Angew. Chem. Int. Ed.* **2014**, 53, 7531-7534.

35. Speiser, S. Photophysics and Mechanisms of Intramolecular Electronic Energy Transfer in Bichromophoric Molecular Systems: Solution and Supersonic Jet Studies. *Chem. Rev.* **1996**, 96, 1953-1976.

36. Turro, N. J., Ramamurthy, V. & Scaiano, J. C. *Modern Molecular Photochemistry of Organic Molecules.* (University Science Books; Sausalito, California; **2010**).

37. Fan, J., Hu, M., Zhan, P. & Peng, X. Energy transfer cassettes based on organic fluorophores: construction and applications in ratiometric sensing. *Chem. Soc. Rev.* **2013**, 42, 29-43.

38. Li, Z. et al. Tetrazole Photoclick Chemistry: Reinvestigating Its Suitability as a Bioorthogonal Reaction and Potential Applications. *Angew. Chem. Int. Ed.* **2016**, 55, 2002-2006.

39. Knorr, G., Kozma, E., Herner, A., Lemke, E.A. & Kele, P. New Red-Emitting Tetrazine-Phenoxazine Fluorogenic Labels for Live-Cell Intracellular Bioorthogonal Labeling Schemes. *Chem. Eur. J.* **2016**, 22, 8972-8979.

40. Kamikawa, Y. et al. Design of a protein tag and fluorogenic probe with modular structure for live-cell imaging of intracellular proteins. *Chem. Sci.* **2016**, 7, 308-314.

41. Hori, Y., Nakaki, K., Sato, M., Mizukami, S. & Kikuchi, K. Development of Protein-Labeling Probes with a Redesigned Fluorogenic Switch Based on Intramolecular Association for No-Wash Live-Cell Imaging. *Angew. Chem. Int. Ed.* **2012**, 51, 5611-5614.

42. Zhang, H. et al. An Off–On COX-2-Specific Fluorescent Probe: Targeting the Golgi Apparatus of Cancer Cells. *J. Am. Chem. Soc.* **2013**, 135, 11663-11669.

43. de Silva, A.P., Moody, T.S. & Wright, G.D. Fluorescent PET (Photoinduced Electron Transfer) sensors as potent analytical tools. *Analyst* **2009**, 134, 2385-2393.

44. Callan, J.F., de Silva, A.P. & Magri, D.C. Luminescent sensors and switches in the early 21st century. *Tetrahedron* **2005**, 61, 8551-8588.

45. Martínez-Máñez, R. & Sancenón, F. Fluorogenic and Chromogenic Chemosensors and Reagents for Anions. *Chem. Rev.* **2003**, 103, 4419-4476.

46. Daly, B., Ling, J. & de Silva, A.P. Current developments in fluorescent PET (photoinduced electron transfer) sensors and switches. *Chem. Soc. Rev.* **2015**, 44, 4203-4211.

47. Men, Y. et al. Rational design and synthesis of fast-response NBD-based fluorescent probes for biothiols. *Tetrahedron Lett.* **2015**, 56, 5781-5786.

48. Georgiev, N.I., Sakr, A.R. & Bojinov, V.B. Design and synthesis of a novel PET and ICT based 1,8-naphthalimide FRET bichromophore as a four-input Disabled–Enabled-OR logic gate. *Sens. Actuators, B* **2015**, 221, 625-634.

49. Yang, X.-F. et al. A dual emission fluorescent probe enables simultaneous detection of glutathione and cysteine/homocysteine. *Chem. Sci.* **2014**, 5, 2177-2183.

50. Zhang, W., Ma, Z., Du, L. & Li, M. Design strategy for photoinduced electron transfer-based small-molecule fluorescent probes of biomacromolecules. *Analyst* **2014**, 139, 2641-2649.

51. Yang, C. et al. An aldehyde group-based P-acid probe for selective fluorescence turn-on sensing of cysteine and homocysteine. *Biosens. Bioelectron.* **2016**, 80, 17-23.

52. Dubey, R.K., Knorr, G., Westerveld, N. & Jager, W.F. Fluorescent PET probes based on perylene-3,4,9,10-tetracarboxylic tetraesters. *Org. Biomol. Chem.* **2016**, 14, 1564-1568.

53. Nawimanage, R.R., Prasai, B., Hettiarachchi, S.U. & McCarley, R.L. Rapid, Photoinduced Electron Transfer-Modulated, Turn-on Fluorescent Probe for Detection and Cellular Imaging of Biologically Significant Thiols. *Anal. Chem.* **2014**, 86, 12266-12271.

54. Shiraishi, Y., Nakamura, M., Kogure, T. & Hirai, T. Off-on fluorometric detection of cyanide anions in an aqueous mixture by an indane-based receptor. *New J. Chem.* **2016**, 40, 1237-1243.

55. Okitsu, K., Misawa, T., Shoda, T., Kurihara, M. & Demizu, Y. Development of an ON/OFF switchable fluorescent probe targeting His tag fused proteins in living cells. *Bioorg. Med. Chem. Lett.* **2017**, 27, 3417-3422.

56. Zhao, Y. et al. Benzimidazo[2,1-a]benz[de]isoquinoline-7-one-12-carboxylic acid based fluorescent sensors for pH and $Fe3^{+}$. *J. Photochem. Photobiol., A* **2016**, 314, 52-59.

57. Lee, J.J. et al. A PET-based fluorometric chemosensor for the determination of mercury(II) and pH, and hydrolysis reaction-based colorimetric detection of hydrogen sulfide. *Dalton Trans.* **2016**, 45, 5700-5712.

58. Liu, Z., Zhou, Y., Du, L. & Li, M. Novel intramolecular photoinduced electron transfer-based probe for the Human Ether-a-go-go-Related Gene (hERG) potassium channel. *Analyst* **2015**, 140, 8101-8108.

59. Kamiya, M. et al. An Enzymatically Activated Fluorescence Probe for Targeted Tumor Imaging. *J. Am. Chem. Soc.* **2007**, 129, 3918-3929.

60. Chen, Y. et al. Coumarin-Based Fluorogenic Probes for No-Wash Protein Labeling. *Angew. Chem. Int. Ed.* **2014**, 53, 13785-13788.

61. Guy, J. et al. Convergent Preparation and Photophysical Characterization of Dimaleimide Dansyl Fluorogens: Elucidation of the Maleimide Fluorescence Quenching Mechanism. *J. Am. Chem. Soc.* **2007**, 129, 11969-11977.

62. Girouard, S., Houle, M.-H., Grandbois, A., Keillor, J.W. & Michnick, S.W. Synthesis and Characterization of Dimaleimide Fluorogens Designed for Specific Labeling of Proteins. *J. Am. Chem. Soc.* **2005**, 127, 559-566.

63. Matsumoto, T., Urano, Y., Shoda, T., Kojima, H. & Nagano, T. A Thiol-Reactive Fluorescence Probe Based on Donor-Excited Photoinduced Electron Transfer: Key Role of Ortho Substitution. *Org. Lett.* **2007**, 9, 3375-3377.

64. Vail, S.L. & Pierce, A.G. Limitations for the addition of amides to formaldehyde and glyoxal. *J. Org. Chem.* **1972**, 37, 391-393.

65. Booker-Milburn, K.I., Baker, J.R. & Bruce, I. Rapid Access to Azepine-Fused Oxetanols from Alkoxy-Substituted Maleimides. *Org. Lett.* **2004**, 6, 1481-1484.